UNIVERSIDADE ESTADUAL DE CAMPINAS
Instituto de Física Gleb Wataghin

MURILO BARBOSA ALVES

Longitudinal collective effects in synchrotrons with double-rf system

Efeitos coletivos longitudinais em síncrotrons com sistema de rf duplo

CAMPINAS
2025

MURILO BARBOSA ALVES

Longitudinal collective effects in synchrotrons with double-rf system

Efeitos coletivos longitudinais em síncrotrons com sistema de rf duplo

Thesis presented to the Gleb Wataghin Institute of Physics of the University of Campinas in partial fulfillment of the requirements for the degree of Doctor of Science, in the area of Physics.

Tese apresentada ao Instituto de Física Gleb Wataghin da Universidade Estadual de Campinas como parte dos requisitos exigidos para a obtenção do título de Doutor em Ciências, na Área de Física.

Supervisor/Orientadora: Liu Lin

Este trabalho corresponde à versão final da tese defendida pelo aluno Murilo Barbosa Alves e orientada pela Profa. Dra. Liu Lin.

CAMPINAS

2025

Ficha catalográfica
Universidade Estadual de Campinas (UNICAMP)
Biblioteca do Instituto de Física Gleb Wataghin
Lucimeire de Oliveira Silva da Rocha - CRB 8-9174

AL87L Alves, Murilo Barbosa, 1996-
Longitudinal collective effects in synchrotrons with double-rf system / Murilo Barbosa Alves. – Campinas, SP : [s.n.], 2025.

Orientador: Liu Lin.
Tese (doutorado) – Universidade Estadual de Campinas (UNICAMP), Instituto de Física Gleb Wataghin.

1. Projeto Sirius. 2. Física de aceleradores. 3. Efeitos coletivos. 4. Dinâmica longitudinal. 5. Instabilidades coletivas. 6. Cavidades harmônicas. 7. Radiofrequência. I. Lin, Liu. II. Universidade Estadual de Campinas (UNICAMP). Instituto de Física Gleb Wataghin. III. Título.

Informações complementares

Título em outro idioma: Efeitos coletivos longitudinais em síncrotrons com sistema de rf duplo
Palavras-chave em inglês:
Sirius Project
Accelerator physics
Collective effects
Longitudinal dynamics
Collective instabilities
Harmonic cavities
Radio frequency
Área de concentração: Física
Titulação: Doutor em Ciências
Banca examinadora:
Liu Lin [Orientador]
Pedro Fernandes Tavares
Renato Pakter
José Antônio Brum
Antonio Rubens Britto de Castro
Data de defesa: 31-03-2025
Programa de Pós-Graduação: Física

Objetivos de Desenvolvimento Sustentável (ODS)
Não se aplica

Identificação e informações acadêmicas do(a) aluno(a)
- ORCID do autor: https://orcid.org/0000-0003-4356-8248
- Currículo Lattes do autor: http://lattes.cnpq.br/4778579260807817

- Profa. Dra. Liu Lin (Centro Nacional de Pesquisa em Energia e Materiais/Laboratório Nacional de Luz Síncrotron) - Presidente e Orientadora

- Dr. Pedro Fernandes Tavares (Lund University/MAX IV Laboratory)

- Prof. Dr. Renato Pakter (Instituto de Física - Universidade Federal do Rio Grande do Sul)

- Prof. Dr. José Antônio Brum (IFGW/ UNICAMP)

- Prof. Dr. Antonio Rubens Britto de Castro (IFGW/ UNICAMP)

A Ata da Defesa, assinada pelos membros da Comissão Examinadora, consta no SIGA/Sistema de Fluxo de Dissertação/Tese e na Secretaria do Programa da Unidade.

Acknowledgements

This PhD thesis is the most important milestone in my nearly 25-year journey as a student. It is impossible to acknowledge everyone who contributed along the way, but I will try to mention those who played a key role in making this thesis a reality. I have the feeling that a special bond forms among those who share the unique experience of an accelerator commissioning. Pursuing this PhD with the same team after commissioning SIRIUS made everything much easier.

My PhD supervisor, Liu Lin. Thank you for your encouragement and unwavering support in pursuing this PhD. I have greatly benefited from your rare ability to maintain a broad perspective while knowing exactly when to focus on the details. I am grateful for your generosity in sharing your vast experience in accelerator physics and for providing me with so many opportunities.

My friend and collaborator, Fernando de Sá. Thank you for teaching me so much, especially about collective effects. Your knowledge, creative way of thinking, and problem-solving skills have been impressing me since the day we met. I feel lucky to work with someone as intellectually generous as you.

My work supervisor, Ximenes Resende. Thank you for your support and openness. Your interest in and suggestions for the problems I was working always pushed me to deepen my understanding.

The colleagues from the groups in the Accelerator Division: FAC, RFQ, IDS, GOP, and EPP. Thank you for the discussions and daily company. Thanks to André Lima and Iago Carvalho for the collaboration of many years. Thanks to Matheus Velloso for proofreading the thesis.

The MAX IV colleagues. Thank you, Francis Cullinan and Åke Andersson, for the collaboration. I learned a lot from your experienced guidance. The month I spent in Lund was special to me; it was where I had the chance to run experiments with harmonic cavities and see snow for the first time. Thank you, Miriam Brosi, for the discussions, support with the streak-camera setup and data processing. Thank you, Henrique Caiafa, for your great help and company during my visit.

The SOLEIL colleagues. Thank you, Alexis Gamelin and Vadim Gubaidulin, for your collaboration and interest in testing `pycolleff`. Our discussions helped me gain a better understanding of many problems and also pushed me to improve the code.

The student and organizing committees of IPAC'21, '22, and '24. Thanks for providing an amazing platform to share my work, learn from the accelerator community, and visit new places. Thank you, Dmitry Teytelman, for finding time in a busy IPAC schedule to discuss about instabilities and feedback systems. Thank you, Gabriele Bassi, for the stimulating discussions at IPAC'24 and during my visit to NSLS-II.

The professors and researchers who kindly agreed to be on my evaluation committees. Thank you, Pedro Tavares (also for supporting the collaboration with MAX IV), Renato Pakter, Antonio Rubens de Castro, José Brum, Tulio da Rocha, and Cristiane Jahnke.

My family. Thank you to my mother, Elaine, my father, Luciano, and my sister, Mirela, for your endless support throughout my life. My self-confidence is built upon your unshakable trust in me. This PhD degree is an achievement for our entire family.

My beloved wife, Ana Clara. You are the light on my path, my daily laughter, and my most sincere partner. If blessings exist, having you in my life is certainly one.

The institutions LNLS/CNPEM and IFGW/Unicamp. Thanks for providing the support, opportunities and infrastructure that made this thesis possible.

I acknowledge "Financiadora de Estudos e Projetos" (FINEP) for funding the research conducted during my visit to MAX IV under Grant FINEP/MAXSIRIUS Nr. 01.18.0007.00. Furthermore, I declare that I have not received any additional financial support from grant agencies during the development of this PhD thesis.

Abstract

Collective effects play an essential role in the stability of electrons in synchrotron light sources, directly influencing the quality and reliability of the produced light. The use of higher harmonic radiofrequency cavities has become a standard strategy in fourth-generation synchrotrons to control these effects by modifying the longitudinal potential-well that confines the electrons in bunches. This thesis focuses on the detailed description of longitudinal collective effects in synchrotrons equipped with passive higher harmonic cavities, where electromagnetic fields are driven by the electron beam itself. Novel semi-analytical methods were developed to enable self-consistent calculations of the longitudinal equilibrium state and the analysis of collective instabilities under generic conditions. These methods were validated through macroparticle simulations, comparisons with experimental data, and the reproduction of results from previous studies as particular cases. The main motivation for this work was the Phase II of SIRIUS, the fourth-generation synchrotron light source at the Brazilian Synchrotron Light Laboratory (LNLS) in Campinas, Brazil. To achieve the nominal current of 350 mA, the installation of a higher harmonic cavity will be required to lengthen the electron bunches in the SIRIUS storage ring. The theoretical and computational tools developed in this thesis supported the studies of a third-harmonic superconducting cavity for SIRIUS. The results indicate that the chosen harmonic cavity model will achieve the required bunch lengthening, enabling stable operation of SIRIUS at 350 mA, achieving the design parameters and ensuring the high brightness of the synchrotron light.

Resumo

Efeitos coletivos desempenham um papel essencial na estabilidade dos elétrons em fontes de luz síncrotron, influenciando diretamente a qualidade e a confiabilidade da luz produzida. O uso de cavidades de harmônicos mais altos de radiofrequência tornou-se uma estratégia padrão em síncrotrons de quarta geração para controlar esses efeitos, alterando o poço de potencial longitudinal que confina os elétrons em pacotes. Esta tese aborda a descrição detalhada de efeitos coletivos longitudinais em síncrotrons equipados com cavidades passivas de harmônico mais alto, nas quais os campos eletromagnéticos são gerados pelo próprio feixe de elétrons. Para isso, foram desenvolvidos novos métodos semi-analíticos que permitem o cálculo auto-consistente do estado de equilíbrio longitudinal e a análise de instabilidades coletivas em condições genéricas. Esses métodos foram validados por meio de simulações de macropartículas, comparativos com dados experimentais e obtenção de resultados de trabalhos precedentes como casos particulares. A motivação central deste trabalho foi o estudo da Fase II do SIRIUS, a fonte de luz síncrotron de quarta geração do Laboratório Nacional de Luz Síncrotron (LNLS) em Campinas, Brasil. Para atingir a corrente nominal de 350 mA, será necessária a instalação de uma cavidade de harmônico mais alto para alongar os pacotes de elétrons no anel de armazenamento do SIRIUS. As ferramentas teóricas e computacionais desenvolvidas nesta tese forneceram suporte aos estudos de uma cavidade supercondutora de terceiro harmônico para o SIRIUS. Os resultados obtidos indicam que o modelo escolhido será capaz de alongar os pacotes de elétrons conforme necessário, permitindo a operação estável do SIRIUS com 350 mA, atingindo as especificações de projeto e garantindo o alto brilho da luz síncrotron.

Glossary

ALBuMS Algorithms for Longitudinal MultiBunch Beam Stability.

3HC third-harmonic cavity.

BBR broadband resonator.

BPMs beam position monitors.

DFT discrete Fourier transform.

FD frequency-domain.

FFT fast Fourier transform.

FP flat potential.

HC harmonic cavity.

HHC higher harmonic cavity.

HOM higher order mode.

IBS intrabeam scattering.

ID Insertion device.

IDFT inverse discrete Fourier transform.

llrf low-level rf.

LMCI longitudinal mode-coupling instability.

LNLS Brazilian Synchrotron Light Laboratory.

MC main cavity.

NC normal-conducting.

NEG nonevaporable getter.

NFP near flat potential.

PI proportional-integral.

PTBL periodic transient beam loading.

SC superconducting.

SD space-domain.

Contents

Begin with an individual, and before you know it you find that you have created a type; begin with a type, and you find that you have created—nothing.

— F. Scott Fitzgerald, *The Rich Boy*

Introduction

Synchrotron storage rings

Relativistic charged particles radiate synchrotron light when subjected to centripetal acceleration [1]. A synchrotron light source is a scientific facility that explores this phenomenon to produce extremely bright light, which is used to study materials at the atomic level. The wide range of multidisciplinary experimental techniques enabled by synchrotron light makes it a powerful tool in various fields. In these facilities, an ultrarelativistic electron beam is maintained under ultra-high vacuum conditions in a stable orbit along a nearly circular storage ring, emitting synchrotron light that is directed to experimental stations called beamlines.

In storage rings, magnetic fields are used to guide the electrons' path, bending and focusing their trajectory in the transverse directions—radial/horizontal and vertical. The centripetal acceleration in the bending magnets and in the insertion devices (IDs) installed in straight sections causes the electrons to emit synchrotron radiation, losing part of their energy in each revolution. This energy loss is replenished by electric fields oscillating in the radiofrequency (rf) range within resonant structures along the ring, called rf cavities. The oscillating fields in rf cavities are synchronized with the electrons' revolution around the ring—hence the name synchrotron. The longitudinal electric fields, parallel to the electrons' path, also create a mechanism for longitudinal focusing, grouping the electrons into bunches.

The current state-of-the-art synchrotron light sources employ 4$^{\text{th}}$-generation storage rings. With a multibend achromat magnetic lattice, these rings store electron beams with ultralow emittances [2–4]. Low emittance corresponds to a beam with small transverse dimensions and divergences—a highly focused and collimated light source. These properties provide emitted photon beams with extremely high brightness and transverse coherence, enabling researchers to explore light-matter interactions in the energy range from infrared to hard X-rays to study a variety of materials [5–11]. Achieving ultralow emittance required overcoming several challenges in accelerator physics and engineering [12–15].

In the accelerator physics field, the electromagnetic interactions between the electrons, either by direct or environment-mediated mechanisms, are referred to as collective effects.

Many aspects that allow 4^{th}-generation storage rings to produce high-brightness synchrotron light also make them prone to intense collective effects [16]. High-intensity electron beams with small transverse dimensions and low energy spread, confined in vacuum chambers with reduced transverse sections, require a detailed understanding of collective effects to achieve the machine design parameters in practice. Uncontrolled collective effects can degrade machine performance, for instance, leading to increased effective emittance and energy spread, reduced beam lifetime, beam-induced heating of machine components, limitations on maximum current, and other issues.

Collective effects are classified as incoherent or coherent, transverse or longitudinal, and single-bunch or multibunch. Incoherent effects can be understood in terms of the individual behavior of particles, such as intrabeam scattering (IBS) and the Touschek effect, which are Coulomb scattering events between electrons within the same bunch, therefore dependent on the bunch charge density. Coherent effects are mediated by electromagnetic fields left behind as electrons pass through vacuum components. These self-driven fields are called wakefields. Wakefields that decay within the bunch length affect intrabunch behavior (single-bunch effects), while slow-decaying wakefields couple the motion of multiple bunches (multibunch/coupled-bunch effects). These wakefields can build up a positive feedback mechanism, leading to collective instabilities that may deteriorate the quality of the produced synchrotron light or, more dramatically, lead to beam losses.

Motivation for higher harmonic rf cavities

Bunches with high charge densities pose significant challenges for synchrotron light sources, especially in 4^{th}-generation storage rings. The bunch volume in phase space is determined by the product of transverse emittances, energy spread, and bunch length. While reducing charge density by lowering beam current or increasing transverse emittances would decrease the photon beam brightness, increasing the bunch length is a more viable approach. Phase modulation of the main rf system can achieve this [17, 18], but it also increases the effective energy spread, which negatively impacts the radiation from higher undulator harmonics.

An effective alternative is the use of higher harmonic cavities (HHCs), which operate at a harmonic frequency of the main rf system [19–24]. By introducing an additional rf voltage, HHCs modify the longitudinal rf potential, lengthening the bunches while preserving transverse emittances and energy spread.

In a single-rf system, the longitudinal dynamics is approximately linear for small amplitudes, with electrons executing harmonic oscillations around the equilibrium. The HHCs in a double-rf system introduces nonlinearities, altering the longitudinal focusing. This can result in either bunch shortening or bunch lengthening, depending on the cavity setting. In hadron accelerators, HHCs have been used in both modes to enhance synchrotron frequency spread, aiming to stabilize the beam via the Landau damping mechanism [25–30]. Consequently, HHCs have also been called Landau cavities [31, 32].

In synchrotron light sources, HHCs are used primarily for bunch lengthening to mitigate the issues of high bunch charge density[1] while maintaining low emittance and energy spread. Moreover, as for hadron machines, HHCs have been useful to cure instabilities in synchrotron light sources [19, 21, 33].

The electromagnetic fields in HHCs can be excited by an external generator (active mode), as is the case for main rf cavities, or by beam-induced wakefields (passive mode). They can be constructed from either normal-conducting or superconducting materials. The use of HHCs for bunch lengthening is now standard in 4$^{\text{th}}$-generation storage rings [34], ensuring that the design brightness, coherence, and beam lifetime can be achieved for high-intensity, low-emittance beams. Recent efforts have explored active harmonic systems [35] and alternative harmonic orders [36–39].

Outline of the thesis

SIRIUS is a 4$^{\text{th}}$-generation synchrotron light source [40, 41], designed, built, and operated by the Brazilian Synchrotron Light Laboratory (LNLS) in Campinas, Brazil. At the time of writing of this thesis, SIRIUS is in Phase I of operation, delivering a 200 mA beam in top-up injection mode for beamline users since November 2024. Achieving this current was only possible after upgrading the main rf system, replacing the temporary normal-conducting cavity with two superconducting 500 MHz rf cavities. To reach the design current of 350 mA and begin Phase II of operation, the installation of a HHC will be necessary for bunch lengthening, mitigating impedance-induced heating in storage ring components due to the higher beam intensity [42, 43].

The general goal of this PhD thesis is to study HHC-related collective effects, with focus on the longitudinal plane and coupled-bunch instabilities. Throughout this process, theoretical and semi-analytical computational methods were developed and applied to the specific objective of studying and specifying a HHC for Phase II of the SIRIUS storage ring. The two main contributions of the thesis involve semi-analytical methods to calculate the equilibrium bunch distributions and longitudinal instabilities, which resulted in the publications fully reproduced in the Appendices A and B.

This introduction chapter provided a brief overview of the research topics addressed in the thesis. Below, the structure of the subsequent chapters is outlined.

Chapter 1. This chapter introduces the fundamental concepts relevant to the thesis. It covers longitudinal single-particle dynamics in single-rf and double-rf systems, discusses

[1] Short bunches result in high charge densities, leading to increased intrabunch scattering, blown-up equilibrium beam parameters, and reduced beam lifetime. Additionally, the power spectrum of short bunches extends to high frequencies, which can couple to machine impedances, causing beam-induced heating and collective instabilities. These topics are discussed in Chapter 1.

wake functions and impedances, and describe some incoherent and coherent collective effects.

Chapter 2. This chapter provides a brief overview of the method for analyzing collective effects with semi-analytical techniques, focusing on the study of equilibrium and instabilities. The complete contributions were published as journal articles and are reproduced in the Appendices A and B.

Chapter 3. This chapter presents the application of the developed framework to the study of a passive HHC for the SIRIUS storage ring. The basic parameter requirements for the HHC are discussed, including a comparison between normal and superconducting cavities. Results for the specified third-harmonic passive HHC are presented, along with specifications for amplitude and detuning stability control. An evaluation of longitudinal instabilities is also included.

Chapter 4. The main contributions and conclusions of the thesis are summarized, and future directions for research are addressed.

The relevant material published during the PhD period is included in the Appendices, which are based on articles that compile the main contributions of this work. While this structure allows each chapter to be read independently, it may result in some repetition of topics. Each one of these appendices include introduction sections that present the motivation for the study and relevant literature reviews, so certain details not covered in this introduction are discussed later. The thesis is not intended to be self-contained and references are provided for additional details where necessary.

Appendix A (published as Ref. [44]). This appendix presents a self-consistent semi-analytical method for calculating the stationary beam-induced voltage in electron storage rings, considering arbitrary filling patterns and impedance sources. The theory is developed in both space and frequency domains, with benchmarking against SIRIUS parameters and macroparticle tracking simulations. A new approach for simulating beam-loading compensation in active rf cavities is explored in frequency domain, and the impact of broadband impedance on longitudinal equilibrium is analyzed. Finally, a study on Touschek lifetime improvement using a passive higher harmonic cavity is included.

Appendix B (submitted for publication as Ref. [45]). This appendix presents a theoretical framework for analyzing longitudinal coupled-bunch instabilities in double-rf systems with even filling patterns, incorporating potential-well distortion and multiple azimuthal modes. The linearized Vlasov equation is solved in frequency domain, unifying different formulations and recovering recent results as special cases. Applications to different types of instability are discussed, with theoretical predictions matching experimental data.

Appendix C (conference proceeding published as Ref. [46]). In this appendix, experiments carried out during the PhD are reported. Appendix C discusses the optimization of Touschek lifetime with harmonic cavities (HCs) at the MAX IV 1.5 GeV ring and the benchmarking of the equilibrium solver developed in Appendix A (Ref. [44]) against experimental data.

For a comprehensive reading of this thesis, we recommend the following order: Introduction, Chapter 1, Chapter 2, Appendix A, Appendix B, Chapter 3, and Chapter 4. For comparisons with experimental results, we refer to Appendix C. The Annex includes a list of publications produced during the PhD.

On AI-based writing tools

The use of AI-based writing tools in this thesis follows the guidelines of the American Physical Society (APS), available at `https://journals.aps.org/authors/ai-based-writing-tools`.

During the preparation of this thesis, `ChatGPT` was used exclusively for language refinement, grammar corrections, and fluency improvements. The scientific content, ideas, analysis, code implementation, and conclusions presented in this work remain entirely the author's responsibility. Nevertheless, in accordance with recommended ethical guidelines, the use of AI-based tools for textual improvements is acknowledged.

At the heart of our problem—and I mean the problem of the accelerator physicist—is the pernicious self-destructive behavior of particle beams. What inherent flaw makes beams destroy themselves?

— A. M. Sessler, *Collective Phenomena in Accelerators* [47]

1
Fundamental concepts

Contents

In this chapter we present the basic theoretical aspects that are necessary for the next chapters. For in-depth discussions, the well-established references for accelerator physics by M. Sands [48], H. Wiedemann [49], and collective effects by A. Chao [50] and K. Ng [51] are recommended.

1.1 Single-particle dynamics

Consider a storage ring with nominal energy E_0 and circumference C_0. We assume ultrarelativistic electrons, such that the Lorentz factor is $\gamma = E_0/m_0c^2 \gg 1$ and $\beta = v/c \approx 1$, where c is the speed of light and m_0 the electron rest mass. The relation between the electrons' energy and momentum is $E_0 \approx p_0 c$. We will denote the elementary charge as $e > 0$. Electrons at the nominal energy complete a revolution within a period $T_0 = C_0/c$. This period is related to the revolution frequency $f_0 = 1/T_0$ and $\omega_0 = 2\pi f_0$.

The rf frequency in which the electric fields oscillate in the rf cavities is an integer multiple of the revolution frequency, $f_{\mathrm{rf}} = hf_0$. The sinusoidal electric field integrated over the transit time along the rf cavities results in an rf voltage, which is a function of the electrons' arrival time at the cavities. Consequently, the energy gain provided by the rf cavities also depends on the arrival time. Consider an electron with the nominal energy E_0 with zero net energy balance per turn: losing the energy U_0 to synchrotron radiation and gaining the same amount from the rf cavities. This electron is defined as the synchronous particle.

In synchrotron light sources, it is standard to refer to the beam current circulating in the storage ring instead of the number of electrons. The total beam current is given by $I_0 = eN_{\mathrm{total}}/T_0$, where N_{total} is the total number of electrons.

1.1.1 Coordinates and equations of motion

The coordinate system in a storage ring is defined with respect to a reference orbit, defined as the path followed by the synchronous particle in the perfect machine (without errors). Figure 1.1 illustrates the reference system. The synchronous electron passing through a bending magnet with constant magnetic field $\vec{B} = -B_0\hat{y}$ will be deflected in a arc of circle with radius given by $\rho = \frac{E_0}{ecB_0}$. The quantity $B_0\rho = E_0/ec$ is a property of the electrons and called magnetic rigidity. The arc length s follows the trajectory of the synchronous electron along the ring, which can be related to time by $s = \beta ct \approx ct$. The transverse coordinates are defined by the horizontal x and vertical y deviations from the reference orbit. We assume small deviations from the reference orbit, such that the paraxial approximation can be made for the transverse momenta: $p_x/p_0 \approx \frac{\mathrm{d}x}{\mathrm{d}s} = x'$ and $p_y/p_0 \approx \frac{\mathrm{d}y}{\mathrm{d}s} = y'$. The transverse dynamics is described in a four-dimensional space, with the position-angle coordinates (x, x', y, y').

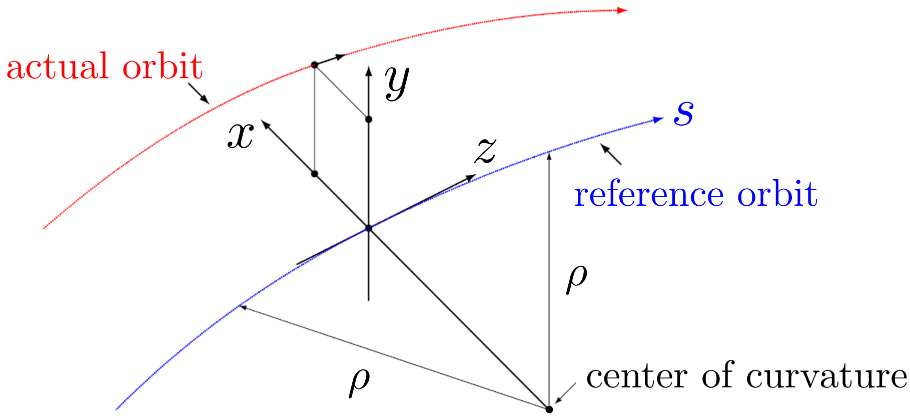

Figure 1.1: Coordinate system for the storage ring. Adapted from [52].

The longitudinal coordinate z for an arbitrary electron is a dynamical variable defined as the difference of its arc length relative to the one of the synchronous particle:

$$z(t) = s_{\text{sync}} - s(t), \tag{1.1}$$

where t is the wall-clock time. With this definition, for an electron behind the synchronous particle the longitudinal coordinate is positive, $z > 0$. The coordinate can also be used in time units simply by $\tau = z/c$.

The other longitudinal coordinate conjugated to z is defined as the relative momentum deviation with respect to the nominal momentum of the synchronous particle:

$$\delta(t) = \frac{p(t) - p_0}{p_0} \approx \frac{E(t) - E_0}{E_0}. \tag{1.2}$$

The ultrarelativistic approximation $E \approx pc$ is considered for electron beams. In this way, the variable δ is regarded as the relative energy deviation and this will be the meaning for δ throughout the thesis. Therefore, the dynamical variables for the longitudinal dynamics are defined by (z, δ).

Rigorously, the dynamics of electrons should be described in a six-dimensional space $(x, x', y, y', z, \delta)$. In this thesis, we focus on the longitudinal plane. A common approach is considering that what happens in the transverse plane has negligible impact on the longitudinal, allowing the longitudinal motion to be described in the two-dimensional space (z, δ). For the following analysis, the only relevant transverse-longitudinal coupling is the dispersion function introduced by the bending magnets. Electrons with different energies are deflected differently by the bending magnets, implying in different orbit lengths. This dependence is captured by the momentum compaction factor α, a dimensionless constant. Neglecting other transverse-longitudinal coupling mechanisms is justified in general, since the longitudinal motion is related to energy oscillations of the electrons, dependent on electric fields parallel to their motion, while the transverse motion depends on magnetic fields in the perpendicular directions that do not modify the electrons' energy. Moreover, the timescale of energy oscillations is orders of magnitude slower than transverse oscillations.

We will now derive the equations of motion for the longitudinal plane. The relation between the relative momentum deviation and the relative orbit length variation is [48, 49]:

$$\frac{\Delta C}{C_0} = \alpha \frac{\Delta p}{p_0}, \tag{1.3}$$

where α is the momentum compaction factor. For the cases of interest here, α is a positive number. The relativistic momentum is $p = \gamma m_0 \beta c$, then the relation between the variations in momentum Δp and velocity $\Delta\beta$ is

$$\frac{\Delta\beta}{\beta_0} = \frac{1}{\gamma^2}\frac{\Delta p}{p_0}. \tag{1.4}$$

With the relation $\beta c = C/T$ and the previous equations, we obtain

$$\frac{\Delta T}{T_0} = \left(\alpha - \frac{1}{\gamma^2}\right)\frac{\Delta p}{p_0}. \tag{1.5}$$

The term $(\alpha - 1/\gamma^2)$ is called slip factor. For ultrarelativistic electrons, $\alpha \gg 1/\gamma^2$ (above transition energy) and the slip factor is approximately α. Consider a fixed s position in the ring and an electron behind the synchronous particle with $z > 0$. For a positive energy deviation, the orbit of this electron is lengthened, thus, after one turn, both its revolution period $\Delta T > 0$ and longitudinal position $\Delta z > 0$ will increase. The two variations are related by $\Delta T = \Delta z/c$.

The electrons only accumulate significant changes in energy after many turns in the ring, thus we can assume the Δz variation is infinitesimal within a revolution. This allows the approximation $\frac{\Delta T}{T_0} = \frac{\Delta z}{C_0} \approx \frac{\mathrm{d}z}{\mathrm{d}s}$. Altogether, these considerations applied to Eq. (1.5) lead to the first equation of motion:

$$\frac{\mathrm{d}z}{\mathrm{d}s} = \alpha\delta. \tag{1.6}$$

The second equation of motion comes from the energy balance. The energy loss to radiation depends on the electron energy. Over one turn, an electron radiates the energy $U_{\mathrm{rad}}(\delta)$ and gains $eV(z)$ from the rf cavity. Normalizing this balance by E_0C_0 and applying the same consideration of infinitesimal variations, we get:

$$\frac{\mathrm{d}\delta}{\mathrm{d}s} = \frac{eV(z) - U_{\mathrm{rad}}(\delta)}{E_0C_0}. \tag{1.7}$$

Equations (1.6) and (1.7) are the two equations of motion for the longitudinal dynamics.

The equations of motion combined with the scheme in Fig. (1.2) are helpful for explaining the phase stability mechanism, a fundamental working principle for synchrotrons. As an approximation, assume that $U_{\mathrm{rad}}(\delta) \approx U_0$. The synchronous particle satisfies $eV(0) = U_0$. Consider a negative derivative of the rf voltage around the synchronous particle[1]. Electrons with $\delta > 0$ have a lengthened orbit, thus arriving later at the rf cavity with $z > 0$. As the $V(z)$ derivative is negative, this implies that $eV(z) < U_0$: a negative energy balance that reduces the excess of energy. The opposite occurs for electrons with $\delta < 0$, leading to a positive energy balance that also push electrons towards the $\delta = 0$ condition. Therefore, the rf voltage derivative acts as a restoring force, focusing the perturbed electrons to the equilibrium fixed-point defined by the synchronous particle. From this analysis it is obvious that a positive derivative of the rf voltage works as a defocusing mechanism.

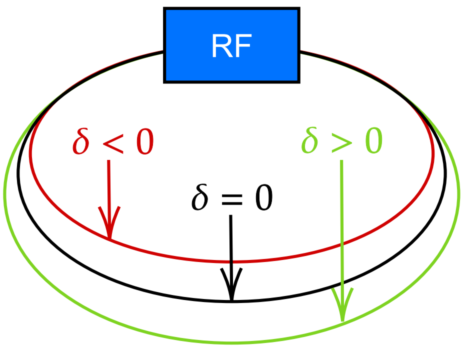

(a) Energy-dependent orbits.

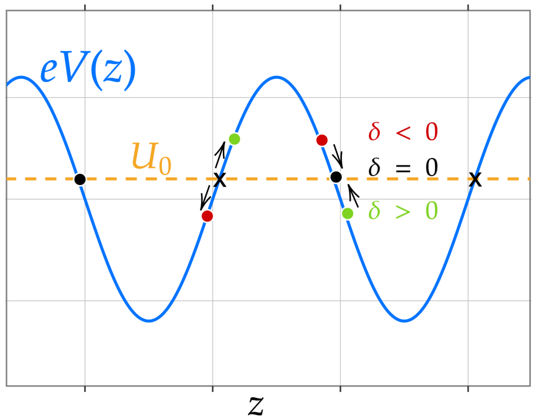

(b) Longitudinal focusing.

Figure 1.2: Phase stability mechanism in synchrotrons.

Under the assumption that $U_{\mathrm{rad}}(\delta) \approx U_0$ (neglecting radiation damping), the equations of motions can be derived from the stationary Hamiltonian:

$$\mathcal{H} = \frac{\alpha\delta^2}{2} + \Phi(z), \tag{1.8}$$

with the definition of rf potential:

$$\Phi(z) = -\frac{1}{E_0 C_0}\int_0^z \mathrm{d}z' \, [eV(z') - U_0]. \tag{1.9}$$

The rf voltage $V(z)$ oscillates h times within a revolution period. Then, $V(z+n\lambda_{\mathrm{rf}}) = V(z)$ for $n = 0, \ldots, h-1$, where λ_{rf} is the rf wavelength such that $\lambda_{\mathrm{rf}} f_{\mathrm{rf}} = c$. By the rf periodicity, the condition $eV(0) = U_0$ is satisfied $2h$ times for each turn, but the derivative of $V(z)$ is negative for only half of these points. This means the harmonic number h is the

[1]Recalling we refer to the $\alpha > 0$ case and electrons above the transition energy. For $\alpha < 0$ or particles below the transition energy, all signs must be reversed in the argumentation.

amount of synchronous stable regions (named rf buckets) along the ring where electrons can be grouped in bunches. The total beam current I_0 is the sum of the stored current in each bunch.

It is possible to determine by the injection instant in which rf bucket the electrons will be stored in the ring. If all buckets are filled with the same charge, this is referred to as uniform filling pattern. Empty buckets (gaps) might be required to counter some instability issues in the storage ring or to allow for time-resolved experiments in the beamlines.

1.1.2 Action-angle variables

The coordinates (z, δ) and (J, φ) are related by canonical transformation. The action variable is a constant of motion, calculated by the momentum integrated in a phase space cycle:

$$J = \frac{1}{2\pi} \oint \mathrm{d}z\, \delta(z). \tag{1.10}$$

With Eq. (1.8), consider a fixed "energy" $\mathcal{H}_0$, in the sense of Hamiltonian dynamics, such that $\mathcal{H}_0 = \alpha\delta^2/2 + \Phi_0(z)$. In general, we have

$$\delta(z) = \pm\sqrt{\frac{2}{\alpha}\,[\mathcal{H}_0 - \Phi_0(z)]}. \tag{1.11}$$

Consider that the potential $\Phi_0(z)$ has a single minimum, with two turning points (left z_L and right z_R) corresponding to $\delta = 0$, that can be obtained by finding the two roots of $\mathcal{H}_0 - \Phi_0(z) = 0$. When $\delta > 0$, the integration in Eq. (1.10) is from $z_\mathrm{L} \to z_\mathrm{R}$ and when $\delta < 0$ it is reversed $z_\mathrm{R} \to z_\mathrm{L}$, thus the signal of the integral is always positive. Combining this, the action is calculated as:

$$J = \sqrt{\frac{2}{\alpha\pi^2}} \int_{z_\mathrm{L}}^{z_\mathrm{R}} \mathrm{d}z\, \sqrt{\mathcal{H}_0 - \Phi_0(z)}. \tag{1.12}$$

The equations of motion in action-angle coordinates are simply

$$\frac{\mathrm{d}J}{\mathrm{d}s} = -\frac{\partial \mathcal{H}_0}{\partial \varphi} = 0, \tag{1.13}$$

$$\frac{\mathrm{d}\varphi}{\mathrm{d}s} = \frac{\partial \mathcal{H}_0}{\partial J} = \frac{\omega_s(J)}{c}. \tag{1.14}$$

Since J is a constant of motion, then $\frac{\partial \mathcal{H}_0}{\partial \varphi} = 0$ and $\mathcal{H}_0$ depends only on the action.

The oscillation frequency $\omega_s(J)$ is also action-dependent in general, a characteristic of nonlinear dynamics. The frequency can be computed by $\omega_s(J) = c\frac{\partial \mathcal{H}_0}{\partial J}$. Alternatively, the oscillation period can be calculated by

$$T_s(J) = \sqrt{\frac{2}{\alpha c^2}} \int_{z_L}^{z_R} \frac{\mathrm{d}z}{\sqrt{\mathcal{H}_0(J) - \Phi_0(z)}}, \tag{1.15}$$

and then the frequency is $\omega_s(J) = 2\pi/T_s(J)$.

1.1.3 Single-rf system

For small amplitudes, the rf voltage can be linearized around $z = 0$. Using $eV(0) = U_0$, we have $eV(z) \approx U_0 + eV'(0)z$. Moreover, the dependence of the energy loss on the electron energy can be linearized around the nominal energy $\delta = 0$, obtaining $U_{\mathrm{rad}}(\delta) \approx U_0 + U'_{\mathrm{rad}}(0)\delta$. Applying these approximations to Eq. (1.7) and combining with Eq. (1.6), with $s = ct$, we obtain the equation for a damped harmonic oscillator:

$$\frac{\mathrm{d}^2 z}{\mathrm{d}t^2} + 2\alpha_z \frac{\mathrm{d}z}{\mathrm{d}t} + \omega_{s0}^2 z = 0, \tag{1.16}$$

$$\alpha_z = \frac{1}{2E_0 T_0} \left.\frac{\mathrm{d}U_{\mathrm{rad}}}{\mathrm{d}\delta}\right|_{\delta=0}, \tag{1.17}$$

$$\omega_{s0}^2 = -\frac{\alpha e}{E_0 T_0} \left.\frac{\mathrm{d}V}{\mathrm{d}z}\right|_{z=0}, \tag{1.18}$$

where α_z is the longitudinal radiation damping rate and ω_{s0} the single-rf synchrotron frequency. Note that an oscillatory solution with $\omega_{s0} \in \mathbb{R}$ is obtained only for $V'(0) < 0$, in accordance with the discussion from §1.1.1. The longitudinal motion is much slower than the transverse. During one synchrotron cycle, the electrons complete hundreds of turns in the ring. The synchrotron tune, defined as $\nu_s = \omega_s/\omega_0$, is typically on the order of 10^{-3}.

Under the small amplitude approximation and neglecting radiation damping, we can show that the rf potential for a single-rf system is quadratic $\Phi(z) \approx \frac{\omega_{s0}^2}{\alpha c^2}\frac{z^2}{2}$, and the canonical transformation is given by:

$$z = \sqrt{\frac{2\alpha c J}{\omega_{s0}}} \cos(\varphi), \tag{1.19}$$

$$\delta = -\sqrt{\frac{2\omega_{s0} J}{\alpha c}} \sin(\varphi). \tag{1.20}$$

The longitudinal Hamiltonian is

$$\mathcal{H} = \frac{\omega_{s0}}{c} J. \tag{1.21}$$

This shows that, for small amplitudes, the longitudinal Hamiltonian is also invariant, with the longitudinal motion drawing ellipses in the phase space (z, δ).

Note that the fundamental physical property that higher energy particles emit more radiation, i.e., $U'_{\mathrm{rad}}(0) > 0$, is responsible for the term α_z being positive, corresponding to a damping rate. When damping is considered, the Hamiltonian is no longer an invariant and the motion is represented in the phase space by lines spiraling inwards to the synchronous fixed-point. Additionally, the radiation emission is a stochastic event that excites synchrotron oscillations [48, 49]. In the equilibrium state, the excitation and damping rates are balanced, resulting in a distribution of electrons with finite energy spread σ_δ and bunch length σ_z that we will address in §1.3.3.

For a storage ring with only main rf cavities, the rf voltage is modeled as:

$$V(z) = \hat{V}_{\mathrm{rf}} \sin(\omega_{\mathrm{rf}} z/c + \phi_s), \tag{1.22}$$

where $\hat{V}_{\mathrm{rf}}$ is the gap voltage, $\omega_{\mathrm{rf}} = h\omega_0$ the rf angular frequency and ϕ_s the synchronous phase. From the synchronous particle condition, this phase is

$$\phi_s = \pi - \arcsin\left(\frac{U_0}{e\hat{V}_{\mathrm{rf}}}\right), \tag{1.23}$$

already considering the second quadrant, such that $V'(0) = (\omega_{\mathrm{rf}}/c)\hat{V}_{\mathrm{rf}} \cos(\phi_s) < 0$. The ratio

$$q = \frac{e\hat{V}_{\mathrm{rf}}}{U_0}, \tag{1.24}$$

is known as overvoltage, which must be greater than one for stability.

With a sinusoidal rf voltage, the longitudinal dynamics is equivalent to the dynamics of a simple pendulum. The region for confined motion is limited by a separatrix in the phase space (z, δ), that defines the rf bucket. The maximum energy deviation δ within the rf bucket is called rf energy acceptance, given by:

$$\delta_{\mathrm{acc}}^{\mathrm{rf}} = \left[\frac{e\hat{V}_{\mathrm{rf}}}{\pi\alpha h E_0}\frac{F(q)}{q}\right]^{1/2}, \tag{1.25}$$

$$F(q) = 2\left[\sqrt{q^2-1} - \arccos(1/q)\right]. \tag{1.26}$$

Thus, the overvoltage is determinant for the rf energy acceptance. Since $F(q) \approx 2q - \pi$ for $q \gg 1$, in the limit of large q the energy acceptance scales with the square root of the rf voltage.

The rf energy acceptance is one contribution to the total energy acceptance. With higher-order elements in the magnetic lattice, such as sextupoles, the transverse dynamics is nonlinear. This implies that there is also a contribution of the magnetic lattice to the energy acceptance, because the nonlinear dynamics might be unstable for electrons with energy deviations above certain values. Therefore, total energy acceptance typically vary along the storage ring and is determined by $\min\left(\delta_{\mathrm{acc}}^{\mathrm{rf}}, \delta_{\mathrm{acc}}^{\mathrm{lattice}}\right)$. Normally, the rf voltage used in operation is high enough such that the lattice energy acceptance is the limiting factor for most of the relevant points in the ring. The rf and lattice energy acceptances for one sector of SIRIUS storage ring is presented in Fig. 3.1(a) from Chapter 3.

For large oscillation amplitudes, the nonlinear contribution from the sinusoidal rf voltage becomes important. Let $z_{\max}$ be the maximum longitudinal amplitude, and for simplicity, we will write the maximum deviation as a phase with $\phi_{\max} = \omega_{\mathrm{rf}} z_{\max}/c$. The amplitude-dependent synchrotron frequency in a single-rf system is given by [51]:

$$\omega_s(\phi_{\max}) = \frac{\pi}{2}\frac{\omega_{s0}}{\mathcal{K}\left(\sin\frac{\phi_{\max}}{2}\right)}, \tag{1.27}$$

where $\mathcal{K}(k)$ is the complete elliptic integral of first kind:

$$\mathcal{K}(k) = \int_0^{\pi/2} \frac{\mathrm{d}\theta}{\sqrt{1 - k^2\sin^2(\theta)}}. \tag{1.28}$$

For short-bunches $\sin(\phi_{\max}/2) \approx \phi_{\max}/2$ and $\mathcal{K}(k) \approx \frac{\pi}{2}\left(1 + \frac{k^2}{4}\right)$ for $k \ll 1$, then:

$$\omega_s(\phi_{\max}) \approx \omega_{s0}\left(1 - \frac{\phi_{\max}^2}{16}\right). \tag{1.29}$$

With this we see that for short-bunches in a single-rf system, the synchrotron frequency decreases with amplitude. Besides, the bunch area in the longitudinal phase space is often much smaller than the rf bucket, so most of the electrons are executing small-amplitude synchrotron oscillations and very few are sampling the nonlinear part of the rf voltage. This implies that the intrabunch synchrotron frequency spread in single-rf systems is typically small. As we will discuss soon, beam stabilization by Landau damping requires sufficient incoherent frequency spread. To increase this spread, the nonlinearity of the longitudinal potential must be enhanced, which can be achieved by introducing HHCs, thus having a double-rf system.

Before discussing the modifications in the longitudinal dynamics due HHCs in a double-rf system, it will be more convenient to introduce some important concepts for collective effects.

1.2 Wakes and impedances

We briefly introduce the definitions and concepts of wake functions and impedances used throughout this thesis. For derivations from first principles and thoughtful discussions on this topic, we recommend the books [50, 51] and the thesis [43]. We will focus on the longitudinal plane.

Consider an electron moving with velocity $v \approx c$ along the ring. Due to discontinuities and the finite resistivity of the vacuum chamber, electrons leave electromagnetic fields (wakefields) behind their path. We refer to this electron as the source particle. A witness electron moving behind the source particle from a distance z will experience the wakefields. Two important approximations are made: (i) the beam is rigid such that source and witness particles move along parallel straight lines with the same velocity and their distance z is unchanged when the wakefields are excited; (ii) the wakefields change the momentum of the witness particle as an impulse. These assumptions are typically called rigid beam and impulse approximations, considerably simplifying the mathematical description of wakefields effects.

The longitudinal wake function, denoted by $W_{\parallel}(z)$, is defined as the total longitudinal momentum variation of a witness particle induced by wakefields from a source particle, both with unity charge and separated by z. With the impulse approximation, the function can be calculated by integrating the longitudinal electric field within the limits $t \in (-\infty, \infty)$. The assumption that particles travel at the speed of light implies there are no wakefields ahead of the source particle, thus $W_{\parallel}(z) = 0$ for $z < 0$. This is often referred to as causality condition. $W_{\parallel}(z)$ is a real function, interpreted as the impulse response of the beam surroundings. We can use $z = c\tau$ to write wake functions in terms of the time delay between source and witness particles.

The wake function is a time-domain description of the interactions of particles in a storage ring. A frequency-domain description can be done with the longitudinal impedance, defined as the Fourier transform of the wake function:

$$Z_{\parallel}(\omega) = \int_{-\infty}^{\infty} \mathrm{d}z\, W_{\parallel}(z) e^{i\omega z/c}. \tag{1.30}$$

Naturally, the wake function is the inverse Fourier transform of the impedance:

$$W_{\parallel}(z) = \frac{1}{2\pi} \int_{-\infty}^{\infty} \mathrm{d}\omega\, Z_{\parallel}(\omega) e^{-i\omega z/c}. \tag{1.31}$$

$Z_{\parallel}(\omega)$ is a complex function, in general. Since $W_{\parallel}(z)$ is a real function, the impedance must be Hermitian, $Z_{\parallel}^{*}(\omega) = Z_{\parallel}(-\omega)$. The impedance can be interpreted as the transfer function from the beam current to the wake-induced voltage.

The total wake voltage induced by several electrons can be calculated as the sum of the contributions of each electron, due to linearity. Considering the continuous limit that the electrons within a bunch follow the longitudinal distribution $\lambda_{\mathrm{b}}(z)$ (normalized to unity), the wake voltage induced by this bunch is given by:

$$V_{\mathrm{wake}}(z; \lambda) = -I_{\mathrm{b}} T_0 \int_{-\infty}^{\infty} \mathrm{d}z'\, \lambda_{\mathrm{b}}(z') W_{\parallel}(z - z'), \tag{1.32}$$

where $I_{\mathrm{b}} = eN_e/T_0$ is the current in the bunch, with N_e denoting the number of electrons. The negative sign is to account for the wake voltage as an energy loss. Equation (1.32) is the wake voltage induced by a single bunch in one turn. It is the convolution of the bunch distribution and the wake function. In §A.2, we will derive the general case for the wake voltage for many turns and many bunches.

In the frequency-domain, Eq. (1.32) is

$$V_{\mathrm{wake}}(\omega;\hat{\lambda}) = -I_{\mathrm{b}}\hat{\lambda}_{\mathrm{b}}(\omega)Z_{\parallel}(\omega), \tag{1.33}$$

where $\hat{\lambda}_{\mathrm{b}}(\omega)$ is the Fourier transform of the bunch distribution $\lambda_{\mathrm{b}}(z)$. Since Eq. (1.33) has the format of $V = I \cdot Z$, referring to $Z_{\parallel}(\omega)$ as impedance is justified.

1.2.1 Resonator model

Analytical models can be used to represent the impedance of some structures and components of the storage ring. A very useful model is the resonator:

$$Z_{\parallel}(\omega) = \frac{R_s}{1 + iQ\left(\frac{\omega_{\mathrm{r}}}{\omega} - \frac{\omega}{\omega_{\mathrm{r}}}\right)}, \tag{1.34}$$

where R_s is the shunt impedance, Q is the quality factor and ω_{r} is the resonant angular frequency. At resonance, this impedance is purely real, $Z_{\parallel}(\omega_{\mathrm{r}}) = R_s$. The Q factor determines the resonance bandwidth, which is ω_{r}/Q. Therefore, high $Q \gg 1$ correspond to resonators with a narrow bandwidth, referred to as narrowband resonators. A broadband resonator is represented by low Q values, on the order of $Q \approx 1$.

The longitudinal wake function for a resonator is given by:

$$W_{\parallel}(z) = \begin{cases} 2\alpha_{\mathrm{r}} R_s e^{-\alpha_{\mathrm{r}} z/c}\left[\cos(\bar{\omega}_R z/c) - \frac{\alpha_{\mathrm{r}}}{\bar{\omega}_R}\sin(\bar{\omega}_R z/c)\right] & \text{for} \quad z > 0, \\ \alpha_{\mathrm{r}} R_s \quad \text{for} \quad z = 0, \\ 0 \quad \text{for} \quad z < 0, \end{cases} \tag{1.35}$$

where $\alpha_{\mathrm{r}} = \omega_{\mathrm{r}}/2Q$ is the resonator damping rate and $\bar{\omega}_R = \sqrt{\omega_{\mathrm{r}}^2 - \alpha_{\mathrm{r}}^2}$. Note that to have $\bar{\omega}_R \in \mathbb{R}$, Q must be greater than $1/2$.

With the time-domain description, we see that narrowband resonators correspond to structures that maintain wakefields trapped for long periods, while in broadband resonators the fields decay faster.

The resonator model will be sufficient for this thesis; however, many other analytical impedance models exist and can be found in books [50, 51, 53, 54].

1.3 Collective effects

In each bunch in a storage ring there are typically more than 10^9 particles. Describing the individual motion of all particles is not only impractical but also unnecessary for obtaining an accurate physical description of the collective behavior of the beam. Particle tracking simulation is an approach used to analyze collective effects by studying the time evolution of macroparticles, which represent many real particles. The effects of wakefields on the dynamics of each macroparticle can be incorporated with relatively few approximations, enabling the simulation of complex phenomena that might be analytically intractable.

However, since we are often interested in the long-term behavior of the beam, tracking simulations can be a time-consuming approach, even with currently available computational power. Additionally, interpreting the physical results from tracking simulations can be challenging in some cases. Analytical and semi-analytical methods for modeling collective effects are often more useful for developing a physical understanding of the phenomena. Moreover, the computational load required to obtain results from these methods is much lighter compared to tracking.

In this section, we will discuss some incoherent and coherent collective effects that are relevant to this thesis.

1.3.1 Touschek effect

Electrons within the same bunch in a storage ring interact via Coulomb scattering. After the scattering event, the momentum of the electrons can significantly change. A particularly important effect is when two electrons are scattered and transverse momentum is transferred to longitudinal momentum, therefore inducing energy deviations of opposite signs to both particles. When the energy deviation is large enough[2] to surpass the energy acceptance of the ring, the scattered electrons are lost. This is the mechanism of the Touschek effect, described by Bruno Touschek in 1963 [55]. The scattering between electrons and residual gas molecules in the vacuum chamber also results in electron losses, by mechanisms that will not be detailed here but can be studied in Ref. [49]. These electron losses imply that the total beam current in a storage ring decrease over time even with a stable beam. The inverse of the current loss rate normalized to current is called beam lifetime.

The Touschek effect is the dominant mechanism of beam lifetime in 4^{th}-generation synchrotron light sources. Its contribution is referred to as Touschek lifetime. The combination of high bunch charge densities and ultra-high vacuum conditions achieved in modern synchrotrons makes Touschek scattering events much more frequent and intense

[2]For ultrarelativistic electrons in a storage ring, the transverse momenta are much smaller than the longitudinal momentum and the transverse velocities might not even be relativistic. Even so, when transverse momentum variations are transferred to the longitudinal plane, where the electron is moving close to the speed of the light, the variation is boosted by the γ factor, which may imply in a large energy deviation.

than electron-gas scattering.

There is also a probability that the momentum variation after Coulomb scattering is insufficient for the particles to exceed the ring acceptance. Such scattering events might occur several times, introducing a stochastic effect that excites the electrons' oscillation amplitudes in both transverse and longitudinal planes. The additional excitation leads the bunches to a different equilibrium state, with increased transverse emittances, energy spread and bunch length. This internal multiple collision process is called intrabeam scattering (IBS), an effect that "heats" the beam equilibrium parameters, and it is also dependent on the bunch charge density. Details on IBS theory will not be addressed in this thesis; the review paper [56] is recommended for detailed derivations, discussions and further references.

The Touschek effect and IBS are incoherent collective effects, not related to self-driven wakefields of the beam, but dependent on the beam properties such as the bunch charge density and the storage ring parameters such as the energy, optics functions and acceptances.

The first theoretical calculations of the Touschek lifetime considered the particular case such that, in the center of mass reference frame, the velocities of the two colliding particles are non-relativistic. The theory was generalized for the relativistic case, arbitrary energies and with the inclusion of the dispersion function. These theories considered a "flat beam" in the transverse plane, only accounting for transference of horizontal momentum to the longitudinal one, so the vertical momentum contribution was neglected. Another limit case with round beam was derived, with full-coupling between horizontal and vertical betatron oscillations.

A general theory was developed by Piwinski [57], dealing with the horizontal and vertical planes on equal footing (dispersion functions included). Moreover, the theory account for variations (derivatives) of linear optics functions. The calculation process involves computing the number of collisions between two electrons in the center of mass reference frame, using the Møller scattering cross-section[3]. The result is transformed to the laboratory reference frame to evaluate momentum variations that exceed the energy acceptance and lead to electron losses. Gaussian distributions are assumed for the six coordinates $(x, x', y, y', z, \delta)$ to compute average values. All these steps can be found in the detailed derivation of Piwinski's work [57] and will not be reproduced here.

The calculations of Touschek lifetime using the "flat beam" approximation [61] and with the generalized theory from Piwinski [57] were implemented in the open-source code `pyaccel` [62]. The results from these lifetime calculations were compared with experimental

[3]Piwinski neglected the spin contribution to the Møller scattering cross-section, calculating the Touschek lifetime for unpolarized electron beams. It is known that the electrons' spin in a storage ring becomes polarized by the Sokolov-Ternov effect [58] and that Touschek scattering rates are reduced for polarized beams. The Touschek lifetime increase due to spin polarization can be significant and measurable, but this effect will not be relevant for this thesis. For more details, see Refs. [59, 60] and their references.

data from SIRIUS storage ring, reported in Ref. [63].

We will just briefly discuss important scaling dependence of the Touschek lifetime. The loss rate due Touschek effect can be generally written as [23, 57]:

$$\frac{\mathrm{d}N_\mathrm{b}}{\mathrm{d}t} = \mathcal{P} \int_V \mathrm{d}V \, \Psi^2(V) \tag{1.36}$$

where $\mathcal{P}$ represents the probability of electrons being scattered beyond the energy acceptance, V is a six-dimensional volume of the coordinates $(x, x', y, y', z, \delta)$ and $\Psi(V)$ is the volume charge distribution of the bunch. The Touschek lifetime is inversely proportional to the loss rate: $\tau_\mathrm{Touschek}^{-1} \propto \frac{\mathrm{d}N_\mathrm{b}}{\mathrm{d}t}$.

It is often a valid approximation to consider that the bunch distribution is separable, so integrations of each volume component can be done independently [57]. This property is useful to evaluate relative variations of the Touschek lifetime, specially when only few parameters are modified. Moreover, the loss probability depends on the energy acceptance of the ring as $\mathcal{P} \propto 1/\delta_\mathrm{acc}^2$.

In general terms, the Touschek lifetime increases with the energy acceptance and decreases with the bunch charge density. For Gaussian bunches, a useful approximate scaling law[4] for the Touschek lifetime can be written as [59]:

$$\tau_\mathrm{Touschek} \propto \sigma_z \delta_\mathrm{acc}^3 \frac{\sqrt{\epsilon_x \epsilon_y}}{I_\mathrm{b}}. \tag{1.37}$$

As mentioned in the Introduction, for a synchrotron light source it is important that the quantities ϵ_x, ϵ_y and I_b are maintained as close as possible to the design values, since they directly affect the brightness and transverse coherence of the synchrotron radiation. In most cases, the energy acceptance δ_acc is limited by the lattice acceptance, which is often not so flexible to be increased in an operating machine (although some heuristic optimizations can be performed, with parameters affecting brightness maintained as constraints). Therefore, the longitudinal charge density (consequently the bunch length σ_z) is the parameter chosen to be modified for Touschek lifetime improvement.

1.3.2 Vlasov equation

For conservative systems under the influence of electromagnetic fields, the time evolution of the charge distribution in the phase space, Ψ, is governed by the Vlasov equation:

$$\frac{\mathrm{d}\Psi}{\mathrm{d}s} = 0. \tag{1.38}$$

[4]The linear optics functions and energy acceptance are considered constant or having small variations along the ring to obtain the scaling law in Eq. (1.37).

The Vlasov equation follows from the collisionless Boltzmann equation for the transport of distributions by electromagnetic fields. It states that the distribution behaves as an incompressible fluid, conserving the phase space volume. In general, Ψ is a six-dimensional distribution, but as already discussed, we will assume the longitudinal coordinates are separable from the transverse. Then, we can focus on the two-dimension distribution, $\Psi = \Psi(z, \delta)$, for the longitudinal plane.

Considering that the Hamiltonian $\mathcal{H}$ determines the longitudinal single-particle dynamics (neglecting damping and excitation effects from radiation), the Vlasov equation for the longitudinal distribution $\Psi(z, \delta; s)$ yields:

$$0 = \frac{\mathrm{d}\Psi}{\mathrm{d}s} = \frac{\partial \Psi}{\partial s} + \frac{\partial \Psi}{\partial z}\frac{\mathrm{d}z}{\mathrm{d}s} + \frac{\partial \Psi}{\partial \delta}\frac{\mathrm{d}\delta}{\mathrm{d}s} \tag{1.39}$$

$$0 = \frac{\partial \Psi}{\partial s} + \{\Psi, \mathcal{H}\}\,, \tag{1.40}$$

where the Hamilton equations $\frac{\mathrm{d}z}{\mathrm{d}s} = \frac{\partial \mathcal{H}}{\partial \delta}$ and $\frac{\mathrm{d}\delta}{\mathrm{d}s} = -\frac{\partial \mathcal{H}}{\partial z}$ were used, and the Poisson bracket is defined as:

$$\{\Psi, \mathcal{H}\} = \frac{\partial \Psi}{\partial z}\frac{\partial \mathcal{H}}{\partial \delta} - \frac{\partial \Psi}{\partial \delta}\frac{\partial \mathcal{H}}{\partial z}. \tag{1.41}$$

The Vlasov equation is rigorously valid for conservative systems, which is not the case for electrons in a storage ring due to the emission of synchrotron radiation. The proper description of the time evolution of Ψ accounting for radiation effects is given by the Fokker-Planck equation [49, 64]:

$$\frac{\partial \Psi}{\partial s} + \{\Psi, \mathcal{H}\} = \frac{2\alpha_z}{c}\left(\Psi + \delta\frac{\partial \Psi}{\partial \delta}\right) + \mathcal{D}_z\frac{\partial^2 \Psi}{\partial \delta^2}, \tag{1.42}$$

where α_z is the radiation damping rate and $\mathcal{D}_z$ the diffusion term. Naturally, when the radiation effects are neglected, $\alpha_z = 0$ and $\mathcal{D}_z = 0$, the Fokker-Planck equation simplifies to the Vlasov equation.

The Vlasov and the Fokker-Planck equations are powerful tools to calculate collective instabilities in synchrotrons. Often the typical timescale for the amplitude growth of an instability is shorter than the timescale related to the radiation damping and diffusion. Under this "fast-growing instability" assumption (which is not too restrictive in practice), the Vlasov equation can be used instead of the Fokker-Planck equation even if radiation effects are present. The impact of radiation damping can be approximately included by comparing the damping rate α_z to the instability growth rate obtained from the Vlasov equation. As will be shown in Appendix B, the Vlasov equation was sufficient to accurately predict the instabilities of interest for this thesis.

In the stationary state, the distribution Ψ must be independent of s, then the Vlasov equation reads

$$\{\Psi, \mathcal{H}\} = 0, \quad \text{thus} \quad \Psi = f(\mathcal{H}). \tag{1.43}$$

Hence, with the Vlasov equation we can only say that the distribution must be a function of the Hamiltonian. The explicit expression for this function is obtained from the Fokker-Planck equation. It can be shown that, when diffusion and damping effects are balanced, the longitudinal distribution Ψ that solves the Fokker-Planck equation is the "thermal Maxwell-Boltzmann" distribution:

$$\Psi(\mathcal{H}) = \frac{1}{\mathcal{N}} \exp\left(-\frac{\mathcal{H}}{\mu}\right), \tag{1.44}$$

where $\mathcal{N}$ is a normalization constant such that the integral of Ψ results in unity and μ is a constant to be explicitly determined next.

For a single-rf system, neglecting damping and wakefields, we showed the Hamiltonian for small amplitudes is approximately

$$\mathcal{H} = \frac{\alpha\delta^2}{2} + \frac{\omega_{s0}^2}{\alpha c^2}\frac{z^2}{2}. \tag{1.45}$$

Therefore, the Ψ distribution is separable as the product of Gaussian distributions:

$$\Psi(z,\delta) = \rho(\delta)\lambda(z), \tag{1.46}$$

$$\rho(\delta) = \frac{1}{\sqrt{2\pi\sigma_\delta^2}} \exp\left(-\frac{\delta^2}{2\sigma_\delta^2}\right), \tag{1.47}$$

$$\lambda(z) = \frac{1}{\sqrt{2\pi\sigma_z^2}} \exp\left(-\frac{z^2}{2\sigma_z^2}\right). \tag{1.48}$$

σ_δ is the energy spread and σ_z the bunch length. Writing $\Psi(z,\delta)$ as the product of Gaussian distributions and using the Hamiltonian from Eq. (1.45) back to Eq. (1.44), we can show that:

$$\mu = \alpha\sigma_\delta^2, \tag{1.49}$$

$$\mathcal{N} = 2\pi\sigma_z\sigma_\delta, \tag{1.50}$$

$$\omega_{s0}\sigma_z = \alpha c\sigma_\delta. \tag{1.51}$$

Equation (1.51) is a matching condition, valid under the approximations of quadratic potential and Gaussian distributions. In action-angle variables, with $\mathcal{H} = \omega_{s0}J/c$ and the conditions above, the distribution takes the format of:

$$\Psi(J) = \frac{1}{2\pi\langle J\rangle} \exp\left(-\frac{J}{\langle J\rangle}\right) \quad \text{with} \quad \langle J\rangle = \sigma_z\sigma_\delta. \tag{1.52}$$

1.3.3 Haïssinski equation

A stationary effect that can be derived from the Vlasov equation is the distortion in the longitudinal potential due to the wakefields. By linearity, the beam-induced wake voltage shown in Eq. (1.32) can be combined to the external voltage provided by rf cavities:

$$V(z) = V_{\text{ext}}(z) + V_{\text{wake}}(z; \lambda). \tag{1.53}$$

Hence, the wakefields also modify the longitudinal potential defined in Eq. (1.9). This is the potential-well distortion effect. It changes the Hamiltonian to:

$$\mathcal{H} = \frac{\alpha\delta^2}{2} + \Phi_{\text{ext}}(z) + \Phi_{\text{wake}}(z; \lambda). \tag{1.54}$$

Note that the wakefields only alter the z part of the Hamiltonian, while the δ part and consequently the distribution $\rho(\delta)$ remains unaffected by stationary wakefields. The distortion in the potential may introduce significant changes in the single-particle longitudinal dynamics, for example, modifying the synchrotron frequency and bunch charge distribution.

From Eq. (1.32), considering the induced wake voltage by a single-bunch, the effect of the modified longitudinal potential in the bunch distribution is

$$\lambda_{\text{b}}(z) = \frac{1}{\mathcal{N}_z} \exp\left[-\frac{\Phi_{\text{ext}}(z)}{\alpha\sigma_\delta^2} + \frac{eI_{\text{b}}}{E_0\alpha c\sigma_\delta^2} \int_0^z \mathrm{d}z' \int_0^\infty \mathrm{d}z''\, \lambda_{\text{b}}(z'') W_\parallel(z' - z'')\right]. \tag{1.55}$$

This integral equation for the bunch longitudinal distribution $\lambda_{\text{b}}(z)$ is called Haïssinski equation, developed and analytically solved for special cases for the first time by Jacques Haïssinski in 1973 [65]. It is a self-consistent equation for $\lambda_{\text{b}}(z)$, encoding the effect that the bunch distribution excites wakefields, that act back on the particles changing their distribution and so on, until some equilibrium state is achieved.

In general, a self-consistent solution for the Haïssinski equation must be obtained numerically. The effects of multiturn and multibunch wakefields can also be accounted in the beam-induced wake voltage to evaluate their impact on the bunch distribution, as will be developed in Appendix A.

1.3.4 Instabilities

The description and calculation of some types of collective instabilities can be done with simplified models that capture the essential physics. For example, the mechanism of the so-called Robinson instability depends on the longitudinal motion of the center of charge (bunch centroid) under the influence of longitudinal impedance [50, 51]. Such instability is well-described by treating the bunches as point-charge macroparticles executing linear synchrotron oscillations. Depending on the different sampling of the synchrotron sidebands on the impedance, the wakefields might introduce a defocusing mechanism such that electrons with $\delta > 0$ lose, on average, less energy to the impedance than electrons with $\delta < 0$, leading to an exponential growth of the oscillation amplitude, i.e., an instability.

The perturbation method applied to the Vlasov equation provides a general framework to study collective instabilities [50]. The main idea is to evaluate the time evolution of small variations with respect to an equilibrium condition.

In the accelerator field, the instability formalism was developed in the early 1970s by F. J. Sacherer [66, 67], for bunched beam instabilities in the transverse and longitudinal planes. For the longitudinal, a linear single-particle dynamics is assumed (no potential-well distortion) and the perturbation in the bunch distribution is decomposed in azimuthal modes of oscillation: dipole (bunch centroid), quadrupole (bunch shape), etc. The developed formalism results in an integral equation, where the unknowns are the coherent frequency Ω and the perturbing distribution that depends on $e^{-i\Omega t}$. This equation is currently known as the Sacherer integral equation [50, 51].

In general, the coherent frequency Ω is a complex number. The perturbed distribution follows $e^{-i\Omega t}$, thus $\mathrm{Re}(\Omega)$ represents the coherent oscillation frequency of the beam. $\mathrm{Im}(\Omega)$ is growth or damp rate of the amplitude. An instability is predicted if $\mathrm{Im}(\Omega) > 0$. The effect of radiation can be approximately included in the Vlasov framework by comparing if the instability growth rate exceeds the radiation damping rate. In many cases this approach provides accurate results, but it is worth mentioning again that a rigorous description of radiation effects requires a framework based upon the Fokker-Planck equation, such as done in Refs. [64, 68, 69].

The longitudinal instabilities can be divided in single-bunch and multibunch. Typically, broadband impedance components may drive single-bunch instabilities, because they generate short-range wakefields that decay within the bunch duration, and it can only affect particles within the same bunch. These wakefields might alter many bunch oscillation modes, potentially coupling/mixing their motion. For instance, this longitudinal mode-coupling mechanism is the explanation of the microwave instability, that increases the energy spread and bunch length [51]. The single-bunch instability thresholds depend on the current per bunch.

Narrowband impedance structures may drive multibunch instabilities, because long-range wakefields are generated. These fields keep resonating for long times, mediating the interaction between different bunches and even between the source bunch with itself on later turns. These wakefields couple the motion of bunches, an effect also commonly referred to as coupled-bunch instabilities. It is often the case that coupled-bunch instabilities affect mainly the dipole motion of the bunches and high order modes of oscillation can be neglected. We will see in Appendix B that with the potential-well distortion effects introduced by HHCs, multiple bunch oscillation modes can be relevant for coupled-bunch instabilities.

We will assume the longitudinal dynamics is parametrized by the action-angle coordinates (J, φ) and use the property that the Poisson bracket is invariant under canonical transformations. Consider that the beam distribution is

$$\Psi(J, \varphi; s) = \Psi_0(J) + \Psi_1(J, \varphi; s), \tag{1.56}$$

where $\Psi_0(J)$ is the equilibrium distribution, known to be a function of J only, and $\Psi_1(J, \varphi; s)$ a small perturbing distribution with zero net charge.

With wakefields, the longitudinal potential depend on the full distribution $\Psi(J, \varphi; s)$. Hence, the Hamiltonian is also perturbed:

$$\mathcal{H}(J, \varphi; s) = \mathcal{H}_0(J) + \mathcal{H}_1(J, \varphi; s). \tag{1.57}$$

Applying the perturbations to the Vlasov equation yields:

$$\frac{\partial \Psi_1}{\partial s} + \{\Psi_0, \mathcal{H}_0\} + \{\Psi_0, \mathcal{H}_1\} + \{\Psi_1, \mathcal{H}_0\} + \{\Psi_1, \mathcal{H}_1\} = 0. \tag{1.58}$$

Assuming small perturbations, the Vlasov equation can be linearized, i.e., the second-order term $\{\Psi_1, \mathcal{H}_1\}$ can be neglected. Moreover, Ψ_0 is a function of $\mathcal{H}_0$, thus $\{\Psi_0, \mathcal{H}_0\} = 0$. With the results $\Psi_0 = \Psi_0(J)$, $\mathcal{H}_0 = \mathcal{H}_0(J)$, $\{\Psi, \mathcal{H}\} = \frac{\partial \psi}{\partial \varphi}\frac{\partial \mathcal{H}}{\partial J} - \frac{\partial \psi}{\partial J}\frac{\partial \mathcal{H}}{\partial \varphi}$ and $\omega_s(J) = c\frac{\partial \mathcal{H}_0}{\partial J}$, we obtain the linearized Vlasov equation:

$$\frac{\partial \Psi_1}{\partial s} + \frac{\omega_s(J)}{c}\frac{\partial \Psi_1}{\partial \varphi} - \frac{\partial \Psi_0}{\partial J}\frac{\partial \mathcal{H}_1}{\partial \varphi} = 0. \tag{1.59}$$

The linearized Vlasov equation is the starting point to develop a theory of longitudinal instabilities, accounting for the effects of potential-well distortion on the equilibrium Hamiltonian $\mathcal{H}_0$ and multiturn, multibunch dynamical effects induced by impedances on the perturbed Hamiltonian $\mathcal{H}_1$. The theory will be further developed on Appendix B.

The mode-approach was introduced by Sacherer to simplify the linearized Vlasov equation. First, the linear single-particle dynamics is described in polar coordinates (r, θ). Then, the perturbation distribution is expanded in azimuthal modes:

$$\Psi_1(r, \theta) = \sum_{m \neq 0} R_m(r) e^{im\theta} e^{-i\Omega s/c}, \tag{1.60}$$

where $m = 0$ is removed since it corresponds to a static term in the phase space. Including this static and the equilibrium $\Psi_0(J)$ would violate charge conservation for the total distribution $\Psi(J, \varphi)$. The radial function $R_m(J)$ encodes the radial dependence of the perturbation in the phase space.

Each azimuthal mode m corresponds to a particular bunch motion in the longitudinal phase space. $m = 1$ is a dipolar motion, rigid oscillations of the center of charge. $m = 2$ is a quadrupolar motion, oscillations of the bunch shape while the center of charge is fixed. The motion of higher order m modes is more difficult to visualize.

Using the expansion from Eq. (1.60) to calculate the beam-induced voltage that perturbs the Hamiltonian and applying the results in the linearized Vlasov equation, we obtain the Sacherer integral equation:

$$(\Omega - m\omega_{s0}) R_m(r) = W(r) \sum_{m' \neq 0} \int_0^{\infty} \mathrm{d}r' \, r' R_{m'}(r') G_{m,m'}(r, r'), \tag{1.61}$$

with the weight function

$$W(r) = -\frac{1}{r} \frac{\mathrm{d}\Psi_0}{\mathrm{d}r}, \tag{1.62}$$

and the kernel

$$G_{m,m'}(r, r') = \frac{i\alpha e I_{\mathrm{b}}}{E_0 \nu_{s0}} i^{m-m'} m \sum_{p=-\infty}^{\infty} \frac{Z_{\parallel}(\omega_p)}{\omega_p} \mathcal{J}_{m'}(\omega_p r') \mathcal{J}_m(\omega_p r), \tag{1.63}$$

where $\omega_p = p\omega_0$ and $\mathcal{J}_m(x)$ is the Bessel function. The synchrotron frequency ω_{s0} is constant (linear longitudinal dynamics), determined by the external rf voltage and the effects of potential-well distortion. In the limit of zero current, the coherent frequencies are $\Omega = m\omega_{s0}$, i.e., real coherent frequencies with zero growth rates (no instability).

The Sacherer integral equation can be analytically solved for some models of the equilibrium bunch distribution. The approach is to expand $R(r)$ in a basis of orthogonal functions, using the orthogonality to convert the integral equation Eq. (1.61) to an eigenvalue-eigenvector equation. The weight function $W(r)$, thus the equilibrium distribution $\Psi_0(r)$, determines which type of orthogonal function must be used to solve the problem. The Gaussian distribution $\Psi_0(r) \propto e^{-r^2}$ is one particular case that Sacherer integral equation can be solved using generalized Laguerre polynomials to expand $R(r)$ [50]. In this case, the coherent frequency Ω can be computed as the eigenvalues of an interaction matrix that contains information of beam, ring and impedance parameters.

For arbitrary rf potentials, the Sacherer integral equation must be generalized to consider the nonlinear single-particle dynamics such that $\omega_{s0} \to \omega_s(J)$ and the kernel $G_{m,m'}(J, J')$ must be modified. In general, it is not possible to find orthogonal functions that simplify the generalized Sacherer equation to a linear problem, and nonlinear methods are required to solve for the coherent frequency Ω.

1.3.5 Landau damping

Landau damping was originally predicted in 1946 by Landau as a collisionless damping mechanism for collective oscillations in plasmas [70]. Landau showed that the distribution of velocities of the charged particles in the plasma is essential for this natural stabilization. Almost 20 years later, in 1965, Landau damping theory was formulated for beams in particle accelerators [71, 72].

For a didactic and more detailed discussion on Landau damping in accelerators we recommend the books [50, 51] and the papers [28–30, 73]. Here, we will only summarize the main concepts and results that are relevant to the thesis. The understanding of the Landau damping mechanism and its mathematical treatment are intricate, and historically, the two have been closely connected. We will follow some derivations from Refs. [30, 50] to introduce the topic. Although the analysis relies on significant approximations that are not strictly valid for the cases studied in the thesis, it provides some interpretation of the mechanism involved.

Consider an ensemble of harmonic oscillators (particles in a beam) characterized by the displacement z and driven by an excitation $f(t) = Ae^{-i\Omega t}$, that is absent for $t < 0$. The equation of motion for a single-particle with frequency ω is

$$\frac{\mathrm{d}^2 z}{\mathrm{d}t^2} + \omega^2 z = Ae^{-i\Omega t}, \tag{1.64}$$

where only the real part is physically meaningful. We assume that the frequencies of the ensemble follow the distribution $\rho(\omega)$, normalized to unity. At this point, we consider that the distribution $\rho(\omega)$ is produced by an external focusing mechanism. We will be interested in the long-term behavior ($t \to \infty$) of the average displacement, given by $\langle z \rangle = \int \mathrm{d}\omega \rho(\omega) z$. Moreover, for simplicity, let us consider the case where the distribution is narrowband and centered at the frequency ω_{s0}. Furthermore, assume the excitation frequency is close to the center frequency, i.e., $\Omega \approx \omega_{s0}$. Under these considerations and with the single-particle solution to the equation of motion, we have:

$$\langle z \rangle(t) = \frac{A}{2\omega_{s0}} e^{-i\Omega t} \int_{-\infty}^{\infty} \mathrm{d}\omega \, \frac{\rho(\omega)}{\omega - \Omega}. \tag{1.65}$$

See Refs. [30, 50, 51] for details.

Note that Eq. (1.65) has a singularity at $\omega = \Omega$, and the integral over ω can be performed with complex analysis techniques. To evaluate the integral, we extend ω into the complex plane and deform the integration contour to avoid the singularity. Equivalently, the pole can be shifted infinitesimally from the real axis using $\Omega \to \Omega + i\epsilon$, where $\epsilon \to 0$, while keeping the integration contour along the real line. For integrals as in Eq. (1.65), we can apply the Sokhotski-Plemelj theorem to get:

$$\langle z \rangle(t) = \frac{A}{2\omega_{s0}} e^{-i\Omega t} \left[\mathrm{P.V.} \int_{-\infty}^{\infty} \mathrm{d}\omega \, \frac{\rho(\omega)}{\omega - \Omega} + i\pi\rho(\Omega) \right], \tag{1.66}$$

where P.V. denotes the Cauchy principal value. Note that the average amplitude $\langle z \rangle$ is bounded for $t \to \infty$.

The work done by the excitation force on the system is given by the product of the driving force, $f(t) = Ae^{-i\Omega t}$, and the average "velocity", $\frac{\mathrm{d}\langle z \rangle}{\mathrm{d}t}$. Hence, we see that the P.V. contribution is out-of-phase with the excitation and corresponds to a reactive part, modifying the collective oscillation frequency (increasing or decreasing the frequency depending on the sign of the integral). The pole contribution is in-phase with the excitation, and since $\rho(\Omega) > 0$, this means work is being done on the system by the external force. This is a resistive part that absorbs energy and act as damping of the external excitation. The in-phase resistive part comes from the proper treatment of the singularity, as pointed out by Landau [70]. Therefore, the condition that the excitation frequency Ω lies within the distribution of frequencies $\rho(\omega)$ is essential to have the Landau damping term.

Kinematic decoherence occurs when all particles in the ensemble are initially disturbed with the same nonzero conditions and then execute free oscillations at different frequencies. Each particle oscillates with a fixed amplitude, but due to the frequency spread, the phases gradually become mixed, reducing the ensemble's average amplitude. Over time, the oscillations may be in-phase again, increasing the average amplitude and leading to a beating process. In contrast, Landau damping can be understood as dynamic decoherence [74], where the frequency spread prevents harmonic driving forces from inducing coherent motion with unbounded amplitudes in the ensemble.

Assuming the initial conditions $z(0) = 0$ and $\frac{\mathrm{d}z}{\mathrm{d}t} = 0$, we can eliminate kinematic decoherence that is not the interest here. With these conditions and assuming $\Omega \approx \omega_{s0}$, the single-particle solution of Eq. (1.64) and its squared amplitude are given by:

$$z(t) = \frac{A}{2\omega_{s0}} e^{-i\Omega t} \frac{\left(1 - e^{-i(\omega-\Omega)t}\right)}{\omega - \Omega} \tag{1.67}$$

$$|z(t)|^2 = \frac{A^2}{\omega_{s0}^2} \frac{\sin^2[(\omega-\Omega)t/2]}{(\omega-\Omega)^2}. \tag{1.68}$$

The total oscillation energy of the ensemble depends on $|z(t)|^2$ integrated over the distribution of frequencies $\rho(\omega)$. For $t \to \infty$, we can use the result $\lim_{t\to\infty} \sin^2(xt/2)/x^2 = \pi t \delta(x)/2$ on Eq. (1.68). This indicates that the energy of the system will be mostly concentrated on resonant particles with $\omega \approx \Omega$. Based on these results, we can show that the total energy of the ensemble of N particles is

$$E_{\text{ensemble}} = N \frac{\pi}{2} \frac{A^2}{\omega_{s0}^2} \rho(\Omega) t, \tag{1.69}$$

i.e., increases linearly with t. Initially, the particles absorb energy from the excitation, but only those in resonance continue gaining energy as $t \to \infty$. Particles with a detuned frequency $\omega - \Omega$ get out-of-phase after the time $t = \pi/(\omega - \Omega)$ and release the absorbed energy. Although the total energy increases linearly with t, most of the energy is concentrated in the oscillation amplitude of the resonant particles with $\omega \approx \Omega$. Furthermore, the resonant condition is maintained within the period t such that $t < 1/(\omega - \Omega)$. The argument for having a bounded average ensemble amplitude is that the number of resonant particles decreases linearly with t as $(\omega - \Omega) \sim 1/t$, and it is mostly the energy of these particles that increases as $E \sim t$. Therefore, as $t \to \infty$, the increasing absorbed energy is contained in a vanishing number of resonant particles, and the average oscillation amplitude keeps bounded.

The relevant approximations involved in this analysis included the consideration of harmonic oscillators, i.e., linear single-particle dynamics, and that the distribution of frequencies $\rho(\omega)$ is given by external factors which do not depend on the particle's amplitude. Of course this is not valid if the single-particle dynamics is nonlinear. With nonlinearities, the frequencies of the particles are action-dependent $\omega(J)$, and, considering there is an action distribution in the ensemble, $\Psi_0(J)$, this leads to a frequency distribution. When the spread in frequencies is produced by nonlinearities, the Vlasov equation should be used to get the average displacement. It can be shown that Eq. (1.65) is modified to

$$\langle z\rangle(t) = \frac{A}{2\omega_{s0}} e^{-i\Omega t} \int_0^\infty \mathrm{d}J \, \frac{\partial \Psi_0}{\partial J} \frac{J}{\omega(J) - \Omega}. \tag{1.70}$$

See Refs. [30, 50, 73].

For collective instabilities in accelerators, the excitation $f(t)$ is not external, but instead self-driven. In a first-order approximation, this excitation depends on the bunch center of mass and the first derivative of the wake function. Consider that the driving force is $f(t) = \mathcal{W}\langle z\rangle(t)$, where $\mathcal{W}$ is only a symbolic constant that depends on the wake function and parameters such as beam current, energy and ring circumference. Additionally, assuming the bunch centroid motion is $\langle z\rangle(t) = Ae^{-i\Omega t}$ implies that Eq. (1.70) must be self-consistent for non-trivial solutions with $A \neq 0$, which results in a dispersion relation. A detailed derivation of the self-driven excitation by wakefields up to first order (dipole motion) shows that the frequency shift caused by wakes, assuming linear single-particle dynamics (no frequency spread), is $\Delta\Omega_{\text{linear}} = (\Omega - \omega_{s0})_{\text{linear}} = \frac{\mathcal{W}}{2\omega_{s0}}$. These self-consistent considerations applied to Eq. (1.70) lead to the dispersion relation

$$1 = \Delta\Omega_{\text{linear}} \int_0^\infty \mathrm{d}J \, \frac{\partial \Psi_0}{\partial J} \frac{J}{\omega(J) - \Omega}, \tag{1.71}$$

which must be solved for Ω.

In this format, the dispersion relation is the basis for the stability boundary diagrams. Since the integral might yield complex values, the growth rate $\mathrm{Im}(\Delta\Omega_{\text{linear}}) > 0$ considering the linear system might result in a stable condition Ω when nonlinearities are accounted. The physical mechanism behind this is Landau damping. Again, the proper calculation of singularities, in this case when $\omega(J) = \Omega$ for some J, combined with the characteristics of the distribution $\Psi_0(J)$, is key for the integral yielding complex values (damping contribution). The example in Eq. (1.71) specifically applies to the dipole mode of the ensemble, while other modes have different dispersion relations. The stability diagram analysis is better suited for studying Landau damping of single modes of collective oscillations.

For a graphical representation of Landau damping, the stability boundary defined by $\mathrm{Im}(\Omega) = 0$ can be drawn in the complex plane by scanning $\mathrm{Re}(\Omega)$ from 0 to $+\infty$. This divides the complex plane in two regions, stable and unstable. The frequency shift for the linear system, $\Delta\Omega_{\mathrm{linear}}$, can be computed and included in the graphic. If it lies within the stability boundary, it means that exists a stable solution for the dispersion relation Eq. (1.71). Otherwise, Landau damping is insufficient to stabilize the mode.

In summary, for Landau damping to manifest, two conditions are required: (i) spread in the incoherent frequencies of the particles, (ii) the frequency of the coherent excitation must be within the range of incoherent frequencies. As remarked in Ref. [30], for the case of particle beams in accelerators, Landau damping is not a dissipative damping, but rather a stabilization mechanism. The spread of incoherent frequencies due to nonlinearities may introduce a dynamical decoherence mechanism that prevents the particles in the beam from organizing coherent motion and driving an instability that would otherwise occur in the absence of frequency spread.

1.4 Higher harmonic cavities

Consider a double-rf system, with higher harmonic voltage with amplitude $\hat{V}_{\mathrm{HC}}$ and phase ϕ_{HC}, with n denoting the rf frequency harmonic. By linearity, the total rf voltage experienced by the beam is

$$V(z) = \hat{V}_{\mathrm{rf}} \sin(\omega_{\mathrm{rf}} z/c + \phi_s) + \hat{V}_{\mathrm{HC}} \sin\left(n\omega_{\mathrm{rf}} z/c + \phi_{\mathrm{HC}}\right). \tag{1.72}$$

1.4.1 Flat potential condition

The flat potential (FP) condition corresponds to zeroing the first and second derivative of the rf voltage:

$$eV(z)\bigg|_{z=0} = U_0, \qquad \frac{\partial V}{\partial z}\bigg|_{z=0} = 0, \qquad \frac{\partial^2 V}{\partial z^2}\bigg|_{z=0} = 0. \tag{1.73}$$

The harmonic amplitude and phase that produce the FP condition are

$$\frac{\hat{V}_{\mathrm{HC}}}{\hat{V}_{\mathrm{rf}}} = \frac{1}{n}\sqrt{1 - \frac{n^2}{n^2-1}\left(\frac{U_0}{e\hat{V}_{\mathrm{rf}}}\right)^2} \tag{1.74}$$

$$\tan(\phi_{\mathrm{HC}}) = \frac{n\frac{U_0}{e\hat{V}_{\mathrm{rf}}}}{\sqrt{(n^2-1)^2 - \left(n\frac{U_0}{e\hat{V}_{\mathrm{rf}}}\right)^2}}, \tag{1.75}$$

and the synchronous phase should be modified to

$$\sin(\phi_s) = \frac{n^2}{n^2-1}\frac{U_0}{e\hat{V}_{\mathrm{rf}}} = \frac{n^2}{n^2-1}\sin(\phi_{s0}), \tag{1.76}$$

where ϕ_{s0} is the single-rf synchronous phase.

This represents the idealized case of an active cavity where both amplitude and phase can be controlled. The comparison of total voltage, longitudinal potential and bunch charge distribution between the single-rf system and the double-rf system tuned to the FP condition is presented in Fig. 1.3.

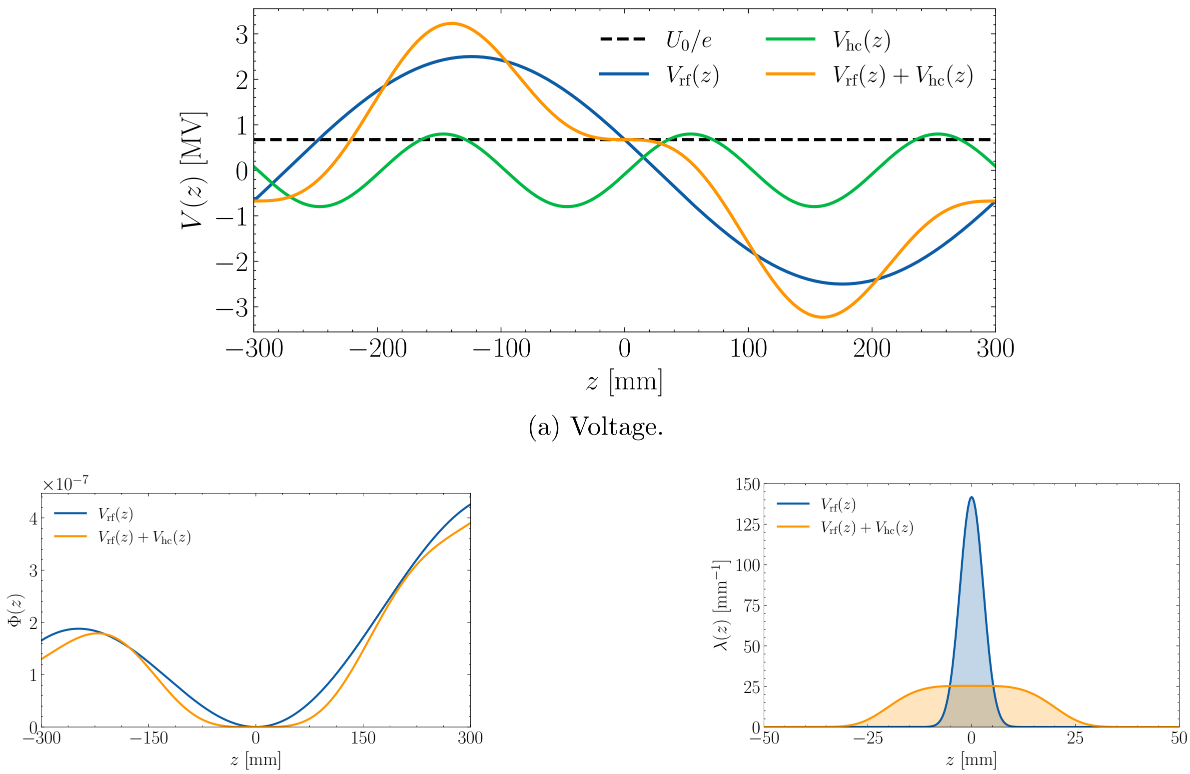

Figure 1.3: Double-rf system at flat potential condition compared to single-rf system.

For passive HCs, which is the focus in this thesis, the beam-induced harmonic voltage for the uniform filling pattern is

$$V_{\mathrm{HC}}(z) = 2I_0|F(n\omega_{\mathrm{rf}})|R_s\cos(\psi)\cos[n\omega_{\mathrm{rf}}z/c + \psi - \Phi_F(n\omega_{\mathrm{rf}})]. \tag{1.77}$$

A derivation of this expression is presented in the last section of Appendix A. The electromagnetic fields in passive HCs are build up from the wakefields excited by the beam, in a process known as beam-loading. The beam-loading voltage contribution is also present in active cavities such as the main rf cavities. However, for active cavities the generator amplitude and phase are adjusted to compensate the beam-loading and to guarantee that the beam is accelerated by a reference rf voltage. Passive HCs can operate with only the beam-loading voltage because the purpose of their additional voltage is to modify the longitudinal potential, not to accelerate the electrons. An external power is mandatory for the main rf cavities, since it is impossible for electrons to gain energy from their self-driven wakefields.

The HC is modelled by a narrowband resonator, Eq. (1.34), with shunt impedance R_s, quality factor Q and resonant frequency ω_{r}. The detuning angle ψ is related to the HC detuning frequency:

$$\tan(\psi) = Q\left(\frac{\omega_{\mathrm{r}}}{n\omega_{\mathrm{rf}}} - \frac{n\omega_{\mathrm{rf}}}{\omega_{\mathrm{r}}}\right). \tag{1.78}$$

For the HC slightly detuned from the nth rf harmonic, we can approximate the detuning angle by $\tan(\psi) \approx 2Q\Delta\omega/n\omega_{\mathrm{rf}}$, where $\Delta\omega = \omega_{\mathrm{r}} - n\omega_{\mathrm{rf}}$. Hence, the detuning frequency affects the phase of the harmonic voltage.

The bunch complex form factor is the Fourier transform of the longitudinal bunch distribution $\lambda(z)$:

$$F(\omega) = \int_{-\infty}^{\infty} \mathrm{d}z\, \lambda(z)e^{i\omega z/c} = |F(\omega)|e^{i\Phi_F(\omega)}, \tag{1.79}$$

which should be evaluated at $n\omega_{\mathrm{rf}}$. For asymmetric bunches, we have a non-zero phase Φ_F, which also contributes to the phase of the harmonic voltage. For Gaussian bunches with zero average, the form factor is real, given by $F(n\omega_{\mathrm{rf}}) = \exp[-(n\omega_{\mathrm{rf}}\sigma_z/c)^2/2]$. For short-bunches, we have $n\omega_{\mathrm{rf}}\sigma_z/c \ll 1$, so $F(n\omega_{\mathrm{rf}}) \approx 1$.

The resonant frequency ω_{r} is the only control parameter of a passive HC. For each beam current I_0, the HC detuning determines both the harmonic amplitude and phase:

$$\hat{V}_{\mathrm{HC}} = 2I_0|F(n\omega_{\mathrm{rf}})|R_s|\cos(\psi)|, \tag{1.80}$$

$$\phi_{\mathrm{HC}} = \psi - \Phi_F(n\omega_{\mathrm{rf}}) - \pi/2. \tag{1.81}$$

For a given set of ring parameters $(I_0, \hat{V}_{\mathrm{rf}}, U_0)$, only a specific combination of R_s and Q of the HC satisfies the FP condition. We can calculate the amplitude and phase for the FP condition with Eqs. (1.74) and (1.75), then compute the optimum shunt impedance R_s to satisfy Eq. (1.80). For typical ring parameters, the optimum R_s, combined with typical cavity geometries that determines the ratio (R/Q), makes the Q factor be on the order of 10^4 to 10^5, common for normal-conducting cavities. Given a Q factor, the resonant frequency can be adjusted to satisfy Eq. (1.81). Therefore, to produce the FP condition with passive HCs, normal-conducting cavities are required. In this case, for fixed values of $\hat{V}_{\mathrm{rf}}$ and U_0, the FP condition can only be achieved for a specific beam current I_0. However, by adjusting the rf voltage $\hat{V}_{\mathrm{rf}}$ within feasible limits, it may still be possible to obtain near flat potential (NFP) conditions over a range of beam currents I_0 and energy losses U_0.

For superconducting cavities, the Q factor is large, on the order of 10^8. By Eq. (1.78), this implies that $\psi \approx \pi/2$ and the harmonic voltage phase is essentially independent of the HC detuning frequency. In this case, the detuning is adjusted to satisfy Eq. (1.80), producing the optimum harmonic amplitude. Typically, by the cavity geometry (R/Q) practical constraints, this implies that the shunt impedance R_s exceeds the optimum value by much and the HC resonance must be considerably far from the nth rf harmonic. Otherwise, the beam would sample an excessively large impedance R_s, inducing too much wake voltage.

In practice, the exact FP condition is often difficult to achieve with passive HCs, since two equations should be satisfied with one control parameter. The impact of 1 % relative error in the harmonic phase with respect to the FP phase is presented in Fig. 1.4. Given $(I_0, \hat{V}_{\mathrm{rf}}, U_0)$, the FP can only be achieved with properly designed normal-conducting HCs parameters. For superconducting HCs, it is still possible to achieve NFP conditions with good performances, where the harmonic amplitude condition can be satisfied, but not the phase.

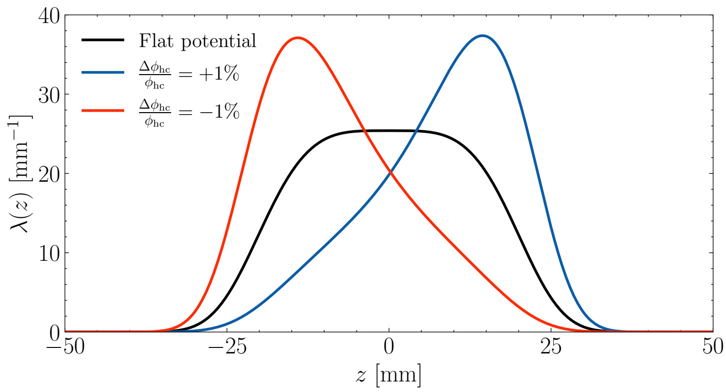

Figure 1.4: Impact of harmonic phase deviation.

For the uniform filling, Eq. (1.77) is a closed formula for the beam-induced voltage in the passive HC. Considering an initial guess for the longitudinal distribution $\lambda(z)$, the harmonic voltage can be computed and, with the Haïssinski equation, used to obtain an updated $\lambda(z)$. The process can be iterated to get a self-consistent equilibrium solution. For generic filling patterns, no closed formula can be obtained, but still semi-analytical methods provide the self-consistent solution, where the equilibrium bunch distribution may vary depending on the bucket. Such methods will be developed in details on Appendix A.

It is possible to linearize the Haïssinski equation with respect to bunch complex form factor variations, solving the fixed-point problem by approximating the Haïssinski map by matrices [75–77]. However, for high beam currents or high harmonic voltages, when the potential-well distortion is intense, the convergence of the iterative linear approach might fail. Then, a more robust approach is required, finding the self-consistent solution with fixed-point iteration methods, such as the Anderson acceleration algorithm employed by Warnock [78] to solve the Haïssinski equation.

The harmonic voltage modifies the longitudinal potential, which in turn affects the longitudinal distribution $\lambda(z)$. An interesting feature of HCs is that their impact on the distribution of energy and transverse positions and angles is negligible. Let us separate the 6D distribution as $\Psi(V) = f(x, x', y, y', \delta)\lambda(z)$. We will denote the longitudinal distributions without the HC as $\lambda_0(z)$ and $\lambda_{\mathrm{HC}}(z)$ with the HC; while $f(x, x', y, y', \delta)$ is assumed to be unaltered by the HC. With Eq. (1.36) and recalling that $\mathcal{P} \propto 1/\delta_{\mathrm{acc}}^2$, the relative variation of the Touschek lifetime due the HC can be estimated by:

$$R = \frac{\tau_{\mathrm{HC}}}{\tau_0} = \frac{\delta_{\mathrm{acc,HC}}^2}{\delta_{\mathrm{acc},0}^2} \frac{\int \mathrm{d}z\, \lambda_0^2(z)}{\int \mathrm{d}z\, \lambda_{\mathrm{HC}}^2(z)}, \tag{1.82}$$

It is often a good approximation to also consider that HC do not change the energy acceptance by much, so $\frac{\delta_{\mathrm{acc,HC}}^2}{\delta_{\mathrm{acc},0}^2} \approx 1$. Figure 1.5 shows an example of separatrix with and without HC, where the energy acceptance is only 3 % lower with the HC than without it.

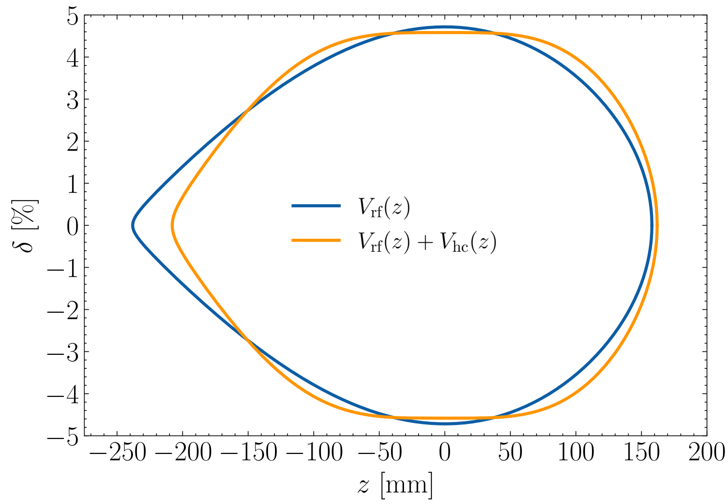

Figure 1.5: rf bucket separatrix.

Note that, more important than lengthening the bunches (increasing the second central moment of $\lambda(z)$), reducing the peak bunch current that is proportional to $\lambda^2(z)$ is the key factor to enhance the Touschek lifetime. The optimum condition in terms of maximizing the Touschek lifetime occurs with harmonic voltages slightly higher than the FP value, producing double-hump bunch distributions with lower peak bunch current than the flat distribution. This case is commonly referred to as overstretched conditions[5]. The use of overstretched conditions to optimize Touschek lifetime will be explored with simulations on Appendix A and verified experimentally on Appendix C.

1.4.2 Quartic potential

The longitudinal dynamics can be analyzed for the FP condition, where the longitudinal potential is approximately quartic. The following results can be found in [79–81].

Consider the total rf voltage in a double-rf system given by Eq. (1.72), with $\phi = k_{\mathrm{rf}} z$, where $k_{\mathrm{rf}} = \omega_{\mathrm{rf}}/c$ is the rf wave number. Assuming that the first and second derivatives of the voltage vanish, the Taylor expansion of the total rf voltage and potential read [79, 80]

$$eV(\phi) \approx U_0 + (n^2 - 1)e\hat{V}_{\mathrm{rf}} \cos(\phi_s)\frac{\phi^3}{6}, \tag{1.83}$$

$$\Phi(\phi) = -\frac{(n^2-1)}{6}\frac{e\hat{V}_{\mathrm{rf}}\cos(\phi_s)}{E_0 C_0 k_{\mathrm{rf}}}\frac{\phi^4}{4}. \tag{1.84}$$

Introducing the constant Λ, such that:

$$\Phi(z) = \alpha\Lambda\frac{z^4}{4}, \tag{1.85}$$

$$\Lambda = -\frac{(n^2-1)}{6}\frac{e\hat{V}_{\mathrm{rf}}\cos(\phi_s)k_{\mathrm{rf}}^3}{E_0 C_0 \alpha}, \tag{1.86}$$

then the Hamiltonian is $\mathcal{H}_0 = \alpha\delta^2/2 + \alpha\Lambda z^4/4$.

Let $z = r$ be the right turning point such that $\delta = 0$, then the Hamiltonian can be written as $\mathcal{H}_0(r) = \alpha\Lambda r^4/4$. As the potential is symmetric, $z = -r$ is the left turning point. The action variable can be calculated by

$$J = \sqrt{\frac{\Lambda}{2\pi^2}}\int_{-r}^{r} \mathrm{d}z\,\sqrt{r^4 - z^4} = \frac{2\mathcal{K}(1/\sqrt{2})}{3\pi}\sqrt{\Lambda}r^3, \tag{1.87}$$

where $\mathcal{K}(k)$ is the elliptic function defined in Eq. (1.28) and $\mathcal{K}(1/\sqrt{2}) \approx 1.854$. The following identities $\mathcal{K}\left(1/\sqrt{2}\right) = \Gamma^2(1/4)/4\sqrt{\pi}$, $\Gamma(1/4)\Gamma(3/4) = \pi\sqrt{2}$ are useful for comparison with results from literature [80–82].

With the relation $\Psi_0(J) = \mathcal{N}^{-1}e^{-\mathcal{H}_0(J)/\alpha\sigma_\delta^2}$, and using J in terms of r, the longitudinal

[5] Although the overstretched case is interesting since it provides the maximum Touschek lifetime, developing an instability theory for this condition is challenging. For instance, the overstretched case has a double-well potential, with two local minima separated by a saddle point. The analysis of single-particle dynamics must be separated for electrons oscillating with small amplitudes around each one of these minima and also with large amplitudes passing through both minima. Then, Vlasov equations must be solved for each one of these cases to get the coherent frequencies and combine them somehow to judge the beam stability.

bunch distribution is given by

$$\Psi_0(r) = \frac{2^{3/4}}{\Gamma^2(1/4)\sigma_z\sigma_\delta}\exp\left[-\frac{2\pi^2}{\Gamma^4(1/4)}\frac{r^4}{\sigma_z^4}\right], \tag{1.88}$$

where the bunch length is defined as

$$\sigma_z^2 = \frac{2}{\sqrt{\Lambda}}\frac{\Gamma(3/4)}{\Gamma(1/4)}\sigma_\delta. \tag{1.89}$$

Note that considering that $\sin(\phi_s) \approx \sin(\phi_{s0})$, i.e., approximating $n^2/(n^2-1) \approx 1$, then we can use the single-rf synchrotron frequency expression $\omega_{s0}^2 = -\frac{\alpha c k_{\mathrm{rf}}}{E_0 T_0} e\hat{V}_{\mathrm{rf}}\cos(\phi_s)$ to rewrite $\Lambda \approx (n^2-1)\omega_{s0}^2 k_{\mathrm{rf}}^2/6\alpha^2 c^2$. Moreover, with the matching condition $\omega_{s0}\sigma_{z0} = \alpha c \sigma_\delta$, Λ can be written in terms of the single-rf bunch length: $\Lambda \approx (n^2-1)\sigma_\delta^2 k_{\mathrm{rf}}^2/6\sigma_{z0}^2$. Under this approximation, from Eq. (1.89) we can estimate the theoretical bunch lengthening factor as

$$\frac{\sigma_z}{\sigma_{z0}} \approx 3^{1/4}\sqrt{\frac{\Gamma(3/4)}{\Gamma(1/4)}}\frac{1}{\sqrt{k_{\mathrm{rf}}\sigma_{z0}}} \approx \frac{0.765}{\sqrt{k_{\mathrm{rf}}\sigma_{z0}}}. \tag{1.90}$$

Typical values for this theoretical bunch lengthening factor are in the range of 4 to 6.

The relation $\omega_s(J) = c\frac{\partial \mathcal{H}_0}{\partial J}$ can be used to obtain the amplitude-dependent synchrotron frequency:

$$\omega_s(r) = \frac{\pi\alpha c}{2\mathcal{K}(1/\sqrt{2})}\sqrt{\Lambda}\, r, \tag{1.91}$$

and we see that for zero-amplitude $\omega_s(0) = 0$, corresponding to the harmonic voltage flattening the first derivative of the rf voltage, and the synchrotron frequency increases linearly with the amplitude of oscillation. This renders a significant frequency spread within the bunch.

The average synchrotron frequency is computed as $\langle\omega_s\rangle = 2\pi\int_0^\infty \mathrm{d}r\,\omega_s(r)\Psi_0(r)\frac{\partial J}{\partial r}$, yielding:

$$\langle\omega_s\rangle = \frac{2\pi 2^{3/4}}{\Gamma^2(1/4)}\frac{\alpha c\sigma_\delta}{\sigma_z}, \tag{1.92}$$

and we see that the format of the matching condition is maintained for the average frequency: $\langle\omega_s\rangle\sigma_z = N\alpha c\sigma_\delta$, where for the quartic potential $N = \frac{2\pi 2^{3/4}}{\Gamma^2(1/4)} \approx 0.803$, while for the quadratic potential, $\langle\omega_s\rangle = \omega_{s0}$ and $N = 1$.

Applying the single-rf matching condition to Eq. (1.92), we get:

$$\frac{\langle\omega_s\rangle}{\omega_{s0}} = \frac{2\pi 2^{3/4}}{\Gamma^2(1/4)}\frac{\sigma_{z0}}{\sigma_z} \approx 0.803\frac{\sigma_{z0}}{\sigma_z}, \tag{1.93}$$

which shows that the bunch lengthening factor and the relative reduction in the average synchrotron frequency are inversely proportional.

Finally, the longitudinal motion in terms of the amplitude r and angle φ, i.e., the

Table 1.1: Comparison of the proportionality of relevant quantities for the longitudinal dynamics in quadratic and quartic rf potentials. r is the turning point in phase space, that defines the oscillation amplitude for the z coordinate.

	Single-rf, $\Phi(z) \propto z^2$	Double-rf, $\Phi(z) \propto z^4$
Action variable $J \propto$	r^2	r^3
Hamiltonian $\mathcal{H}_0(J) \propto$	J	$J^{4/3}$
Bunch distribution $\Psi_0(r) \propto$	e^{-r^2}	e^{-r^4}
Synchrotron frequency $\omega_s(J) \propto$	constant	$J^{1/3}$
Canonical transformation $z(J,\varphi) \propto$	$J^{1/2}\cos(\varphi)$	$J^{1/3}\mathrm{cn}(\varphi;1/2)$

canonical transformation for the quartic potential is written in terms of $\mathrm{cn}(x;1/2)$, the Jacobi elliptic function with parameter 1/2:

$$z = r\ \mathrm{cn}\left(\frac{2}{\pi}\mathcal{K}(1/\sqrt{2})\varphi; 1/2\right). \tag{1.94}$$

The Fourier expansion of the Jacobi elliptic function is

$$z(r,\varphi) = \frac{\pi\sqrt{2}}{\mathcal{K}(1/\sqrt{2})} r \sum_{p=0}^{\infty} \frac{\cos[(2p+1)\varphi]}{\cosh[\frac{\pi}{2}(2p+1)]}, \tag{1.95}$$

exhibiting that in a quartic potential, the longitudinal motion contains all odd-order harmonics. Nevertheless, the first term $p = 0$ associated to $\cos(\varphi)$ is the dominant contribution, since $1/\cosh[\frac{\pi}{2}(2p+1)]$ decreases exponentially with p:

$$z(r,\varphi) = \frac{\pi\sqrt{2}}{\mathcal{K}(1/\sqrt{2})\cosh(\pi/2)} r \left[\cos(\varphi) + 0.045\cos(3\varphi) + 0.0019\cos(5\varphi) + \cdots\right], \tag{1.96}$$

and the approximation $z(r,\varphi) \approx \frac{\pi\sqrt{2}}{\mathcal{K}(1/\sqrt{2})\cosh(\pi/2)} r\cos(\varphi)$ can be often used for analytical development of instability theory in quartic rf potentials [81, 82].

The main differences between the longitudinal dynamics in single-rf (quadratic potential) and double-rf (quartic potential) are summarized in Table 1.1.

Truth... is much too complicated to allow anything but approximations.

— John von Neumann

2 Semi-analytical methods

The calculations of collective effects in accelerator physics relies on computational methods. Semi-analytical approaches provide a balance between the interpretability of analytical formulations and the efficiency of numerical implementations. The method of analysis followed in this thesis is divided into two steps:

1. Determination of the equilibrium state. The first step involves solving for the equilibrium state by determining the fixed-point solution of the Haïssinski equation, accounting for both external and self-induced fields acting on the beam. This solution provides the equilibrium wake voltages, longitudinal potentials, and bunch distributions. However, obtaining the equilibrium solution numerically does not always imply that this steady-state condition can be achieved in practice. Therefore, the stability of the equilibrium under perturbations must be evaluated in a second step.

2. Analysis of collective dynamics. After the equilibrium state is obtained, the next step is to analyze the collective dynamical behavior of the beam. By considering small coherent perturbations with respect to the equilibrium distribution, the Vlasov equation can be linearized to solve for the coherent frequency Ω, which is generally a complex number. This analysis yields the coherent frequency of oscillation $\mathrm{Re}(\Omega)$ and the growth rate $\mathrm{Im}(\Omega)$.

The following sections provide an overview of the thesis contributions, which employ semi-analytical methods to study the equilibrium state and coupled-bunch instabilities, highlighting the advantages and practical implications of this approach. These contributions were written as journal articles and are fully reproduced in Appendices A and B.

The semi-analytical methods were implemented in `python3` and are available in the open-source package `pycolleff` [83]. These methods were applied in studies for the higher harmonic cavity choice for SIRIUS, with results reported in Chapter 3. Some of these methods were also applied in the collaborative development of the open-source package Algorithms for Longitudinal MultiBunch Beam Stability (`ALBuMS`) [84], also implemented in `python3`.

2.1 Self-consistent calculation of equilibrium

The full content of this part is presented in Appendix A, published as Ref. [44]. Below, we briefly outline its main contributions.

The first contribution of this thesis presents two approaches for computing the equilibrium beam-induced voltage in electron storage rings with arbitrary filling patterns and impedance sources. The space-domain method was formulated for resonator wake functions. This part has a review aspect, as similar developments were reported in previous publications referenced in the introduction of Appendix A. Nevertheless, we generalized the method to consider the most generic resonator wake function, while previous works assumed the approximate formula for a narrowband resonator. Moreover, we believe the formulas presented are more compact, with direct physical interpretation, and accessible for numerical implementation.

In contrast, the frequency-domain framework allowed for arbitrary impedance functions and offered a straightforward calculation using discrete Fourier transforms (DFTs). This method proved computationally efficient due to fast Fourier transform (FFT) algorithms and was benchmarked against the space-domain calculations and macroparticle tracking simulations, showing excellent agreement. The parameters of SIRIUS storage ring were considered for this study.

Additionally, a different method for modeling beam-loading compensation in active rf cavities was introduced using a closed-loop impedance concept, which is only suitable in the frequency-domain approach. This method offers a more flexible and realistic description of generic low-level rf system topologies. The frequency-domain framework also facilitated the direct evaluation of the broadband impedance budget, avoiding intermediate fitting steps or numerical convolutions required in the space-domain approach.

Finally, the impact of a passive superconducting harmonic cavity on Touschek lifetime was analyzed, considering different detuning scenarios and the full impedance model of SIRIUS, accounting for contributions from the main cavities and broadband machine impedance. The study confirmed that an overstretched bunch profile provided the best lifetime gain. While equilibrium calculations do not guarantee stability in real machines, the developed framework served as a basis for analyzing longitudinal dynamics and instabilities. The results demonstrated that the frequency-domain approach is more general, numerically stable, and computationally efficient, making it a useful tool for storage ring design and impedance studies.

2.2 Instabilities with arbitrary rf potentials

The full content of this part is presented in Appendix B, submitted for publication as Ref. [45]. Below, we briefly outline its main contributions.

This contribution develops a theoretical framework for analyzing longitudinal coupled-bunch instabilities in double-rf systems with harmonic cavities, considering potential-well distortion and multiple azimuthal modes. The approach is based on frequency-domain perturbation theory, leading to the Lebedev equation for calculating coherent frequencies. The theory extends recent publications, Refs. [81, 82, 85], recovering their results as particular cases.

It is demonstrated that dispersion relations for any azimuthal mode can be directly obtained from the Lebedev equation in the case of narrowband resonators and elliptic orbits in the longitudinal phase space. Additionally, an approximated model considering a constant effective synchrotron frequency (amplitude-independent) was derived from the Lebedev equation. This model proved useful in comparing results for instability thresholds computed with and without the contribution of the frequency spread, i.e., Landau damping.

The methods were applied to study Robinson dipole-quadrupole mode coupling and the periodic transient beam loading (PTBL)/mode-1 instability, using parameters from ALS-U, HALF, and MAX IV. The theoretical predictions for the mode-1 instability threshold showed excellent agreement with experimental data from MAX IV, a novel result. The analysis revealed that the PTBL instability is a zero-frequency effect for coupled-bunch mode 1. The low-frequency feature makes this instability unaffected by Landau damping, as numerically demonstrated by the equivalence between results obtained with the Lebedev equation and the approximated effective frequency model. We showed that the essential mechanism for accurate prediction of this instability is the interaction between multiple azimuthal modes, an effect neglected in previous models.

Describing the PTBL as a zero-frequency instability helped in understanding the dependence of instability thresholds on parameters such as the main rf voltage and the harmonic cavity's (R/Q). Moreover, the zero-frequency condition led to an approximate formula for the threshold, whose scaling law agrees with previous studies. These new findings suggest further studies on mitigation strategies, including tests with feedback systems designed to prevent the coherent frequencies of coupled-bunch mode 1 from reaching lower values as the longitudinal potential is flattened by the higher harmonic cavity.

Prediction is very difficult, especially if it's about the future.

— Niels Bohr

3 Applications to SIRIUS

Contents

This chapter investigates the implementation of a passive third-harmonic cavity (3HC) in the SIRIUS storage ring to enhance bunch lengthening and improve beam stability during the Phase II of operation at 350 mA. To achieve this, we apply the frameworks and tools developed in the Appendices A and B (Refs. [44] and [45]), to evaluate the equilibrium solution and the growth rates of coupled-bunch instabilities. This approach allows for the analysis of the benefits and challenges of implementing the 3HC in improving beam quality under high current conditions.

3.1 Basic parameters

The requirements for the HHC parameters depend on the storage ring parameters. The relevant parameters of the storage ring and main rf system are presented in Table 3.1.

Table 3.1: Main parameters for SIRIUS storage ring and main rf system.

Parameter	Symbol	Value
Energy	E_0	3 GeV
Nominal current	I_t	350 mA
Circumference	C_0	518.39 m
Harmonic number	h	864
Revolution frequency	f_0	578.32 kHz
Momentum compaction factor	α	1.645×10^{-4}
Energy loss per turn (dipoles + IDs)	U_0	$(475 + 200)$ keV
Relative energy spread	σ_δ	8.436×10^{-4}
Longitudinal damping time	τ_δ	12.9 ms
Main rf frequency	f_{rf}	499.667 MHz
Number of main cavities (MCs)	N_{MC}	2
MCs max. total voltage	$N_{\mathrm{MC}}\hat{V}_{\mathrm{MC}}$	3.0 MV
MC geometric factor	$(R/Q)_{\mathrm{MC}}$	89 Ω
MC unloaded quality factor	$Q_{0,\mathrm{MC}}$	2×10^9
External quality factor	Q_{ext}	1.58×10^5
Cavity coupling factor	β_c	12 657
MC detuning	Δf_{MC}	−4.9 kHz

Two quantities are essential to compute the FP condition: the rf voltage $\hat{V}_{\mathrm{rf}}$ and the energy loss per turn U_0. In 4$^{\mathrm{th}}$-generation storage rings, the IDs have a significant contribution to U_0. Therefore, the total U_0 is variable, depending on the IDs state. The overvoltage, $q = e\hat{V}_{\mathrm{rf}}/U_0$, determines the synchronous phase and the rf energy acceptance of the ring. The total energy acceptance is defined by the minimum between the rf and the lattice acceptance, which depends on the nonlinear transverse dynamics. The energy acceptance for one sector of SIRIUS storage ring is shown in Fig. 3.1(a).

Whenever feasible, the overvoltage should be high enough such that the rf acceptance is not the limiting factor for the total acceptance. For SIRIUS, the highest value for the lattice energy acceptance is 4.8 % in the straight sections. Recall the rf energy acceptance expression:

$$\delta_{\mathrm{acc}}^{\mathrm{rf}} = \left[\frac{e\hat{V}_{\mathrm{rf}}}{\pi\alpha h E_0}\frac{F(q)}{q}\right]^{1/2}, \tag{3.1}$$

$$F(q) = 2\left[\sqrt{q^2-1} - \arccos(1/q)\right]. \tag{3.2}$$

Therefore, the rf voltage should result in $\delta_{\mathrm{acc}}^{\mathrm{rf}} \geq 4.8\,\%$, for the range of values of U_0. Since higher rf voltages means higher power consumption and shorter bunches, the best approach is using the minimum rf voltage that satisfies the rf acceptance requirement.

The rf acceptance as a function of the rf voltage for two values of U_0, only accounting

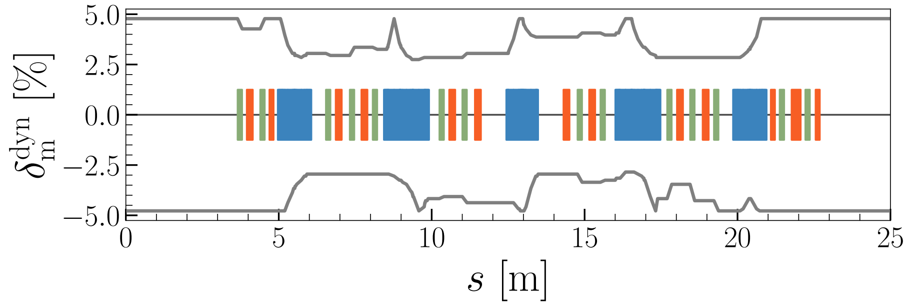

(a) Lattice energy acceptance for one section of SIRIUS storage ring. The gray curve is the nominal acceptance. Dipoles, quadrupoles and sextupoles are represented as blue, orange and green blocks, respectively.

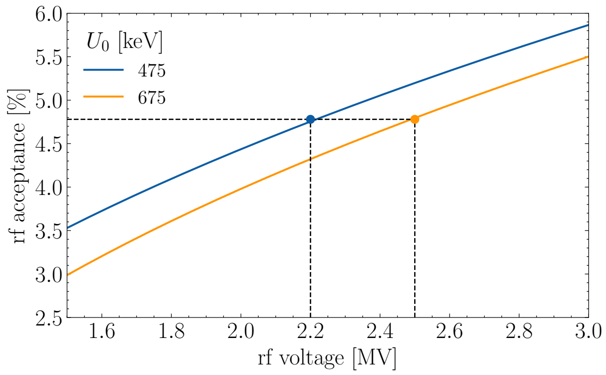

(b) rf energy acceptance vs. rf voltage considering U_0 with and without the IDs contribution.

Figure 3.1: Energy acceptance of SIRIUS lattice and rf acceptance for different rf voltages and energy losses per turn to synchrotron radiation.

for dipoles and including the IDs contribution, is presented in Fig. 3.1(b). Note that $\delta_{\text{acc}}^{\text{rf}} = 4.8\,\%$ is obtained for the rf voltage ranging from 2.2 MV to 2.5 MV.

In these conditions, the bunch length is about 3 mm, which for the beam current of 350 mA would provide unacceptable impedance-induced heating of some components of the storage ring. Additionally, the Touschek lifetime at this current is about 5 h, which would pose severe challenges for the SIRIUS injector system to maintain the top-up operation.

We will be focused on the passive 3HC case for bunch lengthening. The third rf harmonic for SIRIUS corresponds to a 1.5 GHz cavity. The ratio of harmonic voltage to main rf voltage for the FP condition is:

$$\frac{\hat{V}_{\text{HC}}}{\hat{V}_{\text{rf}}} = \frac{1}{3}\sqrt{1 - \frac{9}{8}\frac{1}{q^2}}, \tag{3.3}$$

which only depends on the overvoltage q.

Table 3.2: Parameters for flat-potential condition with passive 3HC.

Parameter	$U_0 = 475\,\text{keV}, \hat{V}_\text{rf} = 2.2\,\text{MV}$	$U_0 = 675\,\text{keV}, \hat{V}_\text{rf} = 2.5\,\text{MV}$
Overvoltage q	4.63	3.70
Single-rf synchrotron frequency f_{s0}	2.32 kHz	2.45 kHz
Natural bunch length σ_{z0}	3.0 mm	2.8 mm
Single-rf synchronous phase ψ_{s0}	167.53°	164.34°
Modified synchronous phase $\psi_{s,\text{HC}}$	165.94°	162.32°
Harmonic voltage ratio $\hat{V}_\text{HC}/\hat{V}_\text{rf}$	0.3245	0.3194
Harmonic voltage $\hat{V}_\text{HC}$	713.8 kV	798.4 kV
Harmonic detuning phase ψ_HC	85.23°	83.93°
Bunch form factor $\lvert F\rvert$	0.9191	0.9233
Optimum shunt impedance $R_{s,\text{opt}}$	13.3 MΩ	11.7 MΩ

3.2 Harmonic cavity technology options

The HC can be normal-conducting (NC) or superconducting (SC). SIRIUS already have a cryogenic plant infrastructure for the main rf cavities, initially designed to support a SC HC as well. Therefore, a SC HC is the more favorable choice for SIRIUS. Nevertheless, we investigate the performance and impact of using NC HCs as an exploratory exercise.

3.2.1 Normal-conducting

According to the material available on models of NC HCs [35, 37, 86–89], the typical quality factor is $Q = 2 \times 10^4$. Depending on the cavity geometry, the (R/Q) parameter may significantly vary, but we can reasonably consider $(R/Q) = 100\,\Omega$ as a typical value. Considering these conditions, each NC cavity will contribute to the shunt impedance of $R_s = 2\,\text{M}\Omega$. Therefore, according to Table 3.2, to reach the optimum shunt impedance of $R_s = 11.7\,\text{M}\Omega$, it would be necessary at least 6 passive NC cavities. This number of cavities is already impractical due to the limited available space in SIRIUS storage ring, where most straight sections are occupied or reserved for undulators serving the beamlines. Moreover, 6 cavities would amount to a total $(R/Q) = 600\,\Omega$. With the approximate threshold formula for the PTBL/mode-1 instability (Appendix B, Ref. [45]):

$$\left[I_0\left(\frac{R}{Q}\right)\right]_\text{threshold} \approx \frac{T_0\sigma_\delta}{n^2\sigma_\tau}\sqrt{\frac{E_0\alpha\hat{V}_\text{rf}}{2\pi e F_n h^3}}, \tag{3.4}$$

we can estimate the threshold for SIRIUS parameters with $I_0 = 350\,\text{mA}$, bunch length of $\sigma_z = 12\,\text{mm}$ (bunch lengthening factor 4) and rf voltage of $\hat{V}_\text{rf} = 2.2\,\text{MV}$, that the maximum total (R/Q) should be $(R/Q)_\text{threshold} \approx 200\,\Omega$. Therefore, the requirement of 6 cavities to produce the FP condition cannot be met due to the large total (R/Q) that would trigger the PTBL instability.

The unstable regime at FP conditions was confirmed with a macroparticle tracking simulations. The uniform filling pattern was considered, but the bunch centroids and lengths did not converge to the same value for all bunches, rather presenting a transient oscillating periodically. A snapshot of this transient is shown in Fig. 3.2. This is an indication of the PTBL instability, also observed in tracking simulations for other rings, for example, in Ref. [90].

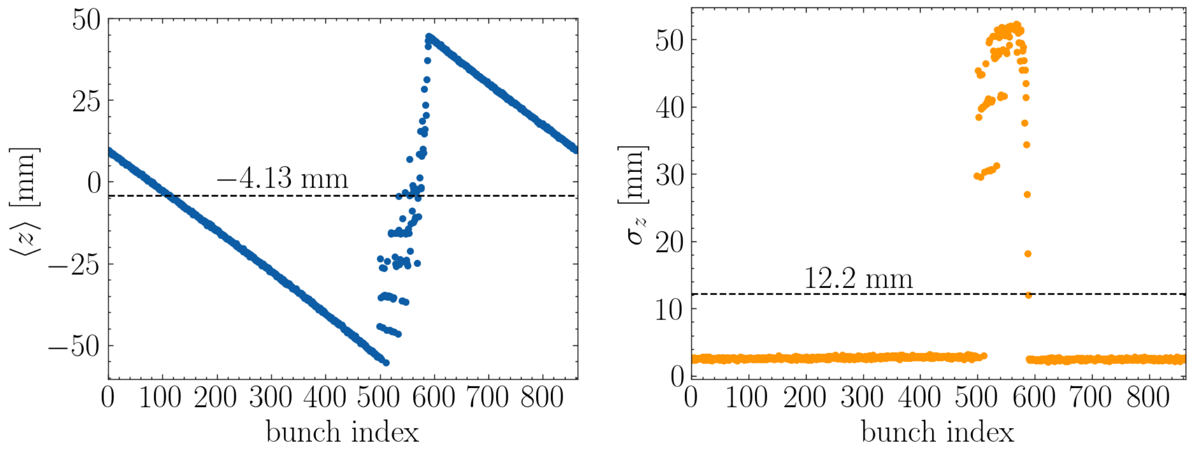

(a) Bunch centroids. (b) Bunch lengths.

Figure 3.2: Snapshot of macroparticle tracking results displaying an instability with 6 NC HCs at flat potential condition. Uniform filling, 200 macroparticles per bunch, 5×10^5 turns. Horizontal dashed lines indicate the expected equilibrium parameters in the FP condition.

We may consider the case of active NC HCs, where, in principle, the number of cavities could be reduced since the voltage is provided by an external power source. However, we observed that the PTBL instability would also limit the operating detuning frequency of the HCs, as shown in Fig. 3.3. The growth rates were calculated using the Gaussian longitudinal mode-coupling instability (LMCI) method described in Ref. [45].

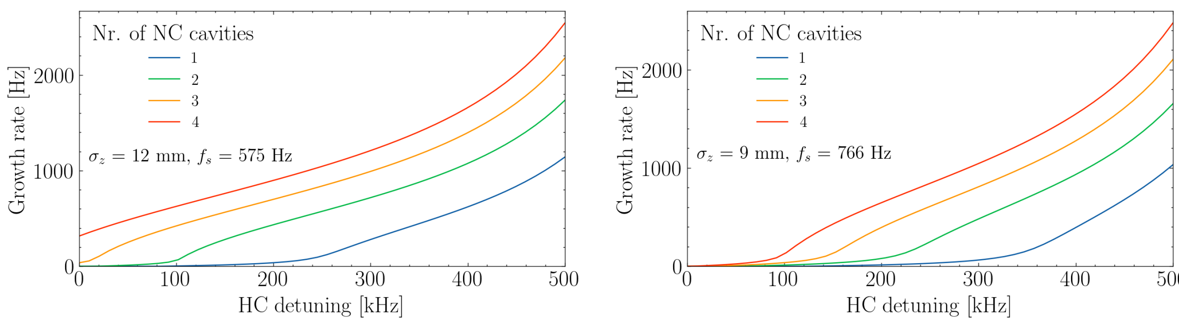

(a) Bunch lengthening factor of 4. (b) Reduced bunch lengthening factor of 3.

Figure 3.3: Growth rates of coupled-bunch mode 1 with the HCs detuning frequency. Nominal parameters for SIRIUS considered. The HC is assumed to be active, where the harmonic voltage (therefore the bunch length and average synchrotron frequency) are independent of the detuning frequency.

Moreover, as the total harmonic voltage required for SIRIUS is about 800 kV, the restriction of maximum voltage per cavity to avoid too much power dissipation limits the minimum number of cavities. The typical value for the maximum voltage per cavity is about 200 kV. The existing cavities operate below this maximum voltage for safety. Therefore, to provide the required voltage for SIRIUS, at least 4 active NC HCs would be necessary. In Fig. 3.3 we see that with 4 cavities, the beam would be mode-1 unstable for the full detuning range of the HCs when a bunch lengthening factor of 4 is considered. Even if the bunch lengthening is reduced to 3 (which is the minimum requirement to avoid impedance-induced heating for operation at 350 mA at SIRIUS), with 4 cavities, the beam would be mode-1 stable only for HC detunings lower than 100 kHz. Besides these small region of stability which constraints the operation of the cavity, for small detunings the beam-loading voltage becomes significant which may pose difficulties to the low-level rf (llrf) control system.

With this analysis, we concluded that both active and passive NC HCs would likely drive longitudinal instabilities in the SIRIUS storage ring. Mitigation strategies for the PTBL/mode-1 instability are currently under study and generally focus on modifying the driving source parameters (cavity impedance), as this instability has proven to be resistant to direct resistive feedback loops [91]. As we will see next, the SC option would avoid longitudinal instabilities and beam stability without the need for active feedback systems is expected. Combining this with the existing cryogenic infrastructure at SIRIUS, the NC option for the 3HC would be considerably more complicated to pursue than the SC option for the double-rf system of SIRIUS.

3.2.2 Superconducting

There are essentially two designs of SC 1.5 GHz cavities with the operation record as harmonic cavities in synchrotron light sources: the Super-3HC and the SINAP-3HC models. The Super-3HC cavity was developed in collaboration between the CEA, SLS (Swiss Light Source, Paul Scherrer Institut) and ELETTRA (synchrotron light source in Trieste, Italy) and it was used for bunch lengthening in both ELETTRA and SLS storage rings since the early 2000s [92–94]. The SINAP-3HC model was developed by the SINAP (Shanghai Institute of Applied Physics) and installed in 2021 in the SSRF (Shanghai Synchrotron Radiation Facility) storage ring [95]. Both cavities have 2-cells. The Super-3HC operates at the temperature of 4.5 K and the SINAP-3HC at 4.2 K.

The institutions LNLS and SINAP have a collaboration history. For instance, SINAP developed, installed, and commissioned the 150 MeV LINAC for SIRIUS, and also manufactured two in-vacuum undulators currently installed in the SIRIUS storage ring. With the recent success in the development and installation of the SC 3HC in the SSRF ring, the option of acquiring one 3HC cryomodule from SINAP is interesting for LNLS. Therefore, we studied the performance of the SINAP-3HC model for bunch lengthening in SIRIUS storage ring. The main parameters for the SINAP-3HC are presented in Table 3.3.

The performance of the SINAP-3HC, including the full impedance model of SIRIUS,

Table 3.3: Parameters of SINAP-3HC.

Geometric factor (R/Q)	$87.5\,\Omega$
Quality factor Q	2×10^8
Shunt impedance R_s	$17.5\,\mathrm{G}\Omega$

with main cavities and the broadband machine impedance budget, was reported in Appendix A (Ref. [44]). For uniform filling, the bunch distribution obtained with the FP voltage is shown in Fig. 3.4(a), compared with the theoretical bunch profile obtained with a quartic potential. The bunch lengthening factor is 4.5 and a similar increase factor is estimated for the Touschek lifetime. This condition was evaluated with tracking simulation, obtaining a convergence to the same equilibrium distribution obtained with the Haïssinski solver, as shown in Fig. 3.4(b). The detuning frequency of the SINAP-3HC to obtain the FP condition is $\Delta f = 53.17\,\mathrm{kHz}$ for $\hat{V}_{\mathrm{rf}} = 2.5\,\mathrm{MV}$ and $\Delta f = 59.15\,\mathrm{kHz}$ for $\hat{V}_{\mathrm{rf}} = 2.2\,\mathrm{MV}$.

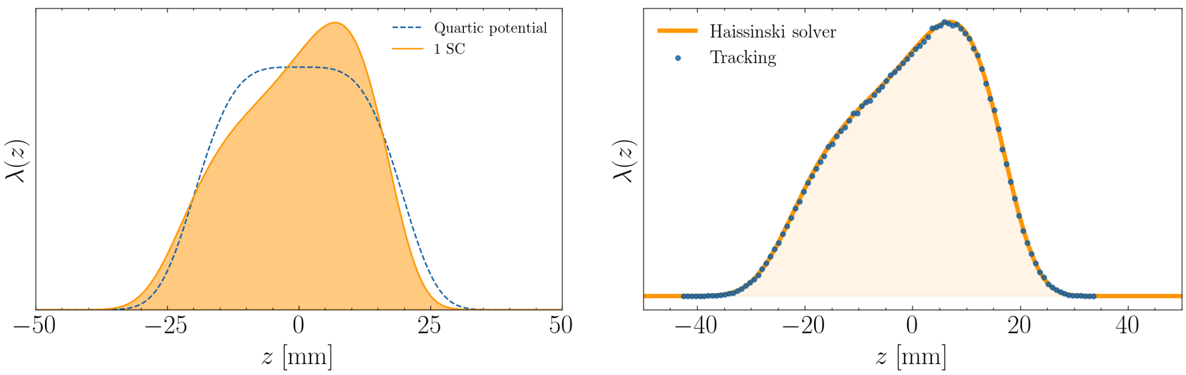

(a) With theoretical flat distribution.

(b) With tracking result.

Figure 3.4: Comparison of equilibrium bunch distribution obtained with the SINAP 3HC. The equilibrium bunch centroid is $\langle z\rangle = -0.27\,\mathrm{mm}$ and the bunch length is $\sigma_z = 12.2\,\mathrm{mm}$.

The time evolution of the centroids and lengths for some bunches in the tracking simulation is presented in Fig. 3.5, showing that the average values converges to the same values obtained with the equilibrium solver. This demonstrates that the equilibrium at FP condition is stable with the SINAP-3HC.

3.3 Equilibrium parameters

The detailed impact of the SINAP-3HC on longitudinal equilibrium parameters for SIRIUS storage ring was evaluated. We considered the parameters of Table 3.1, with $I_0 = 350\,\mathrm{mA}$ in uniform filling pattern, $U_0 = 675\,\mathrm{keV}$ and $\hat{V}_{\mathrm{rf}} = 2.5\,\mathrm{MV}$. The equilibrium solution was obtained self-consistently with the frequency-domain framework developed in Appendix A (Ref. [44]). The longitudinal parameters for the single-rf system are shown in Fig. 3.6. The single-particle dynamics is linear, with Gaussian bunch distribution, quadratic potential,

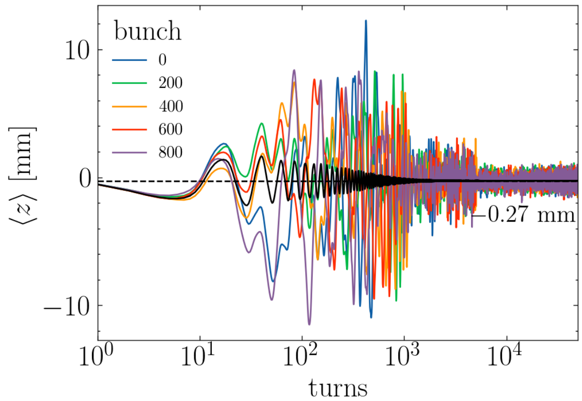

(a) Bunch centroids.

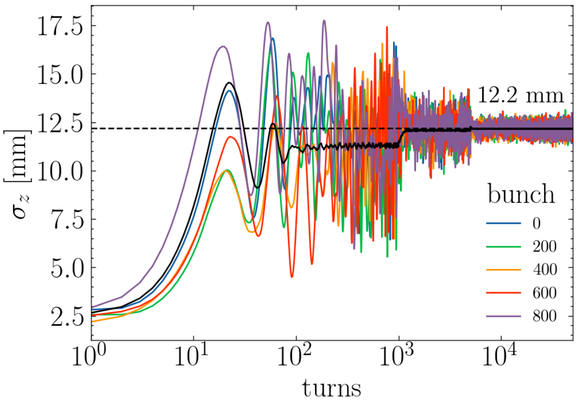

(b) Bunch lengths.

Figure 3.5: Convergence of bunch centroids and lengths with macroparticle tracking simulations. The tracking setting was 1000 macroparticle per bunch and 5×10^5 turns. The black curves indicate the average values over the bunches. Sudden variations in the average values corresponds to the strategy employed to speed up the tracking simulation, where the number of macroparticles was increased in steps, similarly as described in Ref. [44], where in the last 1×10^5 turns, 1000 macroparticle per bunch were tracked.

constant synchrotron frequency and elliptical orbits in the phase space. In this case, the synchrotron frequency is 2.4 kHz.

The SINAP-3HC impedance was included with the parameters of Table 3.3 for different detuning frequencies. The nonlinear relation between the HC detuning and the induced HC voltage is shown in Fig. 3.7(a). Note that the voltage only considerably increases for detunings below 150 kHz. However, even with the HC significantly detuned, close to the first revolution harmonic at 578 kHz, the induced voltage can still reach 100 kV. Nevertheless, compared to the main rf voltage of $\hat{V}_{\mathrm{rf}} > 2\,\mathrm{MV}$, this induced voltage is low enough to not significantly modify the bunch distribution.

The bunch length and the Touschek lifetime improvement with the increment of HC voltage is presented in Fig. 3.7(b) and (c). The bunch length is computed as the second central moment of $\lambda(z)$ and the lifetime improvement by the ratio $\frac{\tau_{\mathrm{HC}}}{\tau_0} = \frac{\int \mathrm{d}z \lambda_0^2(z)}{\int \mathrm{d}z \lambda_{\mathrm{HC}}^2(z)}$, where τ_0 is the lifetime for the single-rf system. The HC provides significant bunch lengthening and lifetime improvement for voltages above 600 kV, i.e., about 75 % of the FP voltage, that is close to 800 kV.

Note that above 800 kV, the second moment σ_z continues to increase, while the lifetime factor reaches a maximum at approximately 850 kV. This occurs because, above the FP voltage, the bunches become overstretched, with a double-hump profile. In this case, the second central moment of the distribution is not a meaningful measure of bunch length, as the distribution is better represented by the combination of two Gaussian functions. On the other hand, since the lifetime factor depends on the integrated squared distribution, which is proportional to the bunch peak current, overstretched distributions can enhance the lifetime, until the two peaks begin to increase again. This behavior was

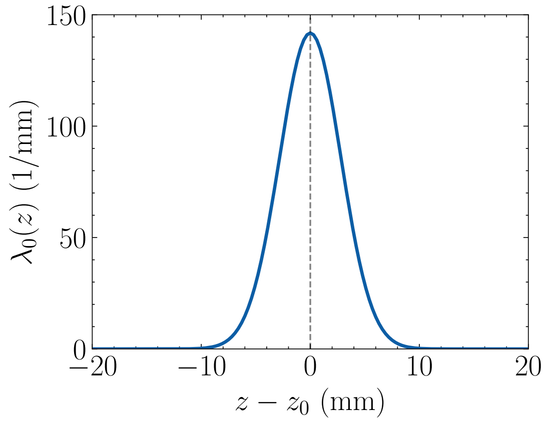

(a) Bunch distribution.

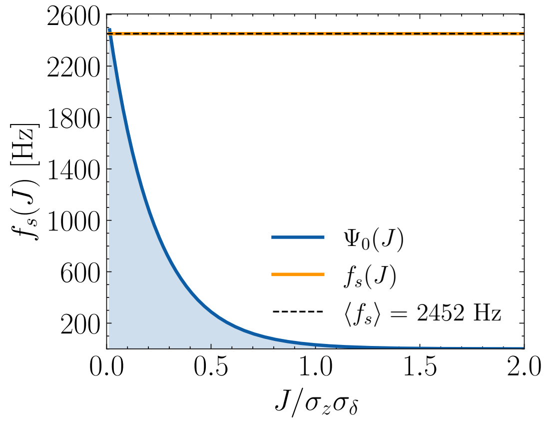

(b) Synchrotron frequency.

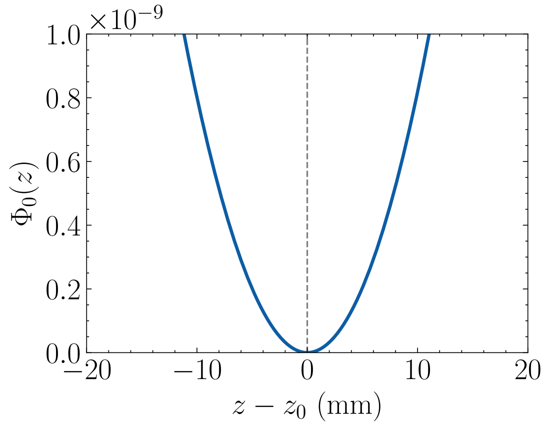

(c) Potential.

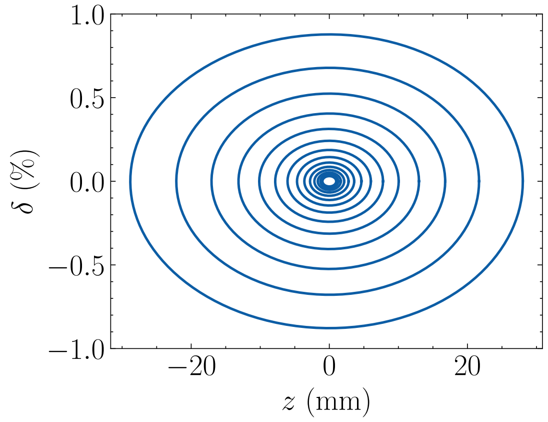

(d) Phase space.

Figure 3.6: Longitudinal distribution, potential, synchrotron frequency and phase space for the single-rf case with SIRIUS parameters. The flat-potential HC voltage is 798.4 kV. z_0 is the position where the potential is minimum.

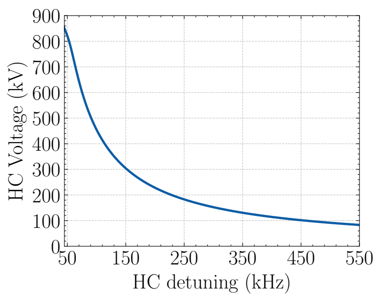

(a) Voltage vs. detuning.

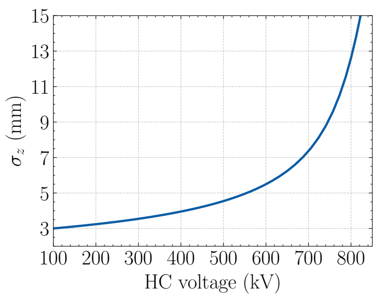

(b) Bunch length.

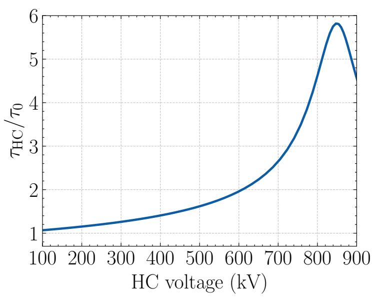

(c) Lifetime increase.

Figure 3.7: Relation between HC detuning and voltage, bunch length and Touschek lifetime improvement factor dependence on HC voltage.

obtained with the semi-analytical method in Appendix A and experimentally verified at MAX IV 1.5 GeV ring, as reported in Appendix C.

The bunch distributions and amplitude-dependent synchrotron frequency for different HC voltages are shown in Fig. 3.8. The average synchrotron frequency and the spread within the bunch were calculated with:

$$\langle f_s \rangle = 2\pi \int_0^\infty \mathrm{d}J f_s(J)\Psi_0(J), \tag{3.5}$$

$$\sigma_{f_s}^2 = 2\pi \int_0^\infty \mathrm{d}J \left(f_s(J) - \langle f_s \rangle\right)^2 \Psi_0(J). \tag{3.6}$$

We see in Fig. 3.8 that, up to 500 kV, the longitudinal parameters are fairly similar to a single-rf system, with Gaussian distributions, negligible frequency spread and the average synchrotron frequency is reduced from 2.4 kHz to 1.5 kHz. At the FP voltage, the bunch distribution become asymmetric, the synchrotron frequency dependence with action is non-monotonic, the frequency spread is enhanced to 100 Hz and the average frequency is 500 Hz.

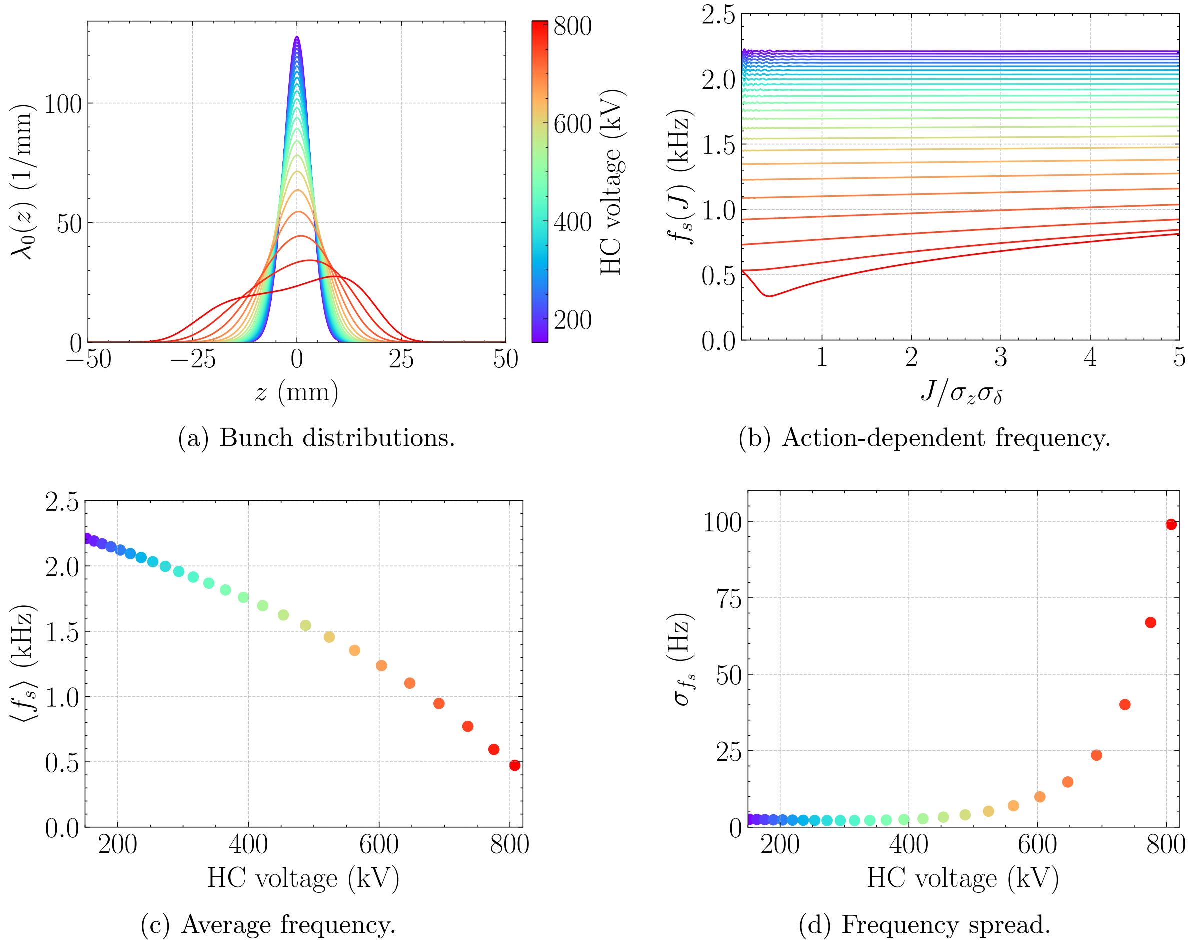

(a) Bunch distributions.

(b) Action-dependent frequency.

(c) Average frequency.

(d) Frequency spread.

Figure 3.8: Longitudinal distributions, amplitude-dependent synchrotron frequency with its average and spread, for different HC voltages. z_0 is the position where the potential is minimum.

The longitudinal parameters for the double-rf system at the FP settings are shown in Fig. 3.9 with more details. It is interesting to compare Fig. 3.9 with the results of single-rf system in Fig. 3.6. With the SINAP-3HC, the potential is asymmetric due to the phase error of the HC voltage—a known feature of SC HCs. This asymmetry implies that the synchrotron frequency dependence with action is non-monotonic[1]. For small actions, the frequency reduces with the amplitude of oscillation and only for higher actions the frequency scales with $f_s(J) \sim J^{1/3}$, as expected for the ideal quartic potential.

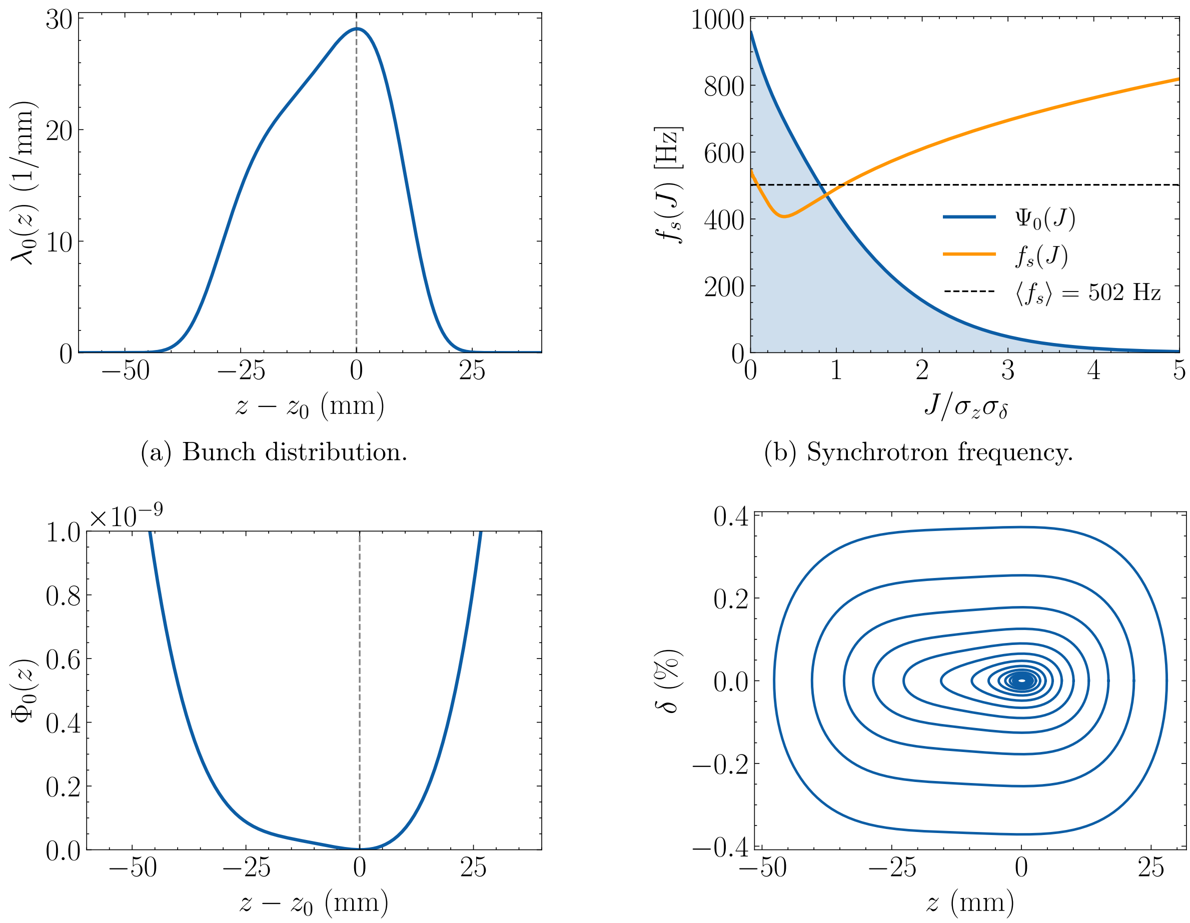

Figure 3.9: Longitudinal distribution, potential, synchrotron frequency and phase space for the double-rf case at flat-potential settings with SIRIUS parameters. z_0 is the position where the potential is minimum.

With the equilibrium solution for general conditions of the SINAP-3HC in uniform filling conditions, we have the bunch profiles, $\lambda_0(z)$, longitudinal potential $\Phi_0(z)$ and the canonical transformation $z(J, \varphi)$. With this, we can compute the action-dependent Hamiltonian $\mathcal{H}_0(J)$ and action distribution $\Psi_0(J)$, from which we can derive the action-dependent frequency $f_s(J)$. These are the main equilibrium parameters required as inputs for the calculation of collective instabilities in generic longitudinal potentials [45].

[1]In some cases, the minimum $\frac{\mathrm{d}f_s}{\mathrm{d}J} = 0$ might be related to instability issues, since particles with actions close to this minimum have similar frequencies and are susceptible to develop coherent motion. This issue is discussed in Ref. [26] but will not be addressed here.

3.4 Collective stability

3.4.1 Harmonic cavity-induced instabilities

Longitudinal coupled-bunch instabilities including the potential-well distortion effects from the 3HC can be evaluated with the semi-analytical methods presented in Ref. [45]. Two main concerning instabilities in a double-rf system were evaluated: the Robinson dipole-quadrupole mode-coupling and the PTBL/mode-1 instability. The results are presented in Fig. 3.10. For both cases, stable coherent frequencies were obtained for all the harmonic voltages. For details on each model, Lebedev, effective $\omega_s(\sigma_z)$ and Gaussian LMCI, see Appendix B (Ref. [45]).

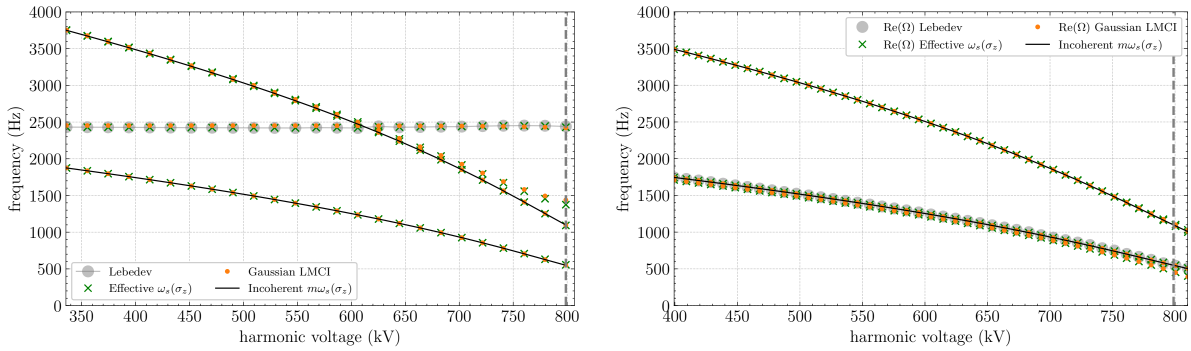

(a) $\ell = 0$. (b) $\ell = 1$.

Figure 3.10: Coherent frequencies of coupled-bunch modes ℓ with the harmonic voltage. SIRIUS parameters with $U_0 = 675\,\mathrm{keV}$, $\hat{V}_{\mathrm{rf}} = 2.5\,\mathrm{MV}$. All conditions are stable, with growth rates $\mathrm{Im}(\Omega) < 0.1\,\mathrm{Hz}$ while the longitudinal radiation damping rate is $\tau_\delta^{-1} = 77.5\,\mathrm{Hz}$.

For the coupled-bunch $\ell = 0$, the quadrupole mode crosses with the dipole mode, but they do not couple to drive an instability. For the coupled-bunch $\ell = 1$, the coherent shift with respect to the incoherent frequency reduction is essentially absent. Thus, the coherent frequency is not shifted towards zero and the PTBL instability is not triggered. As calculated previously, the PTBL threshold for SIRIUS is $(R/Q)_{\mathrm{threshold}} \approx 200\,\Omega$, thus the $(R/Q) = 87.5\,\Omega$ of the SINAP-3HC is more than two times lower than the threshold.

3.4.2 Mitigation of instabilities

After the rf system upgrade with the installation of two SC main rf cavities on SIRIUS storage ring, longitudinal coupled-bunch instabilities were observed, starting from the total beam current of 90 mA. The bunch-by-bunch feedback system was necessary to accumulate a stable 200 mA beam.

The growth rates of all coupled-bunch modes were measured below the instability threshold, at 80 mA, with the growth-damp functionality of the Dimtel bunch-by-bunch system [96]. Many coupled-bunch modes, from 450 to 650, displayed high growth rates, with resonant peaks that could be distinguished. This feature indicates that this instability might be related to several narrowband impedance contributions distributed over the ring. According to previous simulations reported in Ref. [97], the gate valves could be the source of such impedances, with the main eigenmode resonant frequency close to 8 GHz. Based on this, the shunt impedance and the quality factor of 13 resonators were fitted, using the difference of the calculated growth rates to the measured ones as the penalty parameter for optimization. For these calculations, we considered the methods available in `pycolleff` for single-rf systems and Gaussian bunches [98]. The resonant frequencies of the resonators were fixed by the frequency of 13 most prominent coupled-bunch modes, with the addition of the closest rf harmonic to 8 GHz. The fitted parameters were on the order of $R_s \approx 5\,\mathrm{k\Omega}$ and $Q \approx 1 \times 10^3$. These values are compatible with electromagnetic simulations for the gate valves [97]. The results are presented in Fig. 3.11(a).

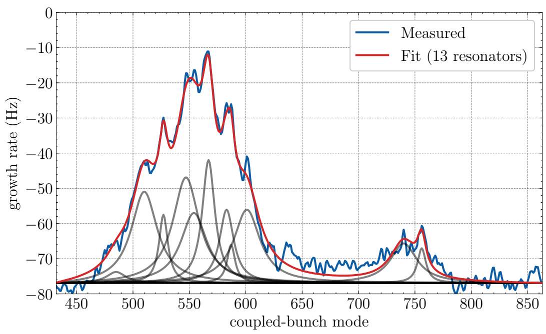

(a) Measured and fitted growth rates. The contribution from each resonator is shown as black curves.

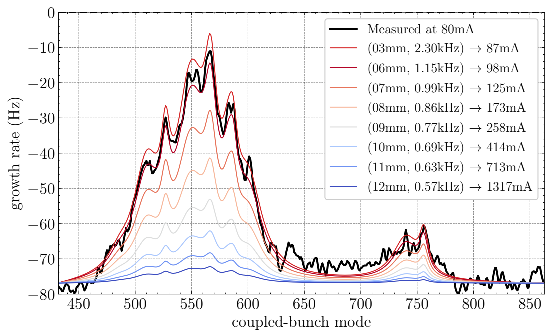

(b) Growth rates depending on the bunch length and average synchrotron frequency. The legend indicates the threshold current when the rates would be positive.

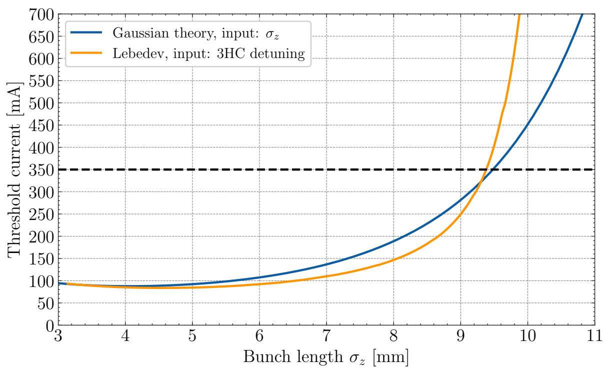

(c) Threshold current improvement with the bunch length computed with the Gaussian theory and Lebedev equation. The horizontal dashed line represents the design current of 350 mA.

Figure 3.11: Coupled-bunch growth rates measured at SIRIUS and dependence with bunch lengthening.

The impact of bunch lengthening induced by the 3HC on this longitudinal instability was estimated using a simplified model. We approximated the 3HC effect by increasing the bunch length and reducing the average synchrotron frequency. Given the reasonable accuracy of the Gaussian LMCI model described in Ref. [45], this approximation is expected to provide a sufficiently reliable estimate of growth rates for these instabilities. The relation $\sigma_z\omega_s = \alpha c\sigma_\delta$ was used to link the bunch length and synchrotron frequency ω_s, assuming fixed values for α and σ_δ. As shown in Fig. 3.11(b), the growth rates decrease significantly as the bunch length increases. This behavior results from the reduction of high-frequency components in the beam spectral power as the bunch becomes longer. Consequently, this reduces the beam-coupling to high-frequency impedances, such as the simulated gate valves around 8 GHz.

The threshold current dependence on the bunch length is presented in Fig. 3.11(c). The results from the simplified Gaussian theory, where the bunch length σ_z is an input parameter, are shown alongside those from the Lebedev equation. In this more general approach, we selected the coupled-bunch mode with the highest growth rate ($\ell = 567$) and used the 3HC detuning frequency as an input parameter, thereby obtaining the equilibrium parameters self-consistently. The difference between the dependencies obtained from each calculation arises from the non-Gaussian bunches and the nonlinearities introduced by the 3HC, which are included in the Lebedev equation but not captured by the simplified theory. Nevertheless, the results indicate that a 10 mm bunch length, provided by the 3HC, would enable stable operation at 350 mA without longitudinal feedback.

3.5 Hybrid filling pattern and guard bunches

Some SIRIUS beamlines have a scientific interest in time-resolved experiments, where the radiation from a single bunch must be isolated from the multibunch train. Running these experiments in parallel with multibunch users requires a hybrid filling pattern. A review of key timing-mode specifications in synchrotrons is provided in the thesis [99].

The bunch spacing for SIRIUS is 2 ns, and with the current technology, this timescale is too short for a mechanical device (for example, a beam chopper) to allow the propagation of the signal from just one bunch and block the radiation from the other bunches. It is therefore necessary to have a gap between the isolated bunch and the multibunch train, to allow sufficient time for the mechanism of the beamlines to block the radiation from the multibunch train and rapidly stop the blockage to use the radiation from the isolated bunch. However, with a passive HC, gaps in the filling pattern introduce inhomogeneous beam loading, leading to significant variations in the bunch distributions and reduced bunch lengthening performance.

We tested a hybrid filling pattern with 25 empty buckets before and after the isolated bunch. This gap corresponds to 50 ns of dark time before and after the radiation pulse of the isolated bunch. We considered that the isolated bunch have 2 mA of current, which corresponds to 3.5 pC of charge. The current of 348 mA should be distributed on the other 814 buckets to keep the total current of 350 mA. If this current is distributed evenly over the buckets, the inhomogeneous beam-loading reduces considerably the bunch lengthening performance of the 3HC, as shown in Fig. 3.12(a). In this case, the effect of the gap is not compensated. A strategy to mitigate the inhomogeneous beam loading caused by the

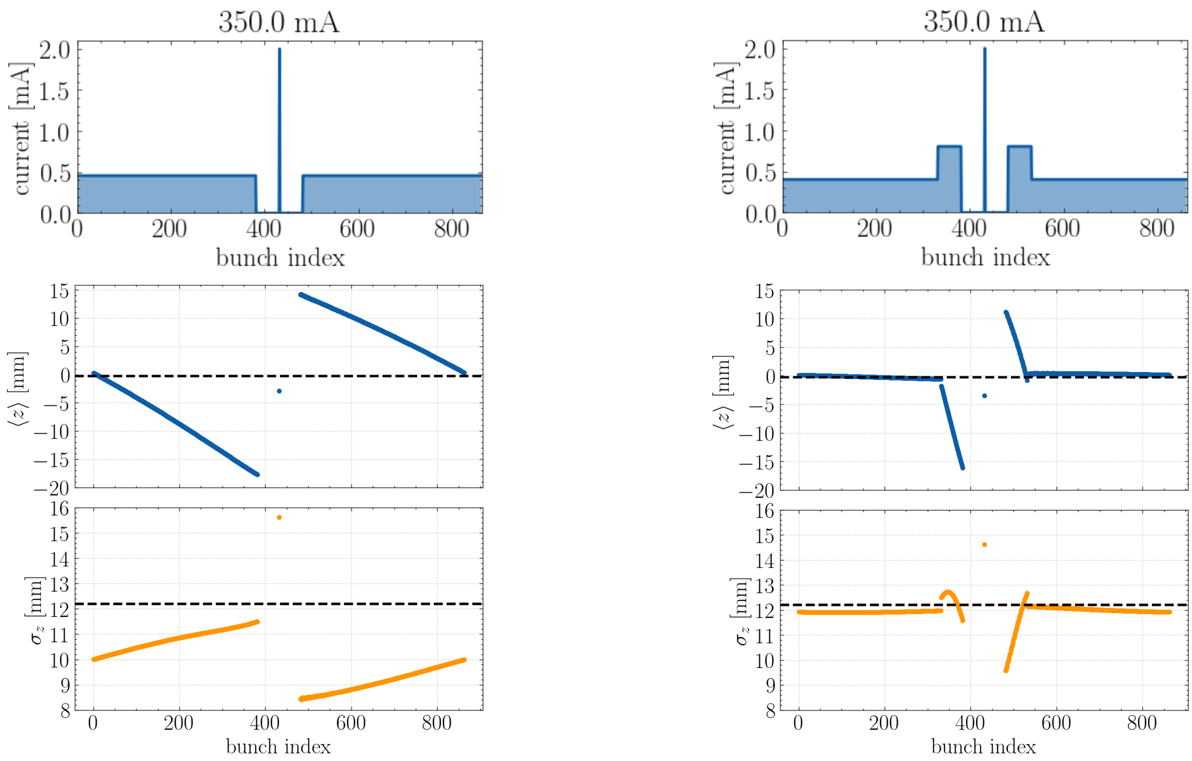

(a) No compensation.

(b) Guard bunches compensation.

Figure 3.12: Inhomogeneous beam loading with 3HC at flat potential detuning, with and without compensation with guard bunches.

gap is to populate nearby buckets with higher current, creating guard bunches [23, 76]. Figure 3.12(b) illustrates this compensation: instead of distributing the missing gap current evenly across all 814 buckets, 25 buckets before and after the gaps were filled with twice the current of the remaining 764 buckets. This approach localizes the bunch lengthening degradation to the 50 guard bunches, while the bunch distributions in the multibunch train remain nearly identical to those in a uniform filling pattern

Fine-tuning of the hybrid filling requirements and the corresponding guard bunch compensation should be done along with discussions with the time-resolved beamlines, in order to guarantee good bunch lengthening performance of the 3HC.

3.6 Frequency detuning control

In passive cavities, the voltage is controlled by the detuning frequency. Therefore, the specifications for the stability of harmonic voltage relies on the stability of the frequency tuning system. A convenient approximate relation between the peak harmonic voltage and the detuning frequency is given by:

$$\hat{V}_{\mathrm{HC}} \approx I_0|F|(R/Q)\frac{3f_{\mathrm{rf}}}{\Delta f}, \tag{3.7}$$

where we considered the 3HC case, $\Delta f = f_{\mathrm{r}} - 3f_{\mathrm{rf}}$ is the detuning frequency and $|F|$ the absolute value of the bunch-form factor evaluated at $3f_{\mathrm{rf}}$. Considering $I_0|F|(R/Q)$ independent of the cavity detuning, the relative variations of harmonic voltage and detuning are simply related by $\delta(\hat{V}_{\mathrm{HC}})/\hat{V}_{\mathrm{HC}} \approx -\delta(\Delta f)/\Delta f$. However, specially close to the FP condition, the bunch-form factor changes significantly with the detuning frequency. This implies that the relation between harmonic voltage and detuning frequency becomes nonlinear. Figure 3.13(a) illustrate this dependence. For the case of SIRIUS, the

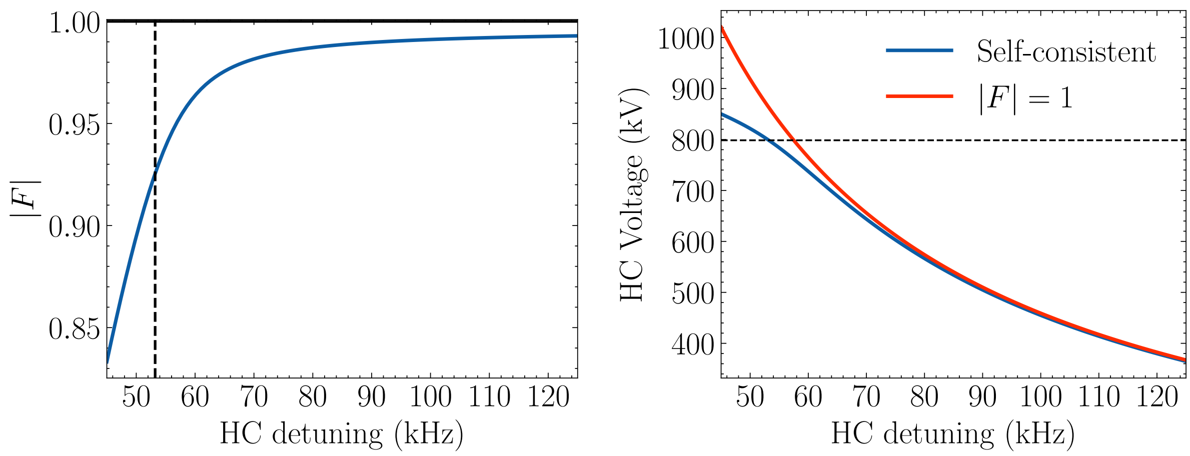

(a) Form-factor vs. detuning.

(b) Harmonic voltage with and without the form-factor dependence.

Figure 3.13: The dependence of the bunch form factor and peak harmonic voltage with the detuning frequency.

nonlinearity between the harmonic voltage and detuning frequency implies that, around the FP condition, 1 % of variation in the harmonic voltage corresponds to 2 % of variation in the detuning frequency and 6 % of variations in the bunch length and Touschek lifetime. To maintain the bunch length and lifetime controlled within 1 %, we must specify that the tuning frequency system should have a stability better than 0.4 %, which in turn would provide a voltage stability better than 0.2 %. The variations of SIRIUS bunch distributions for two different relative variations of the harmonic voltage are shown in Fig. 3.14. Considering that the 3HC detuning frequency to provide the FP for SIRIUS is close to 50 kHz, the relative stability requirement of 0.4 % implies in absolute stability within 100 Hz. As reported in Refs. [100, 101], the fine-tuning precision of the tuner system for the SINAP-3HC is 10 Hz, sufficient to meet the stability requirements for SIRIUS.

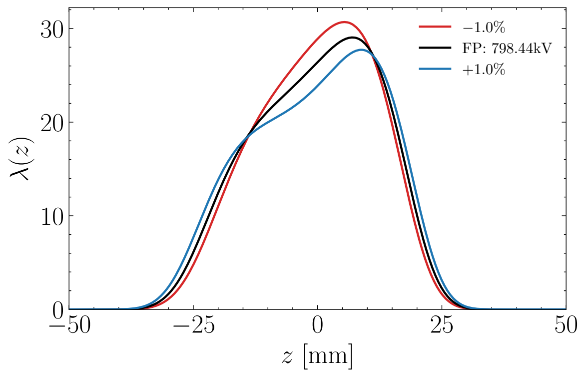

(a) 1 % voltage stability.

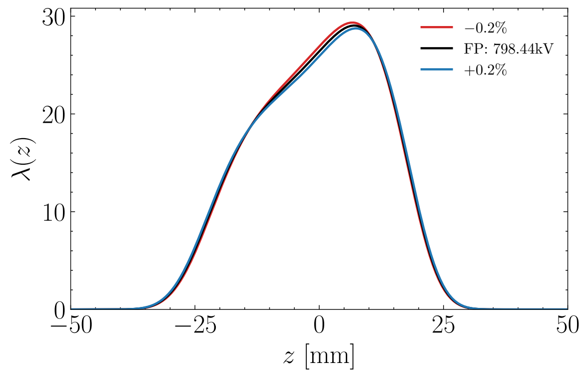

(b) 0.2 % voltage stability.

Figure 3.14: Comparison of bunch distribution for different relative variations of harmonic voltage. Uniform filling case.

3.7 Mapping operation points

In 2-cell cavities, two resonant modes, referred to as 0-mode and π-mode, have the highest values of shunt impedance. The phase relation between the longitudinal electric fields for each of these modes is represented in Fig. 3.15(a). The cavity is optimized for operation in the π-mode. The high impedance of the 0-mode can be regarded as a higher order mode (HOM) of the cavity that can potentially couple with the beam and drive some longitudinal coupled-bunch instability.

The design of the SINAP 3HC was optimized so the (R/Q) of the 0-mode could be minimized to $(R/Q)_0 = 0.1\,\Omega$, while the value for π-mode is $(R/Q)_\pi = 87.5\,\Omega$ [100, 102]. Even so, as the cavity is superconducting and the Q value is high, the estimated shunt impedance 0-mode would be above the threshold for longitudinal coupled-bunch instabilities for SIRIUS, as shown in Fig. 3.15(b). The resonant frequencies of the two modes are separated by $f_\pi - f_0 = 34.5\,\text{MHz}$. Therefore, the possibility of the impedance 0-mode matching with some coupled-bunch mode was a point of attention.

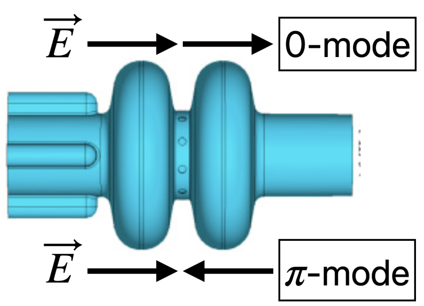

(a) Longitudinal electric fields phase relation.

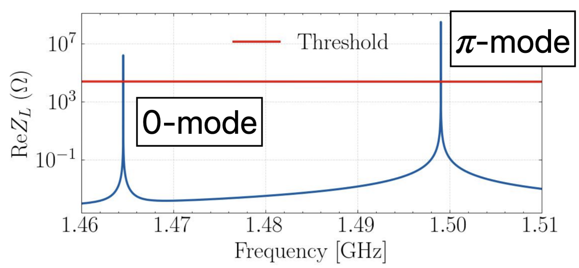

(b) Real impedance of the 0-mode and π-mode compared with SIRIUS impedance threshold for longitudinal coupled-bunch instabilities.

Figure 3.15: Electric fields relation and real impedance of two resonant modes in a 2-cell cavity.

Given their high quality factor, both 0-mode and π-mode impedances have a very narrow bandwidth. This implies that a small variation in the resonant frequency is sufficient to significantly modify the impedance sampled by the beam. As the detuning mechanism modifies the resonant frequency of the π-mode to control the induced harmonic voltage, it is expected that the resonance of the 0-mode is modified by approximately the same frequency shift. Thus, if for some detuning condition the 0-mode happens to drive some instability, small changes in the detuning would be sufficient to shift the 0-mode impedance and to modify its coupling with the beam. To support this strategy, the bunch lengthening performance of the 3HC with different detunings should be evaluated.

The flattening of the rf voltage depends on the ratio between the harmonic and main rf voltages. If the main rf voltage is modified, the harmonic voltage required to produce the FP condition will be different as well. For passive cavities, assuming the same beam current, different voltage means different detunings. Therefore, with this strategy it is possible to obtain similar bunch distributions with different conditions of main rf voltage, cavity detuning and harmonic voltage. The mapping of the performance on the bunch-length and Touschek lifetime for different main rf voltages and 3HC conditions are presented in Fig. 3.16. Obtaining this map in a fine grid with a negligible computational time ($\sim 1\,\text{min}$) was only possible due to the low computational load of the semi-analytical method developed to solve the equilibrium bunch distributions.

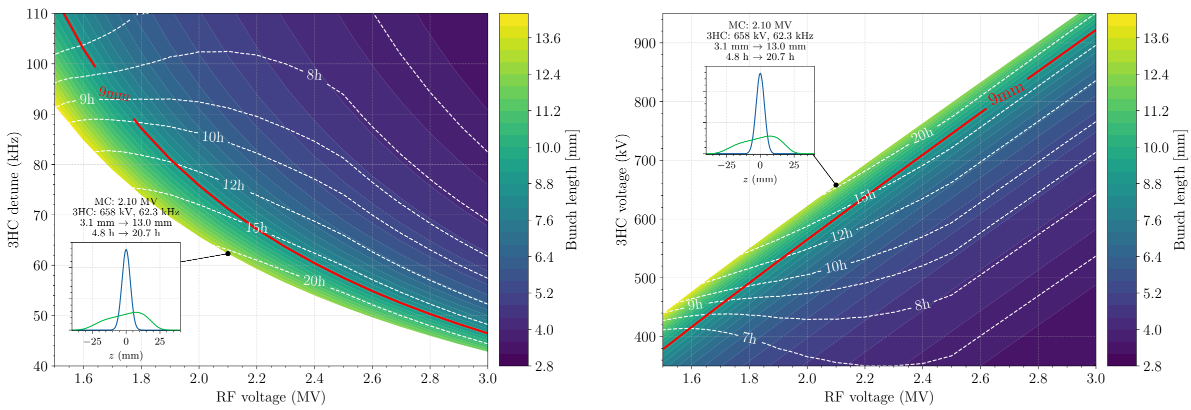

(a) Detuning frequency. (b) Harmonic voltage.

Figure 3.16: Mapping of bunch length and Touschek lifetime for different rf voltages, 3HC detunings and corresponding harmonic voltage.

3.8 Conclusions

In this chapter, we explored the implementation of a 3HC in SIRIUS for bunch lengthening and to improve beam stability for Phase II of operation at 350 mA. An initial evaluation of normal-conducting cavities revealed that, to provide the necessary harmonic voltage, a larger number of cavities would be required, leading to a high total (R/Q) factor. This poses a risk for coupled-bunch instabilities, challenging stable operation at high beam currents. In contrast, a superconducting cavity, such as the SINAP-3HC, offer a lower (R/Q) factor, reducing the risk of instabilities while efficiently delivering the harmonic voltage needed for bunch lengthening.

We investigated hybrid filling patterns for time-resolved experiments in parallel with multibunch users. The inhomogeneous beam loading caused by gaps in the filling pattern considerably reduces the bunch lengthening performance of the 3HC. However, the use of guard bunches can effectively mitigate this effect, keeping the multibunch train distributions similar to the one achieved with a uniform filling pattern. Fine-tuning of this approach will require collaboration with the beamlines to meet their requirements while achieving sufficient bunch lengthening performance with the 3HC.

We evaluated the sensitivity of the harmonic voltage to frequency detuning, particularly near the FP condition. The nonlinear relation between detuning and voltage stability was quantified, emphasizing the importance of precise frequency control to maintain stable bunch length and lifetime. The analysis showed that frequency stability better than 0.4% and voltage better than 0.2% are required to limit bunch length and lifetime variations within 1%. The fine-tuning capabilities of the SINAP-3HC tuner system meet this requirement.

Additionally, we investigated the potential instability induced by the unwanted 0-mode of the 2-cell cavity. While its peak shunt impedance is above the threshold for instability, we propose that small detuning adjustments could mitigate the issue by shifting the mode's resonant frequency away from exciting coupled-bunch modes. A mapping of bunch lengthening performance for different main rf voltages and 3HC conditions supported the feasibility of this strategy. The computational speed provided by the semi-analytical method developed in this work proved to be very helpful, since it enabled large parameter scans with negligible computational time.

Implementing a passive 3HC for bunch lengthening will be necessary for operation with 350 mA in the Phase II of SIRIUS. The choice of the superconducting SINAP-3HC model is well-supported by its better performance in providing stable bunch lengthening while minimizing instability issues. The SIRIUS cryogenic infrastructure already supports the superconducting 3HC. After the 3HC installation, experimental studies will be essential to ensure reliable operation with higher beam currents in the Phase II of SIRIUS.

The best that most of us can hope to achieve in physics is simply to misunderstand at a deeper level.

— Wolfgang Pauli

4 Summary and conclusions

This thesis has presented advancements in the study of longitudinal collective effects in synchrotron storage rings, with a particular focus on double-rf systems with passive harmonic cavities. The main contributions addressed two key topics: calculating the self-consistent equilibrium state of the electron beam and evaluating thresholds for collective instabilities. The novel semi-analytical frameworks introduced in this thesis are detailed in Appendices A (Ref. [44]) and B (Ref. [45]).

In Appendix A, two approaches were developed to calculate the beam-induced voltage for arbitrary filling patterns: the space- and frequency-domain methods. The space-domain approach, based on wake functions, extended previous works [76–78] by employing a compact notation and a general resonator expression, beyond the high-Q approximation. However, its dependence on a resonator model can limit its application to broadband impedances. The frequency-domain approach, introduced as a novel contribution of this thesis, overcomes this limitation by allowing for generic impedance models. This framework efficiently handles both broadband and narrowband resonators and takes advantage of FFT algorithms to significantly speed up some computation steps. Additionally, it enables more general modeling of rf feedback systems in active cavities. The developed expressions for the beam-induced voltage were used to solve the Haïssinski equation self-consistently using a robust fixed-point algorithm. The equivalence of the space- and frequency-domain methods was demonstrated using SIRIUS storage ring parameters and machine impedance budget, including a model of a superconducting third harmonic cavity. The advantages of the semi-analytical methods were further validated through comparisons with macroparticle simulations, achieving excellent agreement at a fraction of the computational cost. Moreover, the equilibrium solver was successfully benchmarked against experimental data from the MAX IV 1.5 GeV ring, where measured and simulated bunch profiles were compared under overstretched conditions with the goal of optimizing the Touschek lifetime. These results are detailed in Appendix C (Ref. [46]).

As the next step to solving the equilibrium state as discussed in Appendix A, Appendix B focused on the dynamic coherent effects to assess beam stability. A general theory for coupled-bunch longitudinal instabilities was developed, accounting for potential-well distortion and multiple azimuthal modes. Starting from the linearized Vlasov equation, the generalized Sacherer integral equation was derived, leading to the Lebedev equation. The relationship between this framework and Venturini's approach [82] was established, highlighting the computational efficiency of the former. Dispersion relations for a narrow-band resonator model, applicable to arbitrary rf potentials and azimuthal modes, were derived from the Lebedev equation. These results recovered dipole [81] and quadrupole [85] instabilities as specific cases. The developed framework was employed to compute coherent frequencies and growth rates for the Robinson dipole-quadrupole instability, yielding good agreement with measured coherent frequencies at the MAX IV 3.0 GeV ring. Furthermore, the measured thresholds for the PTBL/mode-1 instability at MAX IV were successfully reproduced. A novel explanation for the mode-1 instability as a zero-frequency mechanism was proposed, explaining its dependence on parameters such as rf voltage, cavity (R/Q), and radiation damping. It was demonstrated that Landau damping has negligible influence on this low-frequency instability, whereas contributions from multiple azimuthal modes are key for accurate predictions of PTBL thresholds. An approximate formula for the threshold was derived, showing its dependence on the product of the cavity (R/Q) and beam current, consistent with scaling laws from previous studies.

In Chapter 3, the developed methods were applied to analyze the effects of a superconducting third harmonic cavity on the SIRIUS storage ring. This study was aimed at supporting the Phase II operation of SIRIUS, which targets a design current of 350 mA. By applying the semi-analytical frameworks for equilibrium and instability analysis developed in this thesis, we evaluated the impact of the third harmonic cavity on beam dynamics, including bunch lengthening performance and stability at high beam currents. The methods allowed us to quantify the potential improvements in beam stability and optimize the cavity's design to achieve efficient bunch lengthening while minimizing risks of coupled-bunch instabilities. The results from this analysis are expected to be fundamental in supporting the commissioning of the third harmonic cavity, ensuring its effective integration into the SIRIUS storage ring. Moreover, the insights gained from this study are anticipated to facilitate various aspects of accelerator studies and operations during Phase II of SIRIUS, helping to optimize beam quality for both time-resolved and multibunch experiments. This work, still in progress, aims to refine operational strategies and provide experimental validation of the theoretical predictions made in the analysis.

In addition to theoretical developments, the computational tools were implemented in the open-source package `pycolleff` [98]. Some functionalities of `pycolleff` were also integrated in the open-source package `ALBuMS` [84]. These tools offer efficient methods for evaluating equilibrium parameters and longitudinal instabilities in modern storage ring designs with double-rf systems, contributing to the development of fourth-generation synchrotrons. The contributions were directly applied to SIRIUS, MAX IV [46], and the SOLEIL II project [103].

Despite these advancements, this thesis is still far from a complete description of the effects of harmonic cavities on electron beam dynamics in synchrotrons. For instance, the impact of harmonic cavities on transverse instabilities was not addressed. Previous studies have investigated the influence of nonlinear longitudinal motion on transverse dynamics [80, 104, 105], demonstrating that harmonic cavities can help to stabilize transverse instabilities as well. Similarly, the impact of modified rf potentials on single-bunch longitudinal instabilities, such as microwave instabilities, was not evaluated. Nevertheless, it is generally understood that longer bunches have higher thresholds for such high-frequency instabilities. The instability calculation framework based on the Lebedev equation is quite general; however, evaluating the impact of broadband impedances, which contribute with many harmonics, might be computationally challenging due to the increased matrix size involved. Investigating methods to deal with these numerical issues could be a subsequent research topic to further expand the applicability of the developed framework. Regarding the PTBL/mode-1 instability, considering its zero-frequency nature and the demonstrated ineffectiveness of resistive feedback systems, testing reactive feedback systems may reveal an effective control strategy with current technology.

After the installation of the third harmonic cavity on SIRIUS storage ring, its commissioning and accelerator studies will provide the opportunity to validate the developed frameworks experimentally. In addition to SIRIUS, the methods developed in this thesis can support future studies on double-rf systems in other synchrotron facilities.

References

[1] Jackson, J. *Classical Electrodynamics* (Wiley, 2021). URL https://books.google.com.br/books?id=6VV-EAAAQBAJ.

[2] Eriksson, M., van der Veen, J. F. & Quitmann, C. Diffraction-limited storage rings – a window to the science of tomorrow. *Journal of Synchrotron Radiation* **21**, 837–842 (2014). URL https://doi.org/10.1107/S1600577514019286.

[3] Liu, L. & Jr, H. W. Towards Diffraction Limited Storage Ring Based Light Sources. In *Proc. IPAC'17*, 1203–1208 (JACoW Publishing, Geneva, Switzerland, 2017). URL https://jacow.org/ipac2017/papers/TUXA1.pdf.

[4] Raimondi, P. & Liuzzo, S. M. Toward a diffraction limited light source. *Phys. Rev. Accel. Beams* **26**, 021601 (2023). URL https://link.aps.org/doi/10.1103/PhysRevAccelBeams.26.021601.

[5] Picoreti, R. & Jr., H. W. Sirius facility update. *Synchrotron Radiation News* **34**, 12–13 (2021). URL https://doi.org/10.1080/08940886.2021.1902713.

[6] Tolentino, H. C. N. *et al.* CARNAÚBA: The coherent x-ray nanoprobe beamline for the Brazilian synchrotron SIRIUS/LNLS. *Journal of Physics: Conference Series* **849**, 012057 (2017). URL https://dx.doi.org/10.1088/1742-6596/849/1/012057.

[7] Meyer, B. C. *et al.* An approach for the optical and mechanical design of an X-ray beamline: application to the plane-wave CDI station CATERETÊ/SIRIUS. *Journal of Physics: Conference Series* **2380**, 012069 (2022). URL https://dx.doi.org/10.1088/1742-6596/2380/1/012069.

[8] Archilha, N. L. *et al.* MOGNO, the nano and microtomography beamline at Sirius, the Brazilian synchrotron light source. *Journal of Physics: Conference Series* **2380**, 012123 (2022). URL https://dx.doi.org/10.1088/1742-6596/2380/1/012123.

[9] Estrada, F. R. *et al.* PAINEIRA beamline at Sirius: an automated facility for polycrystalline XRD characterization. *Journal of Physics: Conference Series* **2380**, 012033 (2022). URL https://dx.doi.org/10.1088/1742-6596/2380/1/012033.

[10] Santos, T. M. *et al.* Synchrotron infrared nanospectroscopy in fourth-generation storage rings. *Journal of Synchrotron Radiation* **31**, 547–556 (2024). URL https://doi.org/10.1107/S1600577524002364.

[11] Tolentino, H. C. *et al.* The CARNAÚBA X-ray nanospectroscopy beamline at the SIRIUS-LNLS synchrotron light source: Developments, commissioning, and first science at the TARUMÃ station. *Journal of Electron Spectroscopy and Related Phenomena* **266**, 147340 (2023). URL https://www.sciencedirect.com/science/article/pii/S0368204823000579.

[12] Hettel, R. O. & Borland, M. Perspectives and Challenges for Diffraction-Limited Storage Ring Light Sources. In *Proc. NAPAC'13*, 19–23 (JACoW Publishing, Geneva, Switzerland, 2013). URL https://jacow.org/PAC2013/papers/MOYAB1.pdf.

[13] Hettel, R. O. Challenges in the Design of Diffraction-limited Storage Rings. In *Proc. IPAC'14*, 7–11 (JACoW Publishing, Geneva, Switzerland, 2014). URL https://jacow.org/IPAC2014/papers/MOXBA01.pdf.

[14] Borland, M. *et al.* Lattice design challenges for fourth-generation storage-ring light sources. *Journal of Synchrotron Radiation* **21**, 912–936 (2014). URL https://doi.org/10.1107/S1600577514015203.

[15] Neuenschwander, R. T., Liu, L., Marques, S. R., Rodrigues, A. R. D. & Seraphim, R. M. Engineering Challenges of Future Light Sources. In *Proc. IPAC'15*, 1308–1313 (JACoW Publishing, Geneva, Switzerland, 2015). URL https://jacow.org/IPAC2015/papers/TUXC2.pdf.

[16] Nagaoka, R. & Bane, K. L. F. Collective effects in a diffraction-limited storage ring. *Journal of Synchrotron Radiation* **21**, 937–960 (2014). URL https://doi.org/10.1107/S1600577514015215.

[17] Sakanaka, S., Izawa, M., Mitsuhashi, T. & Takahashi, T. Improvement in the beam lifetime by means of an rf phase modulation at the KEK photon factory storage ring. *Phys. Rev. ST Accel. Beams* **3**, 050701 (2000). URL https://link.aps.org/doi/10.1103/PhysRevSTAB.3.050701.

[18] Abreu, N. P., Farias, R. H. A. & Tavares, P. F. Longitudinal dynamics with rf phase modulation in the Brazilian electron storage ring. *Phys. Rev. ST Accel. Beams* **9**, 124401 (2006). URL https://link.aps.org/doi/10.1103/PhysRevSTAB.9.124401.

[19] Ng, K.-Y. Passive Landau cavity for the LNLS light source electron ring. *FERMILAB-FN-0696* (2000).

[20] Mosnier, A. Cures of Coupled Bunch Instabilities. *18th Biennial Particle Accelerator Conference* (1999). URL https://cds.cern.ch/record/553141.

[21] Bosch, R. A. & Hsue, C. S. Suppression of longitudinal coupled-bunch instabilities by a passive higher harmonic cavity. In *Proceedings of International Conference on Particle Accelerators*, 3369–3371 (IEEE, 1993). URL https://ieeexplore.ieee.org/abstract/document/309653/.

[22] Byrd, J. *et al.* Commissioning of a higher harmonic rf system for the advanced light source. *Nuclear Instruments and Methods in Physics Research Section A: Accelerators, Spectrometers, Detectors and Associated Equipment* **455**, 271–282 (2000). URL https://www.sciencedirect.com/science/article/pii/S0168900200005040.

[23] Byrd, J. M. & Georgsson, M. Lifetime increase using passive harmonic cavities in synchrotron light sources. *Phys. Rev. ST Accel. Beams* **4**, 030701 (2001). URL https://link.aps.org/doi/10.1103/PhysRevSTAB.4.030701.

[24] Shaposhnikova, E. N. Cures for beam instabilities in the CERN SPS and their limitations. In *Proc. HB'06*, 153–155 (JACoW Publishing, Geneva, Switzerland, 2006). URL https://jacow.org/abdwhb06/papers/TUBX05.pdf.

[25] Linnecar, T. P. R. & Shaposhnikova, E. N. Analysis of the voltage programs for the PPbar double frequency rf system. Tech. Rep., CERN, Geneva (1992). URL https://cds.cern.ch/record/703261.

[26] Shaposhnikova, E. N. Bunched beam transfer matrices in single and double rf systems. *Technical Report No. CERN-SL-94-19-rf* (1994).

[27] Bohl, T., Linnecar, T. P. R., Shaposhnikova, E. & Tückmantel, J. Study of Different Operating Modes of the 4th rf Harmonic Landau Damping System in the CERN SPS. *CERN-SL-98-026-RF* (1998). URL https://cds.cern.ch/record/360139.

[28] Hereward, H. G. *The elementary theory of Landau damping*. CERN Yellow Reports: Monographs (CERN, Geneva, 1965). URL http://cds.cern.ch/record/276334.

[29] Hofmann, A. Landau damping. *CAS - CERN Accelerator School: Intermediate Accelerator Physics* (2006). URL https://cds.cern.ch/record/941315.

[30] Herr, W. Introduction to Landau damping (2014). URL https://cds.cern.ch/record/1982428.

[31] Georgsson, M., Andersson, A. & Eriksson, M. Landau cavities at MAX II. *Nucl. Instrum. Meth. A* **416**, 465–474 (1998).

[32] Georgsson, M. Landau cavities in third generation synchrotron light sources. In *PACS2001. Proceedings of the 2001 Particle Accelerator Conference (Cat. No.01CH37268)*, vol. 4, 2689–2691 vol.4 (2001).

[33] Cullinan, F., Andersson, A. & Tavares, P. Longitudinal Stability with Landau Cavities at MAX IV. In *Proc. IPAC'20*, 44–48 (Caen, France, 2020). URL https://doi.org/10.18429/JACoW-IPAC2020-WEVIR05.

[34] Cullinan, F., Andersson, A. & Tavares, P. Review of Harmonic Cavities in Fourth-generation Storage Rings. *JACoW* **FLS2023**, MO2L3 (2024).

[35] Perez, F. *et al.* Active harmonic eu cavity: Commissioning and operation with beam. *Nuclear Instruments and Methods in Physics Research Section A: Accelerators, Spectrometers, Detectors and Associated Equipment* **1072**, 170195 (2025). URL https://www.sciencedirect.com/science/article/pii/S0168900224011215.

[36] Wu, C.-F. *et al.* The 4th Harmonic Cavity for Hefei Light Source-II. In *Proc. IPAC'16*, no. 7 in International Particle Accelerator Conference, 837–839 (JACoW Publishing, Geneva, Switzerland, 2016). URL https://jacow.org/ipac2016/papers/MOPOW054.pdf.

[37] D'Elia, A., Jacob, J., Serriere, V. & Zhu, X. W. Design of 4th Harmonic rf Cavities for ESRF-EBS. In *Proc. IPAC'21*, 1031–1033 (JACoW Publishing, Geneva, Switzerland, 2021). URL https://jacow.org/ipac2021/papers/MOPAB332.pdf.

[38] Gamelin, A., Foosang, W., Marchand, P., Nagaoka, R. & Yamamoto, N. Beam Dynamics with a Superconducting Harmonic Cavity for the SOLEIL Upgrade. In *Proc. IPAC'22*, no. 13 in IPAC'22 - 14th International Particle Accelerator Conference, 2229–2232 (JACoW Publishing, Geneva, Switzerland, 2022). URL https://jacow.org/ipac2022/papers/wepoms003.pdf.

[39] Tsakanian, A. Development of the 3.5rd harmonic cavities at HZB. In *HarmonLIP 2024* (2024). URL https://indico.esrf.fr/event/122/contributions/678/attachments/384/767/HarmonLIP2024_Tsakanian.pdf.

[40] Liu, L., Resende, X. R., Rodrigues, A. R. D., Sá, F. H. & Westfahl, H. Sirius: A 5BA low-emittance lattice with superbends for the new Brazilian synchrotron light source. *Synchrotron Radiation News* **26**, 34–38 (2013). URL https://doi.org/10.1080/08940886.2013.791215.

[41] Liu, L., Milas, N., Mukai, A. H. C., Resende, X. R. & de Sá, F. H. The SIRIUS project. *Journal of Synchrotron Radiation* **21**, 904–911 (2014). URL https://doi.org/10.1107/S1600577514011928.

[42] de Sá, F. *et al.* Broadband impedance induced heating proxy for operation at higher total current at SIRIUS. In *Proc. IPAC'24*, 3090–3093 (Nashville, TN, USA, 2024).

[43] de Sá, F. H. *Study of impedances and collective instabilities applied to Sirius*. Ph.D. thesis, Universidade Estadual de Campinas, Campinas, Brazil (2018). URL http://repositorio.unicamp.br/jspui/handle/REPOSIP/331867.

[44] Alves, M. B. & de Sá, F. H. Equilibrium of longitudinal bunch distributions in electron storage rings with arbitrary impedance sources and generic filling patterns. *Phys. Rev. Accel. Beams* **26**, 094402 (2023). URL https://link.aps.org/doi/10.1103/PhysRevAccelBeams.26.094402.

[45] Alves, M. B. Theoretical models for longitudinal coupled-bunch instabilities driven by harmonic cavities in electron storage rings. *Phys. Rev. Accel. Beams* **28**, 034401 (2025). URL https://link.aps.org/doi/10.1103/PhysRevAccelBeams.28.034401.

[46] M. Alves, A. A. & Cullinan, F. Optimizing Touschek lifetime with overstretched bunch profiles in the MAX IV 1.5 GeV ring. In *Proc. IPAC'24*, 2586–2589 (Nashville, TN, 2024). URL https://indico.jacow.org/event/63/contributions/4501.

[47] Sessler, A. M. Collective Phenomena in Accelerators. In *Proc. LINAC'72*, Linear Accelerator Conference, 291–299 (JACoW Publishing, Geneva, Switzerland, 1972). URL https://jacow.org/l72/papers/K02.pdf.

[48] Sands, M. The Physics of Electron Storage Rings: An Introduction. *Conf. Proc. C* **6906161**, 257–411 (1969).

[49] Wiedemann, H. *Particle Accelerator Physics*. Graduate Texts in Physics (Springer International Publishing, 2015). URL https://books.google.com.br/books?id=oR0_CgAAQBAJ.

[50] Chao, A. *Physics of Collective Beam Instabilities in High Energy Accelerators*. Wiley Series in Beam Physics and Accelerator Technology (Wiley, 1993). URL https://books.google.com.br/books?id=MjRoQgAACAAJ.

[51] Ng, K. Y. *Physics of intensity dependent beam instabilities* (World Scientific, 2005). URL https://doi.org/10.1142/5835.

[52] Deniau, G. R. L., Grote, H. & Schmidt, F. MAD-X: User's reference manual version. http://madx.web.cern.ch/madx/webguide/manual.html (2019).

[53] Zotter, B. & Kheifets, S. *Impedances and Wakes in High-energy Particle Accelerators*. G - Reference,Information and Interdisciplinary Subjects Series (World Scientific, 1998). URL https://books.google.com.br/books?id=2sRsN4m-010C.

[54] Chao, A., Tigner, M., Weise, H. & Zimmermann, F. *Handbook Of Accelerator Physics And Engineering (Third Edition)* (World Scientific Publishing Company, 2023). URL https://books.google.com.br/books?id=zVjcEAAAQBAJ.

[55] Bernardini, C. *et al.* Lifetime and beam size in a storage ring. *Phys. Rev. Lett.* **10**, 407–409 (1963). URL https://link.aps.org/doi/10.1103/PhysRevLett.10.407.

[56] Martini, M. Intrabeam Scattering: Anatomy of the Theory. *CERN Yellow Rep. School Proc.* **3**, 291–351 (2017).

[57] Piwinski, A. The Touschek effect in strong focusing storage rings (1999). URL https://arxiv.org/abs/physics/9903034. physics/9903034.

[58] Sokolov, A. A. & Ternov, I. M. On polarization and spin effects in the theory of synchrotron radiation. *Dokl. Akad. Nauk SSSR* **153**, 1052–1054 (1963).

[59] Carmignani, N. *Touschek Lifetime Studies and Optimization of the European Synchrotron Radiation Facility*. Ph.D. thesis, Pisa U. (2014).

[60] Fu, H., Duan, Z. & Wang, J. New analytical formula on the touschek lifetime of the polarized electron beam in electron storage rings. *Phys. Rev. Accel. Beams* **27**, 124401 (2024). URL https://link.aps.org/doi/10.1103/PhysRevAccelBeams.27.124401.

[61] Le Duff, J. Single and multiple Touschek effects. *LAL-RT-88-08* (1995). URL https://cds.cern.ch/record/399406.

[62] Resende, X., Mukai, A. H., Vilela, L. N., de Sá, F. H. & Alves, M. Pyaccel. A Python module for beam dynamics tracking and optics calculations in particle accelerators. (2024). URL https://github.com/lnls-fac/pyaccel.

[63] Alves, M. B., Liu, L., Resende, X. R. & de Sá, F. H. Beam Lifetime Measurements in SIRIUS Storage Ring. In *Proc. IPAC'22*, 2186–2189 (Bangkok, Thailand, 2022). URL https://jacow.org/IPAC2022/papers/WEPOTK055.pdf.

[64] Lindberg, R. R. Fokker-Planck analysis of transverse collective instabilities in electron storage rings. *Phys. Rev. Accel. Beams* **19**, 124402 (2016). URL https://link.aps.org/doi/10.1103/PhysRevAccelBeams.19.124402.

[65] Haïssinski, J. Exact longitudinal equilibrium distribution of stored electrons in the presence of self-fields. *Il Nuovo Cimento* **18**, 72–82 (1973).

[66] Sacherer, F. J. Methods for computing bunched-beam instabilities. *CERN/SI-BR Report No. 72-5* (1972). URL https://cds.cern.ch/record/322545.

[67] Sacherer, F. J. A longitudinal stability criterion for bunched beams. *CERN-MPS-INT-BR-73-3* (1973). URL https://cds.cern.ch/record/322639.

[68] Suzuki, T. Theory of longitudinal bunched beam instabilities based on the Fokker-Planck equation. *KEK-PREPRINT-82-34, Part. Accel.* **14**, 91–108 (1983).

[69] Suzuki, T. Fokker-Planck theory of transverse mode coupling instability. *Part. Accel.* **20**, 79–96 (1986).

[70] Landau, L. D. On the vibrations of the electronic plasma. *J. Phys. (USSR)* **10**, 25–34 (1946).

[71] Neil, V. K. & Sessler, A. M. Longitudinal resistive instabilities of intense coasting beams in particle accelerators. *Review of Scientific Instruments* **36**, 429–436 (1965). URL https://doi.org/10.1063/1.1719594. https://pubs.aip.org/aip/rsi/article-pdf/36/4/429/19259168/429_1_online.pdf.

[72] Laslett, L. J., Neil, V. K. & Sessler, A. M. Transverse resistive instabilities of intense coasting beams in particle accelerators. *Review of Scientific Instruments* **36**, 436–448 (1965). URL https://doi.org/10.1063/1.1719595. https://pubs.aip.org/aip/rsi/article-pdf/36/4/436/19259192/436_1_online.pdf.

[73] Hereward, H. G. Landau damping by non-linearity. *CERN-MPS-DL-69-11* (1969). URL https://cds.cern.ch/record/1114390.

[74] Ng, K. Y. Decoherence and Landau Damping. *Technical Report FN-0763-AD* (2005). URL https://inspirehep.net/files/527e26f4a9c1ed7634d90d1b35ea2d1f.

[75] Olsson, T., Cullinan, F. J. & Andersson, A. Self-consistent calculation of transient beam loading in electron storage rings with passive harmonic cavities. *Phys. Rev. Accel. Beams* **21**, 120701 (2018). URL https://link.aps.org/doi/10.1103/PhysRevAccelBeams.21.120701.

[76] Warnock, R. & Venturini, M. Equilibrium of an arbitrary bunch train in presence of a passive harmonic cavity: solution through coupled Haïssinski equations. *Phys. Rev. Accel. Beams* **23**, 064403 (2020). URL https://link.aps.org/doi/10.1103/PhysRevAccelBeams.23.064403.

[77] Warnock, R. Equilibrium of an arbitrary bunch train in the presence of multiple resonator wakefields. *Phys. Rev. Accel. Beams* **24**, 024401 (2021). URL https://link.aps.org/doi/10.1103/PhysRevAccelBeams.24.024401.

[78] Warnock, R. Equilibrium of an arbitrary bunch train with cavity resonators and short range wake: enhanced iterative solution with Anderson acceleration. *Phys. Rev. Accel. Beams* **24**, 104402 (2021). URL https://link.aps.org/doi/10.1103/PhysRevAccelBeams.24.104402.

[79] Hofmann, A. & Myers, S. Beam dynamics in a double rf system. *CERN-ISR-TH-RF-80-26* (1980). URL https://cds.cern.ch/record/879237.

[80] Venturini, M. Harmonic cavities and the transverse mode-coupling instability driven by a resistive wall. *Phys. Rev. Accel. Beams* **21**, 024402 (2018). URL https://link.aps.org/doi/10.1103/PhysRevAccelBeams.21.024402.

[81] Lindberg, R. R. Theory of coupled-bunch longitudinal instabilities in a storage ring for arbitrary rf potentials. *Phys. Rev. Accel. Beams* **21**, 124402 (2018). URL https://link.aps.org/doi/10.1103/PhysRevAccelBeams.21.124402.

[82] Venturini, M. Passive higher-harmonic rf cavities with general settings and multibunch instabilities in electron storage rings. *Phys. Rev. Accel. Beams* **21**, 114404 (2018). URL https://link.aps.org/doi/10.1103/PhysRevAccelBeams.21.114404.

[83] de Sá, F. H. & Alves, M. B. pycolleff and cppcolleff: modules for impedance analysis and wake-field induced instabilities evaluation. (2024). URL https://doi.org/10.5281/zenodo.14217110. (v1.0.4).

[84] Gamelin, A., Gubaidulin, V., Alves, M. B. & Olsson, T. ALBuMS (2024). URL https://doi.org/10.5281/zenodo.14286600. (1.0.0), https://gitlab.synchrotron-soleil.fr/PA/collective-effects/albums.

[85] Cullinan, F. J., Andersson, A. & Tavares, P. F. Quadrupole stability in nonuniform fill patterns. *Phys. Rev. Accel. Beams* **25**, 044401 (2022). URL https://link.aps.org/doi/10.1103/PhysRevAccelBeams.25.044401.

[86] Tavares, P. F., Leemann, S. C., Sjöström, M. & Andersson, Å. The MAXIV storage ring project. *Journal of Synchrotron Radiation* **21**, 862–877 (2014). URL https://doi.org/10.1107/S1600577514011503.

[87] Luo, T. H. *et al.* Design Progress of ALS-U 3rd-Harmonic Cavity. In *Proc. IPAC'21*, 1481–1484 (JACoW Publishing, Geneva, Switzerland, 2021). URL https://jacow.org/ipac2021/papers/TUPAB053.pdf.

[88] Yamaguchi, T., Yamamoto, N., Naito, D., Takahashi, T. & Sakanaka, S. Design and low-power measurement of 1.5 ghz tm020-type harmonic cavity for kek future synchrotron light source. *Nuclear Instruments and Methods in Physics Research Section A: Accelerators, Spectrometers, Detectors and Associated Equipment* **1053**, 168362 (2023). URL https://www.sciencedirect.com/science/article/pii/S0168900223003522.

[89] Karau, S., Bousonville, M., Choroba, S. & Hülsmann, P. Development of single mode cavity at 1.5 GHz for the third harmonic RF-system in PETRA IV. In *Proc. IPAC'23*, no. 14 in International Particle Accelerator Conference, 1091–1094 (JACoW Publishing, Geneva, Switzerland, 2023).

[90] Bellafont, I., Perez, F. & Solans, P. Longitudinal beam dynamics studies with a third harmonic RF system for ALBA-II. *JACoW* **IPAC2023**, WEPL179 (2023).

[91] Lindberg, R. Coupled-bunch longitudinal instabilities with a harmonic cavity. In *Proc. IPAC'23*, no. 14 in IPAC'23 - 14th International Particle Accelerator Conference, 3538–3541 (JACoW Publishing, Geneva, Switzerland, 2023). URL https://indico.jacow.org/event/41/contributions/2213.

[92] Bosland, P. *et al.* Third Harmonic Superconducting Passive Cavities in ELETTRA and SLS. In *Proc. SRF'03*, 239–243 (JACoW Publishing, Geneva, Switzerland, 2003). URL https://jacow.org/SRF2003/papers/TUO06.pdf.

[93] Pedrozzi, M. *et al.* SLS Operational Performance with Third Harmonic Superconducting System. In *Proc. SRF'03*, 91–94 (JACoW Publishing, Geneva, Switzerland, 2003). URL https://jacow.org/SRF2003/papers/MOP25.pdf.

[94] Pedrozzi, M. *et al.* First Operational Results of the 3rd Harmonic Super Conducting Cavities in SLS and ELETTRA. In *Proc. PAC'03*, 878–880 (JACoW Publishing, Geneva, Switzerland, 2003). URL https://jacow.org/p03/papers/MPPB024.pdf.

[95] Zhou, Y., Leng, Y., Lai, L., Xu, X. & He, T. Experimental verification and analysis of the beam loading effect based on precise bunch-by-bunch 3d position measurement. *Nuclear Instruments and Methods in Physics Research Section A: Accelerators, Spectrometers, Detectors and Associated Equipment* **1051**, 168201 (2023). URL https://www.sciencedirect.com/science/article/pii/S0168900223001912.

[96] Dimtel. Dimtel iGp12 bunch-by-bunch processor unit. URL https://www.dimtel.com/products/igp12.

[97] Duarte, H. O. C. *et al.* Analysis and countermeasures of wakefield heat losses for Sirius. In *Proc. IPAC'17*, 3052–3055 (Copenhagen, Denmark, 2017). URL https://doi.org/10.18429/JACoW-IPAC2017-WEPIK055.

[98] de Sá, F. H. & Alves, M. B. PyColleff. Python module for impedances and instability analysis in electron storage rings. (2023). URL https://github.com/lnls-fac/collective_effects/pycolleff.

[99] Olsson, T. *Timing Modes for the MAX IV Storage Rings*. Ph.D. thesis, Lund University, Faculty of Science, MAX IV Laboratory (2018).

[100] Pu, X. Y. *et al.* Frequency sensitivity of the passive third harmonic superconducting cavity for SSRF. *Nuclear Science and Techniques* **31**, 31 (2020). URL https://doi.org/10.1007/s41365-020-0732-x.

[101] Gong, P.-P. *et al.* Tuning control system of a third harmonic superconducting cavity in the shanghai synchrotron radiation facility. *Nuclear Science and Techniques* **30**, 157 (2019). URL https://doi.org/10.1007/s41365-019-0669-0.

[102] Yu, H. *et al.* Studies on Higher Order Modes Damper for the 3rd Harmonic Superconducting. In *Proc. IPAC'10*, 2600–2602 (JACoW Publishing, Geneva, Switzerland, 2010). URL http://accelconf.web.cern.ch/IPAC10/papers/WEPEA050.pdf.

[103] Gamelin, A., Gubaidulin, V., Alves, M. B. & Olsson, T. Semi-analytical algorithms to study longitudinal beam instabilities in double rf systems (2024). URL https://arxiv.org/abs/2412.06539. 2412.06539.

[104] Cullinan, F. J., Nagaoka, R., Skripka, G. & Tavares, P. F. Transverse coupled-bunch instability thresholds in the presence of a harmonic-cavity-flattened rf potential. *Phys. Rev. Accel. Beams* **19**, 124401 (2016). URL https://link.aps.org/doi/10.1103/PhysRevAccelBeams.19.124401.

[105] Lindberg, R. R. Stabilizing effects of chromaticity and synchrotron emission on coupled-bunch transverse dynamics in storage rings. *Phys. Rev. Accel. Beams* **24**, 024402 (2021). URL https://link.aps.org/doi/10.1103/PhysRevAccelBeams.24.024402.

[106] Tavares, P. F., Andersson, A., Hansson, A. & Breunlin, J. Equilibrium bunch density distribution with passive harmonic cavities in a storage ring. *Phys. Rev. ST Accel. Beams* **17**, 064401 (2014). URL https://link.aps.org/doi/10.1103/PhysRevSTAB.17.064401.

[107] Byrd, J. M., De Santis, S., Jacob, J. & Serriere, V. Transient beam loading effects in harmonic rf systems for light sources. *Phys. Rev. ST Accel. Beams* **5**, 092001 (2002). URL https://link.aps.org/doi/10.1103/PhysRevSTAB.5.092001.

[108] Milas, N. & Stingelin, L. Impact of filling patterns on bunch length and lifetime at the SLS. *IPAC 2010 - 1st International Particle Accelerator Conference* 4719–4721 (2010).

[109] Ruprecht, M. *et al.* Influence of transient beam loading on the longitudinal beam dynamics at BESSY VSR. *6th International Particle Accelerator Conference, IPAC 2015* 141–143 (2015).

[110] Phimsen, T. *et al.* Tracking code simulation for passive harmonic cavity in the SSRF storage ring. *Radiation Detection Technology and Methods* **2** (2018).

[111] Yamamoto, N., Takahashi, T. & Sakanaka, S. Reduction and compensation of the transient beam loading effect in a double rf system of synchrotron light sources. *Phys. Rev. Accel. Beams* **21**, 012001 (2018). URL https://link.aps.org/doi/10.1103/PhysRevAccelBeams.21.012001.

[112] He, T., Li, W., Bai, Z. & Wang, L. Longitudinal equilibrium density distribution of arbitrary filled bunches in presence of a passive harmonic cavity and the short range wakefield. *Phys. Rev. Accel. Beams* **24**, 044401 (2021). URL https://link.aps.org/doi/10.1103/PhysRevAccelBeams.24.044401.

[113] Weisstein, E. W. Heaviside step function. MathWorld–A Wolfram Web Resource https://mathworld.wolfram.com/HeavisideStepFunction.html (2023).

[114] Weisstein, E. W. Bilateral Laplace transform. MathWorld–A Wolfram Web Resource https://mathworld.wolfram.com/BilateralLaplaceTransform.html (2023).

[115] Berenc, T. & Borland, M. Modeling rf feedback in elegant for bunch lengthening studies for the Advanced Photon Source upgrade. *6th International Particle Accelerator Conference, IPAC 2015* 540–542 (2015).

[116] Rivetta, C., Mastorides, T., Fox, J. D., Teytelman, D. & Van Winkle, D. Modeling and simulation of longitudinal dynamics for low energy ring–high energy ring at the positron-electron project. *Phys. Rev. ST Accel. Beams* **10**, 022801 (2007). URL https://link.aps.org/doi/10.1103/PhysRevSTAB.10.022801.

[117] Baudrenghien, P. & Mastoridis, T. Fundamental cavity impedance and longitudinal coupled-bunch instabilities at the High Luminosity Large Hadron Collider. *Phys. Rev. Accel. Beams* **20**, 011004 (2017). URL https://link.aps.org/doi/10.1103/PhysRevAccelBeams.20.011004.

[118] Karpov, I. & Baudrenghien, P. Transient beam loading and rf power evaluation for future circular colliders. *Phys. Rev. Accel. Beams* **22**, 081002 (2019). URL https://link.aps.org/doi/10.1103/PhysRevAccelBeams.22.081002.

[119] Boussard, D. Control of cavities with high beam loading. *IEEE Transactions on Nuclear Science* **32**, 1852–1856 (1985).

[120] Liu, L. *et al.* Status of SIRIUS operation with users. *Proc. 14th International Particle Accelerator Conference - IPAC'23* (2023).

[121] Seraphim, R. M. *et al.* Vacuum system design for the SIRIUS storage ring. *6th International Particle Accelerator Conference, IPAC 2015* 2744–2746 (2015).

[122] Cullinan, F. J., Andersson, A., Breunlin, J., Brosi, M. & Tavares, P. F. Longitudinal beam dynamics in ultra-low emittance rings. in Proceedings of I. FAST Workshop 2022, Karlsruhe, Germany (2022) https://indico.scc.kit.edu/event/2592/sessions/2576/attachments/5004/7619/IFASTatKIT2022_Cullinan.pdf (2022).

[123] Cullinan, F. J., Andersson, A. & Tavares, P. F. Harmonic-cavity stabilization of longitudinal coupled-bunch instabilities with a nonuniform fill. *Phys. Rev. Accel. Beams* **23**, 074402 (2020). URL https://link.aps.org/doi/10.1103/PhysRevAccelBeams.23.074402.

[124] Chin, Y. Longitudinal stability limit for electron bunches in a double rf system. *Nuclear Instruments and Methods in Physics Research* **215**, 501–509 (1983). URL https://www.sciencedirect.com/science/article/pii/0167508783904854.

[125] Chin, Y., Satoh, K. & Yokoya, K. Instability of a bunched beam With synchrotron frequency spread. *Part. Accel.* **13**, 45–66 (1983).

[126] Krinsky, S. & Wang, J. M. Longitudinal instabilities of bunched beams subject to a nonharmonic rf potential. *Part. Accel.* **17**, 109–139 (1985). URL http://cds.cern.ch/record/1108025.

[127] Leemann, S. C. Interplay of Touschek scattering, intrabeam scattering, and rf cavities in ultralow-emittance storage rings. *Phys. Rev. ST Accel. Beams* **17**, 050705 (2014). URL https://link.aps.org/doi/10.1103/PhysRevSTAB.17.050705.

[128] Bassi, G. & Tagger, J. Longitudinal beam dynamics with a higher-harmonic cavity for bunch lengthening. *International Journal of Modern Physics A* **34**, 1942040 (2019). URL https://doi.org/10.1142/S0217751X19420405.

[129] Oide, K. & Yokoya, K. Longitudinal single-bunch instability in electron storage rings. Tech. Rep., KEK, Tsukuba (1990). URL http://cds.cern.ch/record/208816.

[130] Oide, K. A Mechanism of longitudinal single bunch instability in storage rings. *Part. Accel.* **51**, 43–52 (1995).

[131] Chao, A., Chen, B. & Oide, K. A weak microwave instability with potential well distortion and radial mode coupling. *SLAC-PUB-6859* (1996). URL https://cds.cern.ch/record/293610.

[132] Dyachkov, M. Longitudinal single bunch stability. *Part. Accel.* **50**, 105–116 (1995).

[133] Ng, K. Y. Mode coupling instability and bunch lengthening in proton machines. *Conf. Proc. C* **950501**, 2977–2979 (1996).

[134] Mosnier, A. Microwave instability in electron storage rings. *Nuclear Instruments and Methods in Physics Research Section A: Accelerators, Spectrometers, Detectors and Associated Equipment* **438**, 225–245 (1999). URL https://www.sciencedirect.com/science/article/pii/S0168900299008323.

[135] Cai, Y. Linear theory of microwave instability in electron storage rings. *Phys. Rev. ST Accel. Beams* **14**, 061002 (2011). URL https://link.aps.org/doi/10.1103/PhysRevSTAB.14.061002.

[136] Karpov, I. Longitudinal mode-coupling instabilities of proton bunches in the cern super proton synchrotron. *Phys. Rev. Accel. Beams* **26**, 014401 (2023). URL https://link.aps.org/doi/10.1103/PhysRevAccelBeams.26.014401.

[137] Lebedev, A. N. Coherent synchrotron oscillations in the presence of a space charge. *Soviet Atomic Energy* **25**, 851–856 (1968). URL https://doi.org/10.1007/BF01121037.

[138] Karpov, I., Argyropoulos, T. & Shaposhnikova, E. Thresholds for loss of Landau damping in longitudinal plane. *Phys. Rev. Accel. Beams* **24**, 011002 (2021). URL https://link.aps.org/doi/10.1103/PhysRevAccelBeams.24.011002.

[139] Alves, M. B. Predictions of slow longitudinal mode 1 instability in storage rings with harmonic cavities. In *HarmonLIP 2024* (2024). URL https://indico.esrf.fr/event/122/contributions/665/attachments/390/777/HarmonLIP2024_PredictMode1_v1.pdf.

[140] Alves, M. & de Sá, F. Slow longitudinal mode 1 instability in electron storage rings with harmonic cavities. In *Proc. IPAC'24*, 782–785 (Nashville, TN, 2024). URL https://doi.org/10.18429/JACoW-IPAC2024-MOPS32.

[141] Schenk, M., Buffat, X., Li, K. & Maillard, A. Vlasov description of the effects of nonlinear chromaticity on transverse coherent beam instabilities. *Phys. Rev. Accel. Beams* **21**, 084402 (2018). URL https://link.aps.org/doi/10.1103/PhysRevAccelBeams.21.084402.

[142] Suzuki, T., Chin, Y. & Satoh, K. Mode Coupling Theory and Bunch Lengthening in SPEAR II. *Part. Accel.* **13**, 179–198 (1983).

[143] Bosch, R. A., Kleman, K. J. & Bisognano, J. J. Robinson instabilities with a higher-harmonic cavity. *Phys. Rev. ST Accel. Beams* **4**, 074401 (2001). URL https://link.aps.org/doi/10.1103/PhysRevSTAB.4.074401.

[144] Bassi, G. Vlasov-Fokker-Planck Simulations of Passive Higher-Harmonic Cavity Effects in ALS-U. In *10th International Particle Accelerator Conference*, MOPGW099 (2019).

[145] He, T., Li, W., Bai, Z. & Wang, L. Periodic transient beam loading effect with passive harmonic cavities in electron storage rings. *Phys. Rev. Accel. Beams* **25**, 024401 (2022). URL https://link.aps.org/doi/10.1103/PhysRevAccelBeams.25.024401.

[146] Cullinan, F. J., Andersson, A., Breunlin, J., Brosi, M. & Tavares, P. F. Experimental observation of a mode-1 instability driven by Landau cavities in a storage ring. *Phys. Rev. Accel. Beams* **27**, 044403 (2024). URL https://link.aps.org/doi/10.1103/PhysRevAccelBeams.27.044403.

[147] He, T. Novel perturbation method for judging the stability of the equilibrium solution in the presence of passive harmonic cavities. *Phys. Rev. Accel. Beams* **25**, 094402 (2022). URL https://link.aps.org/doi/10.1103/PhysRevAccelBeams.25.094402.

[148] Zotter, B. Turbulent bunch lengthening and the microwave instability. *IEEE Transactions on Nuclear Science* **28**, 2602–2604 (1981).

[149] Ruth, R. D. Transverse mode coupling with feedback. *AIP Conf. Proc. C* **C830811**, 389 (1983). URL https://cds.cern.ch/record/2048901.

[150] Ruth, R. D. Reactive feedback in the two particle model. *CERN-LEP-TH-83-22* (1983). URL https://cds.cern.ch/record/144983.

[151] Myers, S. Effect of Reactive Feedback on the Transverse Mode Coupling Instability Using the Few-Particles Model and Simulation. *IEEE Trans. Nucl. Sci.* **32**, 2341–2343 (1985).

[152] Myers, S. Stabilization of the Fast Head-Tail Instability by Feedback. *Conf. Proc. C* **870316**, 503 (1987).

[153] Balewski, K. Is feedback able to counteract the transverse mode coupling instability? *Part. Accel.* **28**, 41–46 (1990).

[154] Karpov, I. & Shaposhnikova, E. Generalized threshold of longitudinal multibunch instability in synchrotrons. *Phys. Rev. Accel. Beams* **27**, 074401 (2024). URL https://link.aps.org/doi/10.1103/PhysRevAccelBeams.27.074401.

[155] Venturini, M. Semi-analytical studies of HHC instabilities in the ALS-U. In *Proceedings of LER8 Workshop 2020, Frascati, Italy* (2020). URL https://agenda.infn.it/event/20813/contributions/110227/attachments/76559/98462/Venturini_LER8_Oct2020.pdf.

[156] MAX IV Detailed Design Report. URL https://www.maxiv.lu.se/beamlines-accelerators/accelerators/accelerator-documentation-2/.

[157] Brosi, M. Diagnosing collective effects in the max iv storage rings. Presented at I.FAST, Karlsruhe, 2022. URL https://indico.scc.kit.edu/event/2592/contributions/10368/attachments/5037/7789/IFAST_presentation_mbrosi.pdf.

[158] Penco, G. & Svandrlik, M. Experimental studies on transient beam loading effects in the presence of a superconducting third harmonic cavity. *Phys. Rev. ST Accel. Beams* **9**, 044401 (2006). URL https://link.aps.org/doi/10.1103/PhysRevSTAB.9.044401.

[159] Daminelli, D. *et al.* Improvements of longitudinal stability with LLRF optimization at SIRIUS. In *Proc. IPAC'24*, no. 15 in International Particle Accelerator Conference, 3435–3438 (JACoW Publishing, Geneva, Switzerland, 2024).

[160] Ascenção, G. *et al.* Impact of Delta undulator on SIRIUS beam dynamics. In *Proc. IPAC'24*, no. 15 in International Particle Accelerator Conference, 3769–3772 (JACoW Publishing, Geneva, Switzerland, 2024).

[161] Alves, M. B. Algebraic solution for the classical harmonic oscillator. *Revista Brasileira de Ensino de Física* **45** (2023). URL https://doi.org/10.1590/1806-9126-RBEF-2023-0152.

[162] Velloso, M. M. S., de Sá, F. H. & Alves, M. B. Fast orbit response matrix measurement via sine-wave excitation of correctors at sirius. *Journal of Physics: Conference Series* **2420**, 012048 (2023). URL https://dx.doi.org/10.1088/1742-6596/2420/1/012048.

[163] Velloso, M. *et al.* Online optimization of SIRIUS nonlinear optics. In *Proc. IPAC'23*, no. 14 in International Particle Accelerator Conference, 3302–3305 (JACoW Publishing, Geneva, Switzerland, 2023).

[164] Ascenção, G., Alves, M., Liu, L. & Resende, X. Study of insertion devices effects in SIRIUS. In *Proc. IPAC'23*, no. 14 in International Particle Accelerator Conference, 1184–1187 (JACoW Publishing, Geneva, Switzerland, 2023).

[165] Liu, L. *et al.* Status of SIRIUS operation with users. In *Proc. IPAC'23*, no. 14 in International Particle Accelerator Conference, 2586–2589 (JACoW Publishing, Geneva, Switzerland, 2023).

[166] de Sá, F. H., Alves, M. B. & Liu, L. Measurements of Collective Effects Related to Beam Coupling Impedance at SIRIUS. In *Proc. IPAC'22*, 34–37 (Bangkok, Thailand, 2022). URL https://jacow.org/IPAC2022/papers/MOOYSP2.pdf.

[167] Resende, X. R. *et al.* Sirius Injection Optimization. In *Proc. IPAC'22*, no. 13 in International Particle Accelerator Conference, 2672–2674 (JACoW Publishing, Geneva, Switzerland, 2022). URL https://jacow.org/IPAC2022/papers/THPOPT038.pdf.

[168] Quentino, J. V., Alves, M. B. & de Sá, F. H. Emittance Exchange at Sirius Booster for Storage Ring Injection Improvement. In *Proc. IPAC'22*, no. 13 in International Particle Accelerator Conference, 2722–2725 (JACoW Publishing, Geneva, Switzerland, 2022). URL https://jacow.org/IPAC2022/papers/THPOPT056.pdf.

[169] Liu, L. *et al.* Status of Sirius Operation. In *Proc. IPAC'22*, no. 13 in International Particle Accelerator Conference, 1385–1388 (JACoW Publishing, Geneva, Switzerland, 2022). URL https://jacow.org/IPAC2022/papers/TUPOMS002.pdf.

[170] Marques, S. R. *et al.* Improvements on Sirius Beam Stability. In *Proc. IPAC'22*, no. 13 in International Particle Accelerator Conference, 226–229 (JACoW Publishing, Geneva, Switzerland, 2022). URL https://jacow.org/IPAC2022/papers/MOPOPT002.pdf.

[171] Alves, M. B. Optics Corrections with LOCO on Sirius Storage Ring. In *Proc. IPAC'21*, 825–828 (JACoW Publishing, Geneva, Switzerland, 2021). URL https://jacow.org/ipac2021/papers/MOPAB260.pdf.

[172] Liu, L., Alves, M. B., Oliveira, A. C. S., Resende, X. R. & de Sá, F. H. Sirius Commissioning Results and Operation Status. In *Proc. IPAC'21* (Campinas, Brazil, 2021). URL https://jacow.org/ipac2021/papers/MOXA03.pdf.

[173] Resende, X. R., Alves, M. B., Liu, L. & de Sá, F. H. Equilibrium and Nonlinear Beam Dynamics Parameters From Sirius Turn-by-Turn BPM Data. In *Proc. IPAC'21*, 1935–1938 (JACoW Publishing, Geneva, Switzerland, 2021). URL https://jacow.org/ipac2021/papers/TUPAB219.pdf.

[174] Oliveira, A. C. S., Alves, M. B., Liu, L., Resende, X. R. & de Sá, F. H. High Level Applications for Sirius Accelerators Control. In *Proc. IPAC'21*, 4314–4317 (JACoW Publishing, Geneva, Switzerland, 2021). URL https://jacow.org/ipac2021/papers/THPAB259.pdf.

Appendices

Publication: Alves, M. B. & de Sá, F. H., "Equilibrium of longitudinal bunch distributions in electron storage rings with arbitrary impedance sources and generic filling patterns". Phys. Rev. Accel. Beams **26***, 094402 (2023). DOI:* https://doi.org/10.1103/PhysRevAccelBeams.26.094402.

A

Article 1: Equilibrium with arbitrary impedances and filling patterns

Contents

A new self-consistent semi-analytical method for calculating the stationary beam-induced voltage in the presence of arbitrary filling patterns and impedance sources in electron storage rings is presented. The theory was developed in space-domain with resonator wake-functions and in frequency-domain with arbitrary impedance functions. The SIRIUS storage ring parameters were used to benchmark the results, demonstrating good agreement between the two approaches and with macroparticle tracking simulations. Additionally, a different approach to simulate the beam-loading compensation of active rf cavities was investigated in frequency-domain, proving to be a more generic description than the methods generally used. The impact of broadband impedance on the longitudinal equilibrium was straightforwardly evaluated with the frequency-domain framework, without intermediate steps such as fitting broadband resonators or convolving short-range wakes with bunch distributions. Finally, a simple study of Touschek lifetime improvement with a passive higher harmonic cavity is presented.

A.1 Introduction

Many developments on semi-analytical methods have been made to calculate the equilibrium longitudinal bunch distributions in electron storage rings as a faster alternative to tracking codes. One of the early motivations was related to the equilibrium of a uniform filling in a double-rf system, where the effect of a passive HHC was investigated. In this case the beam-induced voltage has an analytical formula that can be added to the main voltage and the bunch distribution can be obtained. However, the co-dependence between these two quantities require the calculations to be iterated until convergence. The bunch profile can be accounted on the calculation of the beam-induced voltage in passive HHCs with a real [23] or complex [106] form-factor.

Synchrotron light sources often operate with nonuniform filling patterns for different reasons, for example, to allow for time-resolved experiments and to mitigate ion and coupled-bunch instabilities. Time-consuming macroparticle tracking simulations were the first attempt to study the inhomogeneous beam-loading (also referred as transient beam-loading) in the presence of passive HHCs. Simplified approaches considered each bunch as a pointlike macroparticle [107–109] or as macroparticles with Gaussian real form-factors [110]. Initially, semi-analytical methods were also non-self-consistent [111], assuming pointlike bunches to iteratively calculate the induced voltage. A self-consistent calculation of the inhomogeneous beam-loading was proposed in Ref. [75], with an iterative matrix formulation based on the linearization of the energy balance equation in the presence of a passive HHC modeled as a resonator. In this solution, complex form-factors were assigned for each bunch.

The problem for arbitrary filling patterns was revisited in Ref. [76], with the development of explicit formulas for the induced voltage of a narrowband resonator, resulting in a system of coupled Haïssinski equations. Newton's method was applied to iteratively solve the problem. The theory was extended in Ref. [77] to include multiple resonators and an algorithm for compensating the main rf cavity beam-loading was proposed. A discussion on the effect of cavities higher order modes and short-range wakefields was presented as well. Some difficulties were reported in the convergence of the Newton iteration scheme for higher currents, when beam-induced voltages are higher. In Ref. [112], phasor notation was applied to describe the induced voltage by resonators and Newton's iteration method was also employed to solve the system of equations. In this case, convergence was improved when, on each iteration, the distributions were updated based on a linear combination of previous and present distributions, with a random coefficient as weight. The Jacobian-based iterative solution method proposed in [76, 77] was reappraised in Ref. [78], where the equations were formulated as a fixed-point problem. The Anderson's acceleration method was introduced to enhance convergence, proving to be a robust and fast algorithm for calculating the equilibrium bunch distributions for general settings of filling patterns and resonators wakefields.

In this chapter we present two semi-analytical approaches in space-domain (SD) and frequency-domain (FD) to obtain the beam-induced voltage. The SD formulation is similar in some aspects to the theory presented in Ref. [76]. The main difference is the fact that we considered the most generic wake-function for a resonator, instead of assuming the approximated formula for large Q factor. Additionally, we employed complex variables to develop the equations in SD, resulting in compact expressions accessible for numerical implementation and with simple interpretation. The main novelty of this thesis lies in the calculation of the beam-induced voltage with a FD framework, which allows for more general impedance models, not restricted to the resonator case. With this framework, broadband impedance and higher-order modes of rf cavities can be easily incorporated. The natural inclusion of broadband impedance sources is a very important feature, since it allows the usage of impedance models obtained from analytical and semi-analytical calculations, for which the wake-function is not available or difficult to be obtained. Moreover, the usage of impedance functions helps to establish a more realistic description of active rf cavities with a llrf feedback control and then evaluate its effects on the beam equilibrium. We will address the question raised in Ref. [77] on whether the proposed algorithm was an accurate model of the feedback mechanism, and discuss its equivalence to a particular controller type.

The chapter is organized as follows: in §A.2 we present the theory to calculate the beam-induced voltage with two approaches. Methods to model active rf cavities and schemes of beam-loading compensation are discussed in §A.3. In §A.4, we briefly review the Haïssinski equation to solve for the longitudinal bunch distributions given the beam-induced voltage. §A.5 presents the application of the developed methods considering the SIRIUS storage ring parameters. Macroparticle tracking was used to benchmark the results for a nonuniform filling pattern. In the Appendix, the theory was applied to the case of uniform filling and narrowband resonator to reproduce a well-known formula for the beam-induced voltage.

A.2 Beam-induced voltage

Throughout this chapter we will work with a set of global reference systems for the longitudinal coordinate z of relativistic electrons in a storage ring, with origin at the center[1] of the corresponding rf bucket n on an arbitrary turn r, and $z > 0$ for trailing particles. Besides, the bucket index is defined such that, if $\ell > n$, then bucket ℓ trails bucket n. In a particular coordinate system where $n = 0$ and $r = 0$, we can express the beam distribution, which extends through the entire real line and is one-turn periodic, as:

$$\lambda_{\mathrm{t}}(z) = \sum_{k=-\infty}^{\infty} \lambda(z + kC_0), \tag{A.1}$$

where C_0 is the ring circumference and $\lambda(z)$ is the one-turn distribution, given by

$$\lambda(z) = \frac{1}{I_{\mathrm{t}}} \sum_{\ell=0}^{h-1} I_\ell \lambda_\ell(z - \ell\lambda_{\mathrm{rf}}), \quad \text{with} \quad I_{\mathrm{t}} = \sum_{\ell=0}^{h-1} I_\ell > 0, \tag{A.2}$$

where h is the harmonic number of the ring, $\lambda_{\mathrm{rf}} = C_0/h$ is the rf wavelength, $I_\ell \geq 0$ is the current of the ℓth bunch and $\lambda_\ell(z)$ is its distribution, which is assumed to be non-zero[2] only for $z \in \mathcal{D} \subset [-\lambda_{\mathrm{rf}}/2, \lambda_{\mathrm{rf}}/2]$ and normalized to unity, which implies the one-turn distribution is also normalized to unity.

With this setup, the longitudinal voltage $V(z)$ induced by this current distribution under the influence of the longitudinal wake-function $W_0'(z)$ is [51]

$$V(z) = -I_{\mathrm{t}} T_0 \int_{-\infty}^{\infty} \mathrm{d}z' \lambda_{\mathrm{t}}(z') W_0'(z - z'), \tag{A.3}$$

where $T_0 = C_0/c$ is the revolution period and c is the speed of light. Substituting Eq. (A.1) into Eq. (A.3) and assuming the integral converges, we can change the order of the summation with the integral. Besides, since the choice of the turn used as origin of the coordinate system is arbitrary, we can make the following change of the integration variable $z' \to z' - kC_0$, which yields:

$$V(z) = -I_{\mathrm{t}} T_0 \sum_{k=-\infty}^{\infty} \int_{-\infty}^{\infty} \mathrm{d}z' \lambda(z') W_0'(z - z' + kC_0). \tag{A.4}$$

Inserting Eq. (A.2) in the equation above, changing the order of the summation with the

[1]The center of a rf bucket is the synchronous phase considering only the energy gain by the main rf cavities and the energy loss by synchrotron radiation.

[2]The distributions are not exactly zero outside a rf period, but for electron beams it typically fall-off exponentially for z sufficiently larger than the bunch length, justifying the assumption.

integral and making the additional change of variables $z' \to z' + \ell\lambda_{\text{rf}}$, we get

$$V(z) = -T_0 \sum_{k=-\infty}^{\infty} \sum_{\ell=0}^{h-1} \int_{-\infty}^{\infty} \mathrm{d}z' I_\ell \lambda_\ell(z') W_0'(z - z' + kC_0 - \ell\lambda_{\text{rf}}). \tag{A.5}$$

Since the choice of the reference bucket was arbitrary, we could get an equivalent result using the center of the nth rf bucket as reference for the coordinate system. This is performed with the change of variables $z \to z + n\lambda_{\text{rf}}$ in Eq. (A.5), which reads

$$V_n(z) = -T_0 \sum_{k=-\infty}^{\infty} \sum_{\ell=0}^{h-1} \int_{-\infty}^{\infty} \mathrm{d}z' I_\ell \lambda_\ell(z') W_0'(z - z' + kC_0 - (\ell - n)\lambda_{\text{rf}}), \tag{A.6}$$

where we introduced the notation $V_n(z) = V(z + n\lambda_{\text{rf}})$ to denote that the beam-induced voltage is calculated with the nth bunch as reference for the coordinate system.

A.2.1 Space-domain

The most generic longitudinal wake-function for a resonator is given by [51]:

$$W_0'(z) = 2\alpha R_s e^{-\alpha z/c} H(z) \left[\cos(\bar{\omega}_R z/c) - \frac{\alpha}{\bar{\omega}_R} \sin(\bar{\omega}_R z/c)\right], \tag{A.7}$$

where $H(z)$ is the Heaviside step function [113], $\alpha > 0$ and $\bar{\omega}_R \geq 0$. When applied to a cavity, these two parameters are related to the quality factor Q and resonant frequency ω_R by the expressions $\alpha = \omega_R/2Q$ and $\bar{\omega}_R = \sqrt{\omega_R^2 - \alpha^2}$, where we note that Q must be larger than $1/2$.

Let $G(z)$ be a complex function defined as

$$G(z) = H(z) e^{-\kappa z} \ , \ \kappa = (\alpha - i\bar{\omega}_R)/c, \tag{A.8}$$

then the wake-function of Eq. (A.7) can be rewritten as

$$W_0'(z) = 2\alpha R_s \left\{ \mathrm{Re}\left[G(z)\right] - \frac{\alpha}{\bar{\omega}_R} \mathrm{Im}\left[G(z)\right] \right\}. \tag{A.9}$$

Substituting this resonator model into Eq. (A.6) we have

$$V_n(z) = -2\alpha R_s T_0 \sum_{k=-\infty}^{\infty} \sum_{\ell=0}^{h-1} \int_{-\infty}^{\infty} \mathrm{d}z' I_\ell \lambda_\ell(z') \left\{ \mathrm{Re}\left[G(\zeta_{k\ell n})\right] - \frac{\alpha}{\bar{\omega}_R} \mathrm{Im}\left[G(\zeta_{k\ell n})\right] \right\}, \tag{A.10}$$

where $\zeta_{k\ell n} = z - z' + kC_0 - (\ell - n)\lambda_{\text{rf}}$ was introduced.

Since the distributions $\lambda_\ell(z)$ are real, if we define the following complex function

$$K_n(z) = \sum_{k=-\infty}^{\infty} \sum_{\ell=0}^{h-1} \int_{-\infty}^{\infty} \mathrm{d}z' I_\ell \lambda_\ell(z') G(\zeta_{k\ell n}), \tag{A.11}$$

then the beam-induced voltage for the nth bunch can be compactly written as

$$V_n(z) = -2\alpha R_s T_0 \left\{ \mathrm{Re}\left[K_n(z)\right] - \frac{\alpha}{\bar{\omega}_R} \mathrm{Im}\left[K_n(z)\right] \right\}. \tag{A.12}$$

The causality property of the wake-function is encoded in the function $G(z)$ by means of the Heaviside step function. Nevertheless, this property should be explicitly manifested in the integration and summation limits to further simplify our expressions. This can be done with the following arguments.

- The bunch distributions $\lambda_\ell(z)$ are assumed to be zero outside the interval $[-\lambda_{\mathrm{rf}}/2, \lambda_{\mathrm{rf}}/2]$, so the limits of integration in Eq. (A.11) could be restricted to this range. With this consideration, we note that $\zeta_{k\ell n} < 0$ for $k < 0$ and the summation over turns can be reduced to non-negative values of k.

- For $\ell = n$ and $k = 0$, i.e., the self-induced voltage of a particular bunch in the present turn, causality is obeyed when $z' \leq z$, limiting the integration domain to $(-\infty, z)$.

- Taking $\ell < n$, which means the source bunch ℓ leads the trailing bunch n, then $k = 0$ should be considered in the summation. For $\ell > n$ only $k > 0$ should be accounted.

Applying these considerations into Eq. (A.11) results in

$$K_n(z) = e^{-\kappa z} \left(I_n S_n(z) + \sum_{\ell=0}^{h-1} M_{n\ell} A_{n\ell} I_\ell \right) \tag{A.13}$$

where $S_n(z)$ is related to the effect of the bunch n on itself in the present turn ($k = 0$), given by

$$S_n(z) := \int_{-\infty}^{z} \mathrm{d}z' \lambda_n(z') e^{\kappa z'}, \tag{A.14}$$

the terms $A_{n\ell}$ are given by

$$A_{n\ell} := \sum_{k=\begin{cases}0, \ell<n \\ 1, \ell\geq n\end{cases}}^{\infty} \nu^k = \begin{cases} \frac{1}{1-\nu}, & \ell < n \\ \frac{\nu}{1-\nu}, & \ell \geq n \end{cases}, \tag{A.15}$$

where $\nu = e^{-\kappa C_0}$, and $M_{n\ell}$ is defined as

$$M_{n\ell} := e^{\kappa(\ell-n)\lambda_{\mathrm{rf}}} \int_{-\infty}^{+\infty} \mathrm{d}z' \lambda_\ell(z') e^{\kappa z'}, \tag{A.16}$$

which depends on the bilateral Laplace Transform [114] of the bunch distribution evaluated at $-\kappa$, which in turn can be identified as $S_\ell(z)$ in the limit that z tends to infinity. Moreover, since $\lambda_\ell(z)$ is zero outside the interval $\mathcal{D} \subset [-\lambda_{\rm rf}/2, \lambda_{\rm rf}/2]$, then the following is valid:

$$\lim_{z\to\infty} S_\ell(z) = S_\ell(\lambda_{\rm rf}/2).$$

Equation (A.13) has a straightforward numerical implementation when we consider a uniformly discretized z domain for each bucket:

$$z_j = \frac{\lambda_{\rm rf}}{a}\left(\frac{j}{N} - \frac{1}{2}\right), \quad j = 0, \ldots, N-1, \tag{A.17}$$

where $1 \leq a \in \mathbb{R}$ and $N \in \mathbb{N}$ should be chosen appropriately, depending on the typical bunch length, resonator frequency and damping rate.

Numerical problems related to floating-point overflow may arise in calculations when high-frequency ($\omega_R \gtrsim 100\,\mathrm{GHz}$) low-$Q$ resonators are involved, due to the exponential with positive real argument in $M_{n\ell}$ when $\ell > n$. In these cases it is recommended to use the identity $g(x)e^x = e^{\log(g(x))+x}$ to avoid such problems, thus $M_{n\ell}A_{n\ell} = e^{\log(M_{n\ell})+\log(A_{n\ell})}$ and the term $-\kappa C_0$ compensates $\kappa(\ell-n)\lambda_{\rm rf}$. For even higher frequencies, the calculation of $S_n(z_j)$ may have similar issues and the same approach can be used for the integrand. Besides, the integral can be suitably truncated once the integrand approaches zero, which will generally be the case, given that the bunch distributions fall-off faster than the exponential term $e^{\kappa z'}$.

It is also straightforward to include an arbitrary number of resonators in the calculations, since, by linearity, the induced voltages for each resonator can be added. However, the calculation time grows linearly with the number of resonators, given that all quantities from Eq. (A.12) and Eq. (A.13) must be re-evaluated as the resonator parameters change.

It is possible to further simplify[3] Eq. (A.13) for a convenient interpretation of the beam-induced voltage:

$$K_n(z) = e^{-\kappa z}\left(I_n S_n(z) + \sum_{\ell=1}^{h} \frac{\nu^{\ell/h}}{1-\nu} S_{n-\ell}(\lambda_{\rm rf}/2) I_{n-\ell}\right). \tag{A.18}$$

In this expression we note that the voltage acting on the nth bunch is the sum of its own action on the current turn and the effect of previous passages of all bunches, including itself, with an appropriate phase and decay factor. It also facilitates to check the continuity of the voltage between adjacent buckets: $K_n(\lambda_{\rm rf}/2) = K_{n+1}(-\lambda_{\rm rf}/2)$. Interestingly,

[3]The calculation steps are: (i) insert the explicit expressions for $M_{n\ell}$ and $A_{n\ell}$ into Eq. (A.13); (ii) rewrite $\nu = e^{-\kappa C_0} = e^{-\kappa h \lambda_{\rm rf}}$; (iii) separate the terms $\ell < n$ and $\ell \geq n$ in the summation; (iv) for the sum with $\ell \geq n$, re-index the summation variable $\ell' = \ell - h$; (v) use the property $I_{\ell\pm h} = I_\ell$ and $\lambda_{\ell\pm h}(z) = \lambda_\ell(z)$; (vi) identify that both summands are equal and unify the sums; (vii) re-index the summation variable $\ell' = n - \ell$.

Eq. (A.18) is free from the numerical issues related to positive arguments in exponential.

A.2.2 Frequency-domain

An arbitrary longitudinal wake-function $W_0'(z)$ is related to a longitudinal impedance $Z(\omega)$ by the inverse Fourier transform [51]:

$$W_0'(z) = \frac{1}{2\pi}\int_{-\infty}^{\infty} \mathrm{d}\omega Z(\omega)e^{-i\omega z/c}. \tag{A.19}$$

Inserting this relation into Eq. (A.4) reads

$$V(z) = -\frac{I_\mathrm{t}T_0}{2\pi}\sum_{k=-\infty}^{\infty}\int_{-\infty}^{\infty}\mathrm{d}z'\int_{-\infty}^{\infty}\mathrm{d}\omega\ \lambda(z')Z(\omega)e^{-i\omega(z-z'+kC_0)/c}. \tag{A.20}$$

Rearranging the exponential terms, we can apply the Poisson sum formula to the summation over turns:

$$\sum_{k=-\infty}^{+\infty} e^{-ik\omega T_0} = \omega_0\sum_{p=-\infty}^{+\infty}\delta(\omega+p\omega_0), \tag{A.21}$$

where $\delta(\cdot)$ is the Dirac delta distribution and $\omega_0 = 2\pi/T_0$. With this change, the integral over ω can be easily performed. The expression simplifies to

$$V(z) = -I_\mathrm{t}\sum_{p=-\infty}^{+\infty} Z^*(p\omega_0)e^{ip\omega_0 z/c}\int_{-\infty}^{\infty}\mathrm{d}z'\lambda(z')e^{-ip\omega_0 z'/c}, \tag{A.22}$$

where we used the property $Z(-\omega) = Z^*(\omega)$, with * denoting the complex conjugate.

The numerical implementation of Eq. (A.22) requires truncation of the infinite sum over harmonics p. Two alternative approaches will be presented to properly select the harmonics. One is based on the DFT of the one-turn distribution, which considers all harmonics up to a specific threshold. The other is based on a selection of the most relevant harmonics, depending on the filling pattern and impedances under consideration. While the first method is generally much faster, since it benefits from the use of the FFT algorithm, the second one is better suited when the impedance is composed of a few narrowband peaks.

A.2.2.1 Implementation with DFT

Consider the case of the discretized z-coordinate from Eq. (A.17) for each bucket with $a = 1$, thus z covers one rf period with N points. This z-coordinate can be used for all h buckets in one-turn, concatenating it h times to form a discretized coordinate with hN elements, extending to the domain $\mathcal{T} = [-\lambda_\mathrm{rf}/2, C_0 - \lambda_\mathrm{rf}/2]$ in which the one-turn distribution $\lambda(z)$

is defined. For a sufficiently small spacing $\Delta z = \lambda_{\mathrm{rf}}/N$, we can approximate the integral from Eq. (A.22) by quadrature to:

$$\int_{\mathcal{T}} \mathrm{d}z' \lambda(z') e^{-ip\omega_0 z'/c} \approx e^{\pi i p/h} \Delta z \sum_{j=0}^{hN-1} \lambda(z_j) e^{-2\pi i \frac{pj}{hN}}. \tag{A.23}$$

To establish notation, the DFT of a sequence of N real numbers $\mathbf{x} = [x_0, x_1, \ldots, x_{N-1}]$ and the inverse discrete Fourier transform (IDFT) are defined as

$$X_k = \mathcal{F}\{\mathbf{x}\}_k = \sum_{n=0}^{N-1} x_n e^{-2\pi i k n/N}, \quad \forall\ k \in \mathbb{Z} \tag{A.24}$$

$$x_n = \mathcal{F}^{-1}\{\mathbf{X}\}_n = \frac{1}{N} \sum_{k=-\lfloor (N-1)/2 \rfloor}^{\lfloor N/2 \rfloor} X_k e^{2\pi i k n/N} \tag{A.25}$$

where $\lfloor \cdot \rfloor$ is the floor operation. Note that, even though the DFT is defined for all $k \in \mathbb{Z}$, only a sequence of N consecutive terms are needed to compute the IDFT.

With those definitions, the summation in Eq. (A.23) can be identified as the DFT of the sequence $[\lambda(z_j)]$. Hence

$$\int_{\mathcal{T}} \mathrm{d}z' \lambda(z') e^{-ip\omega_0 z'/c} \approx e^{\pi i p/h} \Delta z \mathcal{F}\{\lambda(z)\}_p .$$

Applying this result to Eq. (A.22) for the discretized coordinate z_n we obtain

$$V(z_n) = -I_{\mathrm{t}} \Delta z \sum_{p=-\infty}^{\infty} Z^*(p\omega_0) \mathcal{F}\{\lambda(z_j)\}_p e^{2\pi i \frac{pn}{hN}}, \tag{A.26}$$

where the phase terms $e^{\pm \pi i p/h}$ nicely canceled each other.

Considering that the grid spacing was properly chosen, the minimum and maximum frequencies calculated by the DFT, $-\lfloor (hN-1)/2 \rfloor \omega_0$ and $\lfloor hN/2 \rfloor \omega_0$, should be large enough so the bunch distribution does not have any significant contribution from frequencies outside this interval. With that in mind, we can truncate the infinite sum over p in Eq. (A.26) to the limits of the IDFT, yielding

$$V(z_n) = -I_{\mathrm{t}} C_0 \mathcal{F}^{-1} \left\{ Z^*(p\omega_0) \mathcal{F}\{\lambda(z_j)\}_p \right\}_n \tag{A.27}$$

where $hN\Delta z = C_0$ was applied since $\Delta z = \lambda_{\mathrm{rf}}/N$.

A.2.2.2 Relevant Harmonics Selection

Starting from Eq. (A.22) we can apply the definition of the one-turn distribution from Eq. (A.2) and rearrange the exponential terms to get

$$V_n(z) = -\sum_{p=-\infty}^{+\infty} Z^*(p\omega_0) e^{ip\omega_0(z+n\lambda_{\mathrm{rf}})/c} \sum_{\ell=0}^{h-1} \int_{-\infty}^{\infty} \mathrm{d}z' I_\ell \lambda_\ell(z') e^{-ip\omega_0(z'+\ell\lambda_{\mathrm{rf}})/c}. \tag{A.28}$$

Observing that the terms in the sum over p become their conjugate for $p \to -p$ and considering that only a subset $\mathcal{P} \subset [0, \infty)$ will be kept in the sum, Eq. (A.28) can be transformed into:

$$V_n(z) = -2\mathrm{Re}\left[\sum_{p\in\mathcal{P}} Z^*(p\omega_0) e^{ip\omega_0 z/c} e^{2\pi ipn/h} \sum_{\ell=0}^{h-1} I_\ell \hat{\lambda}_\ell^*(p\omega_0) e^{-2\pi ip\ell/h}\right] \tag{A.29}$$

where

$$\hat{\lambda}_\ell(\omega) := \int_{-\infty}^{+\infty} \mathrm{d}z' \lambda_\ell(z) e^{i\omega z'/c} \tag{A.30}$$

is the Fourier transform of the longitudinal distribution.

The determination of a subset $\mathcal{P}$ that keeps the truncation error small can be done as follows: (i) calculate the DFT of the filling pattern $\mathbf{I}_b = [I_0, I_1, \ldots, I_{h-1}]$, (ii) sample the impedance at harmonics $p \in \mathcal{P}_{\mathrm{max}} = [0, 1, \ldots, p_{\mathrm{max}}]$, where p_{max} must be larger than the maximum relevant frequency, depending on the distribution and impedance under consideration, (iii) determine the subset

$$\mathcal{P} = \{p \in \mathcal{P}_{\mathrm{max}} \mid \xi(p) \geq \xi_{\mathrm{min}}\}, \tag{A.31}$$

where $\xi(p) = |Z(p\omega_0)\mathcal{F}\{\mathbf{I}_b\}_p|$ and $\xi_{\mathrm{min}} \in \mathbb{R}$ is a minimum threshold. Including the filling pattern frequency spectrum is important because for arbitrary fills the beam samples the impedance at revolution harmonics and the most relevant modes might be non-trivial. The threshold can be set as $\xi_{\mathrm{min}} = \max[\xi(\mathcal{P}_{\mathrm{max}})]\,\varepsilon$, where ε can be made as small as needed so that no considerable change is observed in the equilibrium solution.

One drawback of this implementation, compared to the DFT approach, is that the Fourier transform of h bunch distributions for all $p \in \mathcal{P}$ must be evaluated via numerical integration. This process has a time complexity of $\mathcal{O}(hN|\mathcal{P}|)$, where $|\mathcal{P}|$ denotes the cardinality of $\mathcal{P}$, while the computation of the one-turn distribution DFT has a complexity of $\mathcal{O}(hN\log(hN))$. On the other hand, the harmonics selection approach allows a free choice of the discretization interval (any $a \geq 1$ in Eq. (A.17)), which can improve accuracy for some cases. Note that the calculations with the SD framework has a time complexity of $\mathcal{O}(hNN_{\mathrm{R}})$, where N_{R} is the number of resonators[4].

[4]Time complexity discussions are appropriate for the limit of large numbers. In this case, for large

A.3 Active rf cavities

For active rf cavities the total voltage inside the cavity, V_t, is the sum of the generator voltage, V_g, supplied by an external power source, and the beam-induced voltage, V_b, commonly called beam-loading. In general, V_g is varied through the action of feedback loops such that V_t is kept close to a constant reference value, V_r, in a narrow bandwidth around the center frequency ω_c. We will assume in the next steps that ω_c is a multiple of the revolution frequency, but not necessarily a multiple of the main rf frequency ω_{rf}.

In tracking simulations it is common to simulate the beam-loading compensation scheme with realistic models of the feedback system [115, 116]. However, in equilibrium simulations the time-dependence of the system is neglected and very idealized models are generally used, which do not take into account the system delays or the effect of the system on neighboring revolution harmonics. In this section we will discuss some conventional methods to simulate the beam-loading compensation and present an approach, with straightforward implementation in the FD framework, that allows for realistic simulation of llrf feedback systems that are typically used to control the voltage in active cavities.

A.3.1 Least squares minimization

A scheme to calculate the generator voltage parameters is to minimize the following difference for each bucket

$$\chi_n^2 = \int_{-\lambda_{rf}/2}^{\lambda_{rf}/2} \mathrm{d}z[V_{g,n}(z) + V_{b,n}(z) - V_{r,n}(z)]^2, \tag{A.32}$$

where $V_{b,n}(z)$ is the beam-loading voltage for bucket n, which can be calculated using the impedance or wake-function model for the cavity and the techniques presented in §A.2. The reference and generator voltages are given by

$$\begin{aligned} V_{r,n}(z) &= \mathrm{Re}\left[\hat{V}_r\, e^{i\omega_c(z+n\lambda_{rf})/c}\right], \\ V_{g,n}(z) &= \mathrm{Re}\left[\hat{V}_g\, e^{i\omega_c(z+n\lambda_{rf})/c}\right], \end{aligned}$$

where we made use of the notation introduced in Eq. (A.6) to take bucket n as reference. Note that, if ω_c is a multiple of ω_{rf}, then both voltages have the same phase relation for all buckets. The phasors are defined by the respective amplitudes and phases with:

$$\hat{V}_r = V_r e^{i(\pi/2-\phi_r)} \text{ and } \hat{V}_g = V_g e^{i(\pi/2-\phi_g)}, \tag{A.33}$$

where ϕ_r is the reference phase.

The minimization of Eq. (A.32) with respect to the amplitude and phase of the

values of N, h, N_R and $|\mathcal{P}|$.

generator voltage can be rewritten as a linear problem with

$$V_{\mathrm{g},n}(z) = A\sin\left(\frac{\omega_\mathrm{c}}{c}(z+n\lambda_\mathrm{rf})\right) + B\cos\left(\frac{\omega_\mathrm{c}}{c}(z+n\lambda_\mathrm{rf})\right)$$

where $A = V_\mathrm{g}\cos(\phi_\mathrm{g})$ and $B = V_\mathrm{g}\sin(\phi_\mathrm{g})$ are free parameters. With this setup, the minimization problem can be formally written as

$$(\tilde{A},\tilde{B}) = \arg\min_{(A,B)} \sum_{\ell=0}^{h-1}\chi_\ell^2. \tag{A.34}$$

The numerical implementation of this method is straightforward and will not be presented here[5].

A.3.2 Phasor compensation

The beam-loading voltage phasor at the center frequency ω_c can be calculated as

$$\hat{V}_\mathrm{b}(\omega_\mathrm{c}) = \frac{2}{C_0}\sum_{\ell=0}^{h-1}\int_{-\lambda_\mathrm{rf}/2}^{\lambda_\mathrm{rf}/2} \mathrm{d}z V_{\mathrm{b},\ell}(z)e^{-i\omega_\mathrm{c}z/c}, \tag{A.35}$$

where we observe that the combination of the sum with the integral is equivalent to an integration along the whole storage ring, which guarantees that only the harmonic $p = \omega_\mathrm{c}/\omega_0$ will influence the phasor. Note that the numerical implementation of Eq. (A.35), as well as Eq. (A.32), requires $a = 1$ in the discretization defined by Eq. (A.17). In that way, no other harmonic of the beam-loading influences the compensation scheme.

With the phasors for induced and reference voltages calculated, the generator voltage phasor can be set as:

$$\hat{V}_\mathrm{g} = \hat{V}_\mathrm{r} - \hat{V}_\mathrm{b}(\omega_\mathrm{c}). \tag{A.36}$$

It is possible to demonstrate that this method is equivalent to the least squares minimization method presented previously.

A.3.3 Closed-loop impedance

While the two previous methods of calculating the beam-loading of active cavities can be implemented either in SD or FD, the next one is particular for the FD approach. In this framework, it is possible to set $V_\mathrm{g} = V_\mathrm{ref}$ and simulate the compensation by using the effective impedance of the cavity seen by the beam in the presence of a llrf control

[5] An equivalent approach was used in Ref. [77], with the derivation of analytic expressions for the Jacobian taking into account the beam response in front of the changing parameters of the generator. In our implementations we noted that a simple numeric estimation of the Jacobian, without accounting for the changes in V_b were enough to reach convergence.

loop [116–118]:

$$Z_{\rm cl}(\omega) = \frac{V_{\rm t}(\omega)}{I_{\rm b}(\omega)} = \frac{Z(\omega)}{1+T(\omega)Z(\omega)}, \tag{A.37}$$

where $Z(\omega)$ is the open-loop impedance of the cavity, which can be modelled as the impedance of an equivalent RLC circuit [51]

$$Z(\omega) = \frac{R_{\rm s}}{1+iQ\left(\dfrac{\omega_R}{\omega}-\dfrac{\omega}{\omega_R}\right)}, \tag{A.38}$$

where R_s and Q are the cavity shunt impedance and quality factor. $T(\omega)$ is the rf plant transfer function apart from the cavity impedance. Thus, the overall open-loop transfer function is $L(\omega) = T(\omega)Z(\omega)$.

A simple model for $Z_{\rm cl}(\omega)$ is obtained by letting $T(\omega) \to \delta(\omega-\omega_{\rm c})$, which assumes perfect compensation of the beam-loading component at the control loop frequency, since $Z_{\rm cl}(\omega_{\rm c}) = 0$, and the loop is transparent for all other frequencies ($Z_{\rm cl}(\omega) = Z(\omega), \forall\, \omega \neq \omega_{\rm c}$). It can be shown that this model is equivalent to the methods presented previously if only static beam-loading is considered[6].

To simulate a more realistic feedback, one can consider the following model for the rf plant transfer function:

$$T(\omega) = C(\omega)\mathcal{K}e^{-i(\omega\tau_{\rm d}-\phi)}, \tag{A.39}$$

which consists of overall gain $\mathcal{K}$ and delay $\tau_{\rm d}$, a controller $C(\omega)$ and a phase ϕ that can be adjusted such that $\phi = \omega_{\rm c}\tau_{\rm d}$, i.e., the overall phase is zero at the control frequency $\omega_{\rm c}$.

Considering a purely proportional feedback, $C(\omega) = k_{\rm p}$, it is possible to show that the flat-response for the closed-loop system is obtained by setting the feedback gain to [119]:

$$\frac{1}{k_{\rm p,f}\mathcal{K}} = \frac{2}{\pi}\left(\frac{R}{Q}\right)\omega_{\rm rf}\tau_{\rm d}, \tag{A.40}$$

which will result in $Z_{\rm cl}(\omega_{\rm c}) = 1/(k_{\rm p,f}\mathcal{K})$.

The proportional-integral (PI) controller is widely used in digital llrf systems. Generally these systems down-convert the rf signal and then adjust the generator voltage amplitude and phase by applying the control law on the digitized quadrature components of the signal in baseband. There are several techniques to accomplish this, whose detailed modelling and description is beyond the scope of this chapter. However, a very simplified model of this type of controller, that does not take into account nonlinear effects nor the

[6]Dynamic beam-loading will also contain frequencies that are not multiple of revolution harmonics, such as multiples of the synchrotron frequency, which will contribute to the calculation of the cost function defined in Eqs. (A.32) and (A.34) and the phasor of Eq. (A.35), since these components are not orthogonal to the $\omega_{\rm c}$ component in the integration and summation domains. On the other hand, they would not be accounted in the generator voltage in this closed-loop impedance method. This scenario, however, is outside the scope of this chapter, since we are concerned only with the equilibrium state.

analog-to-digital and digital-to-analog conversions, is presented below:

$$C(\omega) = k_{\mathrm{p}} + \frac{k_{\mathrm{i}}}{i(\omega - \omega_{\mathrm{c}})},\ \omega \geq 0 \tag{A.41}$$

where k_{i} is another free parameter. The domain restriction to non-negative frequencies and the term $(\omega - \omega_{\mathrm{c}})$ are related to the up-conversion of the integrator applied in baseband. The relation $C(-\omega) = C^*(\omega)$ must be used to evaluate the transfer function for negative frequencies. This controller model also strongly suppress the beam-loading at the control frequency, but, differently from the previous methods, it allows for the evaluation of the control system impact on neighboring revolution harmonics. In practice this effect will largely depend on the specificities of each system, such as the strength of k_{p} and k_{i}, the filters that are used to limit the bandwidth of the controller or even other factors such as the unmodeled dynamics. However, in principle it should be possible to improve the model of the rf plant of interest and use the corresponding closed-loop impedance on the FD framework to have a reasonable characterization of the effect of llrf control loop on equilibrium parameters.

A.4 Equilibrium bunch distributions

The equilibrium longitudinal distribution of bunch n, $\lambda_n(z)$, in an electron storage ring is given by the Haïssinski equation [65]:

$$\lambda_n(z) = A_n \exp\left\{\left(-\frac{\Phi_n(\lambda; z)}{\alpha_c \sigma_\delta^2}\right)\right\}, \text{ with} \tag{A.42}$$

$$\Phi_n(\lambda; z) = -\frac{1}{E_0 C_0}\int_0^z \mathrm{d}z'\,[eV_{\mathrm{t},n}(\lambda; z') - U_0], \tag{A.43}$$

where $\lambda = \lambda(z)$ is the equilibrium one-turn distribution, given by Eq. (A.2), σ_δ is the equilibrium relative energy spread, A_n is a normalization constant, α_c is the momentum compaction factor, E_0 is the ring nominal energy, $e > 0$ is the elementary charge, U_0 is the energy loss per turn from synchrotron radiation and

$$V_{\mathrm{t},n}(\lambda; z) = V_{\mathrm{g},n}(z) + V_{\mathrm{b},n}(\lambda; z)$$

is the total voltage, written in terms of the generator voltage and the beam-induced voltage at the nth bunch, given by Eq. (A.6).

Equation (A.42) can be solved numerically by different methods, for example, calculating the self-consistent distribution with fixed-point algorithms [78] or with a Jacobian-based algorithm as Newton's method [76, 77, 112]. In this thesis, we employed Anderson's algorithm to enhance fixed-point iterations, and we refer to Ref. [78] and its references for more information on this subject.

To determine the convergence of the iterative process, it is convenient to define a functional $\Delta : \mathbb{R}^{hN} \times \mathbb{R}^{hN} \to \mathbb{R}$ (N is the number of points on the z grid) that measures the difference of two one-turn distributions $\lambda(z')$ and $\eta(z')$ by:

$$\Delta(\lambda, \eta) = \max_n \Delta_n(\lambda_n, \eta_n), \text{ with} \tag{A.44}$$

$$\Delta_n(\lambda_n, \eta_n) = \int_{-\lambda_{\mathrm{rf}}/2}^{\lambda_{\mathrm{rf}}/2} \mathrm{d}z' |\lambda_n(z') - \eta_n(z')|. \tag{A.45}$$

The iterative process can be terminated at iteration k if the last two distributions are sufficiently close, i.e., if $\Delta\left(\lambda^{(k)}, \lambda^{(k-1)}\right) < \Delta_{\min}$ is satisfied, where $\Delta_{\min}$ is a convergence parameter.

A.5 Applications for SIRIUS

We will discuss in this section some interesting cases to benchmark the formulas presented previously and also to highlight the advantages of using the FD over the SD approach. The numerical implementation was carried out in python3 and the code is open to access [98]. The solution of the Haïssinski equation was computed with fixed-point iterations accelerated by Anderson's algorithm [78]. Gaussian distributions for all bunches were always taken as the initial condition. The results from semi-analytical methods for a nonuniform filling pattern were benchmarked against a macroparticle tracking code that was also implemented in python3 [98]. The implementation is similar to the one described in Ref. [111], computing the time evolution of the longitudinal dynamic variables of several macroparticles in each rf bucket in the presence of resonator wakefields, with the effects of radiation damping and quantum excitation taken into account. We followed the strategy of tracking just a few macroparticles per bunch at the initial turns to speed up computing time. Then the number was gradually increased by oversampling the existing particles with a small random variation of their coordinates.

In all semi-analytical simulations reported in this chapter we used $N = 2001$ and $a = 1$ in Eq. (A.17) to discretize the z coordinate. The relaxation parameter in Anderson's acceleration method was fixed at the value of 0.1 and provided fast convergence for all evaluated cases. It was sufficient to consider a linear combination of three previous distributions to update the distribution for the next iteration. In the notation established in Ref. [78], we set $m = 3$ and $\beta_k = 0.1$. It was checked that the convergence criteria of $\Delta_{\min} = 10^{-8}$ was a good trade-off to obtain a reliable fixed-point solution while reducing the total number of iterations. Regarding the tracking simulations, we adhered to the following schedule for increasing the number of particles: 100 particles per bunch in the first 50 000 turns; then 1000 particles per bunch in the following 20 000 turns; and 10 000

Table A.1: Main parameters for SIRIUS storage ring

Parameter	Symbol	Value
Energy	E_0	3 GeV
Nominal current	I_t	350 mA
Circumference	C_0	518.39 m
Harmonic number	h	864
Momentum compaction factor	α	1.645×10^{-4}
Energy loss per turn (with IDs)	U_0	870 keV
Relative energy spread	σ_δ	8.436×10^{-4}
Natural rms bunch length	$\sigma_{z,0}$	2.6 mm
rf frequency	f_rf	499.667 MHz
Number of MCs	N_MC	2
MCs total voltage	$N_\mathrm{MC} V_\mathrm{MC}$	3.0 MV
MC geometric factor	$(R/Q)_\mathrm{MC}$	89 Ω
MC unloaded quality factor	$Q_{0,\mathrm{MC}}$	2×10^9
External quality factor	Q_ext	1.58×10^5
Cavity coupling factor	β_c	12 657
MC detuning[7]	Δf_MC	−4.9 kHz
Number of HHCs	N_HC	1
HHC rf harmonic	$\omega_\mathrm{HC}/\omega_\mathrm{rf}$	3
HHC geometric factor	$(R/Q)_\mathrm{HC}$	87.5 Ω
HHC quality factor	$Q_{0,\mathrm{HC}}$	4×10^8
HHC flat-potential voltage ratio	$V_\mathrm{HC}/N_\mathrm{MC} V_\mathrm{MC}$	0.317
HHC detuning[8]	Δf_HC	45 kHz

particles per bunch in the final 10 000 turns. All calculations were performed on the same personal computer with quite modest hardware configurations: an 8th generation Intel Core i7 processor, 32 GB of RAM memory and no graphics processing unit capabilities.

The SIRIUS storage ring, a fourth-generation synchrotron light source built and operated by the LNLS in Campinas, Brazil [120], was used to exemplify the application of the formulas developed in the previous sections. The main parameters for the machine are described in Table A.1. We could not compare the presented simulated results with experimental data since SIRIUS storage ring is operating with a temporary normal conducting PETRA 7-cell rf cavity and the 3HC is not installed yet. The definitive rf system for SIRIUS will have two superconducting CESR-B MCs and a superconducting passive 3HC, according to the parameters presented in Table A.1.

A.5.1 Benchmarking

A.5.1.1 Uniform filling

First we simulated the case of nominal current in uniform filling with a superconducting passive 3HC modeled as a resonator, following the parameters from Table A.1. Under these conditions, all bunches are equivalent and there is an analytical formula for the beam-induced voltage in the resonator, given by Eq. (A.55), which was used to benchmark the calculations. We considered that formula in the fixed-point iteration to solve for the corresponding longitudinal distribution, which we will denote as $\lambda_\mathrm{A}(z)$. The resulting distribution centroid is $-0.23\,\mathrm{mm}$ and the rms bunch length is $11.88\,\mathrm{mm}$, yielding a bunch lengthening factor of 4.6 with respect to the natural bunch length. The main contribution to the induced voltage in the 3HC comes from its impedance at the fundamental harmonic $3\omega_{\mathrm{rf}}$. The result computed with FD framework taking only the $3\omega_{\mathrm{rf}}$ mode into account has an agreement of $\Delta\left(\lambda_{\mathrm{A}}, \lambda_{\mathrm{FD}}^{3\omega_{\mathrm{rf}}}\right) \approx 7\times10^{-12}$, which was expected given that both models are very similar in terms of the approximations involved. For the result from implementation with DFT, the agreement is $\Delta\left(\lambda_{\mathrm{A}}, \lambda_{\mathrm{FD}}^{\mathrm{DFT}}\right) \approx 1.5\times10^{-3}$ and for the result from SD method $\Delta\left(\lambda_{\mathrm{A}}, \lambda_{\mathrm{SD}}\right) \approx 1.7\times10^{-3}$. The equivalence between all equilibrium bunch profiles for uniform fill was confirmed in our results even though it was never assumed *a priori*.

A small systematic difference between the SD and FD frameworks was observed, with value of $\Delta\left(\lambda_{\mathrm{SD}}, \lambda_{\mathrm{FD}}^{\mathrm{DFT}}\right) \approx 3\times10^{-4}$. In our tests, this difference seems to be insensitive to the number of points considered in the z discretization and its origin is not clear. Nevertheless, we believe that this level of disagreement between methods is too small to have a considerable impact for practical purposes.

The computation time is also an important metric for the comparison of the several approaches discussed here. Considering the hardware described previously, the evaluation of the analytical formula for the induced voltage took $20\,\mathrm{ms/step}$. For the FD framework, the method of selecting the most relevant harmonics (only one, in this case) was slightly faster ($70\,\mathrm{ms/step}$) than the implementation with DFT ($100\,\mathrm{ms/step}$). The SD calculation was also quite fast ($130\,\mathrm{ms/step}$), since just one resonator was considered. The numerical iterations of Anderson's acceleration algorithm contributes to approximately $270\,\mathrm{ms/step}$. The analytical implementation and the FD with mode selection converged after 56 iterations. The calculation with FD using DFT converged in 52 iterations and for the SD framework convergence was achieved after 72 iterations. Overall, each simulation took less than $30\,\mathrm{s}$ to run. It is worth mentioning that the implementation of FD approach with DFT is independent of the number of impedance sources or on the filling pattern, while the other methods are expected have a strong dependency of the computation time on these factors.

A.5.1.2 Hybrid filling

The nonuniform filling pattern considered here[9] consists of a high-charge bunch of $2\,\mathrm{mA}$ at bucket 432, two gaps of 50 buckets ($100\,\mathrm{ns}$ gap) around it, and the remaining 763 buckets evenly filled to add up to the total current of $350\,\mathrm{mA}$. In this example, the equilibrium solution was calculated with the SD framework and three different conditions for the FD approach: including 1, 10 and 100 modes in the summation of Eq. (A.29). The relevant harmonics were selected by means of Eq. (A.31) as illustrated in Fig. A.1, where the normalized spectrum, $\xi(\omega)/\max\left[\xi(\omega)\right]$, is shown. The 3HC remained adjusted to the

[9]This specific hybrid filling pattern is used only as a case study. It does not reflect any plan for operation in SIRIUS storage ring.

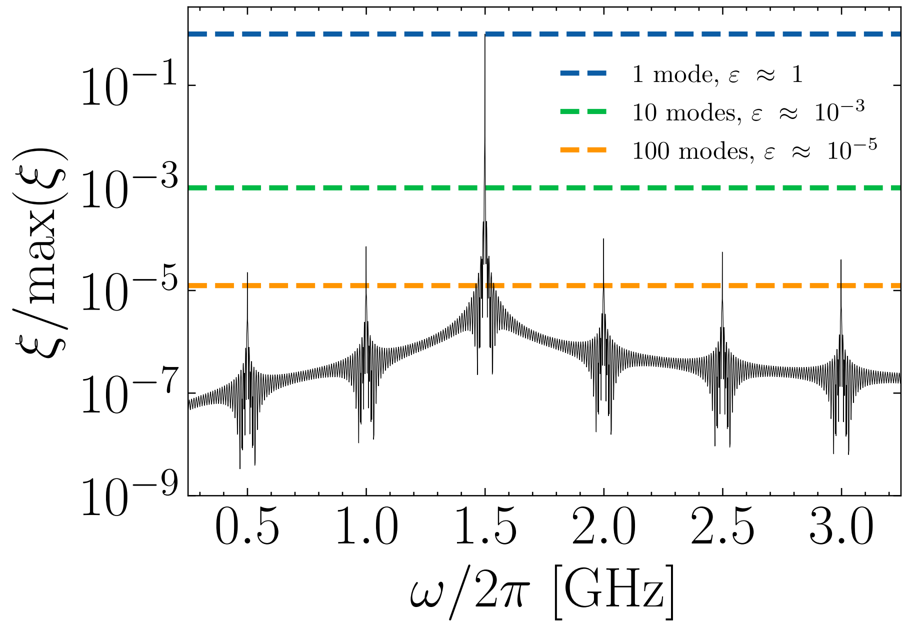

Figure A.1: Spectrum $\xi(\omega) = |Z(\omega)\,\mathcal{F}(\mathbf{I}_b)|$ normalized by its maximum value for the hybrid filling pattern and 3HC impedance. Horizontal dashed lines represent the thresholds for including 1, 10 and 100 modes.

detuning for flat-potential in uniform filling.

As more harmonics are included in the calculation of the beam-induced voltage with the FD framework, it is expected that its results become more similar to the one from the SD framework. This behavior was verified and it is shown in Fig. A.2. When

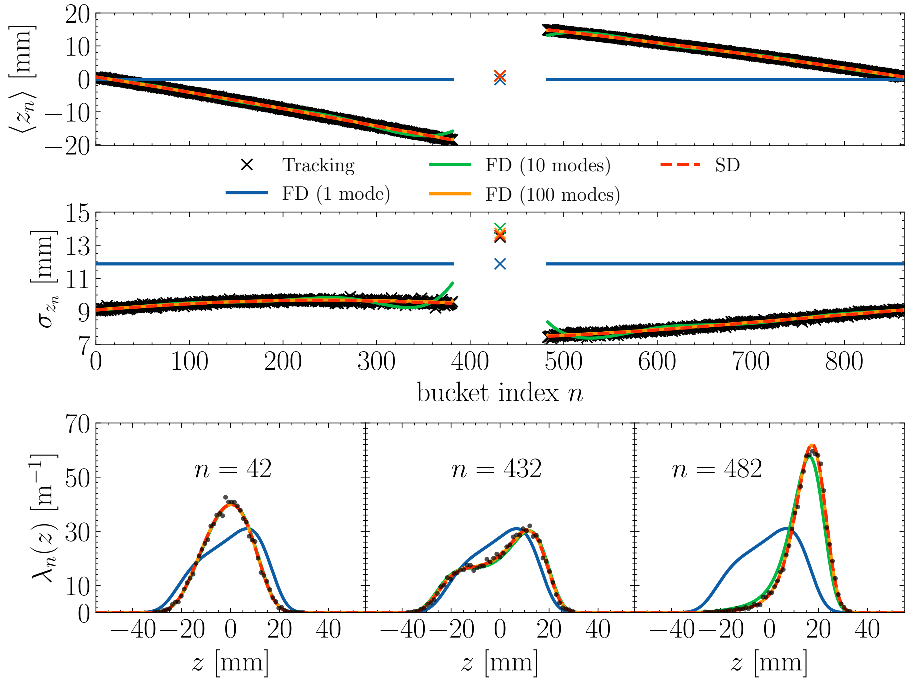

Figure A.2: Equilibrium bunch distributions obtained for the hybrid filling pattern with macroparticle tracking, SD and FD approaches for increasing number of modes in the FD framework. The 3HC detuning was set to $\Delta f = 45\,\text{kHz}$. Empty buckets are omitted. Bunch centroids $\langle z_n \rangle$ and bunch lengths σ_{z_n} are shown in the top plot. In the bottom plot, the profiles for three bunches (high-charge bunch in the middle) are compared to tracking results (dots).

only 1 mode is included, the beam-induced voltage contains only the contribution from the impedance at $3\omega_{\mathrm{rf}}$ and the distributions are analogous to the uniform filling case, missing the inhomogeneous beam-loading features. Including 10 modes, all of which are revolution harmonics still around $3\omega_{\mathrm{rf}}$, most of the inhomogeneous pattern is captured. With 100 modes, the criteria defined in Eq. (A.31) indicates that other rf harmonics are more relevant to the induced voltage than some revolution harmonics around $3\omega_{\mathrm{rf}}$. In this case, the solution from the FD approach shows good agreement with the results obtained from SD method and from tracking as well. The calculation in FD using the DFT approach proved to have the same level of agreement but is not shown in Fig. A.2. In terms of computing time, the macroparticle tracking simulation for this example took 3.6 h to run. The calculations with SD framework and the FD approach using DFT reached the equilibrium solution within 30 s, the same computing time reported for the uniform filling case. The slowest semi-analytical calculation was with the FD framework considering 100 selected modes, which took 2 min to reach the equilibrium solution.

A.5.2 Effect of llrf feedback

The beam-loading from MCs may have a substantial influence on the longitudinal equilibrium, specially for nonuniform fillings. We used the hybrid filling pattern described in the previous section to illustrate this effect. The equilibrium distributions calculated considering only the passive 3HC were compared with the case where the MCs beam-loading is included as well. Different compensation schemes were also tested. In the FD framework[10] we used the model for the llrf feedback given by Eq. (A.39). For simplicity, we set the overall gain to $\mathcal{K} = 1$. The overall delay considered was $\tau_{\mathrm{d}} = 1.9\,\mu\mathrm{s}$, which is the measured value for the current SIRIUS rf plant. In this scenario, two types of controllers were investigated: one purely integral, with $k_{\mathrm{i}} = 0.01\,\Omega^{-1}\mathrm{s}^{-1}$ and other purely proportional, with $k_{\mathrm{p}} = k_{\mathrm{p,f}}$, where $k_{\mathrm{p,f}} = 2.96 \times 10^{-6}\,\Omega^{-1}$ is the flat-response gain from Eq. (A.40) for SIRIUS parameters. In the SD framework we applied the phasor compensation scheme. It was verified that the least squares minimization method provided equivalent results, as expected, with the disadvantage of being slower than the phasor method.

The absolute values for the MCs open-loop and closed-loop impedance for each llrf feedback setting are shown in Fig. A.3. The integral (I) controller heavily suppresses the impedance at the fundamental frequency and acts only on a very narrow bandwidth around it, since a low integrator gain was chosen. The proportional (P) controller does not compensate the beam-loading contribution from ω_{rf} perfectly, but it does reduce the absolute impedance in a considerably broad range of frequencies around ω_{rf}. For the cases presented here, neither controller has considerable influence at frequencies of neighboring revolution harmonics. This is commonly the case when only digital llrf are used to control

[10]The implementation with DFT was used to obtain the results from FD framework that are reported in the present and subsequent subsections.

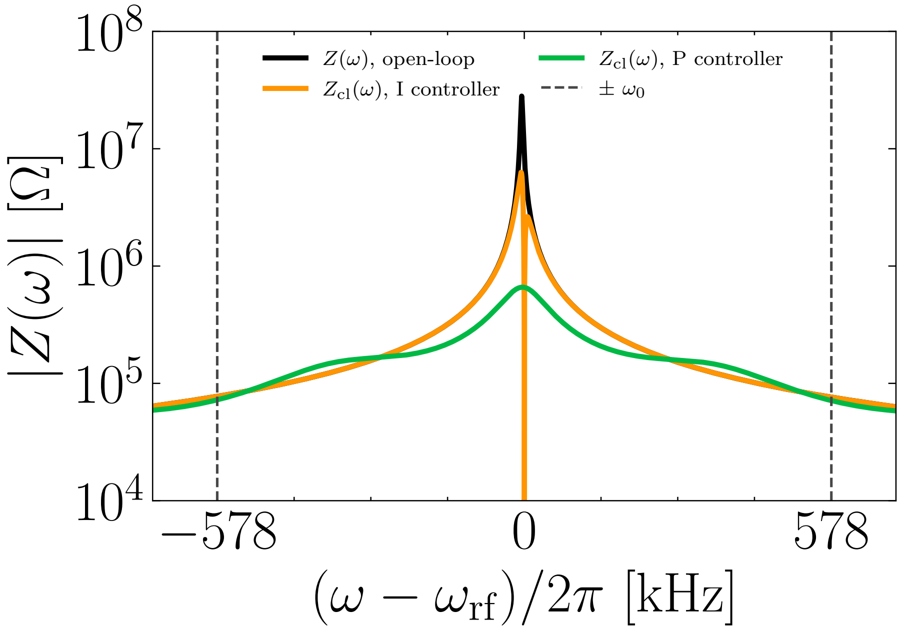

Figure A.3: Absolute value of impedance for the MCs in open-loop and closed-loop for two llrf settings, integral (I) and proportional (P) controllers. Revolution harmonics are represented by vertical gray dashed lines.

the generator voltage, due to the action of low-pass filters on the measured cavity signal. However, when fast proportional analog feedbacks or more complex topologies are used, the llrf system may impact the beam equilibrium and also the beam stability through its influence on the impedance close to revolution harmonics [117–119].

Figure A.4 shows the results for equilibrium bunch centroids and rms bunch lengths for all cases studied. It is clear the equivalence between the solution obtained with SD framework and the one from FD approach using a purely integral controller. We also note that, with the inclusion of MCs beam-loading, the bunch lengthening is systematically reduced for all buckets. With a proportional gain on llrf feedback, the absolute value for the MC closed-loop impedance at rf frequency is about 1 MΩ. The residual real part of this impedance causes an additional energy loss which induces a negative shift on all bunch centroids and its imaginary part slightly changes the rms bunch length along buckets.

A.5.3 Broadband impedance

Figure A.5 shows the model of the longitudinal impedance budget of the SIRIUS storage ring and a fitting done with several broadband resonators (BBRs), whose parameters are listed in Table A.2 [43]. The bellows and beam position monitors (BPMs) are the main contributors for the real part of the impedance and the second most relevant sources to the imaginary part. The narrow peaks at frequencies close to 9 GHz and 12 GHz are related to trapped modes in the bellows cavity and the broader peak around 18 GHz is due to BPMs. SIRIUS vacuum chamber is mostly composed of a copper cylindrical tube with 12 mm of

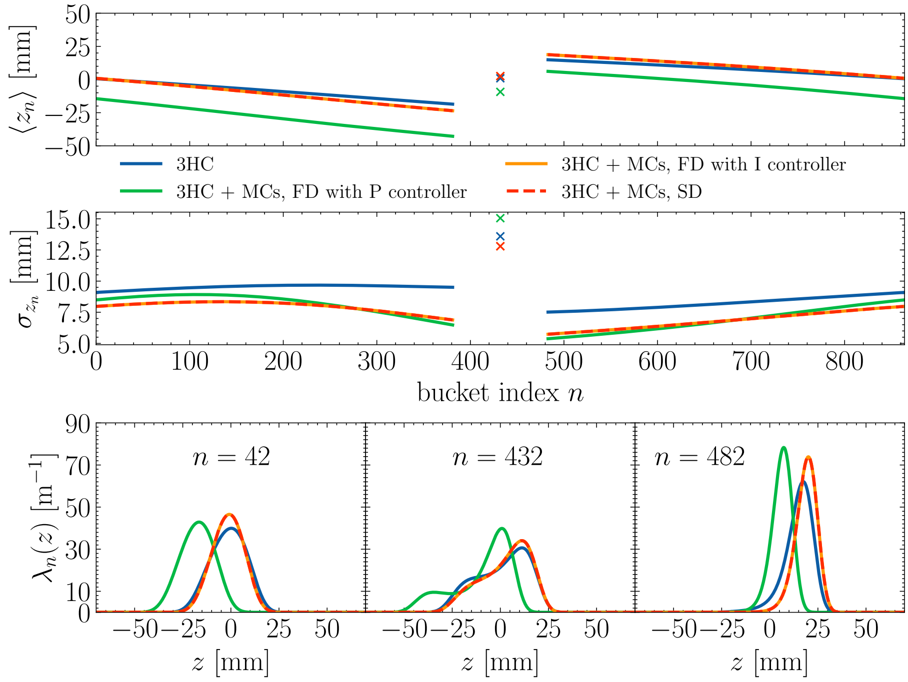

Figure A.4: Equilibrium bunch distributions for the hybrid filling pattern for different impedance configurations. 3HC only (blue) and 3HC plus active MCs with beam-loading compensation in three scenarios: with llrf parameters in FD with proportional (green) and integral controller (orange), and phasor compensation in SD (dashed red). Bunch profiles for three buckets are shown in the bottom plot.

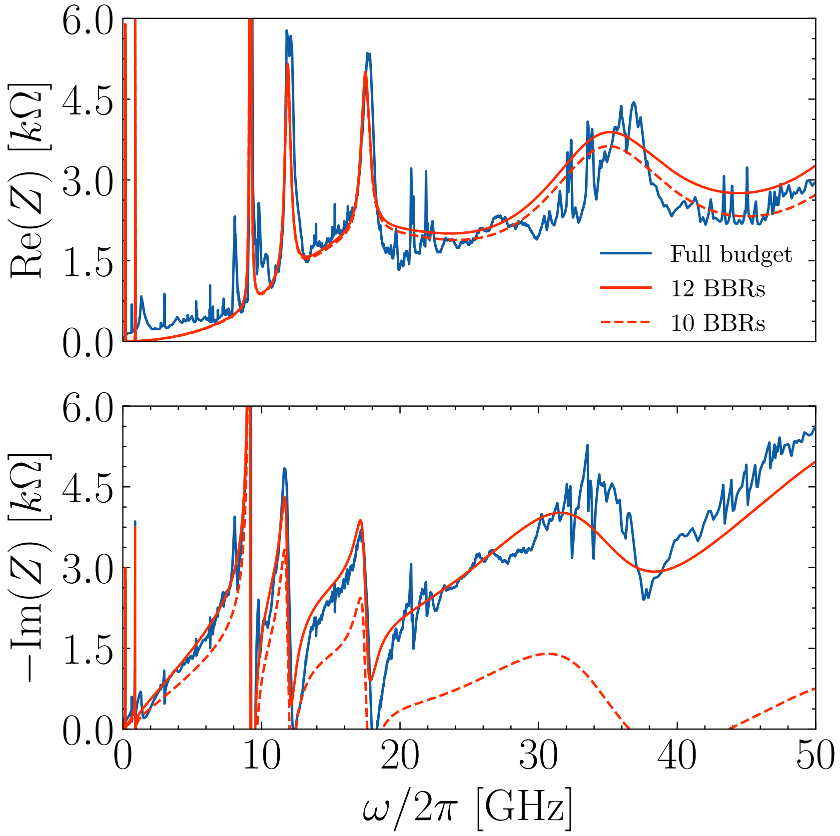

Figure A.5: SIRIUS longitudinal impedance for the full budget, 12 BBRs and without the first two BBRs from Table (A.2).

Table A.2: Fitted parameters to capture the main features of SIRIUS longitudinal impedance budget.

f_R [GHz]	R_s [kΩ]	Q	$\omega_R/2Q$ [GHz]
716.2	30.0	0.7	3216.1
206.9	6.5	1.3	500.0
138.4	2.0	4.0	108.7
79.6	2.0	1.0	250.1
57.3	2.5	4.5	40.0
35.0	2.5	3.0	36.6
17.8	1.7	1.0	55.9
17.5	3.0	24	2.29
11.9	4.0	24	1.56
9.2	20.0	100	0.29
0.9	7.0	261	0.011
0.2	6.0	263	0.002

inner radius and coated with nonevaporable getter (NEG) [121]. The finite resistivity of these chambers is responsible for most of the imaginary part of the impedance budget. This feature is captured by the BBR fitting via the first two resonators from Table A.2, which have a very high resonant frequency and low quality factor. Figure A.5 highlights the contribution of these two resonators to the overall fitting.

The inclusion of a full broadband impedance model in the FD framework is straightforward. It is sufficient to get the impedance of each contribution at the revolution harmonics, add them and use Eq. (A.29) to calculate the total beam-induced voltage. Besides, the computational time in this case does not depend on the number of sources. On the other hand, one possible way of achieving the same result for the SD formulation is to use BBR models to fit the impedance, calculate the induced voltage for each one of them using Eq. (A.12) and then sum the contributions. Drawbacks of this procedure include not capturing the exact impedance budget, having a time complexity linear with the number of BBRs and invoking non-physical constructions to represent a physical impedance source. As an example, take the first two BBRs of Table A.2, which do reproduce the inductive impedance of the resistive-wall wake at low frequencies, but have no physical connection to the original impedance source. Besides, these high frequency resonators are somewhat difficult to simulate due to the numerical problems discussed. Another method to include the effect of broadband impedance in the SD framework is to directly convolve the total wake-function with each bunch distribution [78, 112]. This approach, however, would not be correct for wakes that span over a few buckets, such as the ones captured by the last three BBRs of Table A.2. Even though a combination of the previous methods can be employed, or even other well-known impedance models can be used to fit the budget (such as a purely inductive wake), there is no elegant and simple way of including broadband impedances when using the SD framework.

The effect of the SIRIUS broadband impedance on equilibrium is presented in Fig. A.6, where we simulated the case for nominal current in uniform filling, in the presence of MCs with beam-loading compensation by an integral controller. The 3HC will be essential for

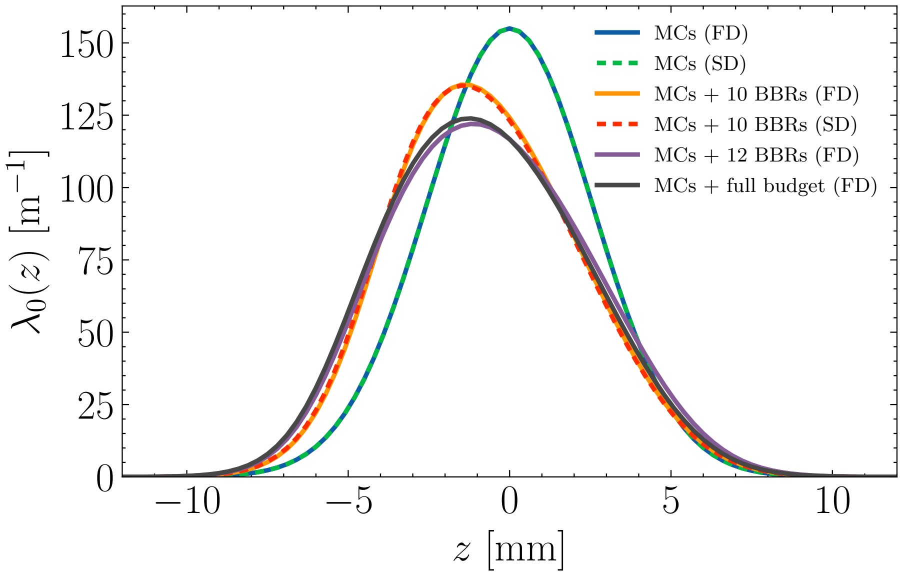

Figure A.6: Effect of broadband impedance on longitudinal bunch distribution for uniform filling in the presence of MCs. All results from FD were computed with the DFT implementation.

reaching the nominal current in the real machine due to components heating issues, but we decided to not include it in this simulation to highlight the effect of the broadband impedance on the beam. Considering the bunch length from Table A.1, the beam interacts with the impedance up to approximately 40 GHz. However, with a bunch lengthening factor of 4 provided by the 3HC, the spectrum would have considerable power only up to 10 GHz. Therefore, it is expected that with a 3HC, the broadband impedance impact on the equilibrium and even on time-dependent effects will be reduced.

For the simulations with the SD framework, we did not include the first two BBRs from Table A.2. Their high resonant frequency would require a much finer discretization of the z domain than the one we used throughout this section. Additionally, the absence of these high frequency resonators helps to emphasize the advantages of the FD framework over the SD approach and their effect on the bunch distribution. We note that the FD simulation with all 12 BBRs is sufficient to reproduce the bunch profile obtained with the full budget, which confirms that the fitting does capture the main features of the impedance. This example indicates that at nominal current the SIRIUS impedance budget would increase the natural bunch length by 18%, from 2.57 mm to 3.04 mm, cause a shift of −0.74 mm in the bunch centroid and make the bunch profile more asymmetric. This rather small bunch lengthening would not sufficiently reduce the heating load at design current, which justifies the need for a HHC.

A.5.4 Touschek lifetime improvement with a 3HC

In this last example, the bunch lengthening provided by the superconducting passive 3HC that is planned to be installed in SIRIUS storage ring will be studied for some filling

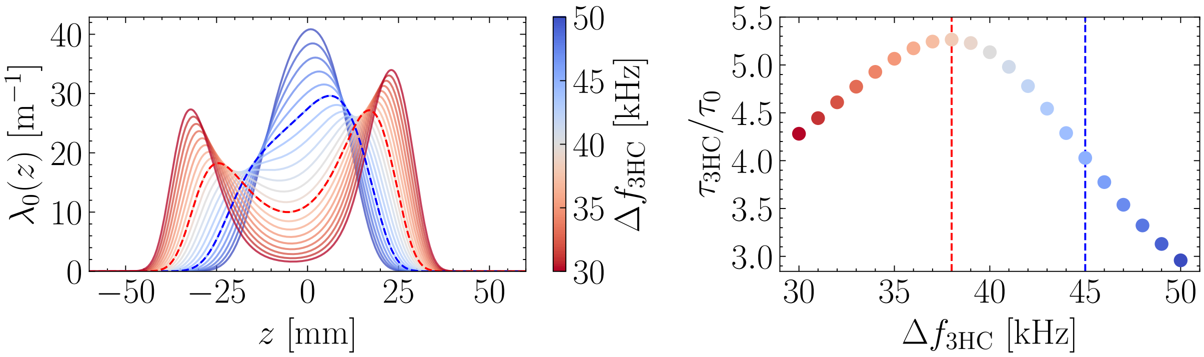

Figure A.7: Longitudinal bunch distribution for different 3HC detunings (left) and the relative lifetime improvement (right) with respect to the case without the 3HC, represented by τ_0. The harmonic voltage for flat-potential condition was obtained with $\Delta f_{3hc} = 45$ kHz and the corresponding distribution is highlighted as a dashed blue curve. The maximum lifetime improvement was obtained with $\Delta f_{3hc} = 38$ kHz and the bunch profile for this condition is emphasized as a dashed red curve.

patterns. With the FD framework we obtained the longitudinal equilibrium for a beam at nominal current, in the presence of the full broadband impedance budget, a passive 3HC and two active MCs. The beam-loading compensation was simulated with a llrf feedback with PI controller. The proportional gain was set to the flat-response value and the integrator gain was adjusted to $k_i = 0.01\,\Omega^{-1}\mathrm{s}^{-1}$. Equilibrium distributions were calculated for 21 sequentially decreasing 3HC detunings from 50 kHz to 30 kHz, taking the solution from the previous detuning as the initial condition for the next one. All calculations took about 10 min to run and no convergence issues were experienced.

The Touschek loss rate is proportional to the integrated square of the longitudinal bunch distribution. Hence, the relative difference in Touschek lifetimes for two distributions $\lambda_a(z)$ and $\lambda_b(z)$ can be calculated as [23]:

$$\frac{\tau_b}{\tau_a} \approx \frac{\int \mathrm{d}z \lambda_a^2(z)}{\int \mathrm{d}z \lambda_b^2(z)}, \tag{A.46}$$

where it is assumed that other parameters that affect Touschek lifetime are the same for the two cases.

Figure A.7 shows the bunch distributions on the left and the Touschek lifetime increase with respect to the case without the 3HC on the right, for the simulated 3HC detunings. It was observed that the MCs beam-loading have a negligible effect on the equilibrium at uniform filling. This was expected due to the heavy suppression of the MCs impedance at ω_{rf} provided by the llrf feedback. Moreover, the influence of the broadband impedance is also reduced in the presence of the 3HC, as discussed in the previous section. With these considerations, the longitudinal bunch distribution is determined mostly by the combination of the generator voltage and the 3HC beam-induced voltage. An interesting result is that the maximum lifetime improvement of 5.3 happens at $\Delta f_{3hc} = 38$ kHz, while at flat-potential condition, a factor 4 is expected. At this optimal condition for lifetime, the bunch is overstretched and the peak harmonic voltage is 1.03 MV, which is 8% higher than the flat-potential voltage.

Figure A.8 shows the equilibrium results for the hybrid filling pattern and the same

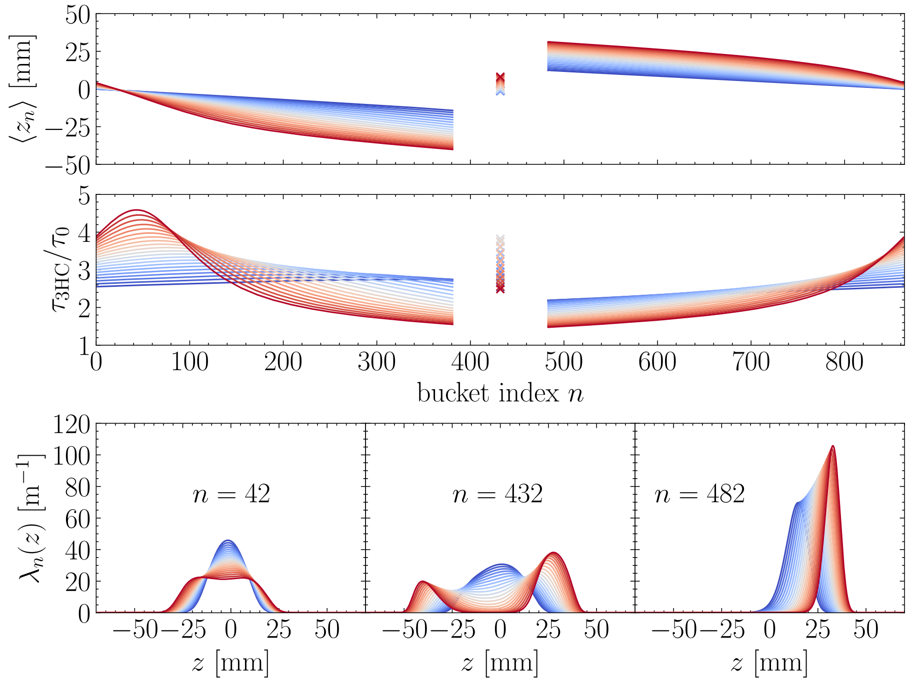

Figure A.8: Bunch centroids and lifetime improvement factor for the hybrid filling pattern with the full impedance model for SIRIUS. The colors indicate different 3HC detunings, following the frequency values from Fig. A.7. Bunch profiles for three bunches are shown in the bottom plot.

set of 3HC detunings from Fig. A.7. The lifetime improvement factor[11] was calculated with respect to the case without the 3HC and the same filling pattern. Note that for lower detunings the inhomogeneous beam-loading effects are more pronounced. The lifetime ratio is better for bunches in the middle of the train (bucket indices 820 to 120). Large bunch centroid shifts and degradation of bunch lengthening for bunches closer to the gaps is observed. The lifetime improvement for the high-charge bunch in the center (index 432) showed a similar qualitative behavior with the reduction of the 3HC detuning, as presented in the right plot of Fig. A.7. From these results it is clear that simply reducing the 3HC detuning is an ineffective approach to improve the overall lifetime for hybrid filling patterns and other strategies should be employed. A better solution can be the introduction of guard bunches to compensate the inhomogeneous beam-loading caused by gaps [75, 76, 108, 112].

[11]We plot the Touschek lifetime improvement factors in Fig. A.8 because the rms bunch length is not an appropriated metric for overstretched distributions, since the bunch profile is a composition of two shorter bunches.

A.6 Conclusion

In this chapter, we derived two approaches to compute the equilibrium beam-induced voltage in the presence of arbitrary filling patterns and impedance sources. The calculation in SD framework is limited to resonator wake-functions. The theory found in the literature [75–78, 112], was revisited, extended to consider the most general resonator model and formulated in a compact equation, convenient for numerical implementation in a uniformly discretized grid. A different approach, based on the FD analysis, allowed the generalization upon arbitrary impedance sources and offered a straightforward process for computing the beam-induced voltage in terms of DFTs. The low computational cost of the FD framework is noteworthy, as it has the benefits from FFT algorithms and its time complexity is constant besides the number of impedance elements. We benchmarked the results using the parameters of SIRIUS storage ring, a fourth-generation synchrotron. For uniform filling and narrowband resonators, it was analytically and numerically demonstrated that the two proposed frameworks reduce to a well-known formula for the beam-induced voltage. For nonuniform filling, the methods were benchmarked against macroparticle tracking and the results exhibited excellent agreement.

The beam-loading compensation of active rf cavities was addressed with the concept of closed-loop impedance. This approach can only be applied in the FD framework and is conceptually different from other methods based on phasor compensation or least square minimization. In the latter the parameters of the external voltage are adjusted to compensate the beam-loading, while the former changes the impedance model of the cavity so that the beam-induced voltage is intrinsically compensated. We observed that the stationary beam-loading compensation methods as described in Ref. [77] are equivalent to a closed-loop impedance of an integral controller with low gain. The proposed approach allows more realistic simulations of active rf cavities and is flexible to model several llrf system topologies.

Another advantage of the FD over the SD framework was illustrated with the simulation of the SIRIUS broadband impedance budget. This was easily accomplished in FD by taking the full impedance budget as a direct input for the calculations. In contrast, in SD the inclusion of broadband impedance requires additional steps, such as fitting BBRs or convolving short-range wake-function with longitudinal distributions [77, 78, 112]. These approaches, however, may introduce several numerical issues that must be handled and typically require a case-by-case analysis to define how each impedance contribution should be simulated.

We also studied the effect of different detunings of a passive superconducting 3HC on Touschek lifetime, taking into account the complete impedance budget for SIRIUS storage ring. For uniform filling, the maximum Touschek lifetime improvement was obtained with an overstretched bunch profile, increasing it by a factor 5.2, while the flat-potential condition is expected to the increase lifetime by a factor of 4. The more involved case of nonuniform filling pattern was briefly discussed only to illustrate the flexibility of the tool. Further investigations and more accurate metrics should be considered to compare performances in this case.

It is important to mention that the existence of equilibrium in simulation does not imply stability in the real machine. The map for reaching the steady-state in simulations is based on robust fixed-point algorithms, while the real dynamics depends on the intricate balance between damping and coherent excitation. As an example, to provide bunch lengthening, HHCs must operate at ac Robinson unstable detunings [51]. Fortunately, MCs can often be adjusted to a Robinson stable detuning and provide enough damping. However, for small HHC detunings as presented in this chapter, this balance should be carefully checked. Other time-dependent effects introduced by HHCs that can limit the achievable bunch lengthening may include, in particular, the recently predicted [82] and observed [122] mode-1 instability and, more generally, some instability induced by the reduction of the average incoherent synchrotron frequency as the longitudinal potential is flattened. A complete study covering time-dependent effects was beyond the scope of this chapter. Nevertheless, the developed framework can be useful in such studies for computing the unperturbed bunch distributions, which are essential inputs for single-bunch and multi-bunch instability thresholds calculation [81, 82, 85, 123].

In summary, the proposed FD methods proved to be more general, numerically stable and faster than the SD framework. This makes it a helpful tool during the design phase of a storage ring, when different specifications are being explored and the impact of machine components impedance on beam parameters should be quantified.

A.7 Limit case of uniform filling and passive narrow-band resonator

In this Appendix we will apply the equations derived in §A.2 to check its limit for a specific scenario: uniform filling pattern and high-Q resonator.

Consider the case of h bunches in a ring evenly filled with the same current per bunch $I_\ell = I_\mathrm{t}/h$. In the equilibrium state, the longitudinal distributions and beam-induced voltage will be equivalent for all bunches. Without loss of generality, we will take the rf bucket 0 as reference for the derivation.

A.7.1 Frequency-domain

Applying the uniform filling considerations to Eq. (A.29) reads

$$V_0(z) = -2(I_{\mathrm{t}}/h)\mathrm{Re}\left[\sum_{p=0}^{+\infty} Z^*(p\omega_0)e^{ip\omega_0 z/c}\hat{\lambda}_0^*(p\omega_0)\sum_{\ell=0}^{h-1} e^{-2\pi ip\ell/h}\right]. \tag{A.47}$$

The geometric series sum over ℓ yields

$$\sum_{\ell=0}^{h-1} e^{-2\pi ip\ell/h} = h\delta_{p,qh} \text{ for } q \in \mathbb{N} \tag{A.48}$$

where $\delta_{p,qh}$ is the Kronecker delta. Thus, the beam samples the impedance only at rf harmonics, which is expected from the symmetry of uniform filling.

Assuming a high-Q narrowband resonator impedance sharply peaked close to the mth rf harmonic, the major contribution to the beam-induced voltage is related to the term $q = m$. Applying Eq. (A.48) into Eq. (A.47) and retaining only the contribution from $\omega_m := m\omega_{\mathrm{rf}}$:

$$V_0(z) = -2I_{\mathrm{t}}\mathrm{Re}\left[Z^*(\omega_m)\hat{\lambda}_0^*(\omega_m)e^{i\omega_m z/c}\right]. \tag{A.49}$$

A convenient parametrization for the Fourier transform of longitudinal bunch distribution is

$$\hat{\lambda}_0(\omega) = F_0(\omega)e^{i\Phi_0(\omega)} \tag{A.50}$$

where, to respect the property $\hat{\lambda}_0(-\omega) = \hat{\lambda}_0^*(\omega)$, $F_0(\omega)$ must be a real-valued even function and $\Phi_0(\omega)$ a real-valued odd function. With this parametrization, Eq. (A.49) can be arranged as

$$V_0(z) = -2I_{\mathrm{t}}F_0(\omega_m)\mathrm{Re}\left[Z^*(\omega_m)e^{i[\omega_m z/c-\Phi_0(\omega_m)]}\right]. \tag{A.51}$$

The model for resonator impedance is given by the RLC circuit impedance from Eq. (A.38), rewritten as:

$$Z(\omega) = \frac{R_s}{1+2iQ\delta_\omega}, \tag{A.52}$$

with the resonator relative detuning defined as

$$\delta_\omega := \frac{1}{2}\left(\frac{\omega_R}{\omega} - \frac{\omega}{\omega_R}\right).$$

For frequencies close to resonance $\omega \approx \omega_R$, the approximated formula $\delta_\omega = \Delta\omega/\omega_R$ with $\Delta\omega = \omega_R - \omega$ is commonly used. The present analysis refers to $\omega_m \approx \omega_R$.

With the RLC impedance model, we are able to cast the wake voltage in the form:

$$V_0(z) = -2I_\mathrm{t}R_s\frac{F_0(\omega_m)}{1+4Q^2\delta_\omega^2}\left[\cos\theta_0(z) - 2Q\delta_\omega\sin\theta_0(z)\right], \tag{A.53}$$

where $\theta_0(z) = \omega_m z/c - \Phi_0(\omega_m)$.

Defining

$$\tan\psi := 2Q\delta_\omega, \tag{A.54}$$

then Eq. (A.53) can be further simplified to

$$V_0(z) = -2I_\mathrm{t}F_0(\omega_m)R_s\cos\psi\cos\left[\omega_m z/c + \psi - \Phi_0(\omega_m)\right] \tag{A.55}$$

which is a well-known formula for the equilibrium beam-induced voltage in uniform filling with a passive narrowband resonator, including the so-called complex bunch form-factor [106].

A.7.2 Space-domain

For high-Q resonators, we shall consider that the $I_0S_0(z)$ contribution in Eqs. (A.13) and (A.18) is negligible as compared to the summation part, since $S_0(z)$ only accounts for the self-induced voltage of a bunch on itself on the present turn. In this case and considering uniform filling, Eq. (A.18) can be simplified to

$$K_0(z) = (I_\mathrm{t}/h)e^{-\kappa z}\frac{S_0(\lambda_\mathrm{rf}/2)}{1-\nu}\sum_{\ell=1}^{h}\nu^{\ell/h} \tag{A.56}$$

We can approximate $\alpha/c \ll 1$ for long-range wakefields and take $e^{-\alpha z/c} \approx 1$. Moreover, since $\alpha/\omega_R = 1/2Q \ll 1$, it follows that $\bar{\omega}_R \approx \omega_R$. Therefore, $e^{\pm\kappa z} \approx e^{\mp i\omega_R z/c}$. In this scope, the Laplace transform can be replaced by the Fourier transform:

$$S_0(\lambda_\mathrm{rf}/2) = \int_{-\lambda_\mathrm{rf}/2}^{\lambda_\mathrm{rf}/2}\mathrm{d}z'\lambda_0(z')e^{\kappa z'} \approx \hat{\lambda}_0^*(\omega_R).$$

The sum over bunches ℓ is the sum of $h-1$ terms of a geometric series with common ratio $\nu^{1/h}$, hence:

$$\sum_{\ell=1}^{h}\nu^{\ell/h} = \nu^{1/h}\frac{1-\nu}{1-\nu^{1/h}}$$

Recall that $\nu^{1/h} = e^{-\kappa C_0/h} = e^{-\kappa\lambda_\mathrm{rf}}$. Applying those partial results into Eq. (A.56) yields:

$$K_0(z) = (I_\mathrm{t}/h)e^{i\omega_R z/c}\frac{\hat{\lambda}_0^*(\omega_R)}{e^{\kappa\lambda_\mathrm{rf}}-1}. \tag{A.57}$$

Following the method applied in Ref. [76], let (ρ, ψ) be polar variables in the complex plane such that

$$\frac{1}{e^{\kappa\lambda_{\rm rf}} - 1} = \rho e^{i\psi}. \tag{A.58}$$

With $\lambda_{\rm rf} = 2\pi c/\omega_{\rm rf}$, then $e^{\kappa\lambda_{\rm rf}} = e^{2\pi\alpha/\omega_{\rm rf}} e^{-2\pi i\omega_R/\omega_{\rm rf}}$. Considering that the resonant frequency is close to the mth rf harmonic, the detuning is $\Delta\omega = \omega_R - m\omega_{\rm rf}$. From this, $e^{-2\pi i\omega_R/\omega_{\rm rf}} = e^{-2\pi i\Delta\omega/\omega_{\rm rf}}$ follows. Besides, assuming a small detuning such that $\Delta\omega/\omega_{\rm rf} \ll 1$, the exponential can be approximated in first order to:

$$\begin{aligned} e^{\kappa\lambda_{\rm rf}} - 1 &\approx (1 + 2\pi\alpha/\omega_{\rm rf})(1 - 2\pi i\Delta\omega/\omega_{\rm rf}) - 1 \\ &\approx \frac{1}{f_{\rm rf}} (\alpha - i\Delta\omega), \end{aligned}$$

where the second order term proportional to $\alpha\Delta\omega/\omega_{\rm rf}^2$ was neglected. Therefore:

$$\rho = \left| \frac{1}{e^{\kappa\lambda_{\rm rf}} - 1} \right| \approx \frac{f_{\rm rf}}{\sqrt{\alpha^2 + \Delta\omega^2}}, \tag{A.59}$$

and the phase can be calculated with

$$\begin{aligned} \psi = \arg\left(\frac{1}{e^{\kappa\lambda_{\rm rf}} - 1}\right) &= -\arg\left(e^{\kappa\lambda_{\rm rf}} - 1\right) \\ &= \arctan(\Delta\omega/\alpha). \end{aligned} \tag{A.60}$$

Note that $\tan\psi = 2Q\Delta\omega/\omega_R$, which is the same relation between the detuning phase ψ and resonator parameters defined in Eq. (A.54).

With those approximations and using Eq. (A.50) for the bunch spectrum, Eq. (A.57) simplifies to

$$K_0(z) = \frac{(I_{\rm t}/h) f_{\rm rf}}{\sqrt{\alpha^2 + \Delta\omega^2}} F_0(\omega_R) e^{i[\omega_R z/c + \psi - \Phi_0(\omega_R)]} \tag{A.61}$$

Applying this result to Eq. (A.12) reads, after some manipulations,

$$V_0(z) = -2I_{\rm t} F_0(\omega_R) R_s \cos\psi \left[\cos\gamma_0(z) - \frac{\alpha}{\omega_R}\sin\gamma_0(z)\right], \tag{A.62}$$

where $\gamma_0(z) = \omega_R z/c + \psi - \Phi_0(\omega_R)$.

The sine term in Eq. (A.62) can be neglected since $\alpha/\omega_R \ll 1$. Additionally, approximating the resonant frequency to its closest rf harmonic $\omega_R \approx \omega_m$, then Eq. (A.62) is equivalent to the formula in Eq. (A.55).

Publication: Alves, M. B. Theoretical models for longitudinal coupled-bunch instabilities driven by harmonic cavities in electron storage rings. Phys. Rev. Accel. Beams ***28****, 034401 (2025). DOI:* https://doi.org/10.1103/PhysRevAccelBeams.28.034401

B

Article 2: Coupled-bunch instabilities with potential-well distortion

Contents

We present a theoretical framework for analyzing longitudinal coupled-bunch instabilities in double-rf systems with even filling patterns, accounting for potential-well distortion and multiple azimuthal modes. The linearized Vlasov equation is solved in the frequency-domain for an arbitrary rf potential to derive the Lebedev equation. We unified different formulations, obtaining results from recent publications as particular cases. Applications to Robinson dipole-quadrupole mode coupling and the periodic transient beam loading (PTBL)/mode-1 instability are presented. Notably, for the first time, theoretical predictions of the mode-1 thresholds show excellent agreement with experimental data. The analysis reveals that the PTBL instability is triggered when coherent focusing is lost for the dipole motion of the coupled-bunch mode 1. We also confirm that this instability is dependent on azimuthal mode interactions and resistant to Landau damping, providing new insights into its mechanism. The methods are implemented in the open-source package `pycolleff`, offering a useful semi-analytical tool for studying instabilities in electron storage rings with harmonic cavities.

B.1 Introduction

Collective instabilities in double-rf systems with HCs have been a concern for synchrotrons for many years [26, 124–126]. In modern synchrotron light sources, passive HCs are employed in the bunch lengthening mode to reduce the bunch charge density, alleviating collective effects such as intrabeam scattering, Touschek scattering and impedance-induced heating of components. These effects have become critical issues for the 4th-generation synchrotron light sources with ultralow transverse emittances [16, 127].

The theoretical description of instabilities in double-rf systems is significantly more challenging than the theory for single-rf systems, for which a well-developed theory exists in the literature [50, 51, 66]. In electron rings with single-rf systems, assuming linear single-particle dynamics (harmonic rf potential) and Gaussian bunch distributions are valid approximations for short-bunches. These approximations considerably simplify the analytical description and calculations of instabilities. In contrast, the single-particle motion in double-rf systems can be significantly modified by potential-well distortion effects induced by the HCs, leading to highly nonlinear dynamics and non-Gaussian bunch distributions [79–82, 128]. The effects of HCs on beam stability can be twofold: they can stabilize the beam by lengthening the bunches, reducing charge density and providing Landau damping through the spread of incoherent synchrotron frequencies; or they can degrade the stability by lowering the average synchrotron frequency and by introducing additional impedance.

For longitudinal coupled-bunch instabilities in single-rf systems, a standard approach is to ignore the interaction between azimuthal (synchrotron) modes. This simplification assumes that the current per bunch is not too high and that multibunch instabilities are typically driven by narrowband impedances (long-range wakefields) that do not significantly affect intrabunch motion. Under these conditions, the azimuthal modes are sufficiently separated, allowing each mode to be studied independently. However, for coupled-bunch instabilities in double-rf systems, the situation may change. Even for low currents per bunch, the azimuthal modes may interact due to the flattening of the rf potential. Therefore, taking into account the potential-well distortion, which was normally required only to study single-bunch instabilities [129–136], might also be important [81, 82].

This work develops a theoretical formulation in the frequency-domain to analyze longitudinal instabilities in double-rf systems, accounting for the nonlinear effects of potential-well distortion and interactions between multiple azimuthal modes. The theory applies to both multibunch and single-bunch cases, assuming an even filling pattern such that every filled bucket sees the same equilibrium potential and has the same bunch distribution. Even though the cases discussed in this work are focused on double-rf systems, the framework is also suited for instability studies involving generic narrowband resonators, such as HOMs from rf cavities, while incorporating the impact of potential-well distortion from the machine broadband impedance. We follow the step-by-step approach in Ref. [82] to manipulate the Vlasov equation and show that the Lebedev matrix equation, originally derived in Ref. [137], can be obtained. The formulation developed here is essentially equivalent in generality to Lebedev's work. For completeness, we derive the Lebedev equation in detail using a modern notation as in Ref. [138], and demonstrate its connection to recent developments [81, 82, 85].

The paper is structured as follows. The theoretical models are developed in §A.2. In §B.3, generic dispersion-relations for narrowband resonators are derived from the Lebedev equation, yielding the models from Refs. [81, 85] as particular cases. §B.4 applies the theory to Robinson dipole-quadrupole mode coupling and PTBL/mode-1 instabilities, benchmarking the predictions with MAX IV experimental data and achieving, for the first time, excellent agreement with measured mode-1 thresholds. In §B.5, details of the PTBL instability mechanism are discussed. §B.6 summarizes the findings and presents the conclusions.

B.2 Theory

We will adopt the definition of the relative longitudinal coordinate z of relativistic particles in a storage ring, whose origin is defined by the synchronous particle with nominal energy E_0. The sign convention $z > 0$ is adopted for trailing particles. All the following derivations assume an even filling condition, i.e., all filled buckets with the same current and identical equilibrium longitudinal bunch distributions $\lambda_0(z)$.

Consider that the longitudinal equilibrium is obtained as a self-consistent solution of the Haïssinski equation considering potential-well distortion effects, for example with the semi-analytical method presented in Ref. [44]. This calculation provides the equilibrium wake voltage $V_{\mathrm{wake}}(z; \lambda_0)$ that is added to the external rf voltage $V_{\mathrm{rf}}(z)$ to result in the total equilibrium voltage $V_0(z) = V_{\mathrm{rf}}(z) + V_{\mathrm{wake}}(z; \lambda_0)$. The equilibrium potential is then calculated as:

$$\Phi_0(z;\lambda_0) = -\frac{1}{E_0 C_0}\int_0^z \mathrm{d}z' \,[eV_0(z';\lambda_0) - U_0], \tag{B.1}$$

with $\lambda_0(z)$ satisfying the Haïssinski equation:

$$\lambda_0(z) = \frac{1}{\mathcal{N}_z}\exp\left[-\frac{\Phi_0(z;\lambda_0)}{\alpha\sigma_\delta^2}\right], \tag{B.2}$$

where the constant $\mathcal{N}_z$ normalizes $\lambda_0(z)$ to unity, σ_δ is the equilibrium relative energy spread, α is the momentum compaction factor (assuming above transition, so the slip factor is $\alpha - 1/\gamma^2 \approx \alpha$), E_0 is the ring nominal energy, C_0 the ring circumference, $e > 0$ is the elementary charge and U_0 is the energy loss per turn from synchrotron radiation.

Considering (z, δ) as canonical coordinates, where $\delta = (E - E_0)/E_0$ is the relative energy deviation, in this equilibrium potential the single-particle equations of motion are [50]:

$$\frac{\mathrm{d}z}{\mathrm{d}s} = \alpha\delta, \tag{B.3}$$

$$\frac{\mathrm{d}\delta}{\mathrm{d}s} = \frac{eV_0(z;\lambda_0) - U_0}{E_0 C_0}, \tag{B.4}$$

where the independent variable s is the longitudinal position of the synchronous particle along the ring. The equations of motion are associated with the unperturbed Hamiltonian

$$\mathcal{H}_0 = \frac{\alpha\delta^2}{2} + \Phi_0(z;\lambda_0). \tag{B.5}$$

It is useful for the following instability analysis to perform a canonical transformation to action-angle variables $(z, \delta) \to (J, \varphi)$. The numerical determination of the canonical transformation can be done, for instance, following the procedure described in the Appendix C of Ref. [82]. With that procedure we obtain the transformation in a rectangular grid $z_{ij} = \zeta(J_i, \varphi_j)$.

The two-dimensional distribution Ψ in the longitudinal phase-space satisfies the Vlasov equation:

$$\frac{\mathrm{d}\Psi}{\mathrm{d}s} = \frac{\partial\Psi}{\partial s} + \{\Psi, \mathcal{H}\} = 0, \tag{B.6}$$

with $\{\Psi, \mathcal{H}\}$ denoting the Poisson brackets.

We consider a small perturbation from the equilibrium that oscillates with a complex coherent frequency Ω. The perturbed distribution will be associated to a perturbation in the Hamiltonian:

$$\Psi(J, \varphi, s) = \Psi_0(J) + \Psi_1(J, \varphi)e^{-i\Omega s/c}, \tag{B.7}$$

$$\mathcal{H}(J, \varphi, s) = \mathcal{H}_0(J) + \Phi_1(J, \varphi)e^{-i\Omega s/c}, \tag{B.8}$$

where $\Psi_0(J) = (2\pi\mathcal{N}_J)^{-1}e^{-\mathcal{H}_0(J)/\alpha\sigma_\delta^2}$ is the equilibrium distribution, also normalized to unity.

Applying this perturbation to the Vlasov equation and linearizing it, leads to

$$-i\Omega\Psi_1 + \omega_s(J)\frac{\partial\Psi_1}{\partial\varphi} - c\frac{\partial\Psi_0}{\partial J}\frac{\partial\Phi_1}{\partial\varphi} = 0, \tag{B.9}$$

where $\omega_s(J) = c\frac{\partial\mathcal{H}_0}{\partial J}$ is the amplitude-dependent synchrotron frequency.

For the even filling case, in the equilibrium state all bunch profiles are identical. However, when a coupled-bunch instability is driven, each bunch can have a different profile and time evolution, governed by a system of coupled Vlasov equations. We will assume there are M equidistant bunches in the ring, with $1 \le M \le h$, where h is the harmonic number. The perturbation distribution for the nth bunch is represented as $\Psi_{1,n}^{(\ell)}(J,\varphi,s) = \Psi_1^{(\ell)}(J,\varphi,s)e^{2\pi in\ell/M}$ with $\ell = 0, 1, \ldots, M-1$ referring to the coupled-bunch mode number. Using the coupled-bunch mode basis, $\{\ell\}$, instead of the bunch index basis, $\{n\}$, decouples the system of Vlasov equations into M independent equations for each coupled-bunch distribution $\Psi_1^{(\ell)}(J,\varphi,s)$. For brevity, we will drop the reference to the coupled-bunch index ℓ in the perturbation distribution. For the single-bunch case, $\ell = 0$ and there is only one Vlasov equation to be solved.

The wake voltage induced by the perturbation is

$$V_1(z;\lambda_1) = -I_0\sum_{p=-\infty}^{\infty}\tilde{\lambda}_{1;p,\ell}(\Omega)Z_{p,\ell}(\Omega)e^{-i\omega_{p,\ell}z/c}, \tag{B.10}$$

where I_0 is the total beam current, $\omega_{p,\ell} = (pM+\ell)\omega_0$, ω_0 the revolution frequency. For compactness, we introduced the notation $\tilde{\lambda}_{1;p,\ell}(\Omega) := \tilde{\lambda}_1(\omega_{p,\ell}+\Omega)$ and $Z_{p,\ell}(\Omega) := Z(\omega_{p,\ell}+\Omega)$. $\tilde{\lambda}_1(\omega)$ is the Fourier transform of the perturbing bunch distribution

$$\begin{aligned}\tilde{\lambda}_1(\omega) &= \int_{-\infty}^{\infty}\mathrm{d}z\, e^{i\omega z/c}\lambda_1(z)\\ &= \int_{-\infty}^{\infty}\mathrm{d}z\, e^{i\omega z/c}\int_{-\infty}^{\infty}\mathrm{d}\delta\,\Psi_1(z,\delta)\\ &= \int_0^{\infty}\int_0^{2\pi}\mathrm{d}\varphi\,\mathrm{d}J\, e^{i\omega\zeta(J,\varphi)/c}\Psi_1(J,\varphi).\end{aligned} \tag{B.11}$$

The approximation $\tilde{\lambda}_{1;p,\ell}(\Omega) \approx \tilde{\lambda}_1(\omega_{p,\ell})$ can generally be done in Eq. (B.10), because $\tilde{\lambda}_1(\omega)$ is a smooth function and $\mathrm{Re}(\Omega) \ll \omega_{p,\ell}$. As the impedance $Z(\omega)$ can be related to narrowband resonators, it is important to keep the Ω dependence in its argument. Note that the term $e^{-i\Omega s/c}$ has already been factored out in Eq. (B.8). $Z(\Omega)$ is well-defined for complex Ω, given that the impedance function is analytic [51]. The corresponding perturbation of the wake potential and its derivative are:

$$\Phi_1(\zeta) = -\int_0^\zeta \mathrm{d}\zeta' \, \frac{eV_1(\zeta';\lambda_1)}{E_0C_0}, \tag{B.12}$$

$$\frac{\partial \Phi_1}{\partial \varphi} = \frac{eI_0}{E_0C_0} \sum_{p=-\infty}^{\infty} \tilde{\lambda}_1(\omega_{p,\ell}) \frac{Z_{p,\ell}(\Omega)}{-i\omega_{p,\ell}/c} \frac{\partial}{\partial \varphi} e^{-i\omega_{p,\ell}\zeta/c}. \tag{B.13}$$

Next, we use the azimuthal symmetry with respect to φ to expand the perturbation in azimuthal modes m:

$$\Psi_1(J,\varphi) = \sum_{m\neq 0} R_m(J) e^{im\varphi}, \tag{B.14}$$

where $R_m(J)$ are real-valued functions. The bunch spectrum from Eq. (B.11) is then written as

$$\tilde{\lambda}_1(\omega_p) = 2\pi \sum_{m\neq 0} \int_0^\infty \mathrm{d}J \, R_m(J) H_{m,p}(J), \tag{B.15}$$

$$H_{m,p}(J) := \frac{1}{2\pi} \int_0^{2\pi} \mathrm{d}\varphi \, e^{im\varphi + i\omega_{p,\ell}\zeta(J,\varphi)/c}. \tag{B.16}$$

As remarked in Ref. [138], the functions $H_{m,p}(J)$ were first introduced by Lebedev in 1968 [137]. The functions $H_{m,p}(J)$ depend on the beam current and impedances as the canonical transformation $\zeta(J,\varphi)$ is modified by the potential-well distortion.

Inserting all these results in the linearized Vlasov equation, multiplying by $e^{-in\varphi}$ and integrating over φ (recall that $\int_0^{2\pi} \mathrm{d}\varphi \, e^{i(m-n)\varphi} = 2\pi\delta_{mn}$) results in

$$(\Omega - m\omega_s(J))R_m(J) + im\kappa \frac{\partial \Psi_0}{\partial J} \sum_{p=-\infty}^{\infty} \frac{Z_{p,\ell}(\Omega)}{\omega_{p,\ell}} H^*_{m,p}(J) \sum_{m'\neq 0} \int_0^\infty \mathrm{d}J \, R_{m'}(J) H_{m',p}(J) = 0, \tag{B.17}$$

where we defined the intensity parameter:

$$\kappa = \frac{2\pi e I_0 c^2}{E_0 C_0}, \tag{B.18}$$

and used the result

$$\frac{1}{2\pi} \int_0^{2\pi} \mathrm{d}\varphi \, e^{-im\varphi} \frac{\partial}{\partial \varphi} e^{-i\omega_{p,\ell}\zeta/c} = imH^*_{m,p}(J). \tag{B.19}$$

Until this point, our derivation closely followed the notation and steps presented in Venturini's paper, e.g., compare Eq. (B.17) here with Eq. (17) in [82]. The goal now is to further manipulate the integral equation (B.17) to obtain a dispersion-relation that must be solved for the coherent frequency Ω.

We will first, for completeness, reproduce Venturini's approach. Then, we will present an extension of Venturini's results that leads to the Lebedev equation. From that, we will introduce an effective model that neglects the Landau damping and present the Gaussian LMCI model discussed in previous investigations [139, 140].

B.2.1 Venturini's approach

Multiplying Eq. (B.17) by $H_{m,p'}(J)$, dividing it by $(\Omega - m\omega_s(J))$ and integrating it over J, we obtain:

$$X_{m,p'} + im\kappa \sum_{p=-\infty}^{\infty} \frac{Z_{p,\ell}(\Omega)}{\omega_{p,\ell}} G_{m,pp'}(\Omega) \sum_{m'\neq 0} X_{m',p} = 0, \tag{B.20}$$

where

$$X_{m,p} = \int_0^\infty \mathrm{d}J \, R_m(J) H_{m,p}(J), \tag{B.21}$$

$$G_{m,pp'} = \int_0^\infty \mathrm{d}J \, \frac{\partial \Psi_0}{\partial J} \frac{H_{m,p'}(J) H^*_{m,p}(J)}{\Omega - m\omega_s(J)}. \tag{B.22}$$

Equation (B.20) can be rewritten as an infinite system of equations:

$$\sum_{p=-\infty}^{\infty} \sum_{m'\neq 0} B_{mm',pp'}(\Omega) X_{m',p} = 0, \tag{B.23}$$

$$B_{mm',pp'}(\Omega) = \delta_{mm',pp'} + im\kappa \frac{Z_{p,\ell}(\Omega)}{\omega_{p,\ell}} G_{m,pp'}(\Omega). \tag{B.24}$$

As in the case of interest of Ref. [82], for a narrowband resonator, only a single harmonic $\pm p_0$ has a significant impedance contribution. Moreover, in practice, the problem is solved by truncating the sum to $\pm m_{\max}$. In this way, $B_{mm',pp'}(\Omega)$ becomes a finite $4m_{\max} \times 4m_{\max}$ matrix. As we are interested in non-trivial solutions, $X_{m,p} \neq 0$, the coherent frequency Ω is computed as the root of the determinant of the $B(\Omega)$ matrix.

B.2.2 Lebedev equation

Equation (B.20) can be further simplified. Applying a summation over m and defining

$$Y_p = \sum_{m\neq 0} X_{m,p} \quad \text{and} \quad G_{pp'}(\Omega) = \sum_{m\neq 0} m G_{m,pp'}(\Omega), \tag{B.25}$$

simplifies Eq. (B.20) to

$$Y_{p'} + i\kappa \sum_{p=-\infty}^{\infty} \frac{Z_{p,\ell}(\Omega)}{\omega_{p,\ell}} G_{pp'}(\Omega) Y_p = 0. \tag{B.26}$$

The infinite system of equations is now

$$\sum_{p=-\infty}^{\infty} B_{pp'}(\Omega) Y_p = 0, \tag{B.27}$$

$$B_{pp'}(\Omega) = \delta_{pp'} + i\kappa \frac{Z_{p,\ell}(\Omega)}{\omega_{p,\ell}} G_{pp'}(\Omega). \tag{B.28}$$

In this format, the system of equations is equivalent to the Lebedev equation [137] as derived in Ref. [138], see Eqs. (33-36) from [138].

From Eq. (B.16) we can derive the property $H_{-m,p}(J) = H_{m,p}(J)$, using that $\zeta(J,\varphi)$ is an even function and 2π-periodic with respect to φ. This symmetry simplifies the matrix $G_{pp'}(\Omega)$, combining positive and negative azimuthal modes:

$$G_{pp'}(\Omega) = \int_0^\infty \mathrm{d}J \, \frac{\partial \Psi_0}{\partial J} g_{pp'}(J,\Omega), \tag{B.29}$$

$$g_{pp'}(J,\Omega) = \sum_{m=1}^{\infty} 2m^2 \omega_s(J) \frac{H_{m,p'}(J) H^*_{m,p}(J)}{\Omega^2 - m^2\omega_s^2(J)}, \tag{B.30}$$

where it was assumed that the integrand does not diverge so the sum over m can be interchanged with the integral.

We introduced the auxiliary function $g_{pp'}(J,\Omega)$. Equation (B.29) for $G_{pp'}(\Omega)$ is quite convenient since the truncation of azimuthal modes can be controlled based on the convergence of the function $g_{pp'}(J,\Omega)$ at run-time for each iteration of the root finding algorithm for Ω.

It is important to highlight that with the Lebedev equation, the dimensionality of the matrix and the number of numerical integrations do not depend on the truncation $m_{\max}$. Hence, we showed that Venturini's formulation is essentially equivalent to the Lebedev equation with the disadvantage of having an avoidable computational complexity that increases with $m_{\max}$.

B.2.3 Effective synchrotron frequency model

What set the requirement of a nonlinear solution method for Ω in the integral equation in Eq. (B.17) are the dependencies of the synchrotron frequency with action $\omega_s(J)$ and the impedance with Ω. With this observation, we will formulate a simplified linear problem with minimal changes.

Suppose that $\omega_s(J)$ is replaced by a constant effective synchrotron frequency $\bar{\omega}_s$. A possible choice for $\bar{\omega}_s$ will be presented in the next section. This change may impact the results by neglecting the frequency spread and Landau damping. Additionally, if we approximate $Z_{p,\ell}(\Omega) \approx Z_{p,\ell}(m\bar{\omega}_s)$, then Eq. (B.17) can be simplified to an eigenvalue equation:

$$\sum_{p=-\infty}^{\infty}\sum_{m'=-\infty}^{\infty} C_{mm',pp'} X_{m',p} = \Omega X_{m,p'}, \tag{B.31}$$

$$C_{mm',pp'} = m\bar{\omega}_s \delta_{mm',pp'} - im\kappa \frac{Z_{p,\ell}\left(m\bar{\omega}_s\right)}{\omega_{p,\ell}} F_{m,pp'}, \tag{B.32}$$

$$F_{m,pp'} = \int_0^{\infty} \mathrm{d}J \, \frac{\partial \Psi_0}{\partial J} H_{m,p'}(J) H^*_{m,p}(J), \tag{B.33}$$

and $X_{m,p}$ is the same as defined in Eq. (B.21). We can proceed by truncating the azimuthals $m_{\max}$ and selecting the harmonics p to find the coherent frequencies Ω as the eigenvalues of $C_{mm',pp'}$.

Note that the nonlinearities can still play a role in this model, not through Landau damping as the frequency spread is neglected, but through the terms $H_{m,p}(J)$ that encodes the nonlinear dynamics in the phase of $e^{i\omega_{p,\ell}\zeta(J,\varphi)/c}$ [141]. Besides, the bunch profile distortions are accounted through the numerical solution of the Haïssinski equation, which is used to compute $\frac{\partial \Psi_0}{\partial J}$ numerically instead of an analytical distribution, as done in the next model we will present.

B.2.4 Gaussian longitudinal mode coupling

Multibunch instability thresholds can be computed by employing Suzuki's frequency-domain solution of Vlasov equation for longitudinal instabilities, which allows mode coupling between different azimuthal and radial modes of the bunch motion [142]. The theory assumes that the single-particle dynamics is linear and that the longitudinal bunch distribution is Gaussian. This makes the theory suitable for studying instabilities in single-rf systems, neglecting potential-well distortion. Nevertheless, in the past some success was achieved in using a linear Gaussian theory to study the instabilities in HC systems [143, 144].

Suzuki expanded the radial function $R(J)$ in a basis of orthogonal functions to solve Sacherer's integral equation. With Gaussian bunch distributions, generalized Laguerre polynomials were used as orthogonal functions. Suzuki's solution yields the infinite matrix equation [142]:

$$\sum_{m'=1}^{\infty}\sum_{k'=0}^{\infty} A^{mk}_{m'k'} b^{(m')}_{k'} = \left(\frac{\Omega}{\omega_s}\right)^2 b^{(m)}_k, \tag{B.34}$$

$$A^{mk}_{m'k'} = m^2 \delta_{m'm}\delta_{k'k} + i\frac{m^2 e c^2 \alpha I_0}{\pi \sigma_z^2 \omega_s^2 E_0} M^{mk}_{m'k'}, \tag{B.35}$$

where (m, m') and (k, k') are indices for the azimuthal and radial modes, respectively. The coupling matrix depends on the longitudinal impedance $Z(\omega)$ and beam spectrum

$$M_{m'k'}^{mk} = \sum_{p=-\infty}^{\infty} \frac{Z(\omega_{p,\ell}+\Omega)}{\omega_{p,\ell}} i^{m'-m} I_{m'k'}\left(\frac{\omega_{p,\ell}+\Omega}{\omega_0}\right) I_{mk}\left(\frac{\omega_{p,\ell}+\Omega}{\omega_0}\right). \tag{B.36}$$

For Gaussian bunches, the functions $I_{mk}(p)$ have the analytic form:

$$I_{mk}\left(\frac{\omega_{p,\ell}}{\omega_0}\right) = \frac{1}{\sqrt{(m+k)!k!}}\left(\frac{\zeta_{p,\ell}}{2}\right)^{m+2k} \exp\left(-\frac{\zeta_{p,\ell}^2}{4}\right), \tag{B.37}$$

where $\zeta_{p,\ell} = \sqrt{2}\sigma_z\omega_{p,\ell}/c$. To solve the matrix problem, the sums are truncated to $m_{\max}$ and $k_{\max}$. Moreover, the approximation $\Omega \approx m\omega_s$[1] is applied to compute the finite coupling matrix $M_{m'k'}^{mk}$. The analysis can be specialized to each coupled bunch mode ℓ. Then, the coherent frequencies Ω are obtained by diagonalization.

The LMCI theory can be applied to coupled-bunch instabilities in double-rf system, requiring a minor yet important adaptation in the calculation process. The values for bunch length and average incoherent synchrotron frequency can be obtained from the self-consistent solution of the Haïssinski equation. With this adaptation, the potential-well distortion caused by the HC is not fully neglected for the instability analysis. However, it is important to note that this scheme also ignores the frequency spread, thus Landau damping effects are neglected. We will refer to this approximate model as "Gaussian LMCI".

Such as in the effective synchrotron frequency model, in the Gaussian LMCI the constant incoherent synchrotron frequency is a crucial input. Considering that the approximation of Gaussian bunch is already made, a simple choice for the constant frequency is to maintain the relation between synchrotron frequency and bunch length that holds for harmonic single-rf systems (quadratic rf potential):

$$\langle\omega_s\rangle_{\text{quadratic}} = \frac{\alpha c\sigma_\delta}{\sigma_z}. \tag{B.38}$$

The synchrotron frequency can be determined by the bunch length (assuming the momentum compaction and energy spread are fixed). In this way, we will be evaluating the instability in a fictitious equivalent quadratic system with the same bunch length as produced by the HC. Such approach was suggested in Refs. [64, 81].

The Gaussian LMCI method has the advantage of being considerably faster than the previous methods of solving the Lebedev equation and the effective synchrotron frequency model, since its matrix elements are computed by analytical expressions, while the others require additional calculations for the numerical canonical transformation and numerical

[1]The approximation $\Omega \approx m\omega_s$ with $m = 1$ for all elements was considered in the `pycolleff` implementation for computational speed, and it was verified that varying m from 0 to 10 did not affect the results presented in this chapter.

integrations. Equation (B.38) will also be the choice for $\bar{\omega}_s$ in the effective model from §B.2.3 used throughout this chapter.

B.3 The dispersion-relation for a narrowband resonator

In this section we will present a theoretical result from our framework. We will demonstrate that the dispersion-relation equations developed in previous works [81, 82, 85] can be obtained from the Lebedev equation as special cases. With that we will prove the equivalence of the two approaches under certain conditions.

For the particular case of a narrowband resonator, we can retain a single harmonic $\pm p_0$ and $G_{pp'}(\Omega)$ is a 2×2 matrix. For this case, the Lebedev equation yields

$$\begin{aligned} 0 = \det &\begin{bmatrix} 1 + i\kappa M_{-p_0-p_0}(\Omega) & i\kappa M_{-p_0 p_0}(\Omega) \\ i\kappa M_{p_0-p_0}(\Omega) & 1 + i\kappa M_{p_0 p_0}(\Omega) \end{bmatrix} \\ &\approx 1 + i\kappa \left(M_{p_0 p_0}(\Omega) + M_{-p_0-p_0}(\Omega) \right), \end{aligned} \tag{B.39}$$

where $M_{pp'} = \frac{Z_{p,\ell}(\Omega)}{\omega_{p,\ell}} G_{pp'}(\Omega)$. The approximation refers to $M_{-p_0 p_0} M_{p_0 -p_0} \approx M_{p_0 p_0} M_{-p_0 -p_0}$, which follows from the property $H_{m,-p}(J) \approx H^*_{m,p}(J)$ that can be checked from Eq. (B.16). The approximation is better for $p_0 h \gg \ell$.

We will assume symmetric elliptical orbits on the longitudinal phase-space, thus the canonical transformation can be approximately factored as

$$\zeta(J, \varphi) \approx f(J) \cos(\varphi). \tag{B.40}$$

This form is exact for a quadratic (harmonic) potential and a good approximation even for a quartic potential, as discussed in the Appendix B of Ref. [81]. With this form, we have that

$$\begin{aligned} H_{m,p}(J) &\approx \frac{1}{2\pi} \int_0^{2\pi} \mathrm{d}\varphi \, e^{im\varphi + i\omega_{p,\ell} f(J) \cos(\varphi)/c} \\ &= i^m \mathcal{J}_m \left(\omega_{p,\ell} f(J)/c \right), \end{aligned} \tag{B.41}$$

where $\mathcal{J}_m(x)$ is the Bessel function of the first kind.

We can use the approximation that the wakefield varies slowly over the length of the bunch. In Refs. [81, 85], this justifies a Taylor expansion of the longitudinal wake function keeping only low-order terms. In our framework, this limit corresponds to consider a short-bunch, $\omega_{p_0,\ell} f(J)/c \ll 1$, so we can use the approximation of the Bessel function for small arguments:

$$\mathcal{J}_m(x) \approx i^m \frac{(x/2)^m}{m!}. \tag{B.42}$$

From the relation between $\Psi_0(J)$ and $\mathcal{H}_0(J)$, we can show that $\frac{\partial\Psi_0}{\partial J} = -\frac{\omega_s(J)}{\alpha c\sigma_\delta^2}\Psi_0(J)$. Then, in the short-bunch limit, the determinant Eq. (B.39) results in:

$$1 = \frac{2i\kappa}{\alpha c\sigma_\delta^2}\sum_{p=\pm p_0}\frac{Z_{p,\ell}(\Omega)}{\omega_{p,\ell}}\int_0^\infty \mathrm{d}J\,\Psi_0(J)\sum_{m=1}^\infty\frac{(\omega_{p,\ell}/c)^{2m}}{(m!)^2}\frac{m^2\left[f(J)/2\right]^{2m}}{\left[\Omega/\omega_s(J)\right]^2-m^2}. \tag{B.43}$$

Let us define the normalized effective impedance of order n:

$$Z^{(n)}_{\mathrm{eff},\ell}(\Omega) = \sum_{p=\pm p_0}\left(\sigma_z\omega_{p,\ell}/c\right)^n Z_{p,\ell}(\Omega). \tag{B.44}$$

Note that the factor $\sigma_z\omega_{p,\ell}/c$ is dimensionless, and it is worth mentioning that the bunch length σ_z (in this work, always taken as the second central moment of $\lambda_0(z)$) was not fundamental, it was introduced only for the purpose of a convenient normalization. In the SSB.7 we show that the normalized impedance of order n can be related to the nth derivative of the wake function.

With κ given by Eq. (B.18), the dispersion-relation for all azimuthals m is:

$$1 = i\frac{4\pi e I_0\sigma_z}{E_0 C_0\alpha\sigma_\delta^2}\int_0^\infty \mathrm{d}J\,\Psi_0(J)\sum_{m=1}^\infty\frac{Z^{(2m-1)}_{\mathrm{eff},\ell}(\Omega)}{(m!)^2}\frac{m^2\left[f(J)/2\sigma_z\right]^{2m}}{\left[\Omega/\omega_s(J)\right]^2-m^2}. \tag{B.45}$$

We define the $\Lambda^{(m)}_\ell(\Omega)$ parameter as:

$$\Lambda^{(m)}_\ell(\Omega) = i\frac{eI_0}{2E_0T_0\sigma_\delta}\frac{Z^{(2m-1)}_{\mathrm{eff},\ell}(\Omega)}{(m!)^2}, \tag{B.46}$$

and replacing this definition into Eq. (B.45) yields:

$$1 = \frac{2\sigma_z}{\alpha c\sigma_\delta}\sum_{m=1}^\infty \Lambda^{(m)}_\ell(\Omega)D_m(\Omega), \tag{B.47}$$

with the dispersion integral for the azimuthal mode m:

$$D_m(\Omega) = \int_0^\infty \mathrm{d}J\,4\pi\Psi_0(J)\frac{m^2\left[f(J)/2\sigma_z\right]^{2m}}{\left[\Omega/\omega_s(J)\right]^2-m^2}. \tag{B.48}$$

The result we have obtained in Eq. (B.47) allows the evaluation of instabilities for arbitrary azimuthal modes independently or combined. The assumptions to achieve this were: (i) elliptical symmetric orbits in the phase-space and (ii) the wakefield length is much longer than the bunch length, i.e., the short-bunch limit.

The dispersion integral can be simplified to specific rf potentials, as done in Refs. [81, 82, 126].

B.3.1 Dipole instabilities

A particularly important instability type regards the bunch centroid motion, referred to as dipole instability. This can be studied by focusing on the $m = 1$ mode contribution for the dispersion-relation.

As in Ref. [81], the canonical transformation can be expanded in Fourier series $\zeta(J,\varphi) = \sum_\nu e^{i\nu\varphi}\hat{f}_\nu(J)$ and the Fourier coefficients $\hat{f}_\nu(J)$ appear in the dispersion-relation instead of the function $f(J)$. For the case $\zeta(J,\varphi) = f(J)\cos(\varphi)$, the only non-zero Fourier coefficients are $\nu = \pm 1$ and the result $\hat{f}_{\pm 1}(J) = f(J)/2$ can be used. Since the canonical transformation is real, $\hat{f}_{-1}(J) = \hat{f}_1(J)$. Under these conditions, the dispersion-relation Eq. (B.47) for $m = 1$ is:

$$1 = \frac{2\sigma_z}{\alpha c \sigma_\delta}\Lambda_\ell^{(1)}(\Omega)\int_0^\infty \mathrm{d}J\, 4\pi\Psi_0(J)\frac{\left[\hat{f}_1(J)/\sigma_z\right]^2}{\left[\Omega/\omega_s(J)\right]^2 - 1}. \tag{B.49}$$

To connect with Lindberg's approach presented in [81], we will first solve the dispersion-relation for an equivalent harmonic problem, i.e., a quadratic potential $\Phi_0(z) \propto z^2$ producing the same bunch length σ_z related to the arbitrary potential of interest. In this case, the following conditions apply:

$$\omega_s(J) = \omega_{s0} = \alpha c \sigma_\delta/\sigma_z, \tag{B.50}$$

$$\mathcal{H}_0(J) = \omega_{s0} J/c, \tag{B.51}$$

$$\Psi_0(J) = \frac{e^{-J/\langle J\rangle}}{2\pi\langle J\rangle} \quad \text{with} \quad \langle J\rangle = \sigma_z\sigma_\delta, \tag{B.52}$$

$$\zeta(J,\varphi) = \sigma_z\sqrt{\frac{2J}{\langle J\rangle}}\cos(\varphi). \tag{B.53}$$

We can initially obtain the coherent frequency $\Omega_{\mathrm{linear},\ell}$ related to the centroid motion of the coupled-bunch mode ℓ with linear dynamics. Additionally, we will assume that we can approximate $\Omega \approx \langle\omega_s(J)\rangle = \omega_{s0}$ in the impedance's argument [81]. Applying these conditions we obtain:

$$D_1(\Omega_{\mathrm{linear},\ell}) = \frac{\omega_{s0}^2}{\Omega_{\mathrm{linear},\ell}^2 - \omega_{s0}^2}, \tag{B.54}$$

$$\Lambda_\ell^{(1)}(\omega_{s0}) = i\frac{eI_0}{2E_0T_0\sigma_\delta}Z_{\mathrm{eff},\ell}^{(1)}, \tag{B.55}$$

$$= \frac{-eI_0\sigma_z}{2E_0\sigma_\delta M}\sum_{k=0}^{+\infty} e^{ik(2\pi\ell+\omega_{s0}T_0)/M}\left.\frac{\mathrm{d}W}{\mathrm{d}\xi}\right|_{\xi=k\frac{cT_0}{M}}, \tag{B.56}$$

where we used Eq. (B.63) to relate $Z_{\mathrm{eff},\ell}^{(1)}$ with the first derivative of the wake function.

Note that $\frac{eI_0\sigma_z}{2E_0\sigma_\delta M} = \frac{e^2\sigma_t N^{\mathrm{part}}}{2\gamma m c T_0\sigma_\delta}$ (for definition of the parameters in the right, see [81]), then we can show that Eq. (B.56) is equivalent to the matrix elements in Eq. (19) of [81], after diagonalization to the basis of coupled-bunch modes. Combining Eqs. (B.54) and (B.55) in the dispersion-relation, the result for point-charge bunches in a single-rf system is recovered:

$$\Omega_{\text{linear},\ell} = \omega_{s0}\sqrt{1 + 2\Lambda_\ell^{(1)}(\omega_{s0})/\omega_{s0}}. \tag{B.57}$$

For small detuning such that $\Lambda_\ell^{(1)}(\omega_{s0})/\omega_{s0} \ll 1$, we get Sacherer's formula $\Omega_{\text{linear},\ell} \approx \omega_{s0} + \Lambda_\ell^{(1)}(\omega_{s0})$. Note that $\Lambda_\ell^{(1)}(\omega_{s0})$ is actually the coherent frequency shift in a harmonic potential.

For comparison with Eq. (B.49), see the dispersion-relation presented in Eq. (24) of [81], where the integral contains a summation over m. There, λ_ℓ is an eigenvalue of the bunch centroids coupling matrix, Eq. (19) in [81]. These eigenvalues λ_ℓ are identical to the $\Lambda_\ell^{(1)}$ defined by Eq. (B.56), where the particularity to $m = 1$ is made explicit in the notation. For $m = 1$, our framework reproduces the results from Ref. [81], considering that all the studies cases of rf potentials in that work considered only the $m = 1$ contribution as well.

To obtain Eq. (24) of Ref. [81] for arbitrary m from Eq. (B.47) of this chapter, we would have to consider $\Omega \approx \omega_{s0}$ to evaluate $\Lambda_\ell^{(1)}(\omega_{s0})$, which is a reasonable approximation, in principle. Besides, we would also have to set $\Lambda_\ell^{(m)} = \Lambda_\ell^{(1)}$ for all azimuthals m and assume that $[f(J)/2]^{2m} = \hat{f}_m^2(J)$, which are considerations that I could not find arguments to support. Therefore, for $m > 1$, it was not possible to establish an obvious connection between our framework and the dispersion-relation in Ref. [81].

B.3.2 Quadrupole instabilities

We will briefly address another type of instability to illustrate how the generality of the presented theory allows to straightforwardly obtain the dispersion-relation for any azimuthal mode. For instance, quadrupolar instabilities were investigated in Ref. [85]. Let us assume that $\Lambda_\ell^{(1)} = 0$, meaning that the dipole coherent shift is fully suppressed. Then, from Eq. (B.47), the next relevant contribution is from the quadrupole mode $m = 2$.

Taking the normalized effective impedance of third order in terms of the wake function from Eq. (B.63), replacing $f(J)/2 = \hat{f}_1(J)$ in the dispersion integral, and rewriting $\Psi_0(J) = -\frac{\alpha c \sigma_\delta^2}{\omega_s(J)}\frac{\partial \Psi_0}{\partial J}$, we get:

$$1 = \frac{4\pi e I_0}{E_0 M}\sum_{k=0}^{+\infty} e^{ik(2\pi\ell + \Omega T_0)/M}\left.\frac{\mathrm{d}^3 W}{\mathrm{d}\xi^3}\right|_{\xi = k\frac{cT_0}{M}} \int_0^\infty \mathrm{d}J\, \frac{1}{\omega_s(J)}\frac{\partial \Psi_0}{\partial J}\frac{\left[\hat{f}_1(J)\right]^4}{\left[\Omega/\omega_s(J)\right]^2 - 4}. \tag{B.58}$$

This dispersion-relation is equivalent to Eq. (16) in Ref. [85], assuming an even filling pattern and diagonalization to the coupled-bunch basis.

Table B.1: Relevant parameters for the longitudinal instability analysis of different 4th-generation storage rings.

Parameter	Unit	ALS-U [82]	HALF [145]	MAX IV [33, 146]
Energy E_0	GeV	2.0	2.2	3.0
Beam current (uniform fill) I_0	mA	500	350	200 to 400
Circumference C_0	m	196.5	480.0	528.0
Harmonic number h		328	800	176
Momentum compaction factor α		2.11×10^{-4}	8.1×10^{-5}	3.06×10^{-4}
Energy loss per turn U_0	keV	217	198.8	363.8
Relative energy spread σ_δ		9.43×10^{-4}	6.43×10^{-4}	7.69×10^{-4}
Natural std bunch length σ_z (σ_τ)	mm (ps)	3.5 (11.8)	2.0 (6.8)	10.9 (36.4) to 12.1 (40.4)
Radiation damping time τ_δ	ms	14.0	22.7	25.2
rf frequency f_{rf}	MHz	500.417	499.654	99.931
Revolution frequency f_0	kHz	1525.66	624.57	567.69
MCs total voltage $\hat{V}_{\mathrm{rf}}$	MV	0.6	0.85	1.0 to 1.2
HC technology		NC	SC	NC
HC rf harmonic		3	3	3
Number of HCs		2	1	2 to 3
HC shunt impedance $R_s = V^2/2P$	MΩ	1.7	45	2.75
HC quality factor Q		2.1×10^4	5×10^5	2.08×10^4
HC geometric factor (R/Q)	Ω	81	90	132
HC flat-potential voltage $\hat{V}_{\mathrm{HC}}$	MV	186.6	283.3	307.5 to 378.6
HC flat-potential detuning Δf_{HC}	kHz	584	157.8	38.8 to 145.2

It is worth mentioning that derivations for dipole instabilities in [81], later also adapted for quadrupole instabilities in [85], required the restriction to these cases as initial assumptions for the theoretical development. This case-by-case approach may be limited if one wants to study an instability related to an azimuthal mode $m \notin \{1, 2\}$ or if multiple m modes are required to accurately compute the instability thresholds, for instance mode-coupling instabilities. Moreover, the mathematical complexity of the process increases with m, as evident from the comparison of Ref. [85] for $m = 2$ with Ref. [81] for $m = 1$.

Interestingly, the connection between an mth-order instability and the derivatives of odd orders $2m - 1$ of the wake function naturally arises in our framework through Eqs. (B.46) and (B.63). This aligns with the physical intuition that derivatives of even orders of the wake function cannot drive instabilities due to their symmetric effects.

B.4 Applications

The developed theory will be applied to two instabilities of interest in recent publications, specially to some 4th-generation storage rings with HCs, whose parameters are presented in Table B.1. For the applications, we will benchmark the results from Lebedev equation, effective synchrotron frequency model and Gaussian LMCI against each other and against experimental data.

B.4.1 Robinson dipole-quadrupole mode coupling

Robinson instabilities can be studied by focusing on the coupled-bunch mode $\ell = 0$. In particular, there is a Robinson instability caused by the coupling of the dipole and quadrupole motion, driven by the HC impedance, that has been studied in simulations [103, 143] and observed experimentally at MAX IV [33, 146].

Figure B.1 shows the coherent frequencies calculated with different methods and the measured values at MAX IV ring [33]. The low total current of 50 mA allowed to measure the coherent oscillation frequencies with a stable beam. The incoherent effective synchrotron frequency calculated by Eq. (B.38) is also shown to indicate its reduction while the HC voltage increases. In contrast, the coherent dipolar frequency for the $\ell = 0$ mode remains essentially constant and equal to the value of the single-rf system (for a physical explanation, Ref. [51], pages 68 and 206). The coherent quadrupolar frequency follows the reduction of the second harmonic of the incoherent frequency. Hence, at some HC voltage the dipole and quadrupole modes will match. For low currents such as $I_0 = 50\,\mathrm{mA}$, the modes actually only cross each other and do not couple to drive an instability. For higher currents these modes typically couple, driving a fast instability that can prevent reaching higher HC voltages, thus better bunch lengthening performance.

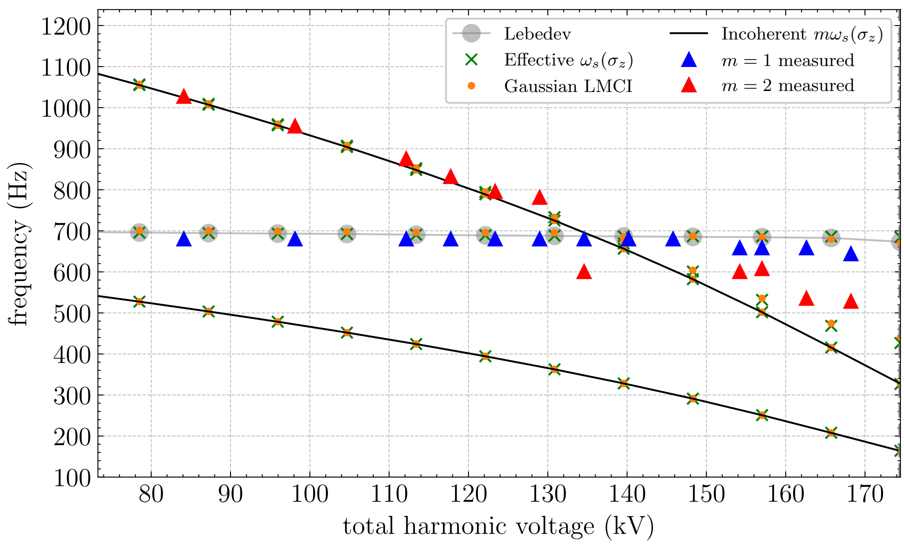

Figure B.1: Robinson ($\ell = 0$) dipole-quadrupole mode coupling for MAX IV parameters: $I_0 = 50\,\mathrm{mA}$, $\hat{V}_{\mathrm{rf}} = 650\,\mathrm{kV}$. The flat-potential harmonic voltage is 174.35 kV. Measured data from MAX IV taken from Ref. [33]. All models predict no instability at this condition, in agreement with the experiment. $m_{\max} = 2$ was used in all methods and $k_{\max} = 1$ was used in Gaussian LMCI.

It is interesting to note that all models produced very similar results. In this condition, solutions with $\mathrm{Im}(\Omega) < 1/\tau_\delta$, where τ_δ is the longitudinal radiation damping time, were found for the Lebedev equation. Other solutions following the quadrupole frequencies could also be found if the initial guess to solve the determinant root was chosen to be close to the second harmonic of the incoherent frequency. In the case of instability, however, an initial guess around the dipole frequency would be sufficient to correctly predict an unstable solution.

The good agreement between all methods and the measured data indicates that the contributions from a non-Gaussian bunch and nonlinearities in the double-rf system are not important for determining the coherent frequencies. It was observed that this still holds for predicting an unstable condition. Thus, only the effects in the bunch length and synchrotron frequency as in an equivalent single-rf system proved to be sufficient to study the Robinson mode coupling instability. This aligns with the observations from previous investigations [33, 143]. Benchmarking of the Gaussian LMCI model with tracking simulations are reported elsewhere [103].

B.4.2 PTBL/mode-1 instability

The PTBL instability, also called by some authors as mode-1 instability, has been recently investigated for 4th-generation storage rings with HCs [82, 145, 146]. In this chapter, PTBL or mode-1 instability refer to the same effect. It was shown that during this instability, the bunch centroids and profiles oscillate in a quasi-stationary motion. Some studies indicate that the effect has different features from a standard coupled-bunch instability [38, 145], yet some success was obtained in computing the thresholds by restricting the analysis to the coupled-bunch mode $\ell = 1$ as it is the dominant mode. This is the justification for the "mode-1 instability" name.

In Ref. [145], the characteristics of PTBL were investigated in detail mainly through tracking simulations, although discussions on the instability mechanism were not addressed. In Ref. [146] the nature of this instability was further explored and the authors elaborated on some conditions that should be met for the mode-1 instability be likely to appear. The experimental data obtained at MAX IV 3 GeV storage ring (see Fig. 11 in Ref. [146]) showed a significant disagreement when compared to results obtained by two theoretical models: Krinsky dispersion-relation for a quartic potential, in the format presented in [81], and T. He formula [147]. We will present the results obtained from the models developed in this chapter, from which we could obtain new insights to understand what features are important to predict PTBL and why previous theories were unsuccessful in some cases.

Figure B.2 shows the coherent frequencies of the mode-1 calculated by different methods for different rings, with the unstable region indicated by the background red color. We note that for ALS-U parameters using the "old" ALS HCs, the mode-1 is unstable for all HC conditions, in accordance with the results presented in Ref. [82]. This motivated a new design of HCs for ALS-U. For HALF parameters with 350 mA, the mode-1 instability is triggered when the HC voltage is 6 % below the flat-potential voltage. This aligns with the results from Ref. [145], reporting a PTBL threshold of 259 mA when the HC is at flat-potential. Finally, for MAX IV parameters with 300 mA and 3 HCs, the mode-1 instability is driven 1 % below the flat-potential voltage.

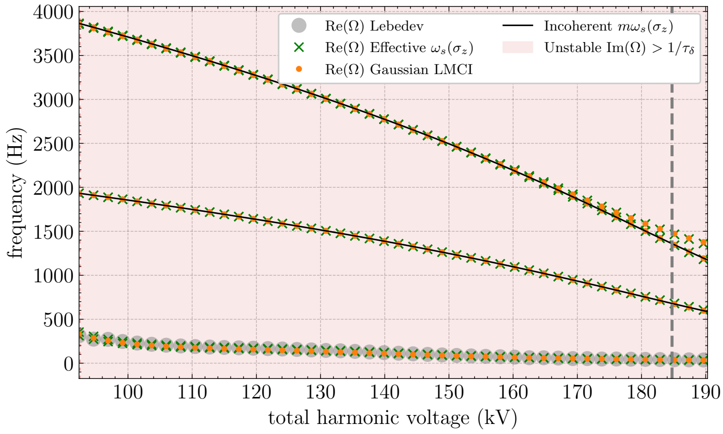

(a) ALS-U.

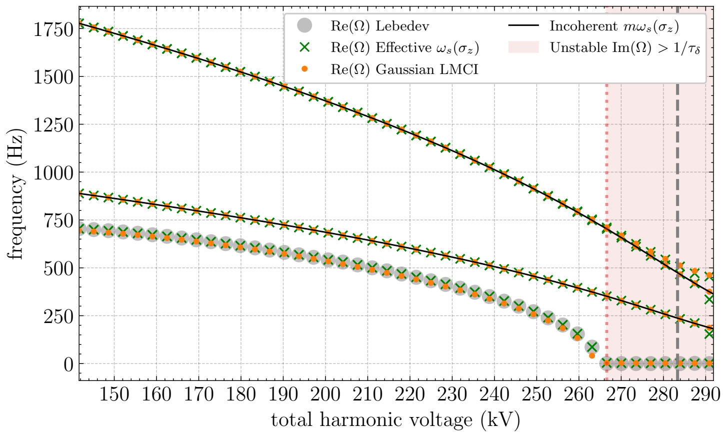

(b) HALF.

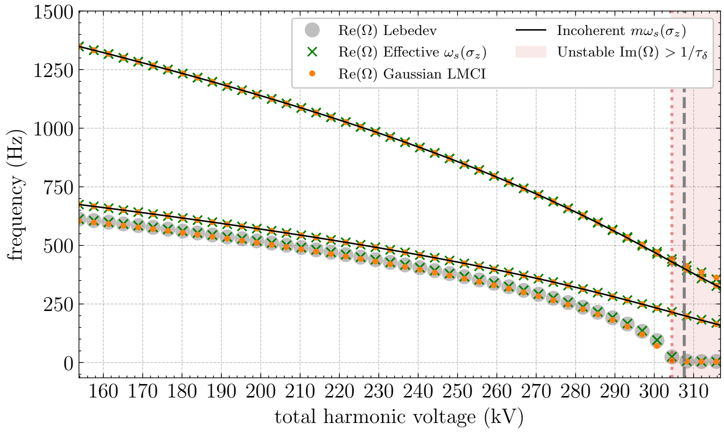

(c) MAX IV.

Figure B.2: Coherent frequencies of coupled-bunch mode $\ell = 1$ as a function of the HC voltage for different storage ring parameters. The vertical gray dashed line indicates the flat-potential voltage. The unstable area is determined by the condition $\mathrm{Im}(\Omega) > 1/\tau_\delta$ with Ω being the solution of Lebedev equation. (a) Unstable for all HC voltages. flat-potential 184.75 kV. (b) Threshold 266.58 kV. Flat-potential 283.35 kV. (c) Threshold 304.48 kV. Flat-potential 307.62 kV. $I_0 = 300\,\mathrm{mA}$, $\hat{V}_{\mathrm{rf}} = 1.0\,\mathrm{MV}$, 3 HCs. $m_{\max} = 2$ was used in all methods and $k_{\max} = 1$ was used in Gaussian LMCI.

The results from Fig. B.2 also reveal that, for the mode-1 instability, calculations with a more complete theory (Lebedev equation) produce essentially the same values as calculations with theories that neglects the Landau damping effect (effective synchrotron frequency and Gaussian LMCI). This is a strong evidence that Landau damping does not play a role on the onset of the PTBL instability, contrary to the conclusions from Ref. [146]. Another relevant observation from Fig. B.2 is that the low coherent frequency feature of PTBL instability was reproduced. In fact, from HALF and MAX IV plots, the coherent frequency is shifted to lower values more than the incoherent frequency, eventually reaching zero. This indicates that the coherent focusing of the mode is lost, and an instability can easily build up. With this picture, the mechanism of the instability associated with the imaginary/reactive part of the impedance can be better understood, because this term is responsible for real frequency shifts. In Fig. B.3 we benchmarked our predictions with the coherent frequencies of mode-1 measured at MAX IV [146], displaying very good agreement as well. The measurements were carried out at 90 mA, when the mode-1 instability is not triggered. We see that for such low current the coherent frequency shift is negligible.

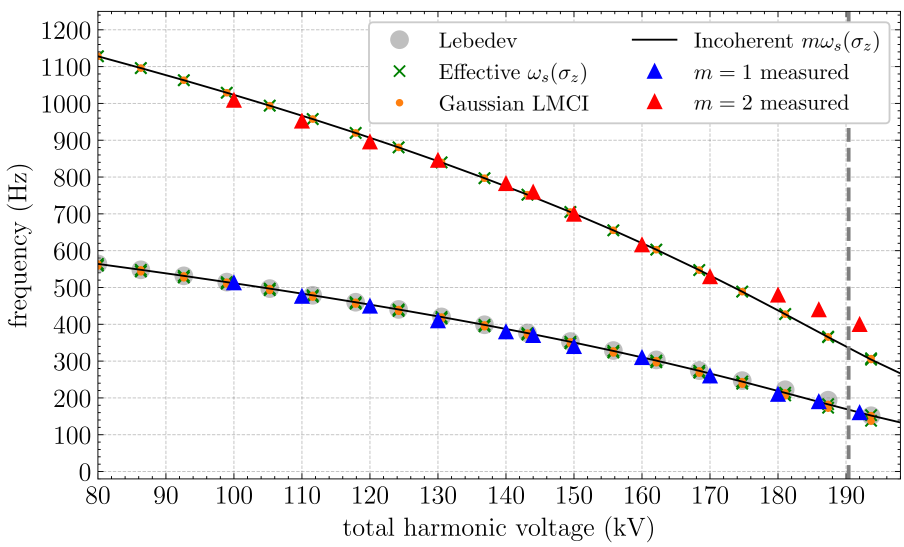

Figure B.3: Coherent frequencies of coupled-bunch mode $\ell = 1$ for MAX IV parameters with 2 HCs, $I_0 = 90\,\mathrm{mA}$, $\hat{V}_{\mathrm{rf}} = 689\,\mathrm{kV}$. The vertical gray dashed line indicates the flat-potential voltage. Comparison between different calculation methods and experimental data (Fig. 15 from Ref. [146]).

An interesting feature, explored in simulations [145] and measured at MAX IV [146], is the dependence of the threshold current with the main rf voltage, which shows a linear trend with positive slope. In the experiments, the HC cavity was always tuned to produce the flat-potential voltage for each current and rf voltage. We benchmarked our calculations with the experimental data from MAX IV and results from other methods as reported in Ref. [146]. The comparison is shown in Fig. B.4. The results obtained from the Lebedev equation and the effective synchrotron frequency model are in excellent agreement with the experimental data when $m_{\max} \geq 2$ azimuthal modes are accounted. The Gaussian LMCI model systematically predicts a lower current threshold, but still much more accurate than the Krinsky and T. He models. The agreement between the result from Lebedev equation

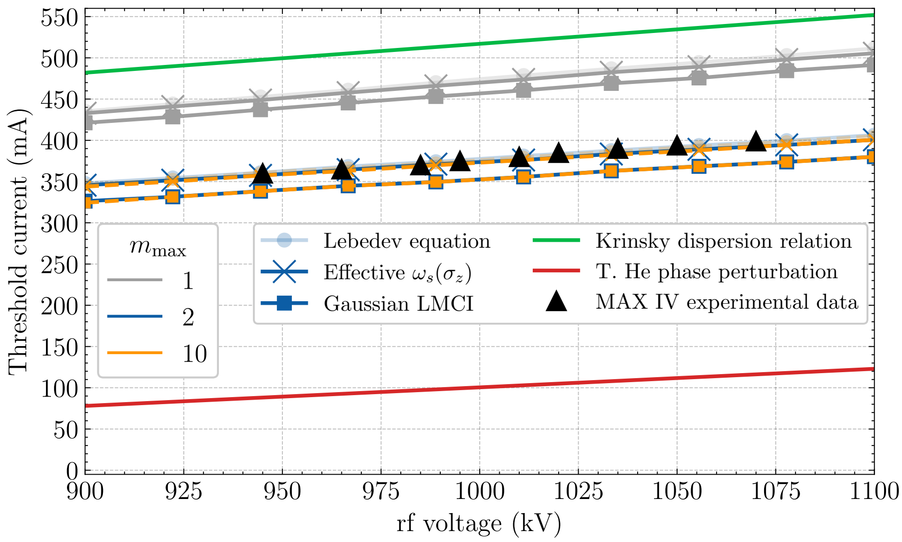

Figure B.4: Threshold currents of the mode-1 instability for different main rf voltages. MAX IV parameters with 2 HCs, tuned to provide the flat-potential voltage. Comparison between different calculation methods and experimental data [146]. Krinsky and T. He curves were obtained from Fig. 11 in [146]. The truncation of azimuthal modes $m_{\max}$ was varied to illustrate the relevance of multiple modes. $k_{\max} = 1$ was used in Gaussian LMCI.

and the effective synchrotron frequency reveals that the effects of Landau damping are not necessary to accurately predict the PTBL/mode-1 instability threshold.

It was proven that the inclusion of the $m = 2$ mode is essential to reproduce the measured thresholds. The calculations with only $m = 1$ predicts a higher threshold such as in the Krinsky model (which only uses $m = 1$). A more detailed discussion about the Landau damping and multiple azimuthal modes will be addressed in §B.5. Besides, the effects of a non-Gaussian beam proved to be relevant because it is the main difference between the effective frequency method and the Gaussian LMCI scheme, with the latter underestimating the threshold. The inclusion of multiple azimuthal modes is one of the main differences from our theoretical models to the models of Krinsky and T. He.

B.5 Discussion on PTBL/mode-1 mechanism

The results in §B.4 help to clarify the underlying mechanism of the PTBL instability. As the HC voltage increases, $\langle\omega_s\rangle$ decreases from its single-rf value. For the $\ell = 0$ coupled-bunch mode, the coherent dipole frequency remains constant. However, this does not generally hold for other coupled-bunch modes. Figure B.2 shows that, particularly for the $\ell = 1$ mode, the coherent frequencies represented by “Re(Ω) Lebedev” exhibit a negative shift relative to $\langle\omega_s\rangle$. This is due to the reactive (imaginary) part of the HC impedance. If the negative shift leads to Re(Ω) ≈ 0, the coherent focusing of mode $\ell = 1$ is lost, triggering an instability.

In past works [129, 148], the microwave instability (a single-bunch effect) has been explained using a similar "zero-frequency" argument, although the interpretation was based on the mode-coupling of $m = \pm 1$ modes. Within our formulation of the Lebedev equation, interactions between positive and negative m modes are accounted for, but this contributions may be overlooked since these modes were combined due to their symmetry. This suggests that the "zero-frequency" threshold for PTBL might also be interpreted as the coupling of $m = \pm 1$ modes associated with the coupled-bunch mode $\ell = 1$. However, an important difference lies in the regime for the coherent frequency shift, or equivalently, mode-coupling. For the microwave instability, large negative shifts occur due to high current per bunch. In contrast, for the PTBL instability, $\langle \omega_s \rangle$ is significantly lowered by the HC voltage, and even at lower currents per bunch, the coherent shift might still be sufficient to couple the $m = \pm 1$ modes.

The "zero-frequency" condition can be used to derive an approximate formula for the PTBL instability threshold (see SSB.8). The formula provides a critical $(R/Q)I_0$ value and a mode-1 instability is expected when this value is exceeded. This dependence aligns with previous studies, which have shown that HCs with low (R/Q) are preferable for avoiding the PTBL instability [80, 82, 103, 147, 147]. Within the proposed instability mechanism, this behavior can be attributed to the lower (R/Q) values reducing the reactive effective impedance for the $\ell = 1$ mode, which in turn reduces the coherent dipole frequency shift.

The linear dependence of the PTBL threshold on the main rf voltage was predicted by tracking simulations [145], verified experimentally [146], and reproduced with our calculations in Fig. B.4. In Fig. B.5, we show the behavior of the incoherent and coherent frequencies for two different main rf voltages, using the HALF parameters. For simplicity, only the results from the Lebedev equation are presented. The result in red corresponds to the condition shown in Fig. B.2b, with $\hat{V}_{\mathrm{rf}} = 0.85\,\mathrm{MV}$. This is compared with a result obtained at twice the rf voltage, 1.70 MV, where the single-rf synchrotron frequency is expected to increase by approximately $\sqrt{2}$. At the higher rf voltage, the coherent negative shift is reduced. This reduction occurs due to the lower HC detuning needed to generate a higher harmonic voltage, which decreases the reactive effective impedance for $\ell = 1$. Combined with the higher incoherent frequency, this implies in an increase in the PTBL threshold current. According to the approximate formula, Eq. (B.70), the threshold depends on $\sqrt{\hat{V}_{\mathrm{rf}}}$, while a linear behavior was observed in simulations [145] and measurements [146]. We can argue that variations considerably larger than those made in these investigations would be required to reveal a $\sqrt{\hat{V}_{\mathrm{rf}}}$ dependence.

For all cases studied here, the positive growth rates for PTBL are on the order of hundreds of Hz or higher. Such large growth rates are typical of mode coupling instabilities, for which radiation damping is known to be ineffective [50, 51, 142]. This observation aligns with the findings in Ref. [145], where tracking simulations indicated that the PTBL threshold is insensitive to changes in the radiation damping time. Additionally, recent

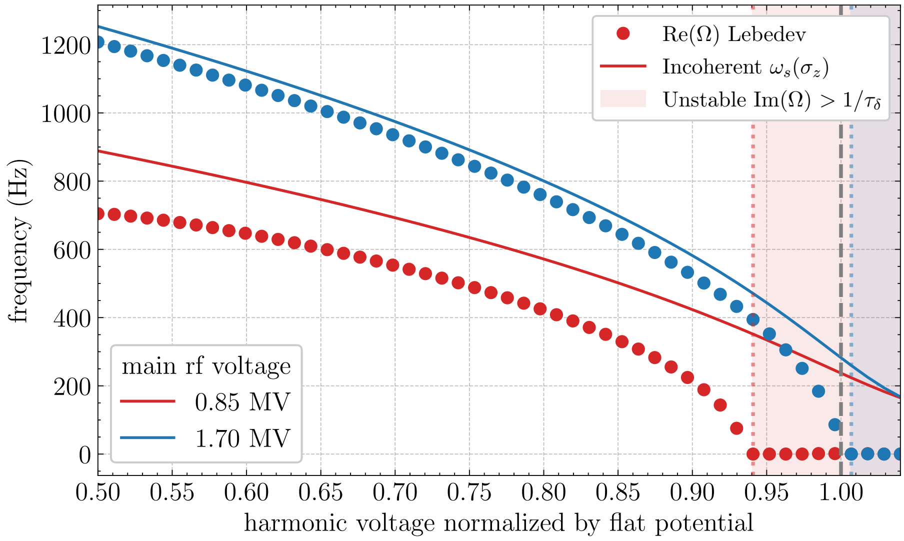

Figure B.5: Coherent frequencies of $\ell = 1$ coupled-bunch mode for HALF parameters with different main rf voltages. The vertical gray dashed line represents the flat-potential condition. Harmonic voltage/detuning at flat-potential for each rf voltage are (red): 283.35 kV/157.79 kHz; (blue): 566.68 kV/80.17 kHz. $m_{\max} = 2$ was used.

studies have showed that a resistive feedback is ineffective in mitigating the mode-1 instability [91]. Investigating the effect of reactive feedback to counteract the negative coherent frequency shift of mode-1 could offer a potential solution to the PTBL issue. Reactive feedback systems have previously been explored to increase the thresholds of transverse mode coupling instabilities, achieving positive results [149–153].

In Refs. [103, 139, 140, 146] it was remarked that, since the PTBL instability is known to have a low coherent frequency, it may be resistant to Landau damping. In addition to the presence of an incoherent frequency spread, Landau damping requires an overlap between coherent and incoherent frequencies to manifest. The argument is that, although double-rf systems significantly increase the frequency spread, the bandwidth may not extend to the very low frequencies involved in the PTBL instability, limiting the effectiveness of Landau damping. Our results provide quantitative support for this argument.

The Krinsky dispersion-relation used in Refs. [81, 146] assumes an ideal quartic rf potential, $\Phi_0(z) \propto z^4$, resulting in an amplitude-dependent incoherent frequency, $\omega_s(J) \propto J^{1/3}$, and isolates the $m = 1$ contribution [81, 82, 126]. However, achieving in practice an exact quartic potential with a double-rf system is unlikely. Even small mismatches in the rf voltage cancellation can significantly alter the potential (see Fig. 3 in Ref. [82], for example), leading to incoherent frequencies that may not reach zero to interact with the coherent frequency. Consequently, the Krinsky model is expected to overestimate Landau damping effects. Combined with the neglect of higher-order m modes, this may explain the discrepancy with the measured mode-1 thresholds shown in Fig. B.4. It is worth noting that the dispersion-relation applied in Refs. [81, 146] is a specific case of the broader framework introduced in Krinsky's original work [126], which is also general enough to include multiple azimuthal modes and arbitrary nonlinear rf potentials.

Finally, we present the $m = 2$ mode contribution to the PTBL instability prediction. Figure B.6 illustrates how the number of azimuthal modes affects the coherent frequencies. The calculations use MAX IV parameters with a beam current of 400 mA, a main rf voltage of 1.0 MV, and two HCs, a condition known to be unstable (see Fig. B.4). For this beam current, considering only $m = 1$ results in an insufficient coherent shift to push the mode towards zero and drive the instability. Including $m = 2$ introduces an additional negative shift, as if the quadrupole mode "repels" the dipole mode, which is enough to drive the instability. Therefore, interaction of higher azimuthal modes also play a crucial role in the PTBL instability.

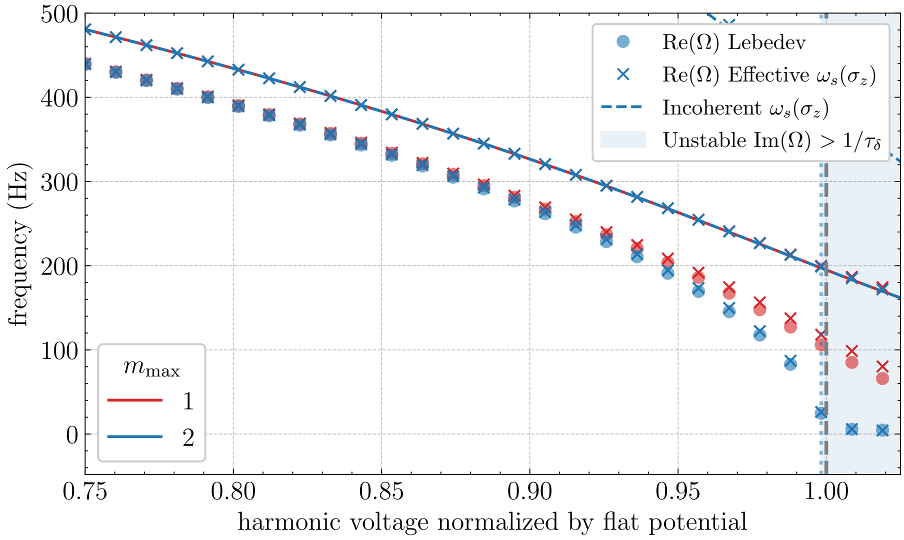

Figure B.6: Coherent frequencies of $\ell = 1$ coupled-bunch mode for MAX IV parameters with 400 mA, main rf voltage 1.0 MV and 2 HCs, considering two truncation values of azimuthal modes $m_{\max}$. The vertical gray dashed line indicates the flat-potential condition.

B.6 Summary and conclusions

We developed a theoretical framework for calculating coupled-bunch instabilities in double-rf systems with HCs, considering nonlinear effects from potential-well distortion and cases where multiple azimuthal modes are relevant. This framework is based on a frequency-domain perturbation theory to solve the linearized Vlasov equation, resulting in the Lebedev equation [137, 138], which provides the coherent frequencies of the beam. We identified an equivalence between the Lebedev equation and the theory developed by Venturini [82], noting that Venturini's method has an avoidable computational complexity that increases significantly with the number of azimuthal modes considered.

Additionally, we presented two approximate models: an effective synchrotron frequency method, which neglects Landau damping but accounts for other effects of an arbitrary rf potential, and a Gaussian LMCI scheme adapted for double-rf systems.

Dispersion-relation equations based on Krinsky's work [126], as presented in recent publications by Lindberg [81] and Cullinan [85], were derived as particular cases of the Lebedev equation. Altogether, this demonstrates an unification of recent theories addressing longitudinal instabilities in double-rf systems.

The framework was applied to study two types of instabilities in the presence of HCs: Robinson dipole-quadrupole mode coupling and PTBL/mode-1. For these studies, we used parameters from the storage rings ALS-U, HALF, and MAX IV. The theory provided excellent agreement with experimental data from MAX IV, a novel result for the mode-1 instability. We drew three significant conclusions about the PTBL instability mechanism: (i) it is triggered when coherent focusing is lost for the dipole motion of the coupled-bunch mode $\ell = 1$, (ii) Landau damping is irrelevant for determining instability thresholds and (iii) the interaction of multiple azimuthal modes is the fundamental effect for accurate threshold predictions. The new insights on the PTBL instability mechanism deepens our understanding of its behavior and dependence on parameters such as the main rf voltage, (R/Q) of the HC, reactive impedance, and longitudinal radiation damping time.

The Python implementation of the models is available in the open-source package `pycolleff` [83], providing a useful semi-analytical tool for studying instabilities in electron storage rings with HC systems.

Interesting directions for future research would be extending the framework to evaluate instabilities with uneven filling patterns and broadband resonators with a reasonable computational complexity, as well as investigating the use of reactive feedback to control the negative coherent frequency shift of the coupled-bunch mode $\ell = 1$ in double-rf systems, aiming to increase the PTBL instability thresholds.

B.7 Effective impedance and wake function derivative

The longitudinal wake function is related to the longitudinal impedance by:

$$W(\xi) = \frac{1}{2\pi}\int_{-\infty}^{\infty} \mathrm{d}\omega\, Z(\omega)e^{-i\omega\xi/c}, \tag{B.59}$$

and it is straightforward to compute the nth derivative of the wake function:

$$\frac{\mathrm{d}^n W}{\mathrm{d}\xi^n} = \frac{(-i)^n}{2\pi c^n}\int_{-\infty}^{\infty} \mathrm{d}\omega\, \omega^n Z(\omega)e^{-i\omega\xi/c}. \tag{B.60}$$

Considering M bunches evenly distributed, we will evaluate the wake function at the harmonics kcT_0/M. Then multiply it by $e^{ik(2\pi\ell+\Omega T_0)/M}$, where ℓ is the coupled-bunch mode. To apply the Poisson formula:

$$\sum_{k=-\infty}^{+\infty} e^{ik\omega T_0/M} = M\omega_0 \sum_{p=-\infty}^{+\infty} \delta(\omega - pM\omega_0), \tag{B.61}$$

with $\omega_0 = 2\pi/T_0$, we will assume the integrand in Eq. (B.60) does not diverge, allowing to interchange the summation with the integral. This is a valid assumption for narrowband resonators at low frequencies, when the impedance is well-represented by a single or few harmonics p, and it can be neglected elsewhere [82, 154].

After these steps, we obtain:

$$\sum_{k=-\infty}^{+\infty} e^{ik(2\pi\ell+\Omega T_0)/M} \left.\frac{\mathrm{d}^n W}{\mathrm{d}\xi^n}\right|_{\xi=k\frac{cT_0}{M}} = \frac{M(-i)^n}{c^n T_0} \sum_{p=-\infty}^{+\infty} (\omega_{p,\ell}+\Omega)^n Z_{p,\ell}(\Omega), \tag{B.62}$$

with $\omega_{p,\ell} = (pM+\ell)\omega_0$. Typically, $\mathrm{Re}(\Omega) \ll \omega_0$, so we can approximate $(\omega_{p,\ell}+\Omega)^n \approx \omega_{p,\ell}^n$. Note that, for generality, the Ω dependence should be kept in the impedance's argument.

Considering the impedance can be neglected except at the harmonic $\pm p_0$, the definition of normalized effective impedance of order n from Eq. (B.44) can be applied into Eq. (B.62) to get:

$$Z_{\mathrm{eff},\ell}^{(n)}(\Omega) = (i\sigma_z)^n \frac{T_0}{M} \sum_{k=0}^{+\infty} e^{ik(2\pi\ell+\Omega T_0)/M} \left.\frac{\mathrm{d}^n W}{\mathrm{d}\xi^n}\right|_{\xi=k\frac{cT_0}{M}}, \tag{B.63}$$

where the causality $W(z<0)=0$ was used to restrict the sum for $k>0$.

B.8 Approximate formulas for the PTBL/mode-1 threshold

We will assume an even filling pattern with all buckets filled, $M = h$. Consider the longitudinal impedance resonator model:

$$Z(\omega) = \frac{R_s}{1 + iQ\left(\frac{\omega_\mathrm{r}}{\omega} - \frac{\omega}{\omega_\mathrm{r}}\right)}, \tag{B.64}$$

where R_s is the shunt impedance, Q the quality factor and ω_r the resonant frequency. For narrowband resonators with high-Q, we can approximate the reactive impedance by:

$$\mathrm{Im}\left[Z(\omega)\right] \approx -\left(\frac{R}{Q}\right)\left(\frac{\omega_\mathrm{r}}{\omega} - \frac{\omega}{\omega_\mathrm{r}}\right)^{-1}. \tag{B.65}$$

We will assume that the resonator is detuned above the nth rf harmonic, $\omega_\mathrm{r} =$

$nh\omega_0 + \Delta\omega$, representing the case of a nth-HC. From Eq. (B.46) for the dipole mode, $\mathrm{Re}\left[\Lambda_\ell^{(1)}(0)\right] \propto -\mathrm{Im}\left[Z_{\mathrm{eff},\ell}^{(1)}(0)\right]$. We will be interested in the limit $\Omega_\ell \approx 0$, so the Ω_ℓ sampling on the impedance was neglected. Evaluating the reactive effective impedance with $p_0 = n$ on Eq. (B.65), yields:

$$\mathrm{Im}\left[Z_{\mathrm{eff},\ell}^{(1)}(0)\right] \approx \sigma_\tau \left(\frac{R}{Q}\right)(nh\omega_0)^2 \frac{\Delta\omega}{(\ell\omega_0)^2 - \Delta\omega^2}. \tag{B.66}$$

We considered $nh \gg \ell$ and $nh\omega_0 \gg \Delta\omega$. HCs typically operate at small detunings, $0 < \Delta\omega < \omega_0$ (see Table B.1), so, for $\ell \neq 0$, $(\ell\omega_0)^2 - \Delta\omega^2 \approx (\ell\omega_0)^2$ is often a valid approximation for the flat-potential detuning. In this approximation, the bunch length, σ_τ, is treated as an independent parameter. Even so, the value of σ_τ used in the formula should be consistent with the equilibrium bunch distribution for each condition.

We can show that the HC peak voltage can be approximated by:

$$\hat{V}_{\mathrm{HC}} \approx I_0 |F_n| \left(\frac{R}{Q}\right) \frac{nh\omega_0}{\Delta\omega}, \tag{B.67}$$

where F_n is the bunch form factor, given by $F_n = \int_{-\infty}^{\infty} \mathrm{d}z\, e^{in\omega_{\mathrm{rf}} z/c} \lambda_0(z)$. For simplicity, we assume symmetric bunches, so the phase of F_n is zero. $Q \gg 1$ was also assumed to obtain Eq. (B.67). The HC amplitude to produce the flat-potential is [106]:

$$\hat{V}_{\mathrm{HC,flat}} = \frac{\hat{V}_{\mathrm{rf}}}{n} \sqrt{1 - \frac{n^2}{n^2-1}\left(\frac{U_0}{e\hat{V}_{\mathrm{rf}}}\right)^2} \approx \frac{\hat{V}_{\mathrm{rf}}}{n}. \tag{B.68}$$

Combining these results and applying to Eq. (B.46), yields:

$$\mathrm{Re}\left[\Lambda_\ell^{(1)}(0)\right] \approx -\frac{\pi e \sigma_\tau |F_n| n^4 h^3}{E_0 T_0^2 \sigma_\delta \hat{V}_{\mathrm{rf}} \ell^2} \left[I_0 \left(\frac{R}{Q}\right)\right]^2. \tag{B.69}$$

Note that $\mathrm{Re}\left[\Lambda_\ell^{(1)}\right] \propto -1/\ell^2$, meaning the most significant negative shift occurs for the $\ell = 1$ mode. Depending on the parameters, $\ell > 1$ modes can also have sufficient coherent shifts to drive instabilities with multiple coupled-bunch modes. This may help to understand the behavior of many coupled-bunch modes excited during the PTBL instability [38].

For simplicity, we will use the approximate case of a dipole instability in an equivalent quadratic potential with the same bunch length in a double-rf system at flat-potential, such as presented in §B.3.1. For this case, the coherent shift is $\Omega_{\mathrm{linear},\ell}^2 = \langle\omega_s\rangle^2 + 2\langle\omega_s\rangle\Lambda_\ell^{(1)}$ with $\langle\omega_s\rangle = \alpha\sigma_\delta/\sigma_\tau$. The condition for the mode $\ell = 1$ instability threshold condition will be set as $\Omega_{\mathrm{linear},\ell=1}^2 \approx 0$, implying $\mathrm{Re}\left[\Lambda_{\ell=1}^{(1)}(0)\right] \approx -\langle\omega_s\rangle/2$. With that, we get the approximate threshold formula:

$$\left[I_0\left(\frac{R}{Q}\right)\right]_{\text{threshold}} \approx \frac{T_0\sigma_\delta}{n^2\sigma_\tau}\sqrt{\frac{E_0\alpha\hat{V}_{\text{rf}}}{2\pi e|F_n|h^3}}. \tag{B.70}$$

A mode-1 instability is expected for $I_0(R/Q)$ values above this threshold. A similar formula was derived by Venturini (see slide 17 in Ref. [155]). Interestingly, both formulas exhibit the scaling $\frac{\sigma_\delta}{n^2}\sqrt{E_0\alpha\hat{V}_{\text{rf}}/|F_n|}$. Venturini's formula is based on a dispersion-relation in a quartic rf potential for the dipole instability of the $\ell = 1$ mode, obtained by calculating the intersection of the effective impedance with the stability diagram boundary. Hence, some differences from our formula are expected. Another formula was derived by T. He (see Eq. (24) in Ref. [147]), which exhibits a different scaling: $\hat{V}_{\text{rf}}/n^2|F_n|$. In Ref. [145], the significant impact of α and σ_δ on the PTBL threshold was demonstrated, while T. He's threshold formula lacks an explicit dependence on $\sigma_\delta\sqrt{E_0\alpha}$.

We do not expect that the formula Eq. (B.70) can provide accurate absolute threshold values due to its various approximations. Nevertheless, it serves as an interesting result for exploring the dependence on relevant parameters and may be useful for comparing relative thresholds.

Publication: M. Alves, A. Andersson, and F. Cullinan, "Optimizing Touschek lifetime with overstretched bunch profiles in the MAX IV 1.5 GeV ring", IPAC'24, Nashville, TN, USA, May 2024, doi:10.18429/JACoW-IPAC2024-WEPR42

C

Experiments: overstretched bunches at MAX IV 1.5 GeV ring

Contents

Synchrotron light sources often use higher-harmonic rf cavities for bunch lengthening to enhance Touschek lifetime. By adjusting the harmonic voltage, a flat-potential condition for the longitudinal voltage can be achieved, typically improving Touschek lifetime by 4 to 5 times. It is known that exceeding the flat-potential voltage results in double-peaked bunch profiles, referred to as overstretched conditions. Simulations suggest overstretched profiles can surpass flat-potential improvements on lifetime. In this paper we report on experimental results from the MAX IV 1.5 GeV storage ring, demonstrating a longer beam lifetime with a stable beam in overstretched conditions compared to the flat-potential case. Additionally, a remarkable agreement between measured bunch profiles using a streak camera and predictions from a semi-analytical equilibrium solver was obtained for all tested harmonic voltages.

C.1 Ring parameters

MAX IV is a synchrotron light source facility in Lund, Sweden. The complex has two storage rings, one operating at 1.5 GeV and the other is a fourth-generation ring operating at 3.0 GeV [156]. This work is focused on lifetime improvement with HCs in the 1.5 GeV ring, whose relevant parameters for these studies are presented in Table C.1. Two passive normal-conducting HCs operating close to the third-harmonic of the rf frequency are installed in the ring.

Table C.1: Main parameters for the MAX IV 1.5 GeV ring.

Energy	E_0	1.5 GeV
rf frequency	f_{rf}	99.931 MHz
Harmonic number	h	32
Momentum compaction	α	3.05×10^{-3}
Energy spread	σ_δ	7.45×10^{-4}
Energy loss per turn	U_0	114.4 keV
HC shunt impedance (V^2/P)	R_s	5.5 MΩ/cavity
HC quality factor	Q	20 800

C.2 Voltage calibration

C.2.1 Main cavities

With a low-current single-bunch stored in the ring and the HCs parked (no HC fields), the synchrotron frequency was measured as $f_s = 7.18$ kHz. For a single-rf system, the relation between synchrotron frequency and main rf voltage is well-known [48]. Given a measured value of synchrotron frequency f_s, the relation can be inverted to determine the main voltage:

$$V_{\text{rf}} = \left[\left(\frac{f_s}{f_{\text{rf}}}\right)^4 \left(\frac{\alpha}{2\pi h E_0}\right)^2 + U_0^2\right]^{1/2}. \tag{C.1}$$

For the parameters of Table C.1, the measured synchrotron frequency corresponds to a main rf voltage of $V_{\text{rf}} = 522.3$ kV. This value was used throughout the analysis.

C.2.2 Harmonic cavities

For zero detuning and uniform fill, the peak HC voltage should be simply $V_{\text{HC}} = R_s I_0$ [23], where R_s is the HC shunt impedance and I_0 is the stored beam current. To calibrate the voltage of the HCs , 2.3 mA was accumulated uniformly in the ring and the HCs were tuned to resonance. This was achieved by maximizing the HC voltage readouts. The stored current was then reduced in steps to 0.3 mA using a beam scraper and the corresponding

HC voltages were recorded for each current value. For each current, the HCs tuning was adjusted to keep the cavities on resonance. A linear calibration curve was obtained from the measured HC voltage in hardware units vs. expected voltage by $R_s I_0$.

C.3 Fitting harmonic voltages from streak-camera measurements

The bunch profiles were measured with a streak-camera. The streak-camera provides a 2d image with an axis corresponding to a fast scan, with a timescale within bunch separations (ns) and an axis related to a slow scan, with a timescale within a revolution period (µs) [157]. In Fig. C.1 an example streak-camera image is shown. The time axis can be converted to the z-coordinate by $\tau = z/c$, where c is the speed of light.

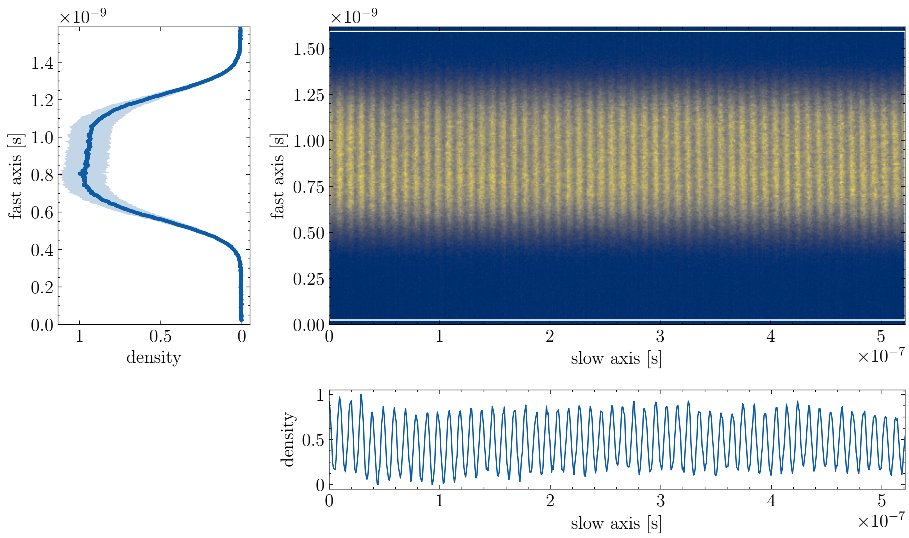

Figure C.1: Example of streak-camera image acquired with 200 mA in uniform fill. Left: the solid curve is the average projection along the slow axis and the shaded region is the std variation over bunches.

The equilibrium bunch profiles in the presence of HC voltage can be calculated by solving self-consistently the Haissinski equation [44]. Let $\lambda_{\text{meas}}(z_i)$ be the measured bunch profile along the axis z_i and averaged over bunches. The goal was to find the HC voltage that best reproduces the measured bunch profile. Two fitting parameters were used: the HC voltage $V_{\text{fit}}(z)$ (amplitude and phase determined by the HC detuning) and an offset z_{fit} to match the measured and simulated z_i-axis. This offset was included as an optional fitting parameter just to automatically account for the undetermined offsets between the axis.

The HC voltages were obtained by solving the least-squares minimization problem:

$$\chi^2 = \sum_i \left[\lambda_{\text{meas}}(z_i) - \lambda(z_i - z_{\text{fit}}, V_{\text{fit}})\right]^2, \tag{C.2}$$

where $\lambda(z, V_{\text{fit}})$ is the equilibrium bunch distribution calculated in the double-rf system. We noted the same results were obtained when including beam-loading voltage from main cavities and, for simplicity, only beam-loading from HCs was considered.

A comparison between measured and calculated bunch profiles is presented in Fig. C.2. The HC voltages needed to match the calculated and measured bunch profiles are

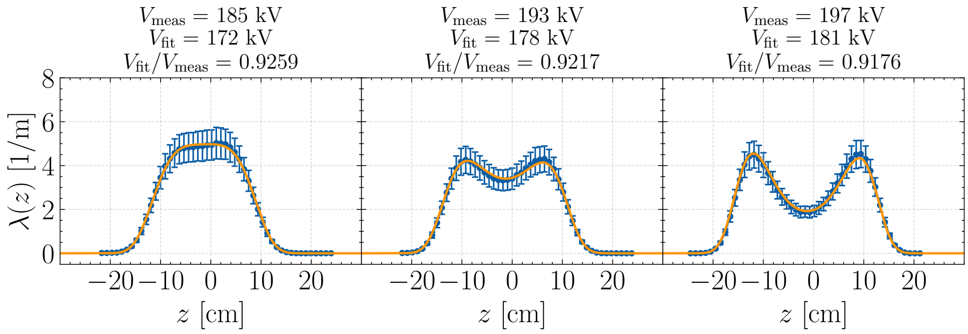

Figure C.2: Measured and calculated bunch profiles for 200 mA. Dots represent the average and error bars represent the variation of charge densities over bunches.

systematically lower than the measured voltages. A constant difference could be explained by an error in the shunt impedance considered in the calibration, for example. However, the discrepancy increases linearly with the total voltage[1], as shown in Fig. C.3.

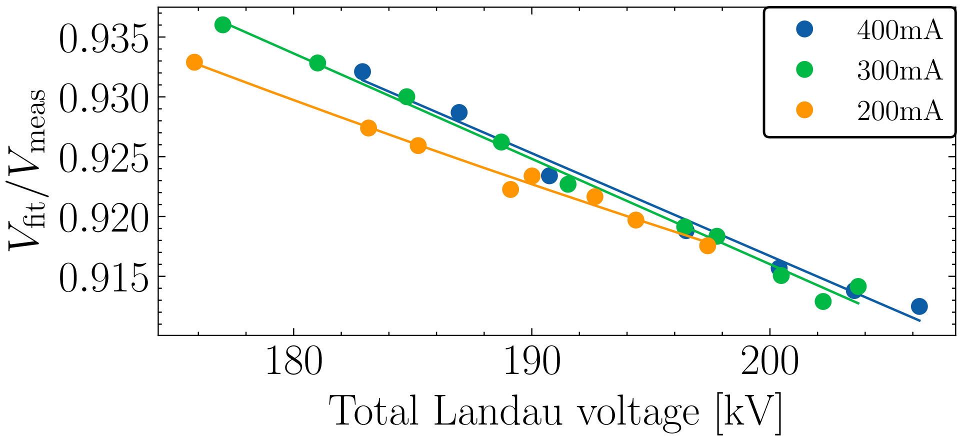

Figure C.3: Ratio between calculated and measured HC voltages for fitting bunch profiles at different beam currents.

Based on the difference between fit and measured voltages, the linear coefficient of HC voltage calibration curve was readjusted by a factor 0.93. This makes the total measured voltage of 180 kV match with the value that reproduces the measured bunch profiles. However, a small discrepancy that increases with the voltage remains, reaching an error of $0.915/0.93 = 0.98$ for the highest measured voltage of 210 kV. The adjustment

[1]The calibration of HC voltages was measured at low currents, setting the cavities on resonance which is impossible at higher currents. The discrepancy makes us question the validity of this linear calibration curve for higher currents. Perhaps some nonlinearity in the voltage measurement device in the cavity could explain a nonlinear calibration curve.

of 0.93 could be interpreted as if the actual shunt impedance of the two HCs is 5.115 MΩ, i.e., 7% lower than the value of 5.5 MΩ considered previously. This estimated error is considerably larger than bench measurements indicate. Even so, for this study, the HC voltage values were adjusted by the 0.93 factor.

C.4 Lifetime optimization

The increment in Touschek lifetime due to the bunch lengthening provided by the HCs can be estimated by [23]:

$$\frac{\tau_{\text{HC}}}{\tau_0} = \frac{\int \lambda_0^2(z)dz}{\int \lambda_{\text{HC}}^2(z)dz}, \tag{C.3}$$

where $\lambda_0(z), \lambda_{\text{HC}}(z)$ are the normalized bunch profiles without and with HC fields, respectively. This calculation assumes that the effect of HCs on energy acceptance is small, which is typically a good approximation.

It is known from simulations that profiles corresponding to HC voltages higher than the flat potential case can be better for lifetime improvement [44, 158]. In this condition, referred as overstretched, the bunch profiles have a double-peaked shape. To investigate this experimentally, the HC voltage was adjusted above flat potential, while measuring the bunch profiles and the beam lifetime as well. For the main rf voltage of 522.3 kV used during the experiment, the flat potential HC voltage is 169.3 kV. The measurements were carried out with three different values of stored currents in uniform fill.

In the first run with 200 mA, we observed that for 185 kV (9% above the flat potential voltage), a coupled-bunch mode-0 instability was excited, probably a Robinson instability driven due the small detuning of the harmonic cavities (130 kHz in this case). The mode-0 instability limited the maximum value of HC voltage for the scan at 200 mA. Figure C.4 show the results for the first sequence of measurements.

For the second run, the stored current was increased to 300 mA. At higher currents the same HC voltage is achieved with a larger detuning, thus the Robinson instability could be avoided. However, for 188 kV, coupled-bunch instabilities were excited by HOMs of the HCs. After temperature tuning of HCs , the HOMs' frequencies shifted and the instabilities were suppressed. At the new operating temperatures, it was possible to further increase the HC voltage while keeping the beam stable. The results obtained at 300 mA are shown in Fig. C.5, where the negative impact of the coupled-bunch instabilities on lifetime is evident at 188 kV.

A final set of measurements at 400 mA was made. The temperature tuning that cured the coupled-bunch instabilities at 300 mA was maintained. Different from the other two cases, the initial value of HC voltage was already set to flat potential voltage of 170 kV, taking into account the identified calibration error. No instabilities were experienced in this run and the results are shown in Fig. C.6.

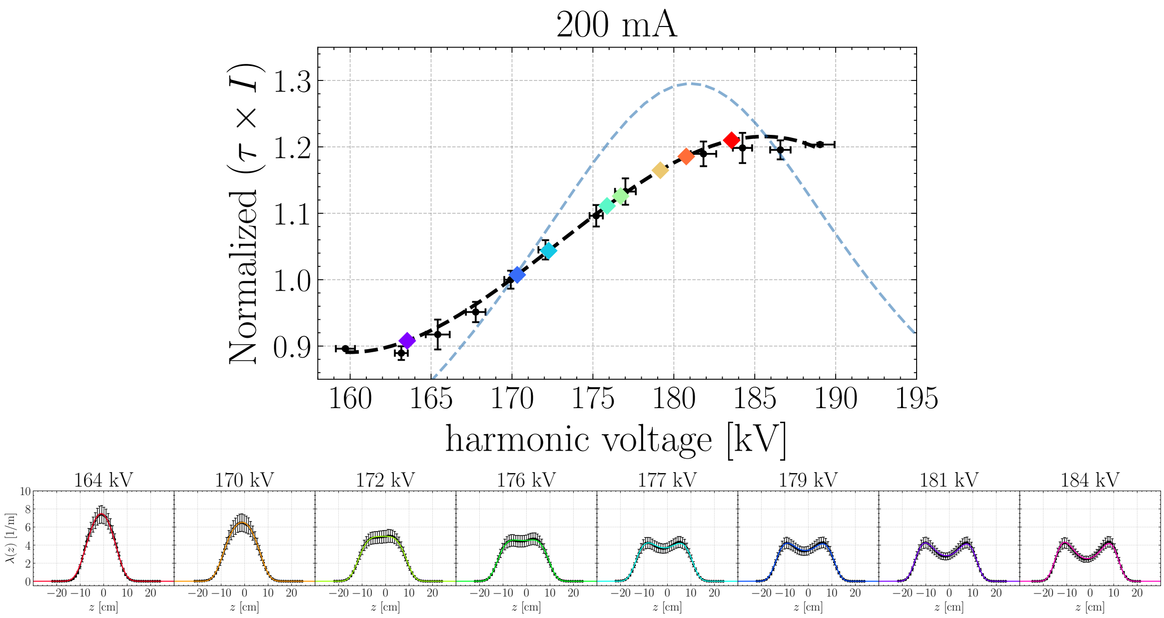

Figure C.4: Experimental results of the product lifetime × current, normalized by the same product measured with HC voltage of 170 kV (flat potential). Measurement carried out with 200 mA in the ring. The normalization value is $(\tau \times I)_{\text{flat}} = 4604\,\text{mA h}$, corresponding to a total lifetime of 23 h at 200 mA. The blue dashed curve is the calculated lifetime from Eq. (C.3) with the corresponding bunch profiles for each HC voltage. The black dots and error bars represent the mean and variation of voltage measured in a short period, respectively. The colored markers indicate the voltages in which bunch profile measurements were taken. The sequence of measured and calculated profiles for each HC voltage is presented in the bottom plots.

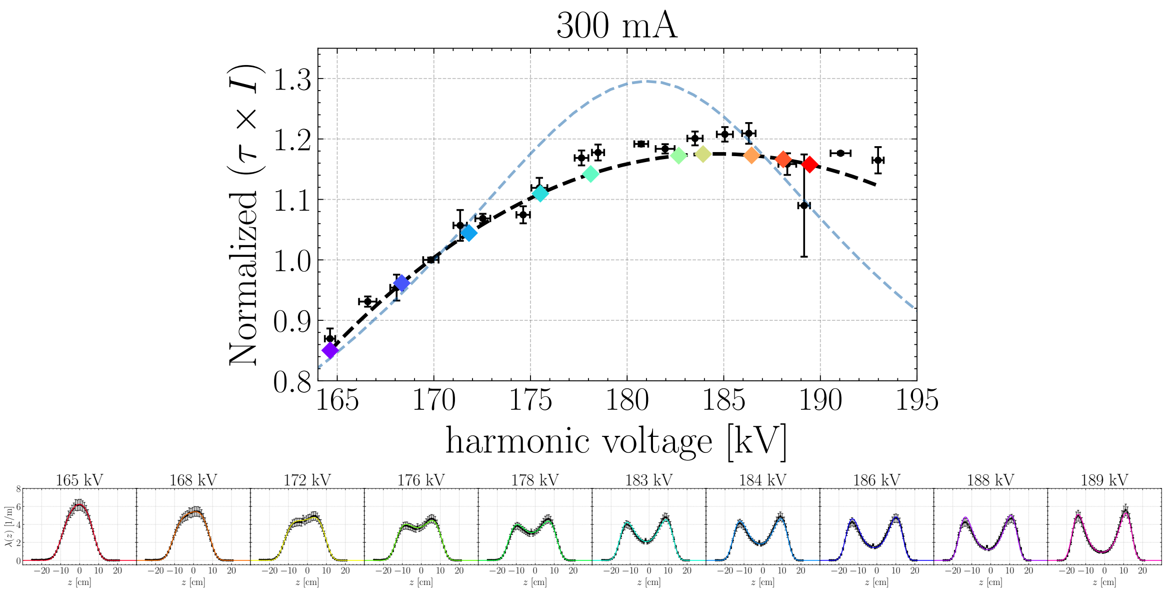

Figure C.5: Same experiment as shown in Fig. C.4 with a higher current of 300 mA. The normalization value measured with HC voltage of 170 kV is $(\tau \times I)_{\text{flat}} = 5712\,\text{mA h}$, corresponding to a lifetime of 19 h at 300 mA.

C.5 Discussion and conclusion

The results shown in Figs. C.4, C.5 and C.6 confirm that operating with HC voltages beyond the flat potential can help to improve beam lifetime. Moreover, we were able

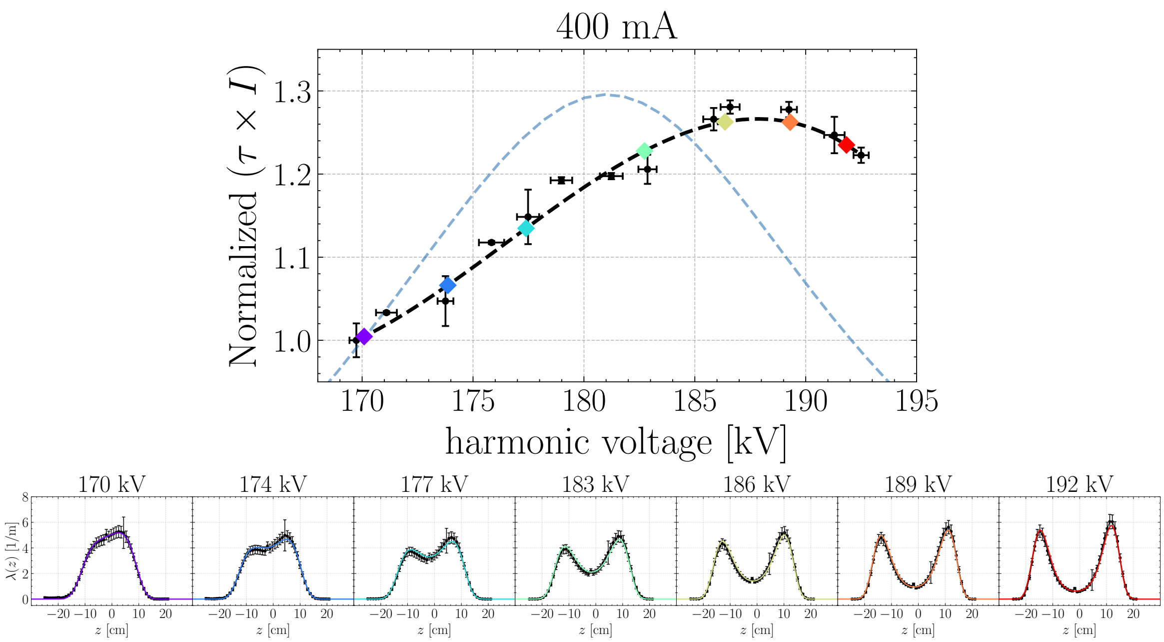

Figure C.6: Same experiment as shown in Figs. C.4 and C.5 with a higher current of 400 mA. The normalization measured with 170 kV of HC voltage is $(\tau \times I)_{\text{flat}} = 4642$ mA h, corresponding to a lifetime of 11.6 h at 400 mA. The point close to $z = 5$ cm with large variation in intensity should be just an artifact from the streak-camera acquisition.

to find in simulation the HC voltages that produced bunch profiles in close agreement with streak-camera measurements. This fitting process has the potential to be useful as a beam-based calibration of HC voltages at high current. Benchmarking against other calibration methods is required for validation.

Experiments with stored beam currents of 200 mA and 300 mA were limited by beam instabilities. The product (lifetime × current) was higher with 300 mA compared to 200 mA and 400 mA, suggesting that other uncontrolled factors were affecting the lifetime in this case. Interestingly, the beam remained stable at the highest current of 400 mA, allowing acquisitions with highly overstretched bunches.

Overall, the observed improvement in lifetime with HCs did not match the theoretical expectation based on Eq. (C.3). The best HC voltage for lifetime was consistently higher than expected and the range of voltages producing longer lifetimes in practice is broader than predicted. This could be because Eq. (C.3) assumes that, except for the longitudinal density, all parameters remain constant, while they may vary in reality. Additionally, the formula only considers the impact of HCs on Touschek lifetime, while the total lifetime was measured. Further studies are needed to investigate these differences.

Annex: List of Publications

The scientific material developed during the four years of the PhD (March 2021–March 2025) has been published in peer-reviewed articles, conference proceedings and open-source codes. The references for the material included in the thesis are presented below. References for additional publications that are not part of the thesis but were made during the PhD period are also provided.

Publications included in the thesis

Peer-reviewed articles

1. **Alves, M. B.** and de Sá, F. H. Equilibrium of longitudinal bunch distributions in electron storage rings with arbitrary impedance sources and generic filling patterns. *Phys. Rev. Accel. Beams* **26**, 094402 (2023). DOI: https://doi.org/10.1103/PhysRevAccelBeams.26.094402
   Appendix A. Published as Ref. [44].

2. **Alves, M. B.** Theoretical models for longitudinal coupled-bunch instabilities driven by harmonic cavities in electron storage rings. *Phys. Rev. Accel. Beams* **28**, 034401 (2025). DOI: https://doi.org/10.1103/PhysRevAccelBeams.28.034401
   Appendix B. Published as Ref. [45].

Conference proceeding

3. **M. Alves**, A. Andersson, and F. Cullinan, Optimizing Touschek lifetime with overstretched bunch profiles in the MAX IV 1.5 GeV ring, IPAC'24, Nashville, TN, USA, May 2024, doi:10.18429/JACoW-IPAC2024-WEPR42
   Appendix C. Published as Ref. [46].

Code implementation

4. de Sá, F. H. and **Alves, M. B.** `pycolleff` and `cppcolleff`: modules for impedance analysis and wake-field induced instabilities evaluation (2024). URL https://doi.org/10.5281/zenodo.14217110 (v1.0.4)

5. Resende, X., Mukai, A. H., Vilela, L. N., de Sá, F. H. and **Alves, M. B.** Touschek lifetime calculations on `pyaccel`—a Python module for beam dynamics tracking and optics calculations in particle accelerators (2024). URL https://github.com/lnls-fac/pyaccel

6. Gamelin, A., Gubaidulin, V., **Alves, M. B.** and Olsson, T. ALBuMS—Algorithms for Longitudinal Multibunch Beam Stability (2024). URL https://gitlab.synchrotron-soleil.fr/PA/collective-effects/albums

Additional publications not included in the thesis

2024

7. Gamelin, A.; Gubaidulin, V.; **Alves, M. B.** and Olsson, T. Semi-analytical algorithms to study longitudinal beam instabilities in double rf systems (2024). ArXiv preprint. URL https://doi.org/10.48550/arXiv.2412.06539
Submitted for publication. Preprint available as Ref. [103].

8. **M. Alves** and F. de Sá, Slow longitudinal mode 1 instability in electron storage rings with harmonic cavities, IPAC'24, Nashville, TN, USA, May 2024, doi:10.18429/JACoW-IPAC2024-MOPS32
Published as Ref. [140].

9. F. de Sá, G. Gomes, I. Carvalho de Almeida, L. Liu, **M. Alves**, and X. Resende, Broadband impedance induced heating proxy for operation at higher total current at SIRIUS, IPAC'24, Nashville, TN, USA, May 2024, doi:10.18429/JACoW-IPAC2024-THPC44
Published as Ref. [42].

10. D. Daminelli, A. Lima, F. K. G. Hoshino, M. Souza, **M. Alves**, and V. Freire, Improvements of longitudinal stability with LLRF optimization at SIRIUS, in Proc. IPAC'24, Nashville, TN, USA, May 2024, pp. 3435-3438. doi:10.18429/JACoW-IPAC2024-THPG69
Published as Ref. [159].

11. G. Ascenção, F. de Sá, L. Lin, M. Velloso, **M. Alves**, and X. Resende, Impact of Delta undulator on SIRIUS beam dynamics, in Proc. IPAC'24, Nashville, TN, USA, May 2024, pp. 3769-3772. doi:10.18429/JACoW-IPAC2024-THPS18
Published as Ref. [160].

2023

12. **M. B. Alves**, Algebraic solution for the classical harmonic oscillator, Revista Brasileira de Ensino de Física, 45, e20230152 (2023). DOI: 10.1590/1806-9126-RBEF-2023-0152
Published as Ref. [161].

13. M. M. S. Velloso, F. H. de Sá, and **M. B. Alves**, Fast orbit response matrix measurement via sine-wave excitation of correctors at Sirius, Journal of Physics: Conference Series, 2420(1), 012048 (2023). DOI: 10.1088/1742-6596/2420/1/012048
Published as Ref. [162].

14. M. Velloso, L. Liu, F. de Sá, **M. Alves**, X. Resende, and X. Huang, Online optimization of SIRIUS nonlinear optics, in Proc. IPAC'23, Venice, Italy, May 2023, pp. 3302-3305. doi:10.18429/JACoW-IPAC2023-WEPL087
Published as Ref. [163].

15. G. Ascenção, **M. Alves**, L. Liu, and X. Resende, Study of insertion devices effects in SIRIUS, in Proc. IPAC'23, Venice, Italy, May 2023, pp. 1184-1187. doi:10.18429/JACoW-IPAC2023-MOPM088
Published as Ref. [164].

16. L. Liu, **M. B. Alves**, F.C. Arroyo, G.O. Brunheira, G.R. Cruz, A.F. Giachero, A.C.S. Oliveira, F.S. de Oliveira, G.S. Ramirez, X.R. Resende, E.N. Rolim, F.H. de Sá, D.O. Tavares, H. Westfahl Jr, Status of SIRIUS operation with users, in Proc. IPAC'23, Venice, Italy, May 2023, pp. 2586-2589. doi:10.18429/JACoW-IPAC2023-WEOGA2
Published as Ref. [165].

2022

15. **M. B. Alves**, L. Liu, X. R. Resende, and F. H. de Sá, Beam Lifetime Measurements in Sirius Storage Ring, IPAC'22, Bangkok, Thailand, Jun. 2022, doi:10.18429/JACoW-IPAC2022-MOOYSP2
Published as Ref. [63].

16. F. H. de Sá, **M. B. Alves**, and L. Liu, Measurements of Collective Effects Related to Beam Coupling Impedance at SIRIUS, IPAC'22, Bangkok, Thailand, Jun. 2022, doi:10.18429/JACoW-IPAC2022-WEPOTK055
Published as Ref. [166].

17. X. R. Resende, **M. B. Alves**, L. Liu, A. C. S. Oliveira, J. V. Quentino, and F. H. de Sá, Sirius Injection Optimization, in Proc. IPAC'22, Bangkok, Thailand, Jun. 2022, pp. 2672-2674. doi:10.18429/JACoW-IPAC2022-THPOPT038
Published as Ref. [167].

18. J. V. Quentino, **M. B. Alves**, and F. H. de Sá, Emittance Exchange at Sirius Booster for Storage Ring Injection Improvement, in Proc. IPAC'22, Bangkok, Thailand, Jun. 2022, pp.

2722-2725. doi:10.18429/JACoW-IPAC2022-THPOPT056
Published as Ref. [168].

19. L. Liu, **M. B. Alves**, F. H. de Sá, R. H. A. Farias, S. R. Marques, A. C. S. Oliveira, X. R. Resende, R. M. Seraphim, H. Westfahl Jr, Status of Sirius Operation, in Proc. IPAC'22, Bangkok, Thailand, Jun. 2022, pp. 1385-1388. doi:10.18429/JACoW-IPAC2022-TUPOMS002
Published as Ref. [169].

20. S. R. Marques, **M. B. Alves**, F.C. Arroyo, G.O. Brunheira, M.P. Calcanha, H.F. Canova, A.C.T. Cardoso, R.B. Cardoso, F.H de Sá, R.J. Leão, L.R. Leão, B.E. Limeira, L. Lin, P.H.S. Martins, S.S. Moreira, R.T. Neuenschwander, R.O. Neto, A.G.C. Pereira, Improvements on Sirius Beam Stability, in Proc. IPAC'22, Bangkok, Thailand, Jun. 2022, pp. 226-229. doi:10.18429/JACoW-IPAC2022-MOPOPT002
Published as Ref. [170].

2021

18. **M. B. Alves**, Optics Corrections with LOCO on Sirius Storage Ring, in Proc. IPAC'21, Campinas, Brazil, May 2021, pp. 825-828. doi:10.18429/JACoW-IPAC2021-MOPAB260.
Published as Ref. [171].

19. L. Liu, **M. B. Alves**, A. C. S. Oliveira, X. R. Resende, and F. H. de Sá, Sirius Commissioning Results and Operation Status, in Proc. IPAC'21, Campinas, Brazil, May 2021, pp. 13-18. doi:10.18429/JACoW-IPAC2021-MOXA03
Published as Ref. [172].

20. X. R. Resende, **M. B. Alves**, L. Liu, and F. H. de Sá, Equilibrium and Nonlinear Beam Dynamics Parameters From Sirius Turn-by-Turn BPM Data", in Proc. IPAC'21, Campinas, Brazil, May 2021, pp. 1935-1938. doi:10.18429/JACoW-IPAC2021-TUPAB219
Published as Ref. [173].

21. A. C. S. Oliveira, **M. B. Alves**, L. Liu, X. R. Resende, and F. H. de Sá, High Level Applications for Sirius Accelerators Control, in Proc. IPAC'21, Campinas, Brazil, May 2021, pp. 4314-4317. doi:10.18429/JACoW-IPAC2021-THPAB259
Published as Ref. [174].